

Experimental and Numerical Modeling of Scour at Offshore Wind Turbines

Von der Fakultät für Bauingenieurwesen und Geodäsie
der Gottfried Wilhelm Leibniz Universität Hannover

zur Erlangung des Grades
DOKTOR-INGENIEUR
Dr.-Ing.

genehmigte Dissertation

von

Dipl.-Ing. Arne Stahlmann
geboren am 4. Februar 1982
in Düsseldorf

2013

Referent: Prof. Dr.-Ing. habil. Torsten Schlurmann
Korreferent: Prof. Dr.-Ing. Thomas Rung
Tag der Promotion: 26. April 2013

Danksagung

Die vorliegende Arbeit entstand während meiner Zeit als wissenschaftlicher Mitarbeiter am Franzius-Institut für Wasserbau und Küsteningenieurwesen der Leibniz Universität Hannover. Die grundlegende Idee zur Untersuchung von Kolkphänomenen an Gründungsstrukturen für Offshore-Windenergieanlagen und insbesondere die Erstellung eines numerischen Modells entstand dabei im Rahmen des BMU Forschungsvorhabens Gigawind alpha ventus. Zusätzlich haben weitere Forschungsvorhaben am Institut auf diesem Gebiet, die ich während meiner Zeit begleiten durfte, ihren inhaltlichen Beitrag geleistet.

Für die eigentliche Anfertigung meiner Dissertation gilt ein besonderer Dank Herrn Prof. Dr.-Ing. habil. T. Schlurmann, für die Begleitung und Förderung, für das mir entgegengebrachte Vertrauen sowie den überlassenen Freiraum zur inhaltlichen Ausgestaltung meiner Arbeit. Die fachlichen Diskussionen, Ideen und Vorschläge waren stets eine Bereicherung. Ein weiterer Dank gilt Herrn Prof. Dr.-Ing. T. Rung für die Anfertigung des Zweitgutachtens und seine Verbesserungsvorschläge für die schriftliche Ausfertigung sowie Herrn Prof. Dr.-Ing. B. Ettmer für die Anfertigung des externen Gutachtens. Auch den weiteren Mitgliedern der Prüfungskommission, Herrn Prof. Dr.-Ing. P. Schaumann mit Übernahme des Prüfungsvorsitzes, Herrn Prof. Dr.-Ing. M. Achmus sowie Herrn Prof. em. Dr.-Ing. W. Zielke möchte ich für ihren Einsatz und ihre Zeit danken.

Bei meinen Kolleginnen, Kollegen und Freunden am Franzius-Institut, die mich über die Jahre begleitet haben, bedanke ich mich herzlich für die stete Unterstützung, Zusammenarbeit und gute Arbeitsatmosphäre. Ein besonderer Dank gilt hierbei meinen beiden Kollegen Dr.-Ing. N. Goseberg und Dr.-Ing. A. Hildebrandt, die sowohl innerhalb, wie auch außerhalb des Institutsbetriebs zu einer stetigen Motivation beigetragen haben. Weiterhin danke ich den technischen Mitarbeitern für ihre Unterstützung im Rahmen der Projekte und Modellversuche, allen studentischen Mitarbeitern und hierbei insbesondere Herrn Dipl.-Ing. D. Gisen, welche alle zum Gelingen dieser Arbeit beigetragen haben. In diesem Zusammenhang gilt ein großer Dank auch Herrn Dr. N.G. Jacobsen für seine Unterstützung bei numerischen Fragestellungen im Rahmen meiner Arbeit.

Mein größter und damit abschließender Dank gilt jedoch meiner Familie. Meinen Eltern für ihre Unterstützung und ihren Zuspruch während meines Studiums und meiner Zeit als wissenschaftlicher Mitarbeiter, meiner Schwester für ihren Einsatz bei der sprachlichen Korrektur der Arbeit, und insbesondere meiner Frau Michaela für ihre immer vorhandene Unterstützung und ihre Geduld.

Abstract

Regarding offshore constructions, there is presently a lack of knowledge of scour progression for complex structures like foundations for offshore wind turbines, which is however essential for cost-effective dimensioning processes. As a step to further develop the share of renewable energies in electricity supply, numerous offshore wind parks will be constructed at the German coasts within the coming years. Detailed knowledge of scour development and its final effects on the stability and usability of the structures is therefore all the more important today. As an example of such complex structure types, tripod foundations are presently constructed in German offshore wind farms.

In order to gain new knowledge on physical processes and influencing factors on scour progression, investigations on scour phenomena for a tripod structure were carried out and will be given in the present thesis. The investigation method consists of both physical model tests in wave flumes and numerical simulations using CFD methods. The physical modeling part is carried out by means of scaled 1:40 laboratory tests in the wave flume of the Franzius-Institute in order to investigate general scour phenomena, as well as by 1:12 large-scale model tests in the Large Wave Flume (GWK) in Hanover. Different wave load conditions and wave-encounter angles of the structure are investigated in both model setups, providing information about the general processes of scour progression and final scour pattern results.

The numerical investigations are carried out within the framework of OpenFOAM software code by use of a multi-phase flow model. The fluid flow approach is based on solving the Reynolds Averaged Navier-Stokes equations, while the $k - \omega SST$ turbulence model is used for turbulence closure. On this basis, a sediment transport model approach is implemented into the code, considering both bed load and suspended load sediment transport processes, and is coupled to the hydrodynamic model. All relevant slope-dependent transport modifications are further incorporated in the model approach. Modified automatic mesh motion algorithms are implemented in order to cope with the mesh motion characteristics for complex structure investigations.

The new numerical model approach is applied to the calculation of local flow fields, bed shear stresses and scour evolution. Here, the flow patterns around a tripod structure and shear stress distributions for varying load conditions are investigated. Finally, local scour development for a vertical cylinder under current flow and a tripod structure under wave load are simulated and compared to experimental data.

Kurzfassung

Bei der Bemessung von Offshore-Bauwerken bestehen derzeit noch zahlreiche Unsicherheiten im Bezug auf die Ermittlung der Kolkgefährdung und finalen Kolkabildung an komplexen Struktursystemen, wie sie beispielsweise für die Gründung von Offshore-Windenergieanlagen eingesetzt werden. Die Abschätzbarkeit von Kolkentwicklungen ist jedoch ein entscheidender Faktor für eine ökonomische Auslegung der Anlagen, insbesondere im Hinblick auf eine Serienfertigung. Im Zuge des weiteren Ausbaus erneuerbarer Energien werden in den kommenden Jahren zahlreiche Windparks in deutschen Küstenregionen entstehen. Daher gewinnen neue, detaillierte Erkenntnisse zur Kolkentwicklung an Gründungsstrukturen unter Offshore-Bedingungen und ihr finaler Einfluss auf die Standsicherheit und Gebrauchstauglichkeit der Anlagen eine immer größere Bedeutung. Ein Beispiel für geometrisch komplexere Strukturen stellen Tripod-Gründungen dar, die derzeit in deutschen Offshore-Windparks errichtet werden.

Zur Gewinnung neuer Erkenntnisse über physikalische Prozesse und Einflüsse auf die Kolkbildung wurden Untersuchungen zur Kolkentwicklung an einer Tripod-Gründungsstruktur durchgeführt, die im Rahmen der vorliegenden Arbeit dargestellt und analysiert werden. Die Untersuchungsmethodik besteht dabei aus einer Kombination physikalischer Modellversuchen in Wellenkanälen und numerischer Untersuchungen mittels CFD. Die Experimente wurden als skalierte Modellversuche im Maßstab 1:40 und 1:12 im Wellenkanal des Franzius-Instituts und im Großen Wellenkanal (GWK) durchgeführt. Hierbei wurden unterschiedliche Belastungsparameter und Wellenlaufrichtungen untersucht, wodurch die generellen Kolkbildungsprozesse und resultierende Kolkbilder bestimmt wurden.

Die numerischen Simulationen wurden anhand des Software-Pakets OpenFOAM mittels Zweiphasen-Modellierung durchgeführt. Für das Fluid-Modell werden hierzu die Reynolds-gemittelten Navier-Stokes Gleichungen gelöst und das $k - \omega$ SST Turbulenzmodell zur Schließung des Gleichungssystems verwendet. Hierauf aufbauend wurde ein Sedimenttransport-Modell erstellt und mit dem Fluid-Modell gekoppelt, das sowohl bodennahe, wie auch suspendierte Transportprozesse und Böschungseffekte berücksichtigt. Algorithmen zur geometrischen Anpassung des Berechnungsgitters wurden für Untersuchungen komplexer Struktursysteme optimiert.

Eine Anwendung des neu entwickelten Modells erfolgte anhand der Berechnung lokaler Strömungsprozesse, Schubspannungen und Kolkphänomene. Hierbei wurden sowohl das Strömungsfeld um eine Tripod-Struktur detailliert untersucht, Bodenschubspannungen für verschiedene Belastungskombinationen ermittelt, wie auch final die Kolkbildung um einen Zylinder unter Strömungseinfluss sowie eine Tripod-Struktur unter Welleneinfluss simuliert.

Keywords

Scour, Offshore Wind Energy, Complex Foundation Structures, Physical Modeling, Numerical Modeling, CFD, OpenFOAM.

Schlüsselwörter

Kolkbildung, Offshore Windenergie, komplexe Gründungsstrukturen, physikalische Modellierung, numerische Modellierung, CFD, OpenFOAM.

Contents

1	Introduction	1
1.1	Motivations	1
1.2	Methodology & Objective	2
1.3	Outline	3
2	Background and Recent Work	5
2.1	Introduction	5
2.2	Hydrodynamic Processes	5
2.2.1	Velocity Distributions	5
2.3	Sediment Transport and Scouring Processes	9
2.3.1	Shear Stress Determination	9
2.3.2	Initiation of Motion	12
2.3.3	Transport Processes	14
2.3.4	Description of Acting Forces	15
2.3.5	Sediment Transport Formulations	16
2.3.6	Modifications in Terms of Sloping Beds	17
2.4	Scour at Marine Structures	17
2.4.1	Previous Investigations	17
2.4.2	Influencing Factors	18
2.4.3	Scour at Cylindrical Structures	19
2.4.4	Scour at Complex Structures	21
2.4.5	In-situ Measured Scour Development	22
2.4.6	Design Guidelines for Offshore Wind Turbines	23
2.5	Numerical Modeling of Scour Processes	26
2.5.1	Remarks on Model Scales	26
2.5.2	Flow and Scour around Objects and other Models	26
2.6	Conclusions	28
3	Tripod Scour Experiments	31
3.1	Methodology and Objective	31
3.1.1	Load Boundary Conditions	31
3.2	Wave-induced Scour on Laboratory Scale	32
3.2.1	Experimental Setup	32
3.2.2	Measuring Equipment	35
3.2.3	Test Procedures	38
3.2.4	Experimental Results on Scour Development, Regular Waves	40
3.2.5	Wave Spectra Representation	53
3.3	Wave-induced Scour on Large Scale	54

3.3.1	Experimental Setup	54
3.3.2	Measuring Equipment	57
3.3.3	Test Procedure	59
3.3.4	Experimental Results	61
3.4	Model Comparison	68
3.4.1	Prototype Scale, Field Data	68
3.4.2	General Remarks on Scaling Effects	69
3.4.3	Model Result Comparison	70
3.5	Conclusions	72
4	Numerical Model of Flow and Scour	75
4.1	Introduction	75
4.1.1	OpenFOAM Software Toolbox	75
4.2	Two-Phase Flow Model	76
4.2.1	Fluid Flow Solver and Governing Equations	77
4.2.2	Turbulence Model	78
4.2.3	Model Domain and Grid Generation	81
4.2.4	General Boundary Conditions	84
4.2.5	Turbulence Boundary Conditions	86
4.2.6	Surface Wave Modeling	89
4.2.7	Non-reflecting Outlet Boundaries	90
4.3	Sediment Transport Model	93
4.3.1	Shear Stress Determination	94
4.3.2	Bed Load Transport	94
4.3.3	Suspended Load Transport	98
4.3.4	Sediment Boundary Conditions	106
4.3.5	Morphological Update	106
4.3.6	Sediment Sliding on Large Bed Slope	108
4.4	Moving Mesh Approaches	110
4.4.1	Distance-based Mesh Motion Function	111
4.4.2	Mesh Motion Function based on Laplace Equation	112
4.4.3	General Remarks and Model Choice	112
4.5	Model Coupling	113
4.5.1	Present Coupling Procedure	114
4.6	Conclusions	115
5	Numerical Model Application	117
5.1	General considerations	117
5.2	Model Verification	117
5.2.1	Wave Modeling	117

5.2.2	Local Flow Characteristics around Tripod Structure	120
5.3	Results of Flow and Shear Stress Calculations	121
5.3.1	Flow Field around Tripod under Waves	122
5.3.2	Shear Stress Distributions	129
5.3.3	Influence of Model Scales	135
5.4	Scour Simulations	140
5.4.1	Choice of Sediment Entrainment Approach	140
5.4.2	Scour around Vertical Cylinder under Steady Current	141
5.4.3	Scour around Tripod under Waves	145
5.4.4	Final Remarks	152
5.5	Conclusions	155
6	Summary & Outlook	157
6.1	Experimental Investigations	157
6.2	Numerical Investigations	158
6.3	Improvements and Future Work	160
	References	163
A	Appendix - WKS Experiments	183
B	Appendix - GWK Experiments	200
C	Appendix - Numerical Model Application	205
D	Curriculum Vitae	211

Nomenclature

α_r	VOF ratio coefficient
$\alpha_{1,\eta}$	threshold value for the location of the free surface
β	bed slope angle
δ	boundary layer thickness
δ_c	grid resolution as edge length
η	free surface location in numerical model
κ	van Karman constant
λ	Froude scaling factor
μ	dynamic fluid viscosity
μ_d	dynamic friction coefficient
μ_s	static friction coefficient
ν	kinematic fluid viscosity
ν_d	artificial viscosity in numerical wave damping zone
ν_t	turbulent viscosity
ω, ϵ	turbulence dissipation
ρ, ρ_f	fluid density
ρ_o	particle or object density
σ_c	turbulent Schmidt number
τ_b	bed shear stress, general definition
τ_c	bed shear stress, current-induced
τ_w	bed shear stress, wave-induced
$\tau_{b,cr}$	critical bed shear stress
θ	Shields number
θ_c, θ_{cr}	critical Shields number
c	volumetric suspended sediment concentration

c_b	suspended sediment reference concentration
c_D, C_D	drag coefficient
c_L	lift coefficient
c_0	maximum sediment concentration
Co	Courant-Friedrichs-Lewy criterion, CFL
D	pile or structure diameter
D	suspended sediment deposition flux
d	grain diameter, general definition
D_*	dimensionless particle diameter
d_{50}	median grain diameter
D_ν	diffusivity
d_m	mean particle diameter
d_N	nominal particle diameter
d_s	particle sieving diameter
E	suspended sediment entrainment flux
F_{drag}	drag force
F_{fric}	friction force
$F_{g,\tau}$	gravity force, in slope direction
g	gravitational acceleration
H_m	mean wave height, regular waves
H_s	significant wave height, wave spectrum
H_{max}	maximum wave height, wave spectrum
k	turbulent kinetic energy
k_s	equivalent sand roughness height
k_s^+	normalized equivalent sand roughness
KC	Keulegan-Carpenter number

q_b	bed load transport rate
R_{ij}	Reynolds stress
Re	Reynolds number
S_c	source/sink term in sediment transport equation
s_{sg}	submerged specific gravity
St	Strouhal number
T_m	mean wave period, regular waves
T_p	peak wave period, wave spectrum
u, v, w	velocities in x,y,z direction
u^+	dimensionless near-wall velocity
u_m	depth-averaged current velocity
u_f, u^*	friction velocity
W_*	dimensionless sediment settling velocity
w_s	concentration-dependent settling velocity
$w_{s,a}$	sediment settling velocity in air
$w_{s,w}$	sediment settling velocity in water
w_{s0}	sediment settling velocity, single particle
y^+	dimensionless wall distance
y_0	zero velocity level or bed roughness length

1 Introduction

When a structure is placed into the marine environment, it is exposed to fluid flow processes of the surrounding water. The flow field itself is affected by the presence of the structure, resulting in typical effects like flow concentration, vortex shedding or wave reflection. As a result, the local flow velocities and shear stresses at the sea bed in the near-field of the structure are increased. For bed material that is vulnerable to erosion under the present conditions, this subsequently leads to enhanced sediment mobility and therefore scouring effects directly at or in the near-field of the structure embedded at the sea floor. Depending on the global scour evolution, boundary conditions and the structural dimensioning, this might have an influence on the stability and usability as well as the durability of the structure and might even lead to a complete collapse of the system.

An important application where the knowledge of scouring processes comes into play is the foundation of offshore wind turbine supporting structures. Offshore wind turbines have been constructed all over the world in recent years, while different effects of scour development could be found. In the marine environment, scour is typically induced by combined load due to waves and tidal currents. Depending on the structural type and given environmental conditions, scour depths of several meters could be observed, developed even within short periods.

As a step to further develop the share of renewable energies in the German electricity supply, numerous offshore wind farms with thousands of planned wind turbines will be constructed at the German coasts within the coming years. Detailed knowledge on scour development is therefore all the more important today. The starting signal for this offshore development at German coasts was given by the construction of the first offshore test site alpha ventus in the North Sea, located 45km off the coast of the Borkum Island. Here, experience on construction, operation and maintenance shall be gained and made available for future offshore wind farms. In the alpha ventus test site, six of the overall twelve turbines installed there are constructed on tripod foundations, whereas the remaining ones are founded on jacket substructures. At the time of final installation, no detailed knowledge on scour progression around tripod foundations was however available.

1.1 Motivations

To date, there are still a lot of open questions regarding scouring effect, although a lot of research on this topic has been carried out over the past decades. The generally complex phenomenon of scouring becomes even more complex when combined loads come into play. Although general mechanisms are well-known from rivers in hydraulic engineering, new problems arise for offshore foundations in intermediate

water depths due to combined wave-current loads on the one hand and the often complex structural shapes on the other hand. Furthermore environmental impacts like liquefaction especially in combination with gravity structures founded on the sea floor, gravity settlement or general biological effects are not yet completely understood or even investigated in detail.

Regarding local scour formation, it can generally be stated that especially for complex foundation types, significant knowledge gaps in scour initiation and progression and its probable effects on the stability and usability of the structure are given, still leading to a lack of practical design guidelines. Therefore, such complex structures are generally constructed on a secure-based, but mostly cost-ineffective strategy. As a main part of the overall costs for offshore wind turbines is given by foundation, the choice of the foundation type, an acceptable scour depth and the choice and dimensioning of a probable scour protection system have a high significance. Current design guidelines and the respective literature therefore give estimating values based on knowledge for pile foundations, however with a high scatter in their results. Complex foundations that differ in shape from single pile foundations are not captured at all. Due to the absence of alternatives, the particular design rules are nevertheless used as well for such complex scour predictions today. A problem of the application for more complex foundation types is however the fact that the design scour depths might either lead to values that are far from reality, especially for gravity based foundations with large diameters, or might not completely capture the actual scour development, as it is the case for local scouring effects underneath structural elements. Stahlmann and Schlurmann (2012b)

Investigations on offshore structures are mainly carried out in terms of physical modeling. In order to minimize possible scaling effects especially regarding the model sediment, large facilities are necessary to model scour processes. As typically only one constellation of structural type and load conditions can be modeled at one time, experimental tests are rather time- and cost-consuming, especially when parameter studies need to be carried out.

1.2 Methodology & Objective

As an extension of the classical physical modeling approach, both costs and time could be reduced when alternatively carrying out parts of the investigations in numerical model simulations. A possible hybrid-model coupling could in this case result in general validation cases carried out by means of laboratory experiments, while parameter studies and further analyses on structural details are conducted in numerical simulations. To the author's knowledge, no numerical investigations on local, wave-induced scour around complex foundations including all relevant transport processes have been carried out so far, or are at least not publicly available.

In order to gain deeper knowledge of local flow characteristics and scour evolution at a tripod foundation for offshore wind turbines, investigations on this topic have been carried out by means of physical model tests and numerical simulations within this work.

The physical modeling part was carried out by means of scaled 1:40 laboratory tests in the wave flume of the Franzius-Institute in order to investigate the general scouring phenomena, as well as by 1:12 large-scale model tests in the Large Wave Flume (GWK) in Hanover.

The numerical investigations were carried out within the framework of the OpenFOAM software code platform by use of a multi-phase fluid flow model containing viscosity and turbulence. The fluid flow approach is based on the Reynolds Averaged Navier-Stokes equations, while the $k - \omega SST$ turbulence model is used for turbulence closure. On this basis, a sediment transport model approach was implemented in the code, including bed load and suspended load transport processes as well as slope-dependent transport modifications. Several methodologies for mesh generation and control, mesh motion procedure and coupling of the hydrodynamic model with the sediment transport part were further implemented. The model captures two interfaces, namely the water-air and water-sediment interface. The free surface is modeled using the Volume of Fluid method, while the water-sediment interface is modeled using a moving mesh approach. As long simulation times are inevitable at morphological processes at complex structures, parallel coding was used throughout.

1.3 Outline

In chapter 2, a summary of relevant hydrodynamic and sediment transport mechanisms is given. Furthermore, previous investigations and findings on scour at marine structures are given, as well as a brief overview of previous numerical model simulations on local scouring and sediment transport. In chapter 3, both the experiments for the 1:40 laboratory tests and the 1:12 large scale tests are described. Both sections start with the general model setup and procedures and give final results in the end. The chapter is closed with a comparison of the scale test results. Chapter 4 starts with a general description of the hydrodynamic model approach including turbulence modeling and boundary conditions. Afterwards, the implementation of the sediment transport model is given in a detailed manner. Finally, the implemented mesh motion approaches are described, as well as the model coupling procedure. In chapter 5, the model is verified and applied to rigid bed flow and shear stress calculations as well as scour simulations, while the latter is carried out on a tripod structure under wave and a cylinder structure under steady current load. Finally, a discussion on the model results, a general conclusion and prospects of future fields of investigations are given in chapter 6.

2 Background and Recent Work

2.1 Introduction

Regarding marine structures and especially foundations for offshore wind turbines investigated here, it is well known that in most cases scouring occurs around the foundations, owing to the presence of the supporting structure and hence affecting changes in the natural flow regime at the sea bed around the foundation, leading to increased sediment mobility. Depending on the depth and extent of scours, serious stability and usability issues might occur. In contrast to fluvial environments, where scour for example at bridge piers occurs mainly due to unidirectional flow or flooding, an interaction of waves (oscillating) and tidal currents (alternating) leads to scour at offshore foundations in case of the marine environment. Due to complex interaction and superposition of the single load components, the effect of sediment mobility and hence resulting scour is typically increased, but can be partly decreased, depending on the temporal and directional superposition.

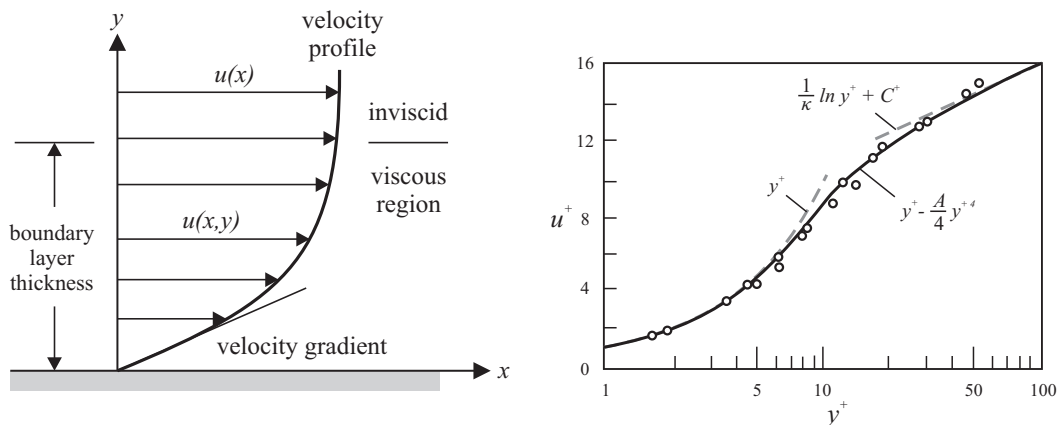
2.2 Hydrodynamic Processes

As the hydrodynamic processes of the marine environment in the near-field of a turbine structure are the driving forces leading to scour effects, a brief description is given in the following. The structure follows the general classification of load conditions found in literature, given as pure flow, pure wave and combined load cases, while the latter gives the natural load climate in most marine areas.

2.2.1 Velocity Distributions

Uniform Flow Conditions Typically, a fluid interacts with the surface of an arbitrary structure when flowing over it. Under ideal conditions, the velocity distribution of such a wall-affected fluid above the surface can be described by use of the boundary layer theory. According to Zanke (1982a), the boundary layer δ reaches from the surface of the structure, where the velocity is zero due to a no-slip condition, up to the point where $\sim 99\%$ of the fluid velocity in the undisturbed flow regime is reached. The thickness of the boundary layer is influenced by the surface roughness, the turbulence flow characteristics and the Reynolds number of the flow. The literature says that the boundary layer is typically subdivided into three layers: the near-surface viscous (laminar) sublayer, the logarithmic (log) layer and the buffer layer in between as given in figure 2.1, while outside the boundary layer, the velocity distribution is nearly uninfluenced by the object surface.

For the viscous sublayer and the logarithmic layer, analytical approximation functions for calculation of the velocities subject to wall distance and surface rough-



(a) Boundary layer development in uniform flow (b) Universal distribution of u^+ over y^+ , after conditions, smooth wall case. Schlichting and Gersten (2006).

Figure 2.1: Boundary layer development and universal y^+ distribution. Symbols in (b): dots: measured, solid line: best fit, dashed line: approximation functions.

ness are existent, while the buffer zone typically has to be bridged by use of blending functions. The approximation functions given in figure 2.1b (dashed lines) correspond to the dimensionless wall-normal distance y^+ and the dimensionless near-wall velocity u^+ normalized by the friction velocity u_f or u^* , which are given as

$$y^+ = \frac{u_f y}{\nu} \quad (2.1)$$

and

$$u^+ = \frac{u}{u_f} \quad (2.2)$$

with y being the orthogonal distance from the point to the wall, u the near-wall velocity and ν the kinematic viscosity of the fluid. In the viscous sublayer, the distribution can be approximated as

$$u^+ = y^+ \quad (2.3)$$

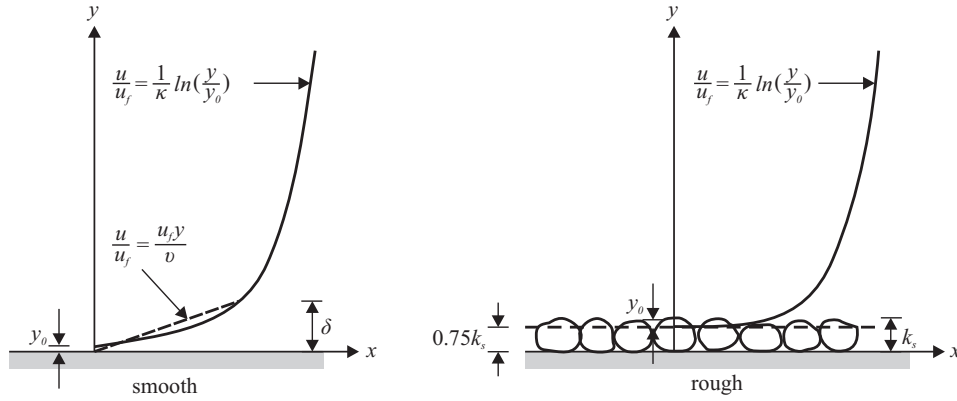
while in the logarithmic layer, the approximation function takes a form of

$$u^+ = \frac{u}{u_f} = \frac{1}{\kappa} \ln y^+ + C^+ \quad (2.4)$$

for hydraulically smooth walls with the van Karman constant $\kappa = 0.41$. According to Schlichting and Gersten (2006), the roughness-dependent constant C^+ further holds a value of 5.0 in the smooth-wall case. For hydraulically rough walls, C^+ is a function of the equivalent sand roughness k_s and tends to $C_r^+ = 8.0$ for cases with high roughness. Again according to Schlichting and Gersten (2006), equation (2.4) then takes the form

Table 2.1: Typical boundary layer classifications depending on y^+

y^+	viscous sublayer	buffer layer	log. layer
Ferziger and Peric (2008) (n^+)	0 - 1	1 - 30/50	> 30/50
Zanke (1982a) (k_s^+)	0 - 3.32	3.32 - 70	> 70
Schlichting and Gersten (2006)	0 - 5	5 - 70	> 70

**Figure 2.2:** Current velocity profiles in smooth and rough bed conditions. Modified after van Rijn (1993).

$$u^+ = \frac{1}{\kappa} \ln y^+ + C^+(k_s^+) = \frac{1}{\kappa} \ln \frac{y}{k_s} + C_r^+(k_s^+) \quad (2.5)$$

According to the experimental work in Nikuradse (1933), the bed roughness k_s is composed of the single grain roughness $k_{s,g}$ and the form roughness $k_{s,f}$ to account for the influence of bed forms like ripples and sand dunes. In the literature, different values for the y^+ layer limits can be found, which is due to the fact that the approximation functions are only valid in particular ranges; strict validity limits can however not be given. Different, widely used layer classifications are therefore given exemplarily in table 2.1.

For rough wall boundary layers, the classification remains the same, y^+ is however replaced by the normalized sand roughness $k_s^+ = k_s u_f / \nu$ then. Smooth and rough walls are defined as follows: If the roughness height k_s is smaller than the viscous sublayer, a hydraulically smooth wall case is given. In contrast, a rough case is given when the bed roughness elements extend into the logarithmic layer, see figure 2.2, meaning that no viscous sublayer is existing. In rough wall flows, the location of the theoretical bed is approximated to be located at a height of 0.75 times the total height of the roughness elements. For hydraulically transitional flow situations, the current velocity distribution is effected by both the bed roughness and the fluid viscosity.

Flow conditions in the boundary layer can generally be laminar or turbulent. According to Zanke (1982a) and van Rijn (1993), the existing turbulence state depends

on the Reynolds number and wall roughness as well as the pressure distribution and turbulence conditions in the outer flow regime. For fully developed, turbulent flow conditions in the fluvial or marine environment, the boundary layer typically ranges over almost the complete water depth up to the free surface. In the mathematical sense, the ideal velocity profile is given according to van Rijn (1993) as

$$u = \frac{u_f}{\kappa} \ln \left(\frac{y}{y_0} \right) \quad (2.6)$$

in which y_0 gives the zero velocity level over ground (sometimes also denoted as roughness length), a theoretical parameter derived when extrapolating the logarithmic velocity profile down to the ground.

For the special case of tidal ocean currents, Whitehouse (1998) alternatively gives an exponential relationship that relates the spatial current velocity to the distance over ground:

$$\begin{aligned} u(y) &= \left(\frac{y}{0.32d} \right)^{1/7} \cdot u_m & \text{for } 0 \leq y \leq 0.5d \\ u(y) &= 1.07 \cdot u_m & \text{for } 0.5d \leq y \leq d \end{aligned} \quad (2.7)$$

with d as the water depth, y as the variable giving the distance to the ground as a function of the water depth and u_m the mean, depth-averaged current velocity.

Natural Wave Conditions Analytical approximations for surface elevation and velocity distributions under wave conditions exist among the particular wave theories, e.g. Airy and Laplace, Stokes, Cnoidal or Stream Function Theory. Although wave theories are generally based on idealizations regarding the particular components and boundary conditions, they nevertheless provide practical and reasonable information for mainly two-dimensional wave modeling cases as they can be found in wave flumes. Due to information on both the free surface location and the particular velocity components over time and space, they can easily be adopted for wave generation techniques as well as for wave propagation validation cases in numerical models.

For practical engineering applications in terms of sediment transport processes, Soulsby (1997) states that the use of 2nd order Stokes wave theory gives adequate results in many cases. For sediment transport, the (horizontal) velocity near the bed is of main interest, which might be calculated from

$$u_{wc} = u_w \left[1 + \frac{3kh}{8 \sinh^3(kh)} \frac{H}{h} \right], \quad u_{wt} = u_w \left[1 - \frac{3kh}{8 \sinh^3(kh)} \frac{H}{h} \right] \quad (2.8)$$

in which u_{wc} and u_{wt} are the velocities under wave crest and trough, respectively due to the natural asymmetry of the waves, k wave number, H wave height, h water depth and u_w the velocity component for monochromatic waves with T as the wave

period, given as

$$u_w = \frac{\pi H}{T \sinh(kh)} \quad (2.9)$$

Natural sea state conditions are however always irregular and consist of a large spectrum of varying wave heights, periods and directions, whose superposition and interaction can be described in waves spectra, while the JONSWAP or Pierson-Moskowitz wave spectra are the most commonly used forms. For numerical applications, it might however be necessary to find corresponding monochromatic wave representations, which are therefore discussed later in §3.2.5.

Combined Wave-Current Conditions In marine environments with tidal flow influence, the typical and predominant condition is a combination of the single wave and current load components given above. Typically, the logarithmic current profile is dominant over a large range of water depth. Near the sea bed where it approaches to zero, the wave-induced velocity is however dominant. According to Soulsby (1997), the interaction of waves and current velocity comprises three main factors: (1) the change in phase velocity and wave length due to current action leading to refraction, (2) the reciprocal change of the boundary layer leading to a nonlinear increase of shear stresses and (3) wave-induced streaming phenomena.

So far, no valid analytical approximation for the velocity distribution under combined wave-current load exists, which is mainly due to the complexity of interactions between the single load components. Therefore, existing approaches are highly based on empirical data.

2.3 Sediment Transport and Scouring Processes

2.3.1 Shear Stress Determination

General Definition Shear stress τ can generally be defined as the component of the stress which is exerted on a material, aligned coplanar with its cross section. In fluids, the inner shear stress is proportional to the local velocity gradient, while the bed shear stress is calculated from the near-wall velocity gradient then, giving

$$\tau_b = \mu \frac{\partial u}{\partial z} \quad (2.10)$$

due to the no-slip condition at the wall boundary, with μ as the dynamic viscosity of the fluid, typically having a value of $\mu = 10^{-3} \text{Ns/m}^2$ for fresh water at 20°C temperature. Although the near-wall velocity as well as the shear stress are typically regarded as scalar quantities, equation (2.10) can be determined in vectorial form in a numerical model approach, thereby giving the direction of the bed shear stress, which is of interest for determination of areal (three-dimensional) sediment transport.

Shear Stress under Uniform Flow Besides applying equation (2.10) to determine the bed shear stress in case that the exact near-wall velocity is known, Soulsby (1997) gives a simplified expression relating the depth-averaged current velocity \bar{u} , which is more often known a priori than the near-wall velocity distribution, to the bed shear stress through the drag coefficient C_D as

$$\tau_c = \rho C_D \bar{u}^2 \quad (2.11)$$

while C_D depends on the bed characteristic in terms of grain size. Different approaches can be applied to determine the drag coefficient, while one method is given by the simple power law based on Manning-Strickler law coefficients, taking

$$C_D = 0.0474 \left(\frac{z_0}{d} \right)^{1/3} \quad (2.12)$$

Shear Stress under Waves Under wave load conditions, the developing thickness of the boundary layer is a key parameter influencing the shear stress. Oscillation of particles through the wave motion character and frictional effects at the bottom lead to oscillating boundary layers, which can not fully develop as it is known from steady flow conditions, hence resulting in thin boundary layers. Therefore, taking the velocity gradient from equation (2.10) results in an increasing shear stress with decreasing boundary layer thickness, i.e. the shear stress under wave conditions is typically much larger than under steady current flow with equal depth-averaged flow speed. According to Soulsby (1997), the shear stress in case of wave motion can be determined from

$$\tau_w = \frac{1}{2} \rho f_w u_w^2 \quad (2.13)$$

while the orbital velocity u_w is given by an appropriate wave theory. The wave friction factor f_w is determined as

$$f_w = 1.39 \left(\frac{A_w}{y_0} \right)^{-0.52} \quad (2.14)$$

for rough and

$$\begin{aligned} f_w &= 2R_w^{-0.5} & \text{for } R_w \leq 5 \cdot 10^5 \\ f_w &= 0.0521R_w^{0.187} & \text{for } R_w > 5 \cdot 10^5 \end{aligned} \quad (2.15)$$

for laminar and smooth turbulent wall cases, with $A_w = u_w T / (2\pi)$ as the wave amplitude and $R_w = u_w A_w / \nu$ the wave Reynolds number. Coefficient y_0 is further given by $d_{50}/12$ in dimensional form here, taking the grain diameter in [mm], which is valid for nearly plane bed areas. In case of large scale ripples or dunes, additional correction is necessary. Shear stresses using above given equations are determined for the maximum near-bed orbital velocities, which are typically reached under the

wave crests due to natural wave asymmetry, as they give the maximum load case. For pure sinusoidal waves, shear stresses under wave crest and wave trough passage are equal but with opposite flow directions over ground.

Shear Stress under Combined Load Due to highly nonlinear interaction between wave and current flow processes in a combined load case, the shear stress cannot be determined from the single components of the particular loads through linear addition. Following Soulsby (1997) this would lead to an underestimation of the real values. Several approaches for shear stress determination under combined wave current load were therefore developed over the past decades. A comparison of such existing model formulations was carried out in Soulsby et al. (1993) and Soulsby and Clarke (2005). All in all, certain scatter of the single model results on the one hand and the disproportionate increase of shear stress under combined load was observed on the other hand, while the latter was determined in all cases, see figure 2.3.

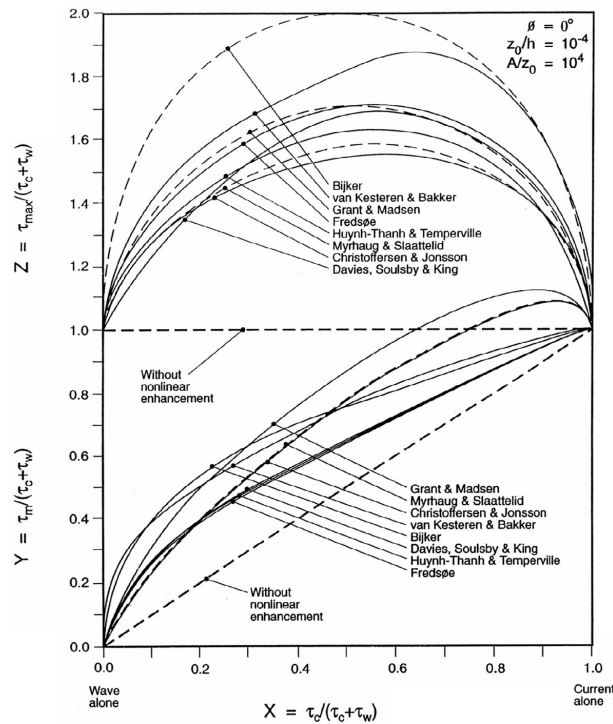


Figure 2.3: Compilation of eight different prediction models for bed shear stress calculation under combined wave-current load, giving the effect of the load components on the resulting stresses τ_m and τ_{max} . Taken from Soulsby and Clarke (2005).

Through parametrization of the existing model data, laboratory and field measurements in the data sets, a simplified approach was later given by Soulsby and Clarke (2005). The application of this approach leads to the calculation of the

cycle-mean shear stress τ_m due to combined wave-current load by taking

$$\tau_m = \tau_c \left[1 + 1.2 \left(\frac{\tau_w}{\tau_c + \tau_w} \right)^{3.2} \right] \quad (2.16)$$

in which τ_c is the shear stress under current flow and τ_w the shear stress under wave load conditions alone. The maximum value can further be determined from

$$\tau_{max} = \left[(\tau_m + \tau_w |\cos \phi|)^2 + (\tau_w |\sin \phi|)^2 \right]^{0.5} \quad (2.17)$$

in which ϕ is the angle between current and wave travel directions. Furthermore, the root-mean-square value of the shear stress value can be calculated from

$$\tau_{rms} = \left(\tau_m^2 + 0.5\tau_w^2 \right)^{0.5} \quad (2.18)$$

2.3.2 Initiation of Motion

Sediment transport generally takes place when the shear forces resulting from a fluid flowing over a movable bed and acting on the grains exceed the critical value of the sediment particle, i.e. the resisting forces are not strong enough to withstand the outer forces, which subsequently sets the grain in motion. Following Zanke (1982a), the shear forces result from the roughness of the bed, which causes pressure fluctuations on the one hand and from the nature of fluids tending to adhere to any solid walls on the other hand. Typical processes of sediment movement contain rolling or jumping of particles at the bed, while finer particles reaching a greater distance to the bed get into suspension. Several studies on the critical threshold value above which sediment particles are set in motion have been carried out by various researchers, e.g. by Shields (1936), Yalin and Karahan (1979), Raudkivi (1990). Most studies relate this critical value to the critical bed shear stress $\tau_{b,cr}$. In the dimensionless form, this value can be expressed by the critical Shields number θ_c (or θ_{cr}) for the initiation of motion. The Shields number itself is defined as

$$\theta = \frac{\tau_b}{s_{sg}\rho g d} \quad (2.19)$$

with τ_b being the actual bed shear stress, ρ the fluid density, g the gravitational acceleration and d the sediment grain diameter. The parameter s_{sg} is the submerged specific gravity of the sediment, defined as

$$s_{sg} = \frac{\rho_o - \rho_f}{\rho_f} \quad (2.20)$$

with ρ_o being the density of the object (the sediment) and ρ_f the density of the surrounding fluid. For quartz sand, s_{sg} can be taken as 1.65, while typically having

a density of $2,650\text{kg/m}^3$. The Shields diagram for the initiation of motion is given in figure 2.4 in a modified form after Sumer and Fredsøe (2002), where θ_{cr} is related to the particle Reynolds number (with $u_* = u_f$)

$$Re_* = \frac{du_*}{\nu} \quad (2.21)$$

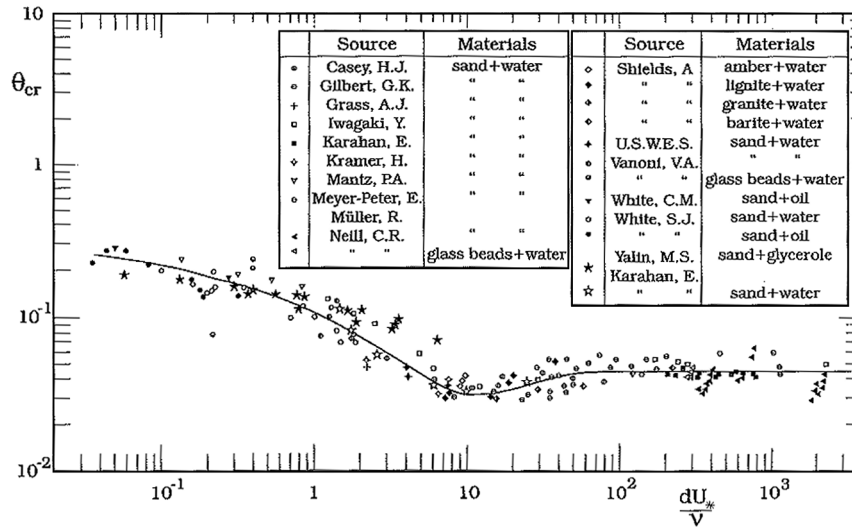


Figure 2.4: Modified Shields diagram for initiation of motion of particles, from Sumer and Fredsøe (2002).

In practical applications, the Shields parameter is still the most widely used formulation for the definition of the critical value for sediment motion, which typically holds a value in the order of $\mathcal{O}(0.05)$. Exact values can however be calculated using numerous parametrizations of the classical Shields curve or modified forms, who mainly relate the critical value to the dimensionless particle diameter D_* . The approach given in Soulsby (1997) was slightly adjusted compared to the original formulation in order to achieve better adjustment to newer experimental data for fine sediment particles, reading

$$\theta_{cr} = \frac{0.3}{1 + 1.2D_*} + 0.055(1 - \exp(-0.02D_*)) \quad (2.22)$$

with the dimensionless particle diameter

$$D_* = d \left[\frac{s_s g}{\nu^2} \right]^{1/3} \quad (2.23)$$

It should be noticed that above given approximations are based on experimental data and might therefore scatter in their results. Furthermore, such parametrizations force data sets into single equations, which might result in certain discrepancies

between approximated and real values. Although θ_{cr} was originally developed for constant current flow conditions, it was shown in Madsen and Grant (1976) and Soulsby (1997) that Shield's approach is suitable for sediment motion under wave conditions as well, as a generally good accordance between theoretical values and measured data could be shown.

Regarding the particle that is set into motion, basic material properties influencing the initiation are the particle size, density and shape, the angle of repose, the sediment fall velocity in case of suspended sediment transport and the porosity of the material composition, where the latter is however only of greater importance if sediment packing and consolidation are considered. In the natural environment, soil material always consists of a mixture of particles with a wider range of grain sizes from gravel or sand to silt or clay and different shapes, while in the marine and fluvial environment, quartz sands and clay are predominant. For clay having a typical grain size <0.063 mm, effects of cohesion play an important role in the sediment transport processes. For the description of the material under consideration, D_* is typically used. The representative particle diameter is taken as the median particle diameter d_{50} resulting from a sieve analysis, the mean particle diameter d_m or values of d_{16} and d_{84} . Other approaches further use the spherical diameter d_v or the sediment fall diameter d_f .

2.3.3 Transport Processes

It is a common practice in the detailed description of morphological processes to classify the transport into the three categories: bed load, suspended load and wash load. Typically, when talking about sediment transport modeling, only the bed load and the suspended load processes are considered. As can be read in Fredsøe and Deigaard (1995), there is actually no precise definition or classification of these two categories. Nevertheless a classification is common as mainly only two different transport mechanisms take place. According to the authors, the bed load is defined as “part of the total load that is in more or less continuous contact with the bed during transport. [...] Thus the bed load must be determined almost exclusively by the effective bed shear stress acting directly on the sand surface”. As the authors say, the suspended load can furthermore be defined as the “part of the total load that is moving without continuous contact with the bed as a result of the agitation of fluid turbulence.” Wash load describes very fine particles that are transported by the fluid flow but are however not directly represented in the bed and do not have a significant influence on the transport process under consideration. Therefore, this part of the transport is typically neglected when modeling near-bed sediment transport processes.

2.3.4 Description of Acting Forces

Considering a steady fluid flow, sediment particles located in the bed will not start to move until the flow velocity becomes so large that the driving forces acting on the particle are larger than the stabilizing forces, i.e. the critical flow velocity is reached. During this process, several forces act on the particle, namely the driving components lift force F_{lift} and drag force F_{drag} , as well as the stabilizing forces F_{fric} due to gravity and friction.

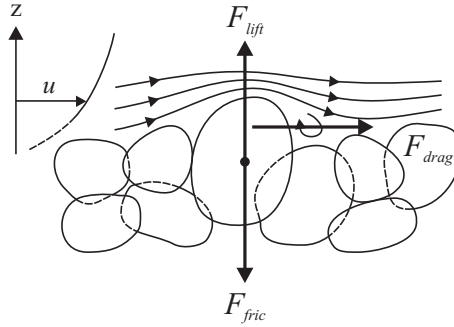


Figure 2.5: Driving and stabilizing forces acting on a bed particle during flow.

Drag is evoked through skin friction on the grain surface leading to pressure differences at the grain sides due to flow separation. From the general drag theory, the drag force acting on a submerged body is, in the general form, given by

$$F_D = \frac{1}{2} \rho c_D u^2 A \quad (2.24)$$

from which the (stream aligned, horizontal) drag force on a sediment particle can be derived as

$$F_{drag} = \frac{1}{2} \rho c_D \frac{\pi}{4} d^2 u^2 \quad (2.25)$$

while assuming the particle to be spherical, with u being the characteristic velocity near the bed, c_D the drag coefficient depending on the local Reynolds number and A the projected area of the particle. As the lift force F_{lift} resulting from a pressure decrease at the top of the particles due to streamline formation and flow separation can be described in a similar manner to above equation (2.25) using the lift coefficient c_L instead, both components can be incorporated into equation (2.25) by use of a modified lift+drag coefficient and incorporating the force resultant. According to Fredsøe and Deigaard (1995), the characteristic near-bed velocity at a distance of one particle diameter from the bed can be approximated as

$$u = au_f \quad (2.26)$$

with a being a dimensionless coefficient that typically takes a value in the order

of $\mathcal{O}(10)$. Following the concept of drag, the stabilizing force due to gravity (and including buoyancy) given as

$$F_g = \frac{\pi}{6} \rho g s_{sg} d^3 \quad (2.27)$$

can be described as a friction force due to friction of the sediment grain and its surrounding particles, in case of a particle resting on a horizontal bed leading to

$$F_{fric} = F_g \mu_s \quad (2.28)$$

where μ_s is the static friction coefficient corresponding to the static friction angle ϕ_s of the sediment, i.e. the angle of repose by $\mu_s = \tan(\phi_s)$. By use of the force balancing terms, the sediment settling velocity can be further evaluated, which is discussed below in §4.3.3.

2.3.5 Sediment Transport Formulations

Several formulations for the calculation of sediment transport fluxes can be found in the literature, which have been developed over the past decades. All formulations have in common that they are mainly based on experimental results from laboratory and are empirically derived. When applying any of the formulations, it therefore has to be kept in mind that reasonable results can only be achieved within the defined parameter ranges, which the formulations have been developed for. Engelund and Fredsøe (1976) furthermore state that “an exact description of forces and particle motion is impossible due to the complex character of the phenomenon.”

One of the first sediment transport formulations regarding bed load processes was developed by Meyer-Peter and Müller (1948), who performed laboratory experiments with both uniform and mixed sand grains. A different approach was later given by Einstein (1950), who primarily developed a stochastic approach that took into account the characteristics of the turbulent flow. Further investigation was carried out by Bagnold (1966), involving physics of the motion and transport process.

Engelund and Fredsøe (1976) developed a mathematical model for sediment transport in straight alluvial channels. The model is based on the ideas earlier introduced by Bagnold (1954). Compared to purely empirical models, the approach has the advantage that it is based on the description of real physical processes and gives information about size and quantity of sand particles, being either transported as bed load or being in suspension.

Further transport formulations were later developed by van Rijn (1984b) and van Rijn (1984c) regarding bed load and suspended load separately, by Zanke (1982a) and Cheng (2002). The approach given in the latter was derived from fitting of experimental data with various shear stress conditions from other works, however not following the concept of critical shear stress for the initiation of motion.

2.3.6 Modifications in Terms of Sloping Beds

When considering scour processes, local bed slopes may drastically increase when scour holes are formed. This bed modification significantly influences the magnitude and direction of the local sediment transport. Therefore, resulting changes in transport rates along sloped beds were studied by numerous researches, e.g. Bagnold (1966), van Rijn (1993), Damgard et al. (1997) or Kovacs and Parker (1994). It was found that an adaption of bed load transport formulations originally designed for almost horizontal beds is necessary in case of steep slopes, either carried out by a modification of the transport rates or by introduction of additional slope factors. All approaches have in common that if the downward slope is in the direction of the near-bed flow and thus resulting in shear stress, the transport rate is increased due to the additional action of gravity force. On the other hand, transport rates might be reduced in case of opposing directions.

In case of differing angles between the slope and the near-bed flow direction, the transport rate vector then has to be modified further, taking both directions into account in the spatial domain. In the works of Luque and van Beek (1976), Kovacs and Parker (1994), Hasbo (1995), Lau and Engel (1999) and Roulund et al. (2005) this has been considered by a slope-dependent modification of the critical Shield parameter θ_c for the initiation of motion.

A further modification of θ_c is necessary regarding general slope effects: in case of a downhill slope, an additional downward-directed force due to gravity increases the mobility of the particle, while it is reduced for an upward slope, related to the direction of flow and shear stress. In these cases, besides the modification of the transport rates, the threshold value for sediment motion further changes, which makes it necessary to modify the critical parameter.

2.4 Scour at Marine Structures

2.4.1 Previous Investigations

Numerous investigations on scouring phenomena around offshore structures have been carried out in the last decades. Data have predominantly been obtained from laboratory tests in wave and current flumes, wave basins or combined laboratory facilities, see e.g. compilations in Hoffmanns and Verheij (1997), Zanke (1982a), Whitehouse (1998), Melville and Coleman (2000), Sumer et al. (2001) and Sumer and Fredsøe (2002), in recent years additionally by the use of numerical model data. Laboratory tests often led to empirical formulations on spatial and time-dependent scour developments. Due to a lack of field data, a validation of the results with regard to prototype scales has rarely been possible. “On the whole, the number of investigations on scour caused by waves or a combination of waves and currents is

rather limited compared to investigations on scour caused by unidirectional currents like in river bed situations” Stahlmann and Schlurmann (2010). Furthermore, the main focus has been on comparatively simple structures like vertical cylinders, which might be due to the fact that cylindrical piers are widely used in fluvial and marine environments.

Furthermore, cylindrical structures led to several damages in recent years, e.g. as foundations for bridge piers. Equilibrium scour depths were mainly regarded, which are the most important factor for overall structural dimensioning and stability analysis.

Regarding scour depths calculated from various of the existing empirical formulations, different results on maximum scour can further be observed, especially when structural dimensions from prototype models and real sea state conditions are examined, partly leading to highly unphysical results, see e.g. Ungruh and Zielke (2003). Due to the complexity of different foundation structures for offshore wind turbines like tripods, jackets or gravity base foundations, approaches developed for cylindrical structures are furthermore not directly applicable in these cases.

2.4.2 Influencing Factors

In the literature, a classification of the particular flow processes and their direct influence on scour evolution is widely used, which can be subdivided by means of structural type and typical diameter as well as by the nature of load. Besides the bed material properties and structural dimensions, influencing factors of load components are mainly given by

- Water depth d, h [m]
- Current velocity u, v [m/s] and Current direction [°]
- Wave height H, H_s [m] and Wave period T, T_p [s]
- Wave length L [m] and Wave direction [°]
- Temporal evolution and Directional changes

On the basis of the aforementioned factors, additional classification is common, however directly related to cylindrical structures only. On the one hand, this is the Keulegan-Carpenter Number KC , a dimensionless number characterizing the flow regime in case of oscillating flow and waves and the diffraction parameter D/L giving the relation between pile diameter and wave length. On the other hand, the Reynolds number Re classifies the degree of turbulence in current flow cases.

According to Whitehouse (1998), the effect of water depth on the equilibrium scour depth at piles can be neglected for values of $h/D > 3$. Although lower depths

were measured for ratios of $h/D < 3$, this has a minor significance for practical offshore applications as here, typically $h \gg D$. For piles with non-cylindrical shapes, deeper scours typically occur compared to cylindrical piles. Whitehouse (1998) and Melville and Coleman (2000) therefore give a multiplication factor of 1.3 for square piles.

Besides general scour effects in terms of local sediment erosion and transport, bed liquefaction and rockage of structures due to wave load might further play a role in the design and dimensioning of the foundation.

2.4.3 Scour at Cylindrical Structures

Scour around cylindrical structures in general and particularly as monopile offshore wind turbine foundations have been widely investigated by various researchers for wave, current and wave-current load cases, see e.g. the works of Eadie and Herbich (1986), Sumer and Fredsøe (2002), den Boon et al. (2004), Sumer et al. (2007), Zanke (1982b) or Zanke et al. (2011).

Single Piles, Wave and Current Load In case of wave load, especially the diameter of the pile with regard to the wave parameters has a significant influence on the evolving flow pattern and hence resulting scour development at the pile. In case of pure current load, no such classification in relation to the pile diameter is needed. Wave load cases are typically classified into two categories. In the first case, $D \ll L$, leading to the definition of 'slender' piles where flow separation and near-wall turbulence occur due to the presence of the pile. In the second case, D/L is that large that no flow separation and therefore no vortex formation occurs, leading to the definition of 'large' piles. Diffraction effects may nevertheless occur in case of large piles, which in turn leads to scour enhancing effects. For the classification of large and slender piles under waves, Sumer and Fredsøe (2002) make use of the aforementioned KC number, which is defined as

$$KC = \frac{U_m T}{D} \quad (2.29)$$

with U_m being the maximum (undisturbed) orbital velocity at the bed in case of regular waves and T the wave period. According to the authors, the best fit for scour depths comparing regular and irregular waves is found taking U_m as U_{rms} being the root mean square value of the orbital velocities at the bed and T as T_p . The pile-related classification according to Sumer and Fredsøe (2002) is given as

$$\begin{aligned} KC > 6 & \quad \textit{slender piles} \\ 1 \leq KC \leq 6 & \quad \textit{medium large piles} \\ KC < 1 & \quad \textit{large piles} \end{aligned} \quad (2.30)$$

A consistent definition is however not found in the literature as different authors give different regime and threshold values for classification. Hoffmanns and Verheij (1997) and the CEM (2002) give a value of $D/L > 0.1$ for the occurrence of diffraction, while Sumer and Fredsøe (2002) and Whitehouse (1998) give a value of $D/L > 0.2$. The latter further defines the flow pattern system by use of the parameters D and h , where slender piles exist in situations where $D/h < 0.5$.

In practical maritime and offshore applications, the predominant number of pile foundations can be taken as slender piles using above classifications. Comprehensive studies can be found in the respective literature, which should be referred to for further information.

For the formation of horseshoe vortices under steady flow conditions, which can be seen as a major effect influencing scour development, Sumer and Fredsøe (2002) give threshold values regarding the pile Reynolds number as $Re_D \geq 800$ and the Reynolds number of the boundary layer as $Re_\delta \geq 150$. In case of waves, the threshold value is given based on KC . Small numbers, i.e. around $KC < 30$ lead to minimal formation of a horseshoe vortex system, in which case the scour evolution is mainly based on the lee wake vortices, while for large numbers, i.e. $KC > 100$, scour development is mainly affected by the horseshoe vortex.

For large and medium large piles, reflections of incident waves at the structure occur at the luv side of the pile, which are then diffracted into the lee side forming circular outward directed waves. Due to interference of incoming and reflected waves, single wave heights might therefore increase locally. Investigations by Sumer and Fredsøe (2002) have shown that effects of steady streaming at the bottom side parts of the pile might occur due to wave interference and pressure gradients, then being mainly responsible for scour formation. This effect is increased with increasing KC number and diffraction ratio.

Wave-Current Interaction It can be concluded from the majority of experimental studies on combined wave-current load and resulting scour development around single cylindrical piles that the additional current action increases the maximum scour depth, compared to pure wave scour development. Most experimental studies have shown that the overall scour shape mainly resembles the case of pure current flow. Regarding the flow processes, it was found that for a sufficiently strong current in the direction of wave propagation, a horseshoe vortex system is permanently present, while however varying according to the orbital wave motion in an alternating sense. It should however be kept in mind that in the natural, offshore environment, a steady current is not present, but varies in flow magnitude and direction according to tidal flow conditions, if present at all. Experimental studies on the combined interaction of waves and current flow and hence resulting scour development can e.g. be found in the works of Wang and Herbich (1983), Eadie and

Herbich (1986), Kawata and Tsuchiya (1988), Saito and Shibayama (1992), Sumer and Fredsøe (2002), Rudolph and Bos (2006) or Zanke et al. (2011).

2.4.4 Scour at Complex Structures

In addition to the aforementioned, comparatively simple cylindrical structures, complex foundation types are widely used in offshore engineering, especially for offshore wind turbine foundations and platforms like tripods, tripiles, jacket, bucket, gravity base or semi-submersible floating platform foundations. Regarding scour formation, only little detailed and general knowledge exists for such complex types. At present, an estimation of scour depths is therefore often carried out by use of an equivalent diameter describing the overall foundation and taking this as an input value for one of the classical scour depth formulations, originally derived for single pile structures. Due to the complexity of occurring flow and scour pattern, this approach is however affected by huge uncertainties. Furthermore, a direct application of pile scour approaches typically leads to unphysically large, theoretical scour depths.

Experience on scour around complex offshore structures is therefore mainly gained by means of physical modeling for the particular cases. A direct application to other foundation types is nearly impossible in most cases. As offshore foundation structures are mainly constructed and erected for industrial purposes, experiments on scour risk and protection mechanisms are mainly carried out in this context, for which reason only little information is made publicly available.

Regarding scour development around such foundations, it can generally be stated that both the flow and hence the resulting scour pattern may significantly differ from those of single pile. In case of composed structures, e.g. given for the majority of offshore wind turbine foundations with a cylindrical tower on top of a submerged substructure, flow fields in the upper part around the structure might be similar to cylinder regimes. The ground may however not be affected by these flow conditions due to blockage and flow disturbance through the structure itself. To the authors knowledge, no publicly available scour investigations on tripod foundations similar to the structure investigated here can be found in the literature.

Pile Groups Due to interaction and interference of flow and sediment transport processes, scour pattern, depths and extents at pile groups might differ from single pile formations. Therefore, distances and alignments of the piles are additional key factors influencing the scour process. In addition to the local scours at single piles, global scour formation around the entire structure may occur due to local obstruction, flow constrictions and further turbulence generation, leading to larger scour depths with deepest local scours typically formed at the edge corners of a pile group. As no general formulation for scour at pile groups has so far been

found due to numerous influencing factors mentioned above, generally leading to differences in scour formation and depths, the reader is referred to the respective literature for further information, see e.g. Myrhaug and Rue (2005).

2.4.5 In-situ Measured Scour Development

Similar to experimental results on scour development at complex offshore foundations, field measurement data on scour have hardly been reported in recent years. With the upcoming change in energy supply and thus resulting erection of new wind farms, more information on actual scour development cases is now available, see e.g. the reports of Rudolph et al. (2004), Hogedal and Tue (2005), Whitehouse et al. (2008), van den Eynden et al. (2010) and Whitehouse et al. (2011). Some results are exemplary summarized here.

Rudolph et al. (2004) report of and analyze scour measurements for different (typical) types of offshore structures installed in the North Sea. Their analysis include bathymetry survey charts, underwater video records and spud can penetration reports. Furthermore, results are compared to empirical formulations. For a monopile foundation with $D=6\text{m}$ in shallow water, i.e. water depth between 5.2m and 11m, erected in 1997 without scour protection, a maximum scour depth of 6.3m ($S/D=1.05$) was observed after about 4.7 years, while an equilibrium stage was not reached. Comparison to empirical scour depth formulations gave best results when applying to flow and tidal flow formulations. In the same report, scour development around a jacket structure, again erected in 1997 but in moderate water with a depth of 24m is given. The so far measured scour depths at the single platform legs reach up to 2.0-3.5m, while a large global scour hole with a radius of 50m developed around the entire structure.

A summary of various wind park monitoring campaigns is given in Whitehouse et al. (2008), all regarding monopile foundations. At Barrow wind farm location, relative scour depths S/D of 1.21 were measured several months after erection. For monopiles installed in Kentish Flats, relative scour depths around $0.34D$ were observed, while depths of up to $1.38D$ were recorded at Scroby Sands wind farm, altogether showing highly different depth developments, depending on the given load conditions at the particular locations.

van den Eynden et al. (2010) give information on scour development for two wind farms at Thornton Bank and Bligh Bank in their report. In the first case, gravity base foundations were installed in 2008, while monopile foundations were erected in the second wind park in 2009. Both structures had in common that dynamic erosion protection systems were installed, i.e. scour pits first developed naturally, which were then later filled with protection material. For both structures, scour pit depths varying between 2 and 6.5m were observed a few months after erection.

2.4.6 Design Guidelines for Offshore Wind Turbines

Several design guidelines for the certification of offshore wind turbines are existent, mainly focusing on the constructive design of the entire wind turbine, with details regarding substructure and foundation, tower, rotor and nacelle. For a project certification, it is necessary that the specific wind turbine and the particular support structure meets all requirements given by the technical guideline. For site assessment, marine conditions including bathymetry, waves, tides, scour, marine growth and soil conditions have to be regarded. Furthermore, requirements for maintenance and monitoring during life time of the turbine are defined.

Regarding the specific process and effects of scour, design recommendations based on literature formulas are partly given in the guidelines, however based on different assumptions and regulations. Detailed information on scour determination are given exclusively for single, vertical pile structures in the guidelines, see the following paragraphs for an exemplary collection.

Germanischer Lloyd, 2005: Guideline for the Certification of Offshore Wind Turbines Structures founded on the sea floor may be affected by “gradual or transient changes of the sea floor”, GL (2005). Scour is given as local scour with steep sided scour pits, global scour of larger extent around a foundation and by “overall seabed movement of sand waves” here. The phenomena of scour thereby results in “removal of vertical and lateral support for foundations”. During the entire life time of the offshore wind turbine, these may influence the natural frequencies of the turbine. Therefore, scour or undermining shall always be investigated and shall be part of the structural analysis. Regarding soil mechanics and sea floor stability, processes like slope failure, erosion, settlement and soil liquefaction have to be taken into account.

Generally, the max. relative scour depth S/D at single pile foundations can be estimated by

$$S/D = 2.5 \quad (2.31)$$

with D as the pile diameter. Less conservative approaches may alternatively be chosen, but have to be verified by a monitoring concept during life time then. No further information and differentiation regarding the load conditions of waves and currents is given here, neither for determination of scour extent and time spans.

Besides single piles, gravity type foundations are mentioned in the guideline; no information on the determination of scour depth and extent is however given for such structure types. Partly, skirts may nevertheless be required to ensure stability and to protect the foundation against local scouring.

In addition to the scour determination itself, the design of a possible scour protection system is proposed. As huge uncertainties and numerous possibilities regarding

the constructive execution however exist, “scour protection remains an uncertain art”. Uncertainties shall therefore be accounted for by robust design and monitoring. In detail, scour protection can be executed as either a) permanent protection lasting for the entire life time of the structure, backup by model tests beforehand or b) dynamic scour protection, in which a certain level of damage is expected. Monitoring of scour and scour protection is required at 6 and 18 weeks after erection then, which may be reduced afterwards in case no damage occurred.

Independent of the structure type, maintenance including periodic monitoring of foundation and scour protection is required in order to maintain validity of the certification for the entire wind turbine.

DNV, 2013: Design of Offshore Wind Turbine Structures Similar to the description of scour origin, phenomena and resulting effects as given above, scour appears as a combination of local and general scour, thus resulting in loss of lateral and axial resistance that has to be considered in the design process.

Generally, scour has to be taken into account “unless it can be demonstrated that the foundation soils will not be subject to scour”, DNV (2013), e.g. by use of physical model tests. Scour is accounted for by a) installation of a scour protection system as early as possible after erection of the foundation, b) removal of structural elements that are subject to scour in the design calculation, c) monitoring and countermeasures to prevent (further) scouring.

For the determination of local scour at a single vertical, cylindrical pile, the following empirical formulation can be used, “unless data, e.g. from model tests, indicate otherwise”

$$S/D = 1.3 (1 - \exp(-0.03(KC - 6))) \quad \text{for } KC \geq 6 \quad (2.32)$$

Here, the single and combined effects of steady current and wave load are taken into account. Caution must however be taken in case of large-diameter piles such as monopiles. The formulation is valid for live-bed conditions only, i.e. $\theta > \theta_{cr}$. “The equilibrium scour depth S can be used as a basis for structural design. For this purpose the equilibrium scour depth, used as a measure of local scour, may be supplemented with some extra safety margin as appropriate.” In addition to scour depth determination, equations for the calculation of scour hole extent and time scale are given in the guideline.

Besides single vertical piles, different foundation structures like gravity base and gravity-pile structures, which require flat soil bases and some form of scour protection, supported monopiles and tripods with suction bucket anchors are mentioned. Again, no information on the determination of scour shape, depth and extent is however given here.

It is noted that an inspection of both scour and installed scour protection systems is required during life time of the foundation by periodic monitoring.

Other guidelines like the BSH standard given in BSH (2007) and the DIN EN 61400-3 given in DIN (2009) regarding the construction of offshore wind turbines both in general and in detail mention that general scouring effects or local movement and washout of seabed, respectively have to be taken into account. They however do not give any explicit information about scour determination for the foundations. The latter guideline is rather focusing mainly on approaches for load calculation on the structure due to sea states, wind and operation.

Empirical approaches on scour determination given in the design guidelines are based on or directly give empirical approaches that can be found in literature and which have proven to give good results for the desired design purpose. One of the approaches for the calculation of scour depth at single vertical piles, which is commonly used in marine scour calculations is the one mentioned in the DNV guidelines given by equation (2.32), originally established by and given in Sumer and Fredsøe (2002). The formulation, amongst others, can also be found in CEM (2002), chapter 5 'Fundamentals of Design', which gives indications for scour determination for different maritime and offshore structures.

Another approach for the calculation of scour depth, again for a single, cylindrical vertical pile under single or combined (short) wave and steady current load is the one given in Zanke et al. (2011), which was derived from fitting of experimental data and dimensional analyses. The universal formulation reads

$$S/D = 2.5 \left(1 - 0.5 \frac{u}{u_c} \right) x_{rel} \quad (2.33)$$

with S as the max. scour depth, D the pile diameter, u the max. near bed orbital velocity for waves and mean velocity for steady currents, respectively, u_c the critical velocity for the beginning of sediment motion and x_{rel} the relative sediment displacement given as a transition function by

$$x_{rel} = x_{eff} / (1 + x_{eff}) \quad (2.34)$$

with x_{eff} as the effective sediment displacement given by

$$x_{eff} = 0.03 (1 - 0.35u_c/u) (KC - 6) \quad (2.35)$$

Different from the former approach by Sumer and Fredsøe (2002), which is independent of the given sea bed parameters, the latter further takes the sediment properties into account. It has to be noted that several, further empirical approaches for

scour determination can be found in literature, however not explicitly given here. The reader is therefore referred to the respective literature.

Concluding remarks All design guidelines or certification rules have in common that scour has to be taken into account when designing an offshore wind turbine. Information about scour calculation and the design of a scour protection system however differ in above given guidelines. Monitoring of either the scour protection system or a possible scour itself is given as one of the key factors regarding the guarantee of life time usability of the wind turbine. If detailed information about the calculation of scour depths (and partly extents and time scales) is given, those explicitly focus on single, vertical piles, i.e. monopiles and are therefore only valid for this type of structure. Although different complex foundations are partly mentioned, no information about scour determination is given then. For those types, detailed analyses including physical model tests are therefore demanded or at least recommended in order to fulfill design requirements.

2.5 Numerical Modeling of Scour Processes

2.5.1 Remarks on Model Scales

For the numerical simulation of scour or general sediment transport processes, typically two- and three-dimensional models are used, while the choice of dimensionality depends on the specific topic under consideration, e.g. sediment transport in rivers, oceans, bays or harbors or local scour phenomena around fluvial or offshore structures. For larger areas, depth-averaged two-dimensional approaches have proven to be sufficient in many cases, as long as no local flow effects around single objects and hence resulting local transport processes shall be investigated in detail. In that case, the flow field is fully three-dimensional and therefore has to be modeled as such, including an appropriate sediment transport model formulation. While three-dimensional models therefore include more information from the physical nature and hence give more detailed results on scour processes, computational costs are much higher than for two-dimensional models considering a similar case.

Several numerical models for local flow field and scour simulations have been developed over the past years and can therefore be found in the literature. Some of these are briefly described below. The compilation is however restricted to three-dimensional models only. It can generally be stated that in all models, only comparatively simple structures were considered.

2.5.2 Flow and Scour around Objects and other Models

It can be noticed that the numerical simulation of flow and scour around cylindrical structure is the case that has mostly been considered in both numerical and exper-

imental studies. This might be due to the fact that the circular cylinder or pier is one of the most widely used geometries for any structures placed in the fluvial and marine environment, as given in §2.4.1.

Olsen and Melaaen (1993) belong to the first ones considering local scour simulations around a cylindrical pier, however not reaching an equilibrium state due to large computational times. The numerical model included a steady-state solution for the flow. Final scour depth results were however published later in Olsen et al. (1998) using a modified model including an unsteady flow solution, bed load, suspended load and free surface calculation for a pure current load case. Scour depth could generally be estimated well in the model compared to experimental data.

Calculations on local scour development around a vertical cylinder have further been carried out in the work of Roulund (2000) and later published in Roulund et al. (2005), using a steady-state flow approach with a rigid lid at the place of the free surface for a steady-current induced scour development. Only bed load was considered here. The model included modifications on the shear stresses to account for sloping beds and an appropriate sediment sliding procedure. Besides the numerical modeling part, the work included experimental modeling of scour around a cylinder and results were used for a verification of the numerical model. Altogether good results compared to the experiments could be achieved, although certain discrepancy for the final scour depth, especially at the downstream part of the cylinder was given.

A similar work was carried out by Weilbeer (2001), who used TELEMAC-3D software code to model scour around a cylindrical structure and other objects for current flow situations. The approach in the code was however limited to simple objects, as a σ -grid was used, which builds up on the approach of a two-dimensional, triangular bottom grid in horizontal plane, which is then projected onto several layers in the vertical. This suppresses modeling of complex object shapes. A general comparison to the data given in Roulund (2000) was carried out and several bed load transport model formulations were compared.

The work of Göthel (2008) further built up on the work of Weilbeer (2001), using the same numerical code. In his work, wave load was considered as the main acting load condition leading to local scour. Furthermore, a soil model was incorporated for investigations on the effect of soil and slope stability by use of a Finite Element approach. Only bed load was considered in the model. Data were compared to experimental results from literature, e.g. the work of Roulund et al. (2005) and test results on wave-induced scour around a circular cylinder carried out in the Large Wave Flume (GWK) in Hanover. Numerical results however slightly differed from the latter experiments.

Another model approach was given by Liu (2008), who considered both a two-dimensional, depth-averaged and a three-dimensional numerical model for local scour

formation. OpenFOAM software code with free surface representation was applied in this work and a sediment transport formulation including bed load and suspended load was implemented. Furthermore, a separate model for soil stability and liquefaction effects was incorporated into the code. For comparison with experiments, several test results from the literature were used, amongst others wave-induced scour around a large cylinder and scour formation behind a sluice gate.

In addition to experimental investigations on local scour formation at a circular, vertical cylinder under steady current flow conditions, Link (2006) carried out numerical simulations on this topic using a vertically layered domain model similar to that given in Weilbeer (2001). Investigations were however limited to an application of an existing flow and sediment transport model here.

Further model approaches for investigations on scour around pipelines, mainly in two-dimensional model versions are given in Beek and Wind (1990), Brørs (1999) and Li and Cheng (2001). Model approaches on general sediment transport processes and scouring effects due to waves and in wave flumes are given in Wu et al. (2000), Wu (2004), Duc et al. (2004), Lesser et al. (2004) and Jacobsen (2011). In the latter, investigations on flow and sediment transport processes under breaker bars were carried out using OpenFOAM software code for the hydrodynamic modeling part, and a sediment transport model formulation including bed load and suspended load was further implemented as an extension of the code. Results were compared to both theoretical assumptions and experimental data, achieving altogether good agreement.

2.6 Conclusions

Regarding marine and coastal structures, with a special focus and foundations for offshore wind turbines as investigated here, it is well known that in many cases, scouring occurs around the foundations. “This is owing to the presence of the supporting structure itself and hence affecting changes in the natural flow regime at the sea bed around the foundation, subsequently leading to increased sediment mobility” Stahlmann and Schlurmann (2012a). Depending on the depth and extent of scour formation, serious stability and usability issues might occur for such structures. Regarding scour formation, only little knowledge exists for complex foundation types like tripod, jacket or gravity base foundations. At present, an estimation of scour depths is therefore often carried out by use of an equivalent diameter describing the overall foundation, which is then taken as an input value for one of the classical scour depth formulations, however originally derived for single pile structures. Due to the complexity of occurring flow and scour pattern, this approach is however affected by huge uncertainties. Furthermore, a direct application of existing pile scour approaches might lead to unphysically large, theoretical scour depths.

Following the general definitions, sediment transport as the global process of scour formation takes place when the shear forces resulting from a fluid flowing over a movable bed in turn acting on the grains exceed the critical value of the sediment particle. In practical applications, the Shields parameter is the most widely used formulation for the definition of the critical value for sediment motion. It is common practice in the description of morphological processes to classify the transport of sediment particles into the three categories: bed load, suspended load and wash load. Typically, when talking about sediment transport modeling, only the bed load and the suspended load processes are considered. Several formulations for the calculation of sediment transport fluxes can be found in the literature, which have been developed over the past decades. All formulations have in common that they are mainly based on experimental results from laboratory test and are therefore empirically derived. In addition to those classical transport formulations, mainly developed for situations with plain bed, modifications are further necessary to account for local scour processes. When considering those, local bed slopes may drastically increase when scour holes are formed. This bed modification significantly influences the magnitude and direction of the local sediment transport.

Besides the classical laboratory tests on scour phenomena around structures, several numerical models for local flow field and scour simulations have been developed over the past years and can therefore be found in the literature. It can thereby be noticed that numerical simulation of flow and scour around cylindrical structure is the case that has mostly been considered, which might be due to the fact that the circular cylinder or pier is one of the most widely used geometries for any structures placed in the fluvial and marine environment. To the authors knowledge, no numerical model directly dealing with complex structures like tripod foundations for offshore wind turbines, esp. in combination with wave and current load conditions, is however existent in literature.

3 Tripod Scour Experiments

3.1 Methodology and Objective

In order to study scour phenomena around a tripod foundation structure under the influence of wave loads, which is typically used as substructure for offshore wind energy converters, physical model tests have been carried out in wave flumes. The overall objective of investigations was to gain general knowledge on physical processes, the local and global scour development as well as local flow patterns leading to scour. Physical model tests were carried out on model scales of $\lambda = 40$ and $\lambda = 12$ by applying the Froude model law (see table 3.1).

In addition to the general knowledge on scour development, the experiments further served as validation tests for the numerical modeling of scour development, see §5.2. Laboratory tests on 1:40 ($\lambda = 40$) laboratory scale furthermore served as a kind of feasibility studies for the later following 1:12 ($\lambda = 12$) large scale experiments. It should be noted that parts of the experimental tests in the Large Wave Flume were conducted on the basis of scientific investigations in the framework of the research project “Gigawind alpha ventus - Sub project 5”, founded by the German Federal Environment Ministry (BMU code 0325032).

Model dimensions regarding the geometry of the tripod structure are similar to those from a prototype foundation installed in the alpha ventus test site in 2009 (final commission 2010), see e.g. RAVE (2010) for further information. Therefore load boundary conditions were generally chosen according to local offshore field data from the test site. The choice of model scales relied on the scaled boundary condition parameters in combination with the limitations in laboratory facilities, i.e. water depths, possibility of wave generation and general blockage effects. It again has to be noted that only the effect of wave load on scour development by means of physical model tests in wave flumes was investigated here.

Table 3.1: Parameter scaling by Froude model law.

Parameter	Froude model	Parameter	Froude model
Length	$L_p = L_m \lambda$	Time	$t_p = t_m \sqrt{\lambda}$
Area	$A_p = A_m \lambda^2$	Velocity	$U_p = U_m \sqrt{\lambda}$
Volume	$V_p = V_m \lambda^3$	Discharge	$Q_p = Q_m \sqrt{\lambda^5}$
Force	$F_p = F_m \lambda^3$	Acceleration	$a_p = a_m$

3.1.1 Load Boundary Conditions

The experiments given here can mainly be seen as dimensional physical model tests. Appropriate boundary conditions therefore had to be defined. Sea state conditions

for the alpha ventus test site location can generally be determined from field measurements at the research platform FINO1, which is located directly near the test site. In addition, a report in DHI (2007) supplies data on extreme events on the basis of Hindcast modeling. The water depth at the test site location is about $d \approx 30\text{m}$ at still water level, which was therefore defined as water depth for the present investigations.

For first preliminary tests, however not further described here, boundary conditions for a 50-year extreme event were chosen as modeling parameters based on these data. In these first test series, only little scour formation was however observed under those conditions. Due to this, final wave boundary conditions were chosen with increased wave period in order to amplify scour effects, especially for a verification of the numerical model. Results might therefore not be directly applicable to natural conditions.

Regarding the data given in DHI (2007), it should be noticed that recent extreme value analysis conducted on the basis of newer FINO1 data furthermore led to a modification of these sea state boundary conditions. As an example, according to DHI (2007), parameters for the 50-year extreme event result in $H_s = 8.5\text{m}$, $H_{max} = 15.8\text{m}$, $T_p = 12.3\text{s}$ for waves and $u_m = 1.3\text{m/s}$ for the tidal flow. Due to extreme storm events in 2006, 2007 and 2011, also in the area of interest here, given extreme values were however already exceeded several times. Including this new data base, values given by recent calculations in Hansen (2011) therefore lead to $H_s = 10.38\text{m}$ and $T_p \approx 13.6\text{s}$ for the 50-year extreme event case.

Concerning the sediment parameters of the sea floor at the alpha ventus test site location, measuring campaigns conducted by the German Federal Maritime and Hydrographic Agency (BSH) show that the sediment is mostly narrow distributed fine sand with a mean grain diameter d_{50} in the range of 0.2-0.25mm.

3.2 Wave-induced Scour on Laboratory Scale

3.2.1 Experimental Setup

The laboratory tests on scour phenomena were carried out in the wave flume of the Franzius-Institute (WKS), which has overall dimensions of 100m length, 2.2m width and 2.0m height. At the front party, a hydraulically driven piston type wave maker is installed, allowing the generation of regular and irregular waves with wave heights up to 0.35m and $\pm 0.30\text{m}$ stroke by a water depth of up to 1.2m. In the rear part of the flume, a beach is installed to passively absorb wave energy in order to minimize reflections. The wave flume is filled and emptied using an inflow/outflow valve installed at the flume bottom near the wave maker. Outflowing water is collected in a low-level tank, which can then be externally pumped into a high-level tank in order to serve as filling water again.

For the tests on scour development around structures, a false bottom was installed in the wave flume as originally, no deep section holding the model sediment was available. The sand bed had a length of about 4.6m, resulting in an overall bed area of about 10.3m^2 , with a bed depth of 0.25m. The bed was installed in combination with sand traps and a covered pump well in front of the test section as well as concrete ramps on both sides. A sketch of the model setup is given in figure 3.1. A drainage system connecting the test section with the pump well as given in figure 3.2a was used to drain the water in the sand bed when the model was dried up for flattening the bed after a test series. The movable bed section was bordered with solid walls in order to prevent it from horizontal flow during flume filling. Parts of the test section where no scour formation was expected were filled with lime sand bricks.

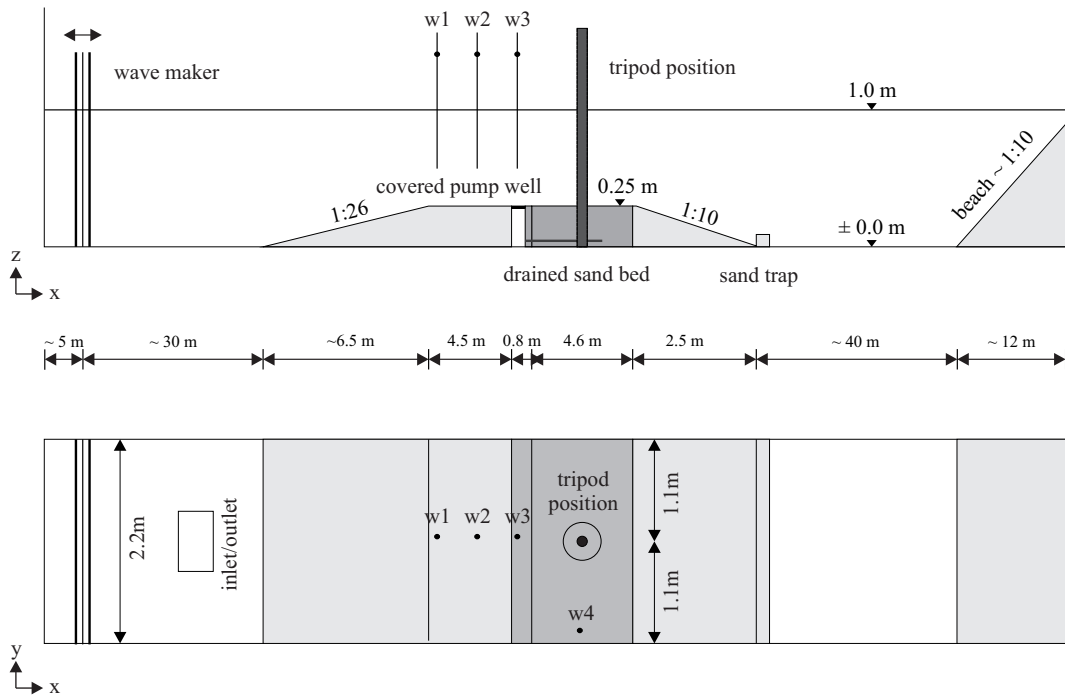


Figure 3.1: Sketch of the experimental setup in the WKS wave flume. Tripod structure is given symbolically.

For the experiments, a tripod model on a length scale of 1:40 was manufactured from aluminum elements. For the flume installation, a turnable bottom mounting system was installed, which allowed to modify the rotating direction of the tripod in relation to the incoming wave direction. The tripod could be turned and fixed in steps of 15° , with a complete rotating range of 180° . In the following descriptions, wave-encounter angles of 0° describe one pile and 180° describe two piles facing the incoming waves, which is a symmetric alignment with regard to the flow direction, while 90° is given for asymmetric alignment with one pile facing one and two piles

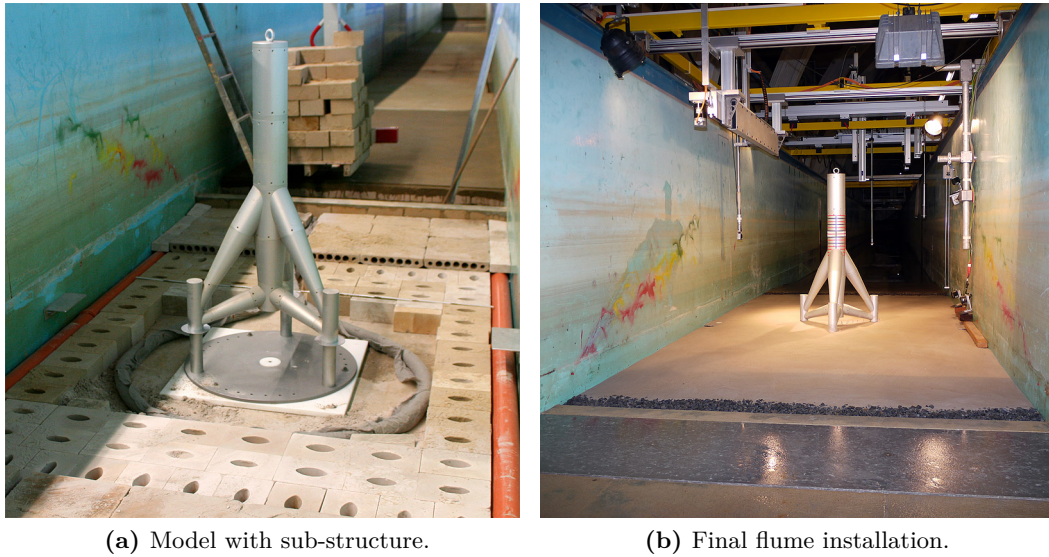


Figure 3.2: Tripod installation in the WKS wave flume for scour experiments.

facing the opposite flume wall. The connection between piles, pile sleeve and bottom mounting parts were designed in detachable form. Therefore, aluminum discs representing the so-called “mud mats” could be installed between piles and pile sleeves for some of the tests. In the prototype scale, these mud mats are designed mainly to prevent the tripod structure from sinking into the sea floor during installation. In the model, main dimensions of the structure are as follows: The upper part of the main column has a diameter of $D_{mc} = 15\text{cm}$, while it reduces to $3/4$ of the diameter at the lower part; pile sleeves have a diameter of $D_s = 7.1\text{cm}$, piles of $D_p = 5.9\text{cm}$ and the mud-mat discs of $D_{mm} = 13.1\text{cm}$; the overall structural diameter covering the pile sleeves is given by about $D_t = 77.1\text{cm}$.

In symmetric installation, i.e. wave-encounter angles of 0° and 180° , the vertically projected area of the tripod is $A_t \approx 0.23\text{m}^2$. This results in an overall blockage ratio of $r_t \approx 0.14$ at still water level, which is however still below the threshold value $r_b = 1/6 \approx 0.167$ after Whitehouse (1998) for influences on the results due to high blockage effects. In asymmetric installation, i.e. a wave-encounter angle of 90° , this overall ratio is even lower.

Sediment Material Properties As bed material, narrow distributed fine sand with a grain size of $d_{50} = 0.148\text{mm}$ was used. The material sieve analysis is given in figure 3.3 and the overall soil parameters are given in table 3.2. The angle of repose was determined by classical laboratory methodology, while taking the mean of three tests for both dry and submerged conditions. The static friction angle for dry sand is calculated as $\mu_s \approx \tan(\phi)$, while the dynamic coefficient is typically slightly lower and therefore takes a value of $\mu_d = 0.85\mu_s$ here. Values of $d_{15.9}$ and $d_{84.1}$ have not

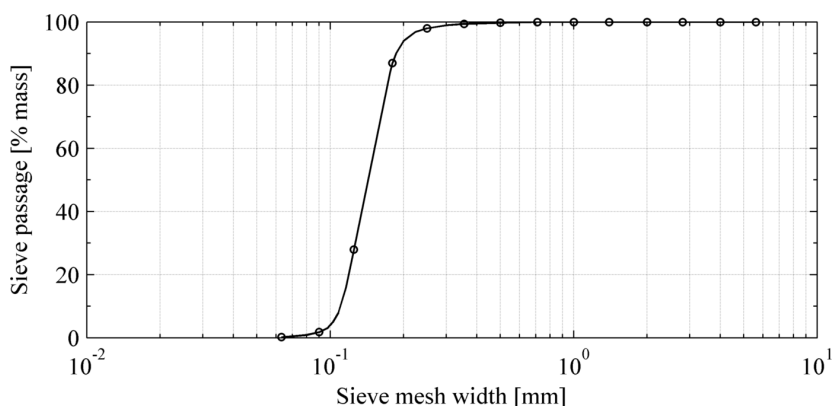


Figure 3.3: Sieve analysis of bed material for scour experiments, $d_{50} = 0.148\text{mm}$.

Table 3.2: Soil parameters of bed material.

Parameter	Symbol	Value	Unit
Grain size	d_{50}	0.148	mm
Grain size	$d_{15.9}$	0.116	mm
Grain size	$d_{84.1}$	0.176	mm
Geometric standard deviation	σ_g	1.23	-
Angle of repose, dry	ϕ_d	30	°
Angle of repose, wet	ϕ_w	26	°
Static friction coefficient	μ_s	0.58	-
Density	ρ_s	2650	kg/m ³

directly been measured, but estimated from the sieve analysis diagram.

The bed material was selected for the test procedure mainly due to the fact that the overall grain size is comparatively small and therefore scaling effects compared to in-situ bed material from typical North Sea areas could be minimized, additionally without significant effects of cohesion. It is however obvious that the experimental sediment does not fully represent in-situ bed material from the test site. As the latter already consists of fine sand as given in §3.1.1, a direct grain size scaling based on the Froude model law was not possible here. Scaling effects will therefore be discussed in §3.4.

The geometric standard deviation of bed material is $\sigma_g = \sqrt{d_{84.1}/d_{15.9}} \approx 1.23$, which is below the critical value of $\sigma_g \approx 1.5$ after Dey (1999) for the occurrence of armoring effects of the material.

3.2.2 Measuring Equipment

In order to measure scour development as well as water surface elevations and orbital motions, the experimental setup was equipped with different measuring instruments further described in the following and summarized in table 3.3. For all measuring devices, voltage outputs of the individual probes were used, i.e. an analog output

Table 3.3: Probes and sensors applied in WKS wave flume experiments.

Probe / Sensor	Technique	Measuring Application
Baumer OADR20 LDS	Laser optical	Scour depth, surface profiling
ABUS UW cameras	Optical, video	Scour depth, with sediment gauges
Wave gauges	Capacitive	Water surface profiles
Delft Hydr. EMS probe	Electromagnetic	2D orbital wave motions
Nortek Vectrino+ ADV	Ultrasound	3D velocities, point-wise

system. Therefore, probes were connected to a National Instruments NI-DAQ NI USB-6259 analog-digital converter in order to sample data in digital form on the measuring system, finally using National Instrument DIADEM sampling and control software for data storage and Mathworks Matlab for post-processing. A sampling rate of 100Hz was used for all probes in order to get consistent data sets and time lines, which has proven to give accurate results for the present investigations.

Scour Development In the present setup, the scour development was measured and recorded using an underwater laser distance sensor (LDS), which was automatically driven over the bed surface around the structure (see figure 3.4a). As LDS, a Baumer OADR20 device sensor was used, which has a measuring range of 100 to 600mm with an accuracy of 0.05-2mm in air. The sensor is submersible up to 30m water depth. Due to different refractivity in water, the measuring range of the sensor was however slightly shifted in practice. Therefore, a recalibration of distance data for the underwater environment was applied.

The LDS was mounted on a movable positioning platform, which could in turn be moved by a rail system along the flume axis. The platform made use of a three-axis guide rail system and step motors, which allowed a movement of the LDS in three dimensions, i.e. longitudinal and perpendicular to the flume axis as well as in vertical direction with an accuracy of 1/10mm. For the programming of the system, a software for CNC control units was used, which allowed an automated movement of the LDS on predefined paths over the bed surface while continuously measuring its distance to the bed. Computer programs based on DIADEM measuring software were developed for an automated data logging and coupling of the different system components. Due to the underwater housing of the instrument, the LDS was completely operated in submerged conditions roughly a few decimeters above the bed surface, i.e. working non-intrusively and without the need to drain the flume or lower the water level.

In addition to that, ABUS underwater cameras were used to visually observe scour development and flow processes. Sediment gauges (see figure 3.7) were furthermore installed under the braces and the main column as well as around the piles of the tripod structure, which is in areas where the bed surface could not be

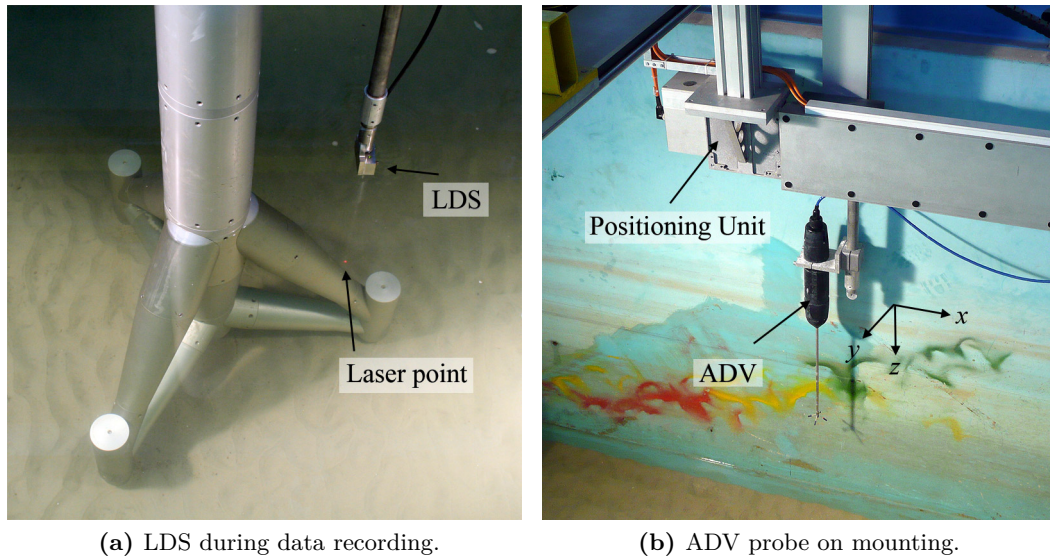


Figure 3.4: Pictures giving LDS Laser distance sensor for surface profile collection and ADV flow measuring probe with positioning platform.

measured using the LDS due to blockage by the structure itself.

Surface Elevation and Flow Fields To measure and control the wave parameters, i.e. wave heights and wave periods in the test section, capacitive type wave gauges were installed at certain locations along the flume as sketched in figure 3.1. The accuracy of the wave gauges thereby lies in a range of $\pm 0.5\%$ of the wave gauge length and 40cm types were used here. The still water level in the flume was controlled by use of a manually controlled tip gauge, which was installed near the movable bed section.

In order to record orbital motions of the wave components in an undisturbed area, an electromagnetic current meter of type Delft Hydraulics EMS was used for measuring velocity components in two dimensions. The instrument was installed at a distance of $\sim 3\text{m}$ in front of the tripod with a distance of 0.2m to the flume side wall. Furthermore, the flow field around the model structure was measured by use of a Nortek AS Vectrino⁺ ADV probe, mainly for validation purpose of the numerical flow model. The probe works by applying the Doppler effect for velocity measurement in three dimensions and is sampling within a defined control volume located at some distance from the probe, which was chosen as 6mm in the present setup, i.e. a point-wise measuring technique. The ADV probe was mounted at the same positioning platform that was used for the LDS sensor (see figure 3.4b). Therefore, an automated driving to predefined measuring locations in x, y, z directions around the tripod was possible as well, within the accuracy of the step motors.

3.2.3 Test Procedures

Before starting a test series, calibration curves were generated for the wave gauges and the LDS, relating voltage signal outputs to the measuring units. No further value calibration was necessary for the electromagnetic and ADV probes. Measuring locations and paths for moving the LDS over bed by use of the positioning platform were defined and coded beforehand. Generally, a more detailed measurement was chosen near the structure compared to free bed areas with less structural influence. Distances between single measuring tracks were in a range of few millimeters (around piles) to some centimeters (free area).

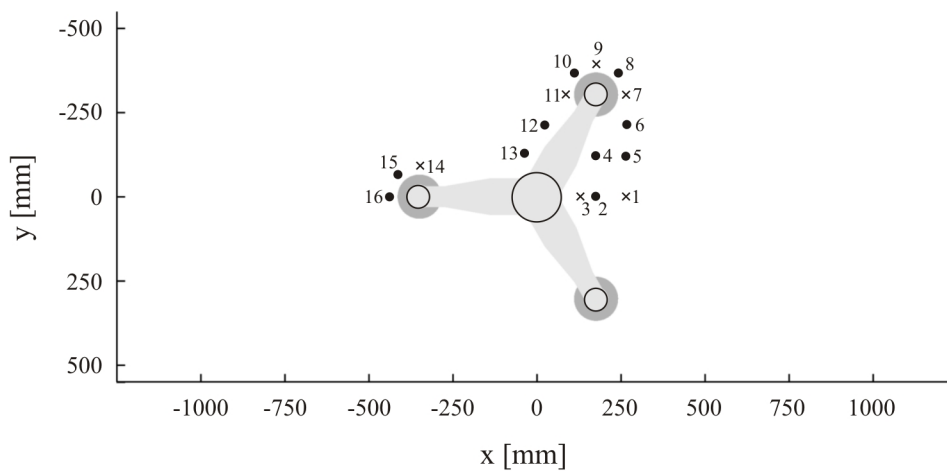
Investigations on Scour Development After installation of the tripod structure in the test section, sand was filled into the bed area and finally flattened by hand. No compaction of the sediment using special equipment was carried out here. Sand was however filled in in completely wet form, so that a saturation of the bed was guaranteed. The flume was then slowly filled with fresh water from the storage system. Finally, the wave maker was started and ran for time spans of 125 to 250 wave cycles per period in order to minimize overall reflections in the flume. Surface elevations and orbital motions were continuously measured during the test runs. The scour development was finally measured after defined wave periods between 125 and 1000 wave cycles in still water conditions. Therefore, the wave maker was stopped during scour measurements in between the wave load periods by use of the LDS device and underwater exposure. Afterwards, the wave maker was started again for the next load intervals. This procedure was repeated until the end of the tests. Due to a more rapid scour development in the beginning, the measuring interval was higher at the start of the tests, while longer measuring intervals were chosen when approaching an end condition. Once a test series was terminated, which was generally the case after 3000 to 7500 wave cycles reaching an almost equilibrium stage, the water level in the flume was lowered to a level where the sand bed could be drained by use of the installed drainage system. Afterwards, the bed was flattened and leveled for the next test series.

Several tests using different experimental configurations of wave heights H_m/H_s , wave periods T_m/T_p and wave-encounter angles were carried out for regular waves and JONSWAP wave spectra; test parameters are given in table 3.4. The water depth was kept constant at $d=0.75\text{m}$ for all test runs.

Local Flow Measurement The point-wise measurement of flow velocities around the structure by use of the ADV probe was carried out independently from the scour development tests. Locations of special interest with structural influence on the flow field were regarded here, e.g. near the pile sleeves, braces or the main column of

Table 3.4: Compilation of conducted experimental scour tests in the WKS wave flume.

Name	wave type	wave height H_m, H_s [cm]	wave per. T_m, T_p [s]	angle [$^\circ$]	mud mats	max. # waves
r2130-01	regular	20.6	3.0	0	no	7500
r2130-02	regular	20.6	3.0	0	no	3000
r2130-03	regular	20.6	3.0	0	yes	4000
r2130-04	regular	20.6	3.0	180	yes	3000
r2130-05	regular	20.6	3.0	90	yes	3000
r1523-01	regular	15.0	2.3	0	no	4000
s2130-02	spectrum	20.8	3.0	0	no	4000

**Figure 3.5:** ADV measuring positions in horizontal (x,y) plane. Crosses give data positions applied for numerical model verification, see §5.2.2.

the tripod. As test conditions, those from test run r2130-01 (see table 3.4) were applied here.

In a first step, the structure was installed in the test section and the bed was straightened, as tests were conducted in moving bed conditions. Afterwards, a total of 192 locations around the structure were defined, resulting from 16 locations in horizontal plane and 12 points per vertical at each location, out of which vertical velocity profiles could be created later. The measurement position coordinates in vertical direction were limited by the minimum distance necessary for a correct measurement of the probe over ground on the one hand and the lowest surface water levels during wave passage on the other hand, which resulted in a minimum distance of 10mm and a maximum distance of 500mm over undisturbed ground. The interim values had distances of 20-50mm. Positions in horizontal plane are given in figure 3.5.

The ADV probe was mounted on the vertical rod of the positioning platform and the measuring positions were coded into the step motor control software in order to achieve an automated measuring system. A wave gauge later used in post-processing

was installed near the flume wall at the position of tripod x axis. Afterwards, the flume was slowly filled to still water level and the wave maker was started. At each measuring location, the velocity components were measured for a time span of ten wave cycles. Velocities were first measured at the vertical positions near the bed and at the top levels in the end in order to minimize influences of local scour formation.

In post-processing, ADV data were first filtered using a butterworth filter approach to reduce noise in the signals. Data for each measuring location were then averaged over the recorded wave cycles in order to generate a mean velocity profile for verification of the numerical model, see §5.2.2.

It should therefore be noted that only mean quantities of flow were regarded here for comparison. In addition to that, Reynolds stresses could however be directly determined from recorded velocity fluctuations, e.g. following an approach given in Liu et al. (2004), which is however not part of the present work. It should further be noted that results of the point-wise flow measurement around the structure are not given here, but partly later in the numerical modeling section, see §5.2.2.

3.2.4 Experimental Results on Scour Development, Regular Waves

In the following, results of the 1:40 tripod scour experiments in the WKS wave flume are given. The local, global and time-dependent scour development was monitored using LDS measurements and visual observations as given in §3.2.2. In the post-processing of the data, different sources were therefore combined in order to generate a general overview of the development. For the final analysis, filtering of the data was conducted in order to filter spikes. This was especially required for the LDS data sets, as certain scatter was observed when regarding neighboring LDS points recorded on a measuring path due to slight differences in the distance calculation caused by reflection on the single grain surfaces. These differences were however in a typical range of 0.5-1.5mm only.

Based on the unstructured measuring point data sets including LDS data and manually erected data from video observations as far as available, surface elevation models based on gridded data sets were finally created by interpolation. For all result plots given in the following, extends of $\pm 640\text{mm}$ in both x and y direction were chosen. Gridded data have a horizontal resolution of 5mm.

It should be noted that results of scour development are mainly given in dimensional form in plots and discussions in the following. Although it is quite common practice to give scour depth results e.g. for circular vertical piles in dimensionless form as relative depths S/D , i.e. depth divided by pile diameter, such an approach is not convenient for the current cases, as the choice of D in this form is rather arbitrary. Furthermore, results will typically rely not on this single value alone, but depend on several factors.

Bed Regime For the wave conditions given in the first five test series of table 3.4, the maximum orbital velocity is $u_{w,max} = 0.38\text{m/s}$, when calculated from wave theory. Applying equations (2.13), (2.14) and (2.19) therefore leads to a maximum shear stress of $\tau_w = 0.54\text{N/m}^2$ and a corresponding Shields value of $\theta_{max} = 0.232$. These values are however only reached as peaks under the wave crest. As the critical Shields value is $\theta_c = 0.059$ for the sediment under investigation, a life-bed regime is given in that case. It should be noticed that for wave load cases, unlike for steady current situations, these values are however not constant but varying over time due to the character of the orbital motion. For the remaining two tests, values are slightly different from those given before, a movable bed regime under maximum load is however given here.

Test Series r2130-01 and r2130-02 Experimental results using scour measurements and visual observations for regular wave cases with $H_m = 20.6\text{cm}$ and $T_p = 3.0\text{s}$ are given in the following. Final results of scour development for test series r2130-01 as plots of the bed surface at the time after 3000 wave load cycles are given in figure 3.6. Furthermore, surface plots in intervals of 250, 500, 1000, 2000, 4000 and 6000 wave cycles are given in figure 3.9 as well as corresponding cross sections in figure 3.10.

As a main result of this test it must be noted that scour formation around the structure significantly differs from typical scour pattern that can be observed at single vertical pile structures or large gravity base foundations with circular footprint.

Scour Mechanisms Three main regions of scour formation can be determined for the tripod structure under the given load conditions. The overall scour pattern shows a combination of local and global scour formation:

1. Around the single piles, while larger depths can be found at the rear piles
2. Under the main column and the lower braces connecting the rear pile sleeves
3. In the back part of the structure with a maximum observed scour depth for the present test series

Although the pile sleeves of the structure have a solid connection to the main column, the lower parts beneath the lower braces could generally be regarded as single objects here, resulting in local scour formation similar to what can be observed for single pile structures. A KC number calculated by use of the pile diameter gives a value of $KC_p \approx 19.3$. This value is lower than the typical threshold value of 30 for occurrence of a horseshoe vortex system. Therefore, no such formation was expected to occur here, which corresponds with visual observations made in the present test case. The main mechanism for scour formation is thus the local flow acceleration

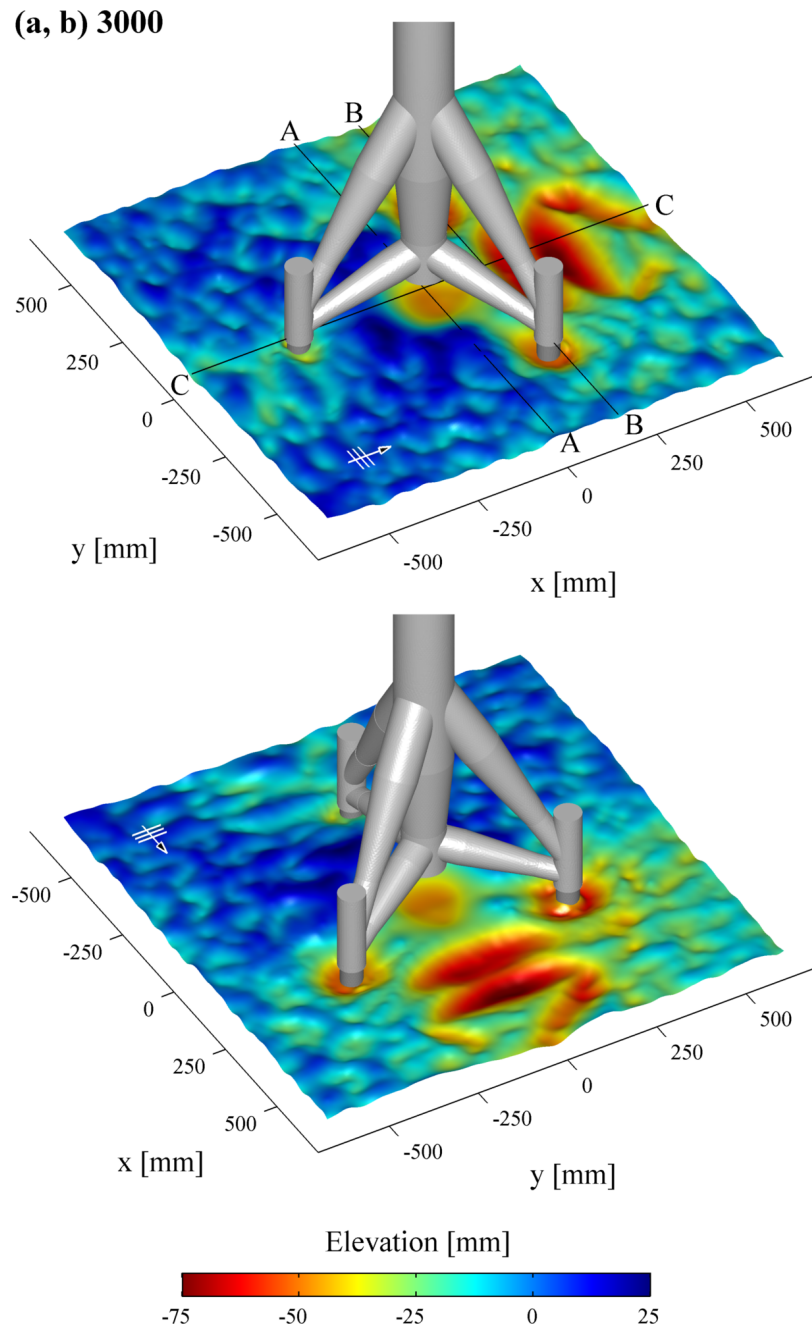


Figure 3.6: Results of scour development for test series r2130-01 after 3000 wave cycles, (a) front view, (b) rear view. Cross section positions for figure 3.10 are given in upper plot (a). Wave-encounter angle 0° .

around the single piles, leading to a quick mobilization and up-lifting of particles. After getting into suspension, these are transported away by the turbulent flow. Sediment suspension can be regarded as the dominating transport process here, see also figure 3.7 for the time-varying sediment suspension around the rear piles.

For the present test series, the local scour at the rear piles reaches values of about 5.0cm ($S/D_p = 0.85$, with D_p as the pile diameter) for the maximum and 4.5cm (0.76) for the mean, respectively. The scour is slightly lower at the front pile, where a depth of 3.5cm (0.59) and 3.0cm (0.51), respectively was observed. It should be noticed that scour depths were collected at one of the rear piles only. Due to slight asymmetry in the overall transport pattern, local depths at the remaining rear pile might therefore differ slightly.

In the region under the main column and the lower braces connecting the pile sleeves with the column, a similar flow acceleration can be observed. This can mainly be explained through general blockage of the structure, which enforces the waves to flow between and under structural elements, i.e. the lower and upper braces as well as the lower part of the main column. In that case, pressure is built up in front of the structure and water is enforced to flow around it. Especially when regarding the lower braces, a similar mechanism can be found at flow around pipelines and thus resulting scour formation, see e.g. the works in Brørs (1999) and Sumer and Fredsøe (2002). The maximum scour depth in the region under the main column reaches a value of 5.0cm ($S/D_{mcl} = 0.44$, with D_{mcl} as the lower main column diameter) in the present case.

The local but however areal scour formation in the rear part of the structure mainly results from accelerated flow under the main column and the braces during the wave crest passage on the one hand and a reverse-directed flow pattern during passage of the wave trough. Furthermore, turbulent and partly downward-directed flow is caused by a large-scale vortex formation in the bend between the upper rear braces and the back side of the main column in the first case, see figure 3.8. Again, sediment suspension can be regarded as the main transport process here. It should however be noticed that local scour formation in the rear-part of the structure is certainly overlaid with other, setup-influenced flow and thus resulting scour effects, as will be discussed later.

Regarding the overall sediment transport in the near-field, certain erosion occurs in the back of the tripod, while areal sediment accumulation takes place in the front party and the bend between front and rear piles. Sediment is thereby partly shifted from back to front, while the larger amount of eroded material could however be found in front of the sediment trap, which was installed at the end of the concrete ramp, i.e. it was transported out of the movable bed section.

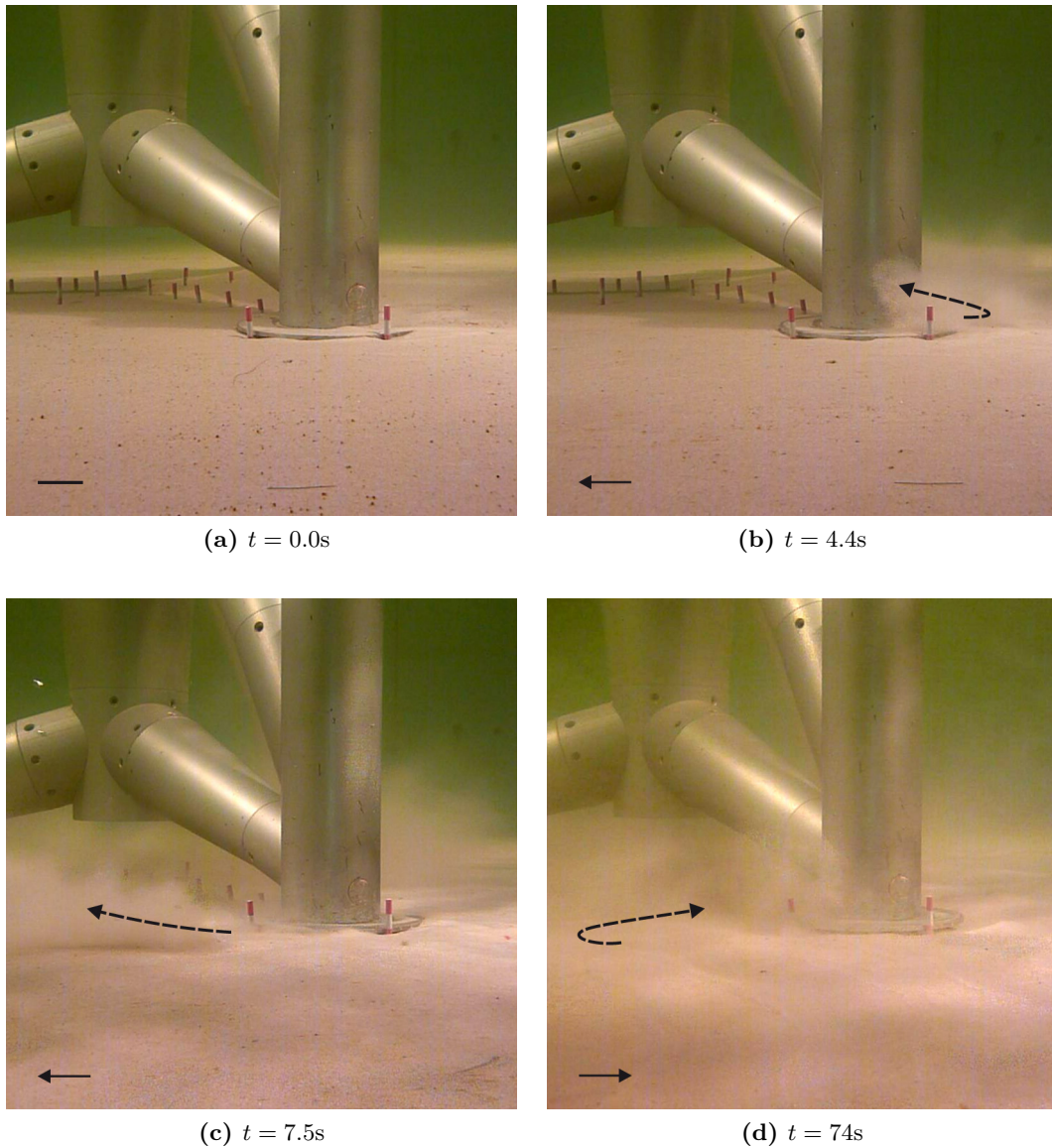


Figure 3.7: Erosion and transport of suspended particles at the rear pile at different time steps during wave passage for test series r2130-03. $H_m=20.6\text{cm}$, $T_m=3.0\text{s}$, $d=0.75\text{m}$, 0° wave encounter angle. Arrows in lower left corners give current near-bottom flow direction.

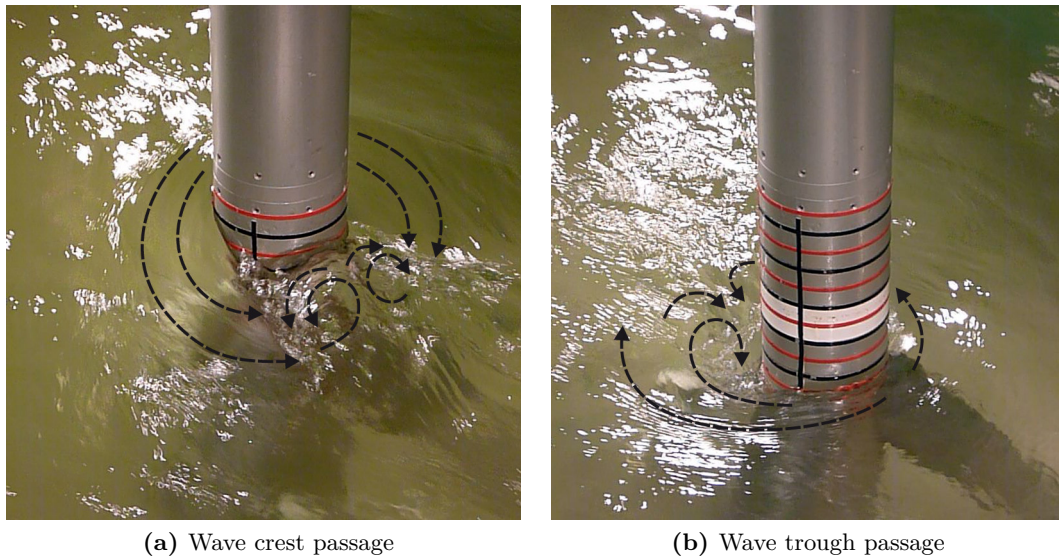


Figure 3.8: Surface elevation and vortex formation during wave passage at the tripod main column at time steps of (a) wave crest, (b) wave trough passage. Wave-encounter angle 0° . Wave direction from upper left to lower right corner.

Time Evolution With regard to the time evolution of scour development, it was observed that the local formation takes place very rapidly, while scours develop at the piles and directly under the main column first, as can be seen from figure 3.11, figure 3.9 and the corresponding cross sections through the bed surface given in figure 3.10. When regarding the trends of scour development over time instead of exact values, scour depths can be seen in an almost equilibrium condition at the stage after 3000 wave load cycles, while about 90-100% of the corresponding values are reached after 1500 waves already. Values in figure 3.11 are given as local mean values, i.e. averaged over three and four depth locations, respectively for the piles. Maximum values at each position are therefore up to 20% higher. An averaged representation was however chosen, as trends are less influenced by local effects of bed ripples. However, certain scatter of depth over time can be observed due to likewise influence of ripples on the one hand and the life bed regime under given load conditions on the other hand. In the area behind the structure, maximum scour depths are reached comparatively slower. Furthermore, fluctuations around equilibrium values can be observed in the near-field of the tripod due to relocation of sand ripples.

Reproducibility The general reproducibility of the experiments was carried out through repetition of the first test series, denoted as r2130-02 in table 3.4. The test was run for max. of 3000 wave cycles. Plots of scour development for this experiment are given in the Appendix in figures A.1 to A.3; a comparison of resulting scour development as cross sections through the bed surface at the time

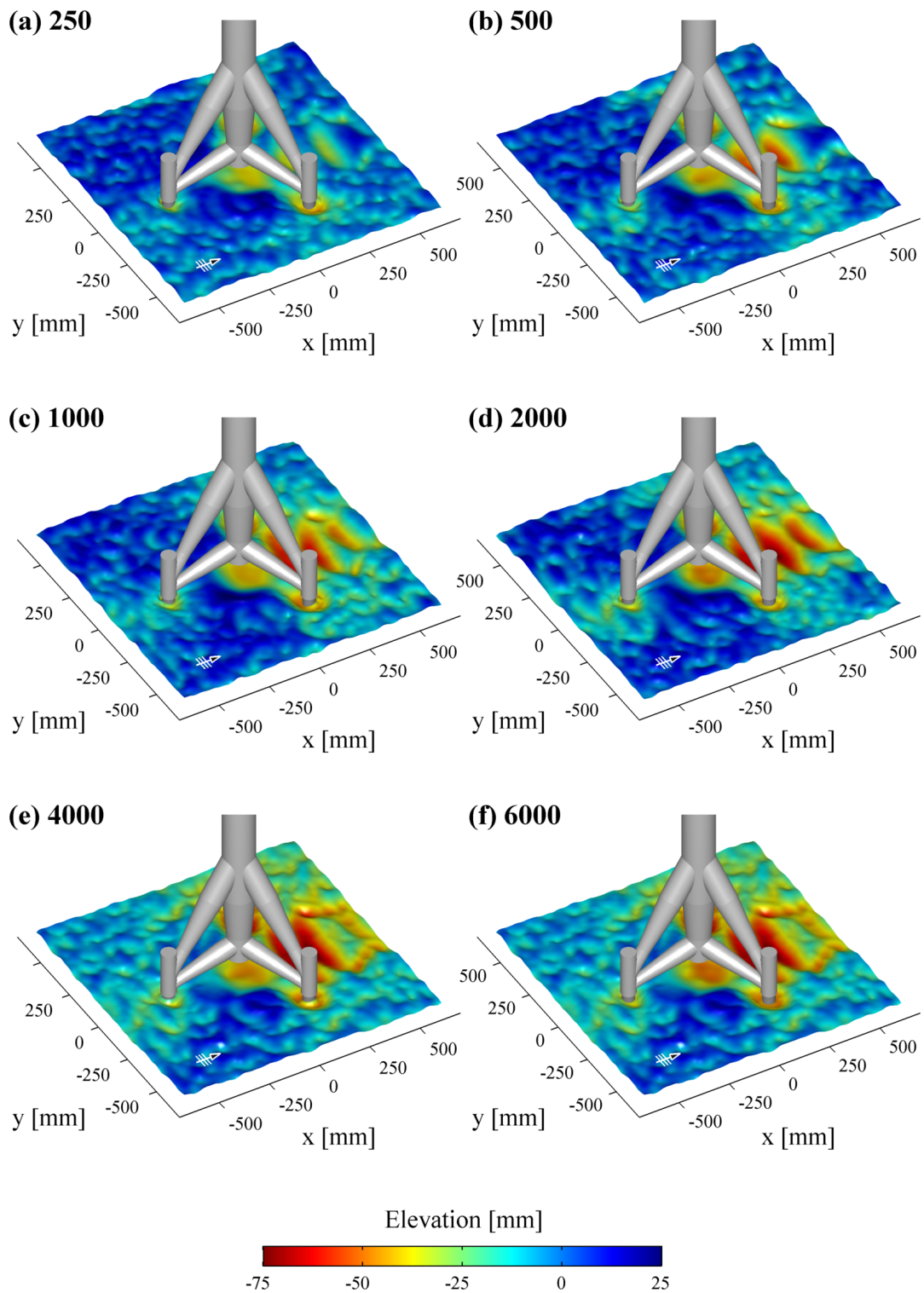


Figure 3.9: Results of scour development for test series r2130-01 in the WKS wave flume experiments at time steps of 250, 500, 1000, 2000, 4000 and 6000 wave cycles.

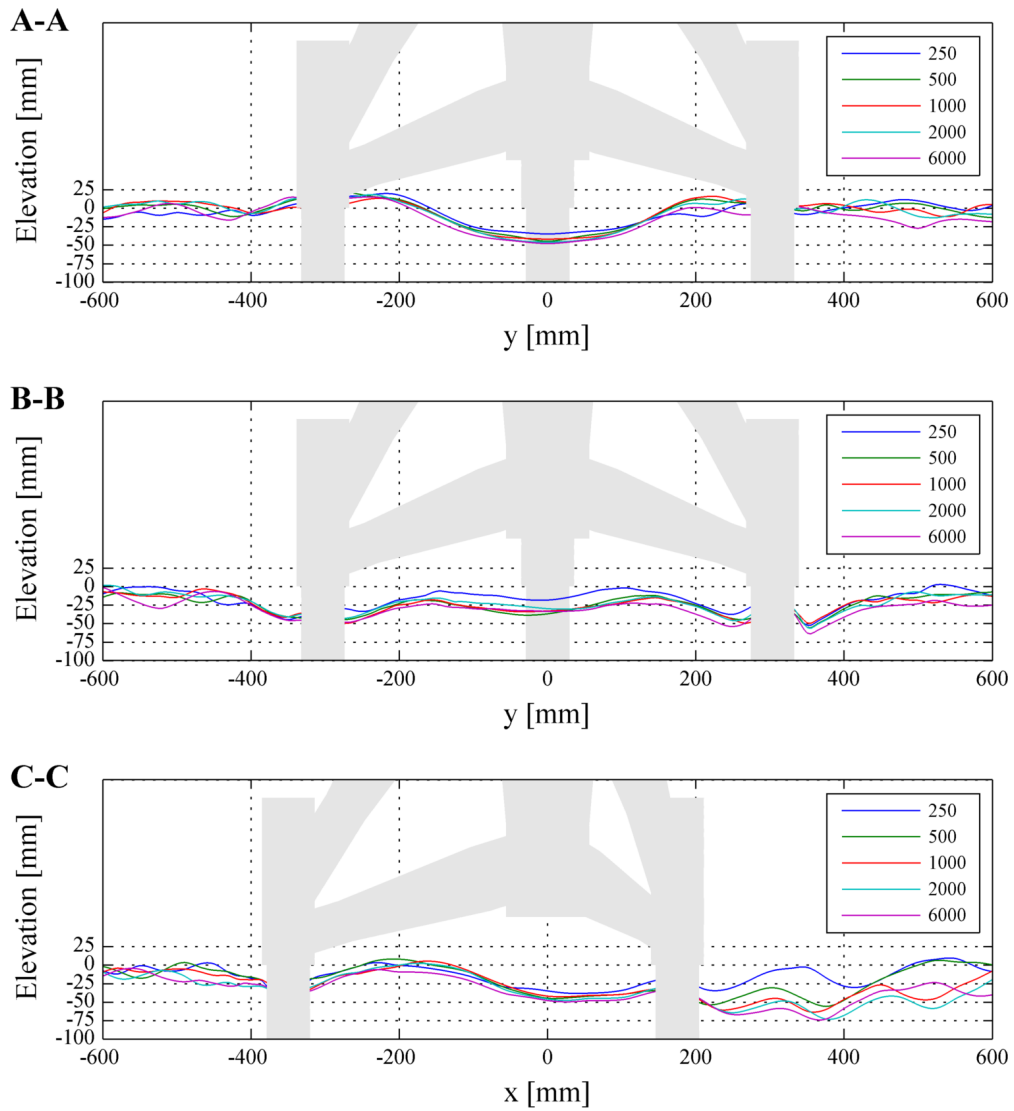


Figure 3.10: Cross sections for test series r2130-01 at time steps of 250, 500, 1000, 2000 and 6000 wave cycles. Positions A-A, B-B and C-C are given in figure 3.6.

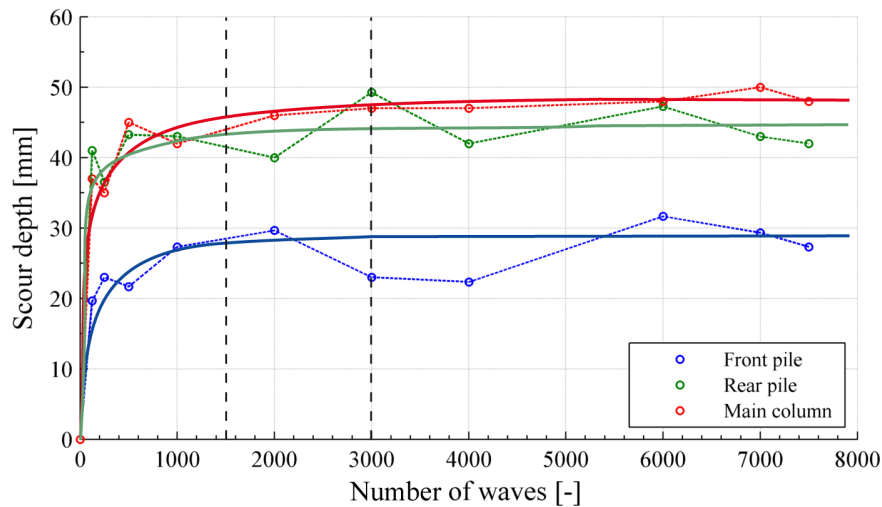


Figure 3.11: Development of local scour depths over time for test series r2130-01, given as local mean values over number of wave cycles. Symbols: dots: moments of record; dashed lines: connection for clarity; solid lines: trends of scour evolution.

after 3000 waves is given in figure 3.12. It can generally be stated that the single test result could be reproduced with sufficient quality. Minor discrepancy can be observed in the near-field of the tripod and the rear piles. Both differences however result from local, small-scale sand ripples in those areas, which make it difficult to directly compare the experimental results at locally-fixed sections. Even better agreement for the two test cases can therefore be found in the Appendix in figures A.4 to A.6 for earlier time intervals of 500, 1000 and 2000 wave cycles, where no such influences of bed ripples were observed.

Influence of Mud Mats In direct comparison with test series r2130-01 and r2130-02, i.e. tripod installation without mud mats in vertical position of the undisturbed bed level, local scour depths are lower in case of a mud mat installation as it was investigated in test series r2130-03. The corresponding surface plots and cross sections are given in figures A.7 to A.9. It was observed that the installation leads to a local reduction of scour depth by 20-25% for the front pile and 30-50% for the rear pile, while the maximum reduction occurs at the outer side of the piles and up to 50% for the area under the main column. Regarding the scour reduction through mud mats at the piles, the effect is thereby similar to what can be observed for collar installations at circular piles near seabed level, see e.g. de Sonnevile et al. (2010), due to shadowing effects of the pile-near flow. The overall, global scour development around the tripod stays nearly uninfluenced.

Test Series r2130-04 and r2130-05 In the following, results for the two test series with wave-encounter angles of 180° and 90° , respectively are summarized.

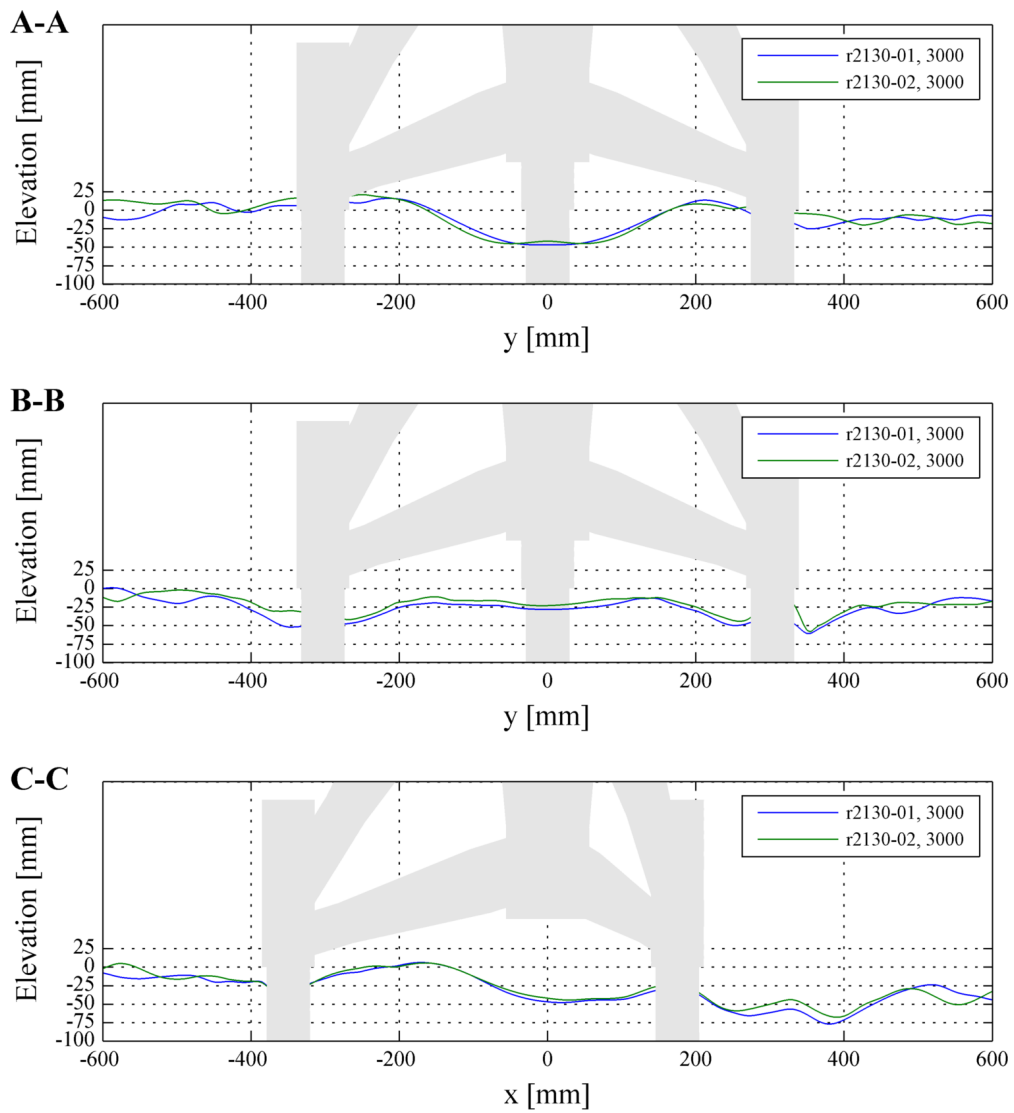


Figure 3.12: Comparison of cross sections for test series r2130-01 and r2130-02 at the time step of 3000 wave cycles. Positions A-A, B-B and C-C are given in figure 3.6.

It should be noticed that the two tests were conducted in an earlier stage of the investigations. For this reason, no scour measurement by use of sediment gauges under structural elements or visual observation was carried out here. Therefore, no information on local scour evolution in these areas and directly at the piles are available for the present experiments, depicted as white surface plot areas in the corresponding figures. Results of general scour development are however given here for comparison.

The plots of the bed surface after a time span of 3000 wave load cycles for test series r2130-04 (180°) and r2130-05 (90°), recorded by the LDS sensor, are given in figures 3.13 and 3.14. Further plots on time-dependent scour development can be found in the Appendix, see figures A.10 and A.11.

For the 180° installation, local scour formation occurs around the piles. Although scour depths at the piles were not directly measured, shapes seem to be generally equal to what could be observed for the 0° wave-encounter angle tests. Unlike the latter, no bed deepening could however be observed in front of the tripod, i.e. between the two front piles; scour formation however occurs in the area behind the main column, as it was given in previous tests. Regarding the overall sediment transport in the near-field, certain erosion occurs in the front part of the tripod, while areal sediment accumulation takes place in the rear part, which stands in contrast to what could be observed for 0° installation. For the 90° installation, bed deepening again takes place around the single piles, while an asymmetric formation is given here due to asymmetric structure installation, leading to more erosion at the lateral, wall-facing pile. Here, the general blockage of the structure is higher due to structural elements located perpendicular to the direction of wave progression, which are hence leading to enhanced flow acceleration. Again, certain bed deepening behind the main column is given. The overall sediment relocation takes place from the areas of higher to lower blockage in the flume.

It can generally be stated that although scour patterns differ locally from those observed in the previous 0° tests, scour mechanisms are however similar, as effects of local structural blockage resulting in flow acceleration, sediment mobilization and further transport occur in the same manner.

It could be investigated in all previous test series with regular waves, irrespectively of the wave-encounter angle, that local scour formation occurred right behind the tripod main column section. It can therefore be assumed that the local scour deepening in this area is certainly overlaid with some model setup influences, rather than being exclusively generated from structural flow pattern.

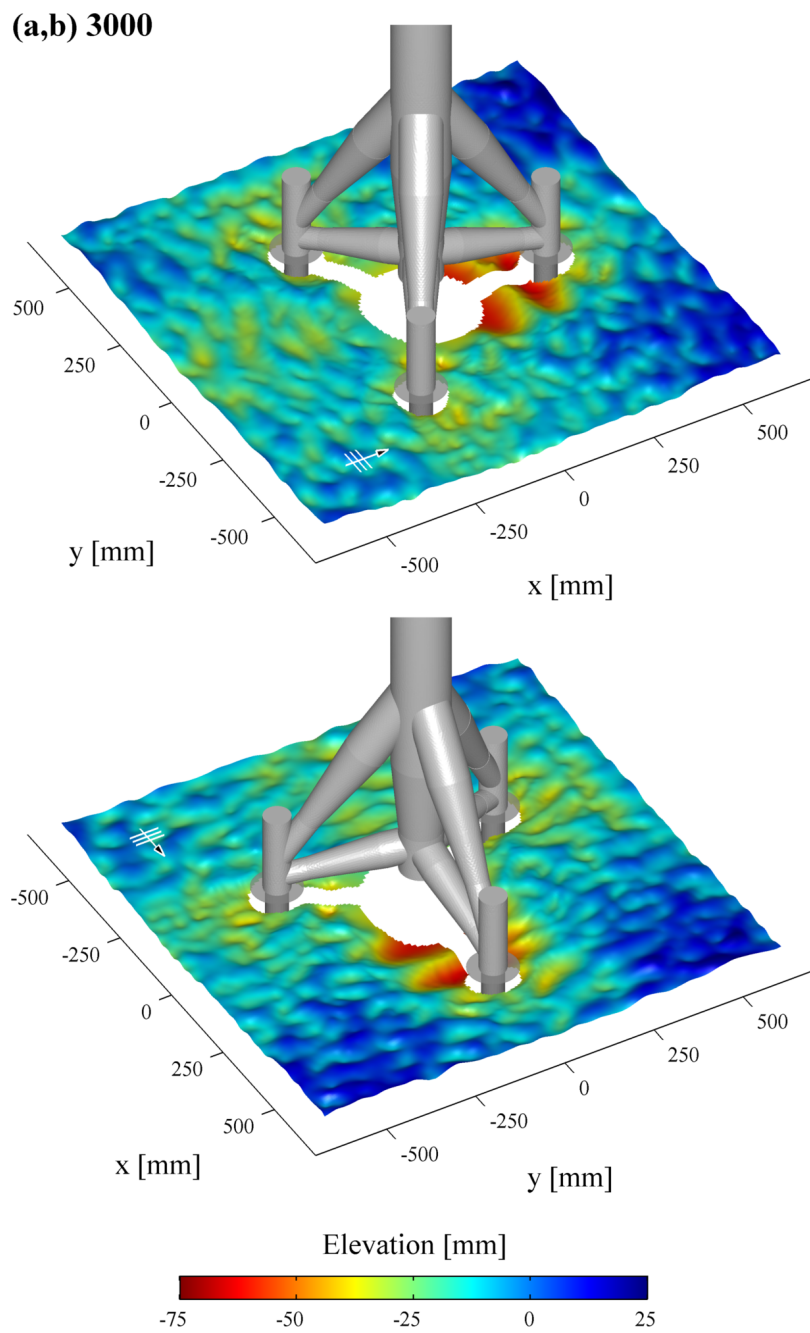


Figure 3.13: Results of scour development for test series r2130-04 after 3000 wave cycles, (a) front view, (b) rear view. Wave-encounter angle 180° .

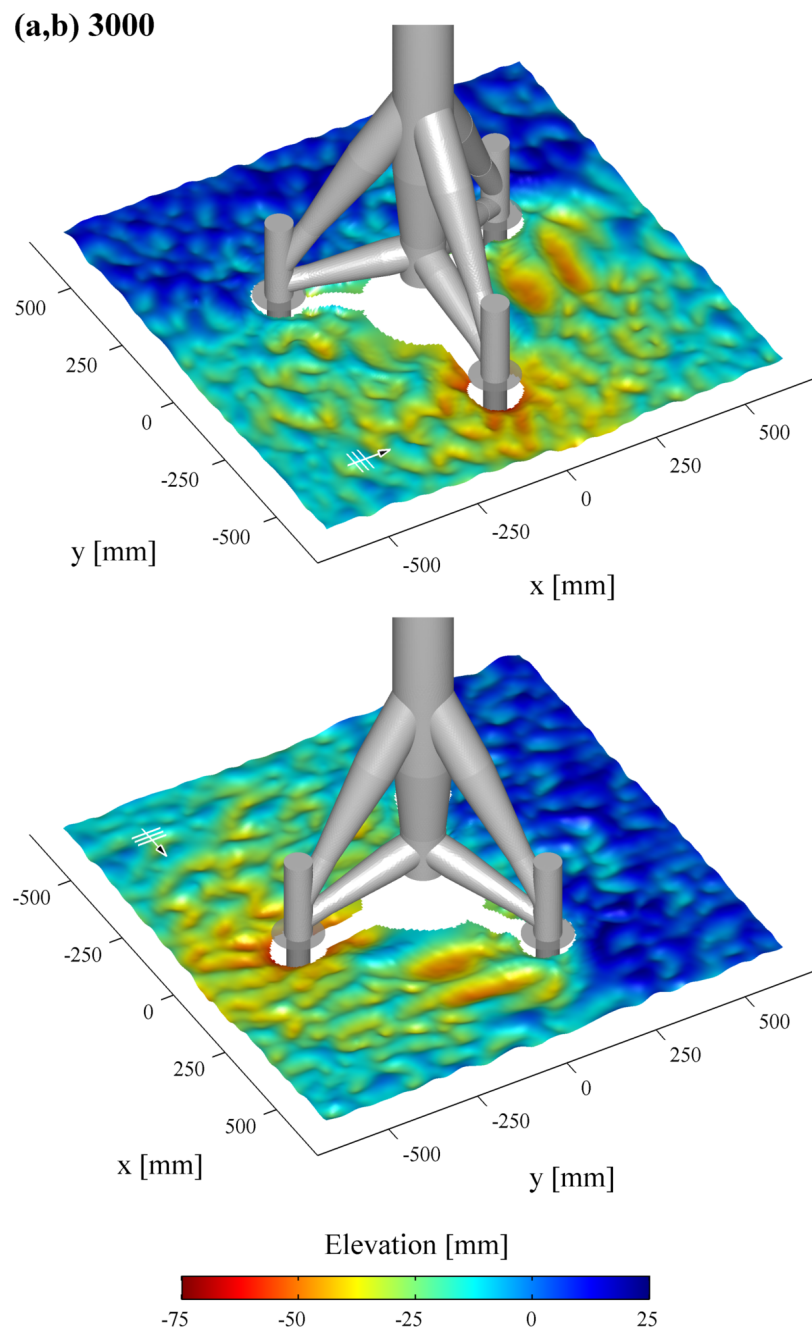


Figure 3.14: Results of scour development for test series r2130-05 after 3000 wave cycles, (a) front view, (b) rear view. Wave-encounter angle 90° .

3.2.5 Wave Spectra Representation

It will be shown later in §5.3 that regular wave load boundary conditions are required for numerical modeling of scour development in the present investigations. Therefore, load cases representing the effects of wave spectra in terms of local and regional scour development in the model had to be found.

In test series s2130-02, the tripod model with 0° wave-encounter angle installation was loaded with a wave spectrum holding parameters of $H_s = 20.8\text{cm}$ and $T_p = 3.0\text{s}$ as given in table 3.4 and $\gamma = 3.3$, i.e. a JONSWAP (Joint North Sea Wave Project) wave spectrum. Test results after 3000 wave cycles giving an almost equilibrium stage are displayed in figure 3.15; the time-dependent scour development and cross sections can be taken from figures A.16 and A.17.

In a direct comparison between regular waves (r2130-01, -02) and the wave spectrum case holding wave parameters $H_m = H_s$ and $T_m = T_p$, it is obvious to see that both the local scour depths at the piles and the overall sediment transport volumes are higher in cases of regular waves. According to Soulsby (1997), a simple approximation for a wave spectrum is to use a monochromatic (regular) wave with parameters $H_m = H_{rms}$ and $T_m = T_p$ as both the energy density and the frequency at the peak of greatest energy are equal then. As $H_{rms} = H_s/\sqrt{2}$, the above given relationship for the tests therefore leads to a higher energy density in case of the regular wave case, which explains the altogether larger sediment transport under the given load conditions.

An approach similar to the first one mentioned above ($H_m = H_s$, $T_m = T_p$) was suggested for numerical model simulations in Göthel (2008). For the present setup and the given results, it could however be shown that this approach is not directly applicable in the present case.

An alternative is proposed in Sumer et al. (1999) for sinking/floating of objects in liquefaction under waves, taking $H_m = H_s/\sqrt{2}$ and $T_m = T_z$, while the latter is the mean zero up-crossing period and differs from the approach by Soulsby (1997). An application of this leads to values of $H_m = 0.15\text{m}$ and $T_m = 2.34\text{s}$ (as $T_z \approx 0.781 \cdot T_p$ for a JONSWAP wave spectrum) for representation of the wave spectrum test, which is given in test series r1523-01 investigated here. Results of the latter in terms of surface plots, time evolution and cross sections are given in figures A.12 to A.14. It was however found that this approach clearly underestimates the local scour depths found in the corresponding wave spectrum case.

A plot of the three aforementioned test results in terms of cross sections through the bed surface is given in figure 3.16. As explained before, the scour depths caused by the wave spectrum are obviously between the results of the remaining two cases, leading to the conclusion that an approximate representation can be found by taking intermediate values here. As $H_m/H_s = 1$, $T_m/T_p = 1$ for the first and $H_m/H_s \approx 0.71$,

$T_m/T_p \approx 0.781$ for the latter case, representative values should therefore lie in a range of 0.8-0.9. The ratio was finally taken as $r_{sr} = 0.9$ for the present investigations in the numerical model, leading to

$$H_m \approx 0.9 \cdot H_s \quad \text{and} \quad T_m \approx 0.9 \cdot T_p \quad (3.1)$$

for the representation of a wave spectrum by regular wave trains in terms of local scour development.

3.3 Wave-induced Scour on Large Scale

3.3.1 Experimental Setup

To further analyze scour phenomena around the tripod structure in detail and under minimized laboratory modeling effects, especially with regard to the scaling of the model sediment, large-scale physical model tests were carried out in the Large Wave Flume (GWK) of the Coastal Research Center, Hanover. The GWK wave flume has a length of roughly 307m, a width of 5.0m and a height of overall 7.0m. The piston-type wave maker installed in the front section of the flume is capable of generating regular and irregular waves with wave heights up to 2.0m while using a stroke of up to ± 2.1 m. Due to the amount of water volume necessary to fill the flume, water is taken from the near-by Mittelland Canal. Inlets and outlets are located in the flume bottom in the front and back part.

Tests were conducted on a model length scale of 1:12 here. Similar to the laboratory tests in the WKS flume, the moving bed modeling area was installed using a false bottom. The test section however consisted completely of sand material, while the horizontal investigation area with a bed depth of 1.2m had a length of 35m, resulting in an area of 175m². Sand ramps in the front and back part had slopes of 1:20 and 1:15, respectively, see figure 3.17. A drainage system was further installed in order to drain water from the test section to the front and back ends when lowering the water level in the flume.

As bed material for the whole section, fine sand as it was already used in the WKS tests was used again, i.e. having a grain size of $d_{50} = 0.148$ mm as given in §3.2.1. This e.g. allowed a direct conclusion on possible scaling effects.

The Tripod model was built as a heavy steel construction, holding dimensions that were directly scaled from the 1:40 WKS flume tests. Main structural dimensions therefore are: $D_{mc} = 0.5$ m as the diameter of the main column in the upper section and $D_p = 0.2$ m as the diameter of the piles. The structure was installed in the center of the horizontal investigation area with a solid connection to the flume concrete bottom, using a modifiable substructure that allowed the installation of the tripod with wave-encounter angles of 0° and 180° as given in §3.2.1.

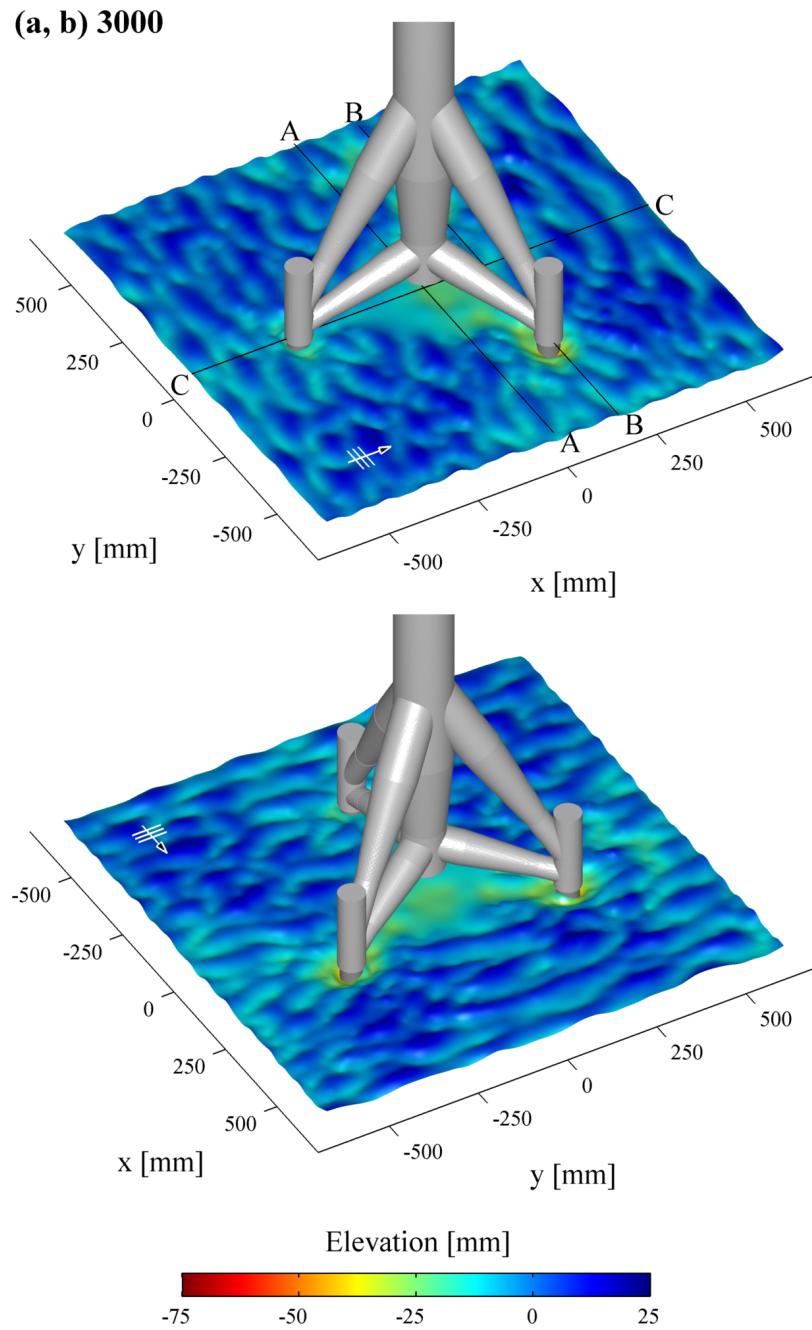


Figure 3.15: Results of scour development for test series s2130-02 after 3000 wave cycles, (a) front view, (b) rear view. Wave-encounter angle 0° .

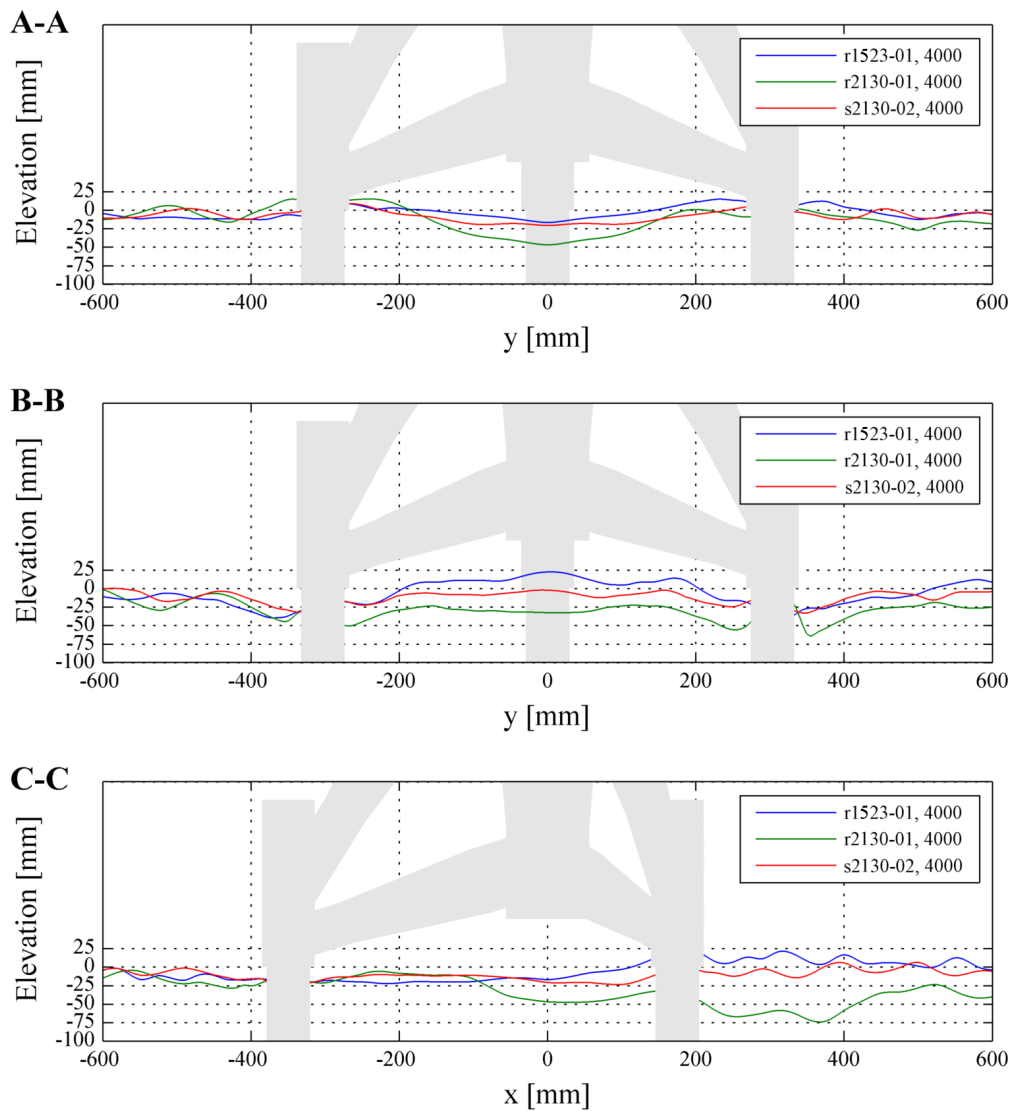


Figure 3.16: Comparison of cross sections for test series r2130-01, r1523-01 and s2130-02 at the time step of 4000 wave cycles. Positions A-A, B-B, C-C are given in figure 3.6.

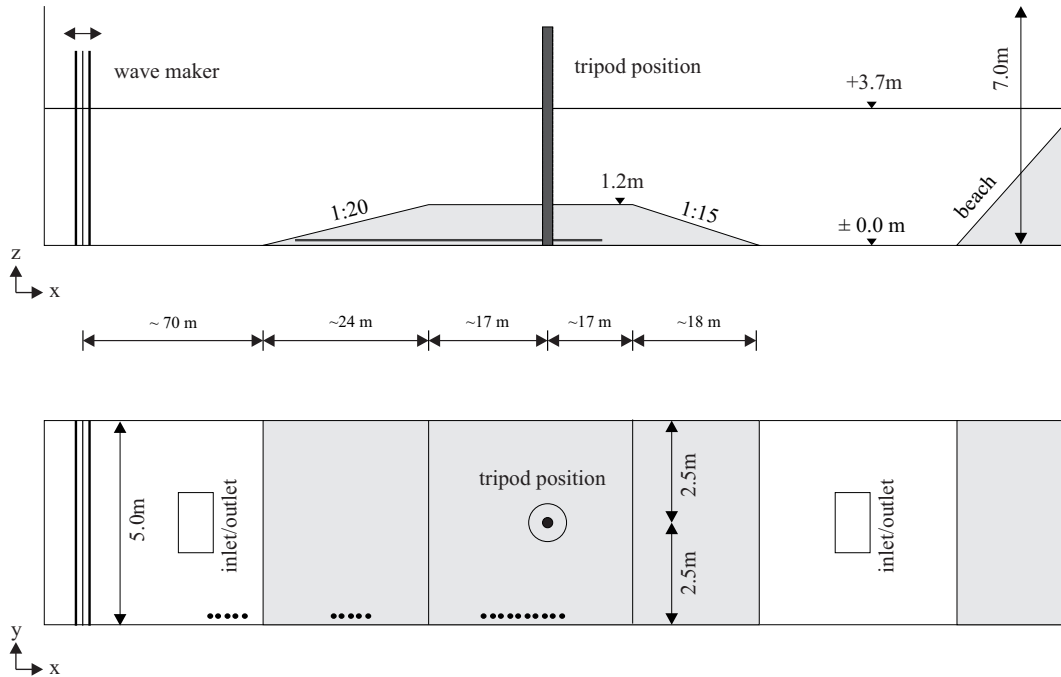


Figure 3.17: Sketch of the experimental setup in the GWK wave flume. Tripod structure is given symbolically.

In this symmetric installation, the vertically projected area of the tripod is $A_t \approx 2.54\text{m}^2$. This results in an overall blockage ratio of $r_t \approx 0.20$ at still water level, which is therefore slightly above the threshold value $r_b = 1/6 \approx 0.167$ according to Whitehouse (1998) for possible influence due to blockage effects. This circumstance was therefore investigated in terms of numerical modeling, see §5.3.3 and is further discussed in §3.4. The applied model scale of 1:12 was given as a compromise between grain scaling, possible wave generation and further investigations on breaking wave influence, see Hildebrandt and Schlurmann (2012) for a description of the latter.

3.3.2 Measuring Equipment

Collection of data on water surface elevations, orbital velocities, local flow pattern and scour development was again carried out using different techniques, while the tripod model itself was equipped with various measuring sensors as further described below and summarized in table 3.5. Voltage outputs of the individual probes were used for all measuring devices, finally connected to an in-house analog-digital converter array, while data were stored in digital form on the measuring system. A sampling rate of 100Hz was used for all probes in order to get consistent data sets and time lines.

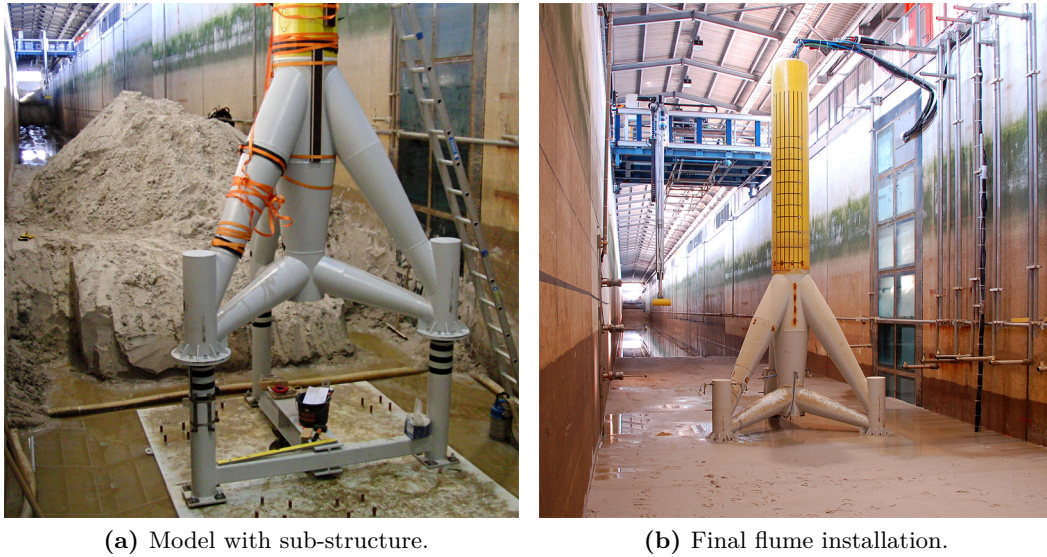


Figure 3.18: Tripod installation in the GWK wave flume for scour experiments.

Table 3.5: Probes and sensors applied in GWK wave flume experiments.

Probe / Sensor	Technique	Measuring Application
Reson SeaBat echo sound.	Echo sounding	Scour depth, surface profiling
Aquatec AQUAScat ABS	Acoust. backscatter	Scour depth, point-wise
ABUS UW cameras	Optical, video	Scour depth, with scale
Wave gauges	Capacitive	Water surface profiles
NSW EMS probes	Electromagnetic	2D orbital wave motions

Scour Development The recording of bed elevation changes and scour development was carried out using several sensors. A multi-beam echo sounder of type Reson SeaBat, which was mounted on a movable positioning platform above the flume, was used for measuring the large-scale, areal development (see figure 3.19). For the latter, a rail system installed along the flume walls and guide rails in horizontal and vertical direction were used, which allowed for the positioning of the sonar head in all spatial directions around the structure in submerged conditions.

In order to continuously collect point-wise bed depth records and for a further validation of collected multi-beam data, two sets of three Acoustic Backscatter probes of type Aquatec AQUAScat 1000 each were installed in a down-looking position at one of the piles sleeves and around the main column, see figure 3.20a. Although originally designed as backscatter sensors, the probes were used as single-beam echo sounders here, i.e. measuring the scour depths in the direct near-field of the two piles. A single-beam echo sounder was additionally installed directly under the main column.

At locations beneath the mud mats of the tripod, where the technique of echo

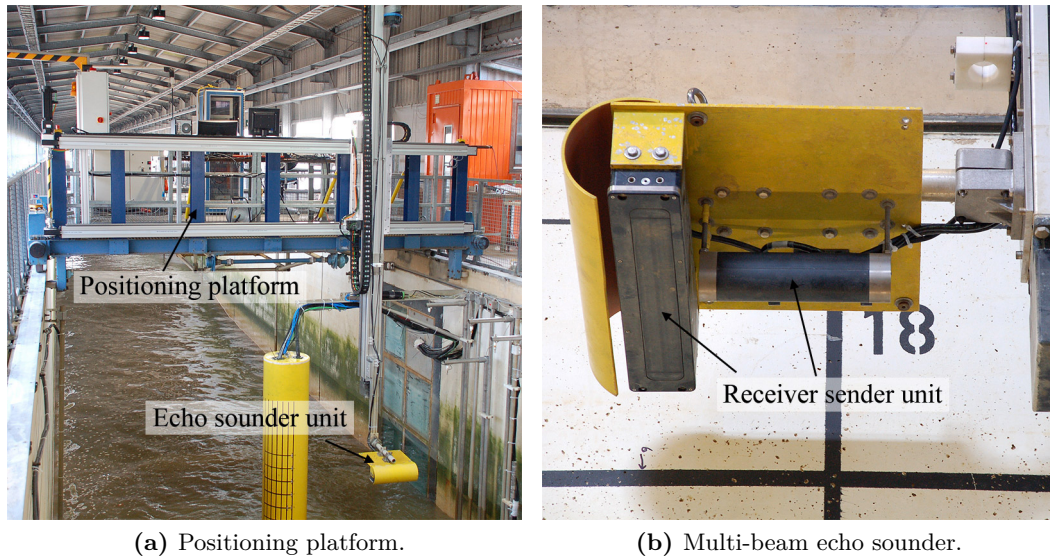


Figure 3.19: Multi-beam echo sounder and positioning platform installation for collection of bed surface profiles during GWK scour experiments.

sounding was not feasible due to structural influence or insufficient space, a total of four ABUS underwater cameras were used for the determination of local bed levels directly at the piles. The cameras were installed in pairs one above the other inside of two of the piles in outward-looking position (see figure 3.20b), so that they could continuously record bed level changes through Plexiglas windows during the experiments.

Surface Elevation and Flow Measurement Wave surface parameters were measured using capacitive type strand wave gauges installed with certain distances along the flume walls and concentrated around the tripod model. The still water level in the flume was controlled by visual observations using a water level gauge in the front part of the flume. Similar to the WKS flume tests, orbital motions in the undisturbed area were recorded by means of NSW electromagnetic current meters (EMS probes) installed at the side walls in the near-field of the tripod, while velocity components in x and z directions were recorded.

3.3.3 Test Procedure

As a first step for model setup, the sand bed profile was installed in the flume by use of a wheel-type loader. The tripod including sub-structure and measuring instrumentation was installed in a building pit of the test section and sand was finally filled into the pit around the structure. Before starting the first test series after installation, the flume was filled and a short test series was run in order to compact the soil material. The water level in the flume was lowered, the bed was

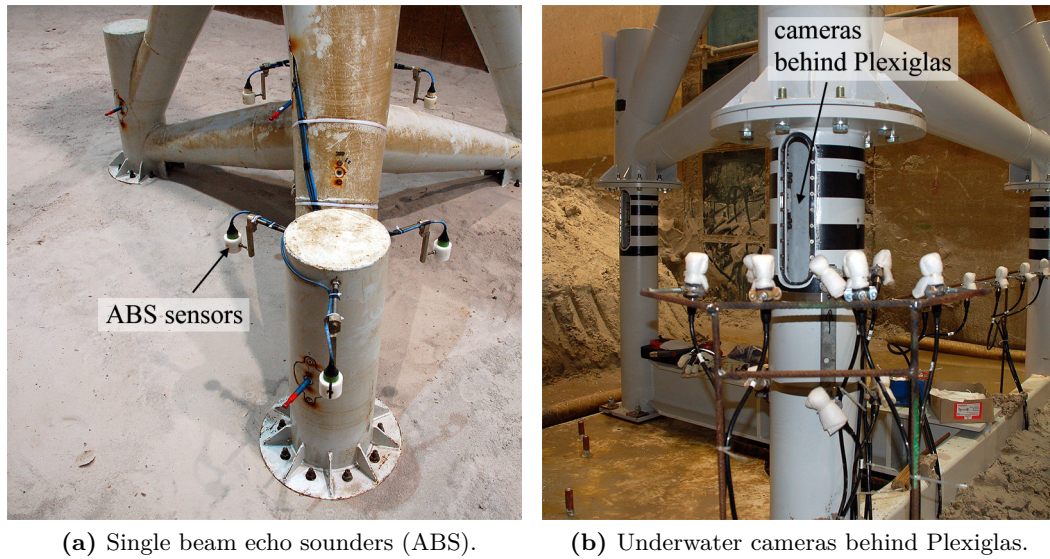


Figure 3.20: Echo sounder and underwater camera installation for point-wise, continuous scour recording in the GWK experiments.

flattened by hand and the flume was finally filled again slowly. For the tests, the wave maker was started and ran for time spans between 250 and 500 wave cycles each. Reflections during the tests were minimized by active absorption control of the wave maker on the one hand and a sand beach at the end of the flume on the other hand. With exception of the multi-beam echo sounder, all instruments given above were continuously collecting data during the test runs.

The areal scour development was measured by use of the multi-beam echo sounder after defined wave periods in intervals of 250, 500 and 1000 wave cycles each in still water conditions, i.e. the wave maker was stopped for bed profile measurement in between the wave load periods. The echo sounder collected overlapping stripes of bed profiles while moved over ground along the flume axis, out of which surface plots of bed elevation were calculated in post-processing. This procedure was repeated until the end of each test. A series was terminated after 3500 wave cycles, achieving an almost equilibrium state. Afterwards, the water level in the flume was slowly lowered and the bed was flattened for the next run.

Selected load conditions derived from the 1:40 experiments in the WKS flume tests were chosen as boundary conditions for the tests. In most cases, these were directly scaled by use of the Froude model law. Resulting test parameters are given in table 3.6. The water level was kept constant at 2.5m for all tests. It should be noticed that although GWK load conditions were initially triggered as directly scaled from WKS flume tests, resulting wave heights at the movable bed section are around 5-10% higher, mainly due to wave steepening at the ramp section in front of the movable bed. Although several other tests on scouring were additionally conducted

Table 3.6: Compilation of conducted experimental scour tests in the GWK wave flume.

Name	wave type	wave height H_m/H_s [m]	wave per. T_m/T_p [s]	angle [°]	mud mats	max. # waves
r7655-01	regular	0.76	5.48	0	yes	3500
r7655-02	regular	0.76	5.48	180	yes	3500
s7255-02	spectrum	0.72	5.52	0	yes	3500

in the GWK flume, the present description is limited to the given experiments, which mainly serve as a comparison to the WKS flume tests.

3.3.4 Experimental Results

It can generally be stated that both the local and global scour development behave similar to what could be observed in the small scale laboratory tests in the WKS wave flume. This is however not astonishing, as flow fields and processes leading to sediment mobilization and hence resulting scour are equal or, influenced through model scaling effects, at least similar in both model setups. Results are therefore discussed only briefly and in summarized form below. For further details, see the descriptions given in §3.2.4 as well as the numerical model results discussed below in §5.3.

Differences in terms of local scour depths and scour shape could be observed, mainly resulting from the larger model scale used in the present setup, as will be discussed in §3.4.

Plots of the final scour and bed surface development after 3000 waves for tests r7655-01, r7655-02 and s7255-02 are given in figures 3.22 to 3.25, while the time-dependent development and corresponding cross sections can be found in figures B.1 to B.5. Furthermore, two photographs of the bed surfaces for tests r7655-01 and r7655-02 after emptying the flume are given in figure 3.21. Similar to the procedure in the WKS flume experiments (see §3.2.3), the areal plots were generated from different measurement records, i.e. multi-beam records single-beam data and visual observations using underwater camera images, which were finally interpolated to a uniform surface elevation grid, holding a horizontal resolution of 2.5cm (x, y) in this case. White areas in the plots reaching from the tripod near-field to one of the side walls could however not be determined by the multi-beam echo sounder due to the installation traverse at the top of the flume (see figure 3.18b) and are therefore not given in the plots.

For all GWK flume tests, it can generally be concluded that a distinct scour pattern has formed, showing local scour formation around the single piles and under the main column, and a global scour formation around the entire structure, while scour merging can be observed for the regular wave tests. For the latter, certain areal

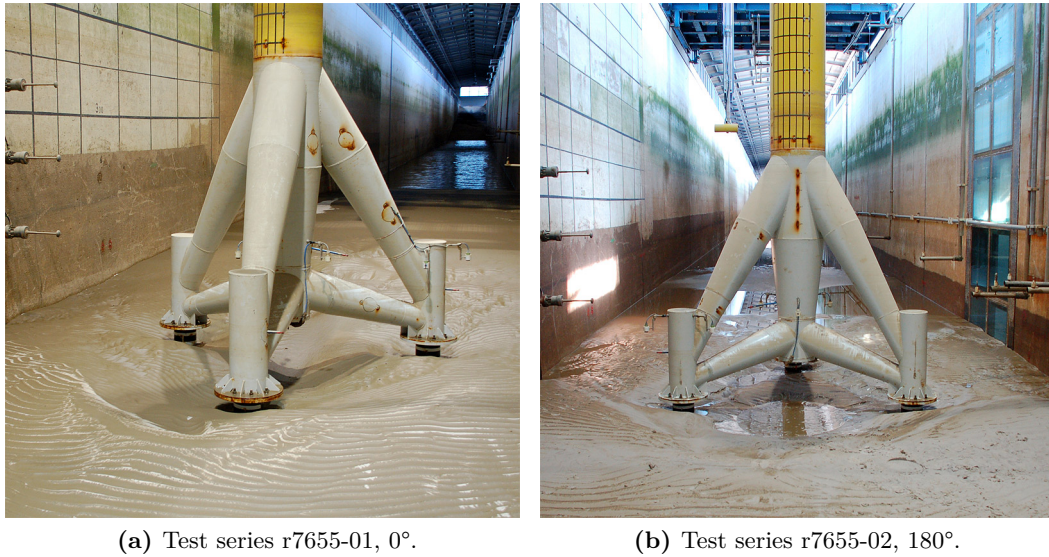


Figure 3.21: Scour development for test series r7655-01 and r7655-02 after 3000 wave cycles in the GWK wave flume. Direction of wave propagation is from front to back.

sediment erosion occurs in the area behind the structure (based on the location of the wave maker), while sediment accumulation can be observed in the front part. This pattern is given in both the 0° and the 180° installation and therefore differs from the observations in the WKS flume experiments. In the front part of the structure, sediment accumulation can be credited to general relocation processes of the ramp in front of the (horizontal) mobile bed section due to life bed conditions, which could be observed over the entire duration of the tests. Thus, no direct structural influence could be determined here. The influence of accumulation on the local scour depths, especially at the front piles, can however be regarded as minor. As can be seen from figure 3.21, influencing effects on scour patterns due to ripple formation of the bed can be regarded as negligible here.

For test r7655-01, i.e. 0° installation, local scour depth relationships for the piles and the section under the main column are similar to the WKS flume experiments, test r2130-01. The local scour at the rear piles reaches values of up to 22.2cm ($S/D_p = 1.13$, with D_p as the pile diameter); the scour is slightly lower at the front pile, where a depth of 15.8cm ($S/D_p = 0.81$) was observed. The maximum scour depth in the region under the main column reaches a value of 23.8cm ($S/D_{mcl} = 0.63$, with D_{mcl} as the lower main column diameter), i.e. giving the maximum scour depth in this case. Regarding the time evolution (trends) of local scour development, scour depths can be seen in an almost equilibrium condition at the stage after about 3000 wave load cycles, while about 90-100% of the corresponding maximum values are reached after 1500 waves already.

For the 180° installation (r7655-02), scour depths are largest under the main

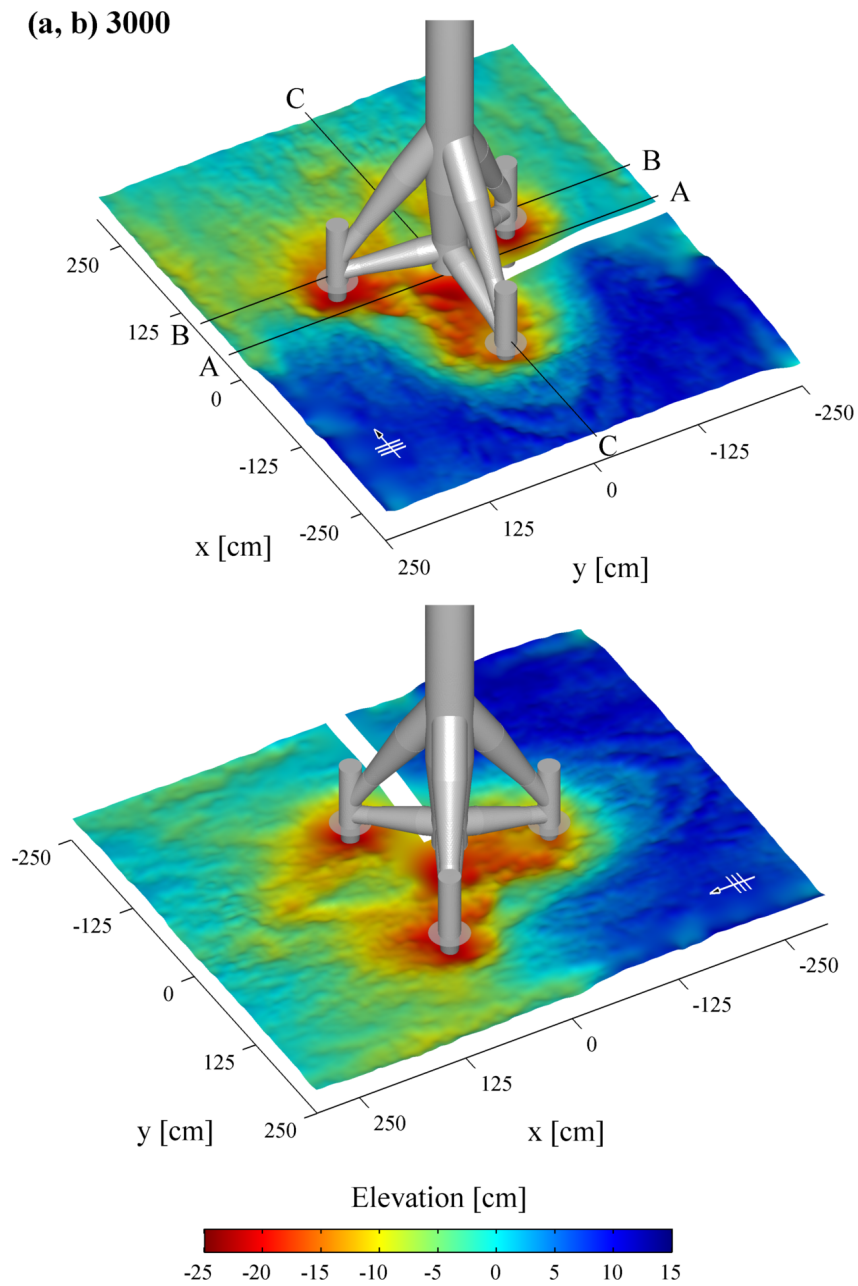


Figure 3.22: Results of scour development for test series r7655-01 after 3000 wave cycles, (a) front view, (b) rear view. Cross section positions for figure 3.10 are given in upper plot (a). Wave-encounter angle 0° .

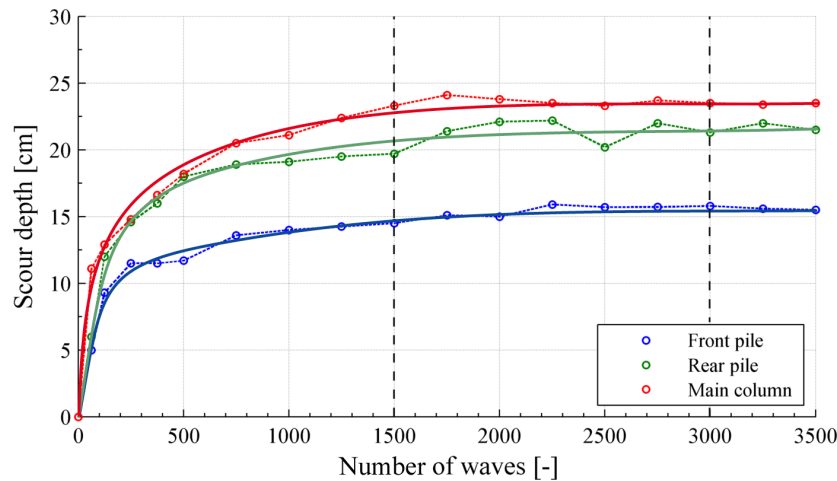


Figure 3.23: Development of local scour depths over time for test series r7655-01, given as local mean values over number of wave cycles. Symbols: dots: moments of record; dashed lines: connection for clarity; solid lines: trends of scour evolution.

column and directly in front of the tripod, in the section of the bend between the front piles and the column. Measured depths in the center reach values of up to 30.5cm ($S/D_{mcl} = 0.81$), while scours at the piles are comparatively lower, up to 21.9cm ($S/D_p = 1.12$) at the rear and 12.4cm ($S/D_p = 0.63$) at the front piles. The reason for the large scour pit in front of the tripod could not be fully figured out. It can however be assumed that the comparatively large resistance of the structure in the 180° installation led to enhanced flow acceleration in front of and under the main section. Furthermore, the present test was conducted before the remaining test series, possibly resulting in less compaction of the soil after tripod installation in the flume. Besides this effect, the remaining local scour patterns, especially around the single piles, are only little influenced.

Compared to the regular wave test at 0° installation, the wave spectrum test series s7255-02 shows generally less areal sediment erosion (and accumulation) in the near-field of the structure. Global scour depths are therefore less pronounced, although local scours at the piles and under the main column are in a similar range compared to the regular wave test case, see figure 3.26 for a comparison given as cross sections after 3000 wave cycles. Regarding the accumulation area in front of the tripod, bed slopes in both regular wave and wave spectrum tests are nearly equal, further proving that the general sediment relocation in the front part has no major effect on the local and global scour pattern. All in all, results correspond well to the findings in the WKS flume experiments, thus confirming the choice of the wave spectrum representation as regular waves for the numerical model approach, see §3.2.5.

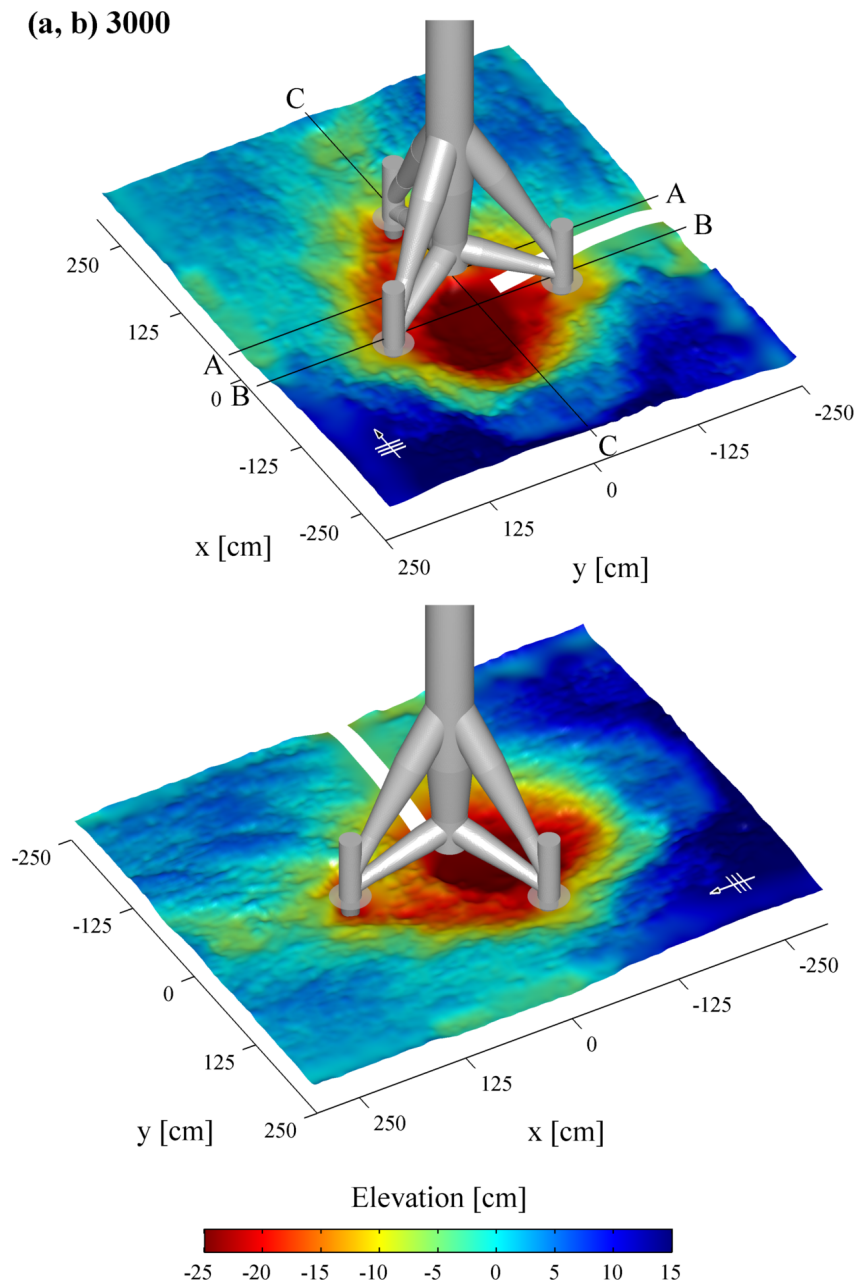


Figure 3.24: Results of scour development for test series r7655-02 after 3000 wave cycles, (a) front view, (b) rear view. Cross section positions for figure 3.10 are given in upper plot (a). Wave-encounter angle 180° .

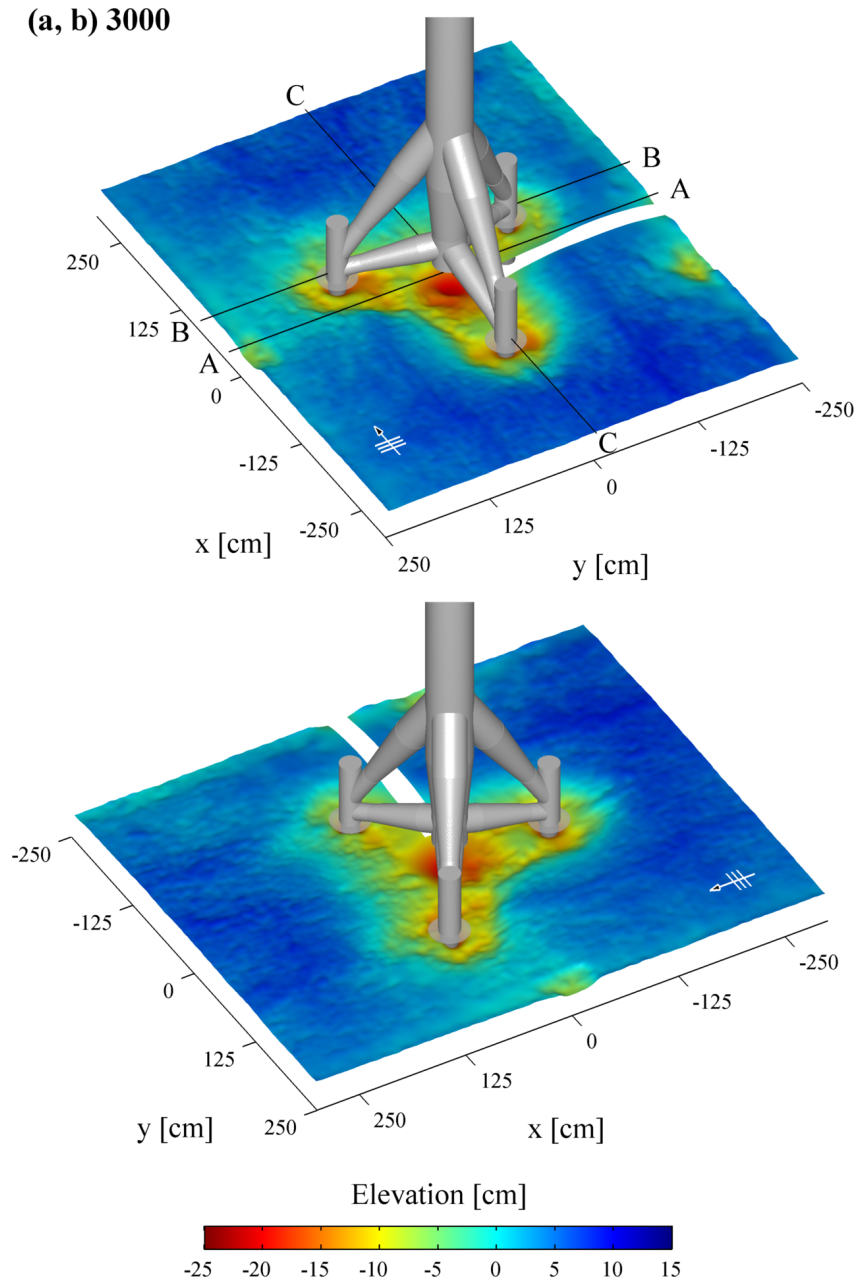


Figure 3.25: Results of scour development for test series s7255-02 after 3000 wave cycles, (a) front view, (b) rear view. Cross section positions for figure 3.10 are given in upper plot (a). Wave-encounter angle 0° .

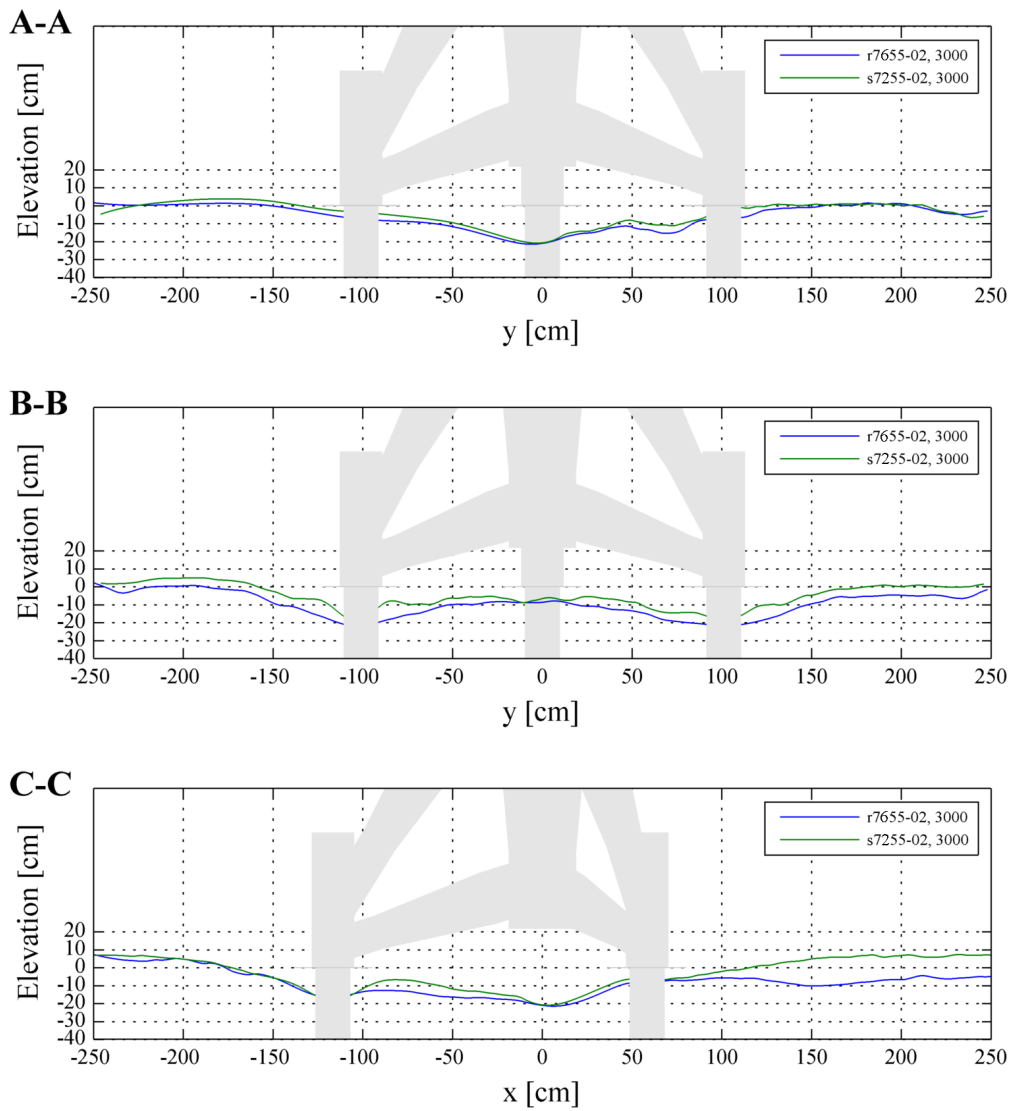


Figure 3.26: Comparison of cross sections for test series r7655-01, s7255-02 at the time step of 3000 wave cycles. Positions A-A, B-B, C-C are given in figure 3.22.

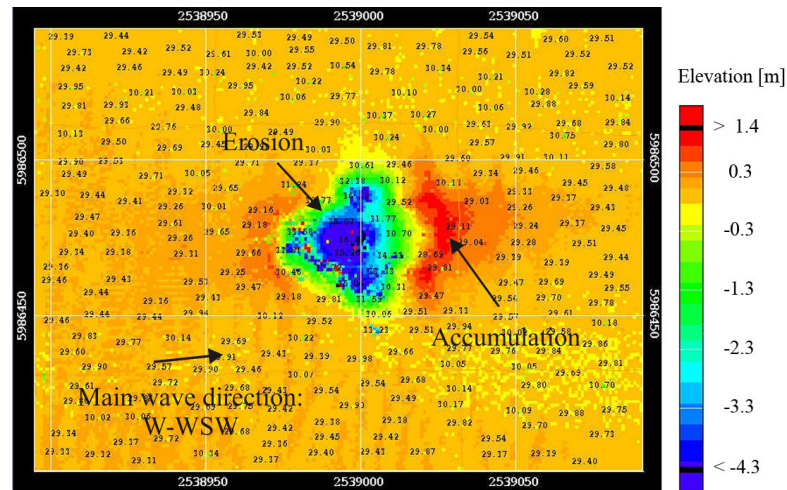


Figure 3.27: Plot of scour depths from a multi-beam survey at the M7 tripod in the alpha ventus test site. Record from April 2010, given as 1x1m grid values. Modified after Lambers-Huesmann and Zeiler (2010).

3.4 Model Comparison

3.4.1 Prototype Scale, Field Data

As part of the research initiative RAVE (Research at Alpha Ventus) supported by the German Federal Ministry for the Environment (BMU), scour measurements at a tripod structure (M7) in the alpha ventus test site were conducted by the German Federal Maritime and Hydrographic Agency (BSH). “The collection was carried out by use of single beam echo sounders installed at the foundation piles and underneath the main column measuring in intervals of a few-minutes, as well as by measuring campaigns using ship-based multi-beam echo sounder recordings of the surrounding sea floor in the vicinity of the structure” Stahlmann and Schlurmann (2012a).

Figure 3.27 gives an impression of scours detected in-situ at the M7 tripod structure, dated April 2010. The maximum measured scour depths at the foundation piles (water depth approximately 30m here) take values between 2.5m to 3.3m and 5.5m to 5.8m below the column. The measured scours, expected to be at a temporary equilibrium stage at the time of admission, had however deepened further, so that in February 2012, scour depths had reached depths of around 2.6m to 3.6m at the piles and 6.8m below the main column. Applying the classical relative scour depth S/D measure, this leads to values of 1.1 to 1.6 and 3.0, with D as the diameter of the piles. When again changing D for the latter value to the diameter of the lowermost (not ground-affiliated) main column segment with 4.5m instead, the relative scour depth S/D would then be given by a value of 1.5 here.

As the wave boundary conditions applied in both the WKS and GWK wave flume experiments differ from the natural sea-state conditions leading to a scour develop-

ment as given in figure 3.27, a quantitative comparison between the experimental results and in-situ data is not feasible at this point. With regard to a qualitative comparison of the results, it can however be stated that an overall good agreement between experiments (GWK wave flume) and nature is given, especially as local and global scour developments with erosion and accumulation areas could be reproduced in sufficient quality in the experiments. The main wave direction is similar to the 0° tripod installation. Nevertheless, relative scour depths in the model give lower absolute values, especially in the area below the main column.

The reasons for this can be found in the simplifications made for the experimental tests: on the one hand, real sea state conditions including tidal current flow were modeled as unidirectional wave load in wave flumes, and general laboratory and scaling effects, especially regarding the model sediment and wall boundaries are given on the other hand.

3.4.2 General Remarks on Scaling Effects

In laboratory experiments on scouring phenomena, scaled down models of the particular structures of interest are typically placed in wave and current flumes on a movable bed section. The model is then loaded with either wave conditions, current flow or combined loads under controlled, simplified boundary conditions. In combined load cases, following or opposing directions are the typical constellations. Depending on the available infrastructure, experiments in wave basins are further carried out, in which directional variations especially of combined load conditions can be investigated. Those tests are however still an exception. Regarding the load conditions, it has to be kept in mind that when modeling wave conditions in two-dimensional wave flumes as either regular waves or wave spectra, smearing of results typically occur due to neglecting the naturally given multi-directional sea states, especially regarding sediment transport processes.

In scaled model approaches, it is typically impossible to ensure a complete similarity of all physical processes and phenomena between the model and a prototype structure, which subsequently leads to certain scaling effects in the model. Following Whitehouse (1998), results of small-scale model tests should therefore be treated only as guidance on possible effects to the natural behavior in prototype scale.

When considering wave or current conditions around offshore structures, in which cases the free surface and the general flow pattern have to be modeled correctly, the model scaling is typically carried out by applying the Froude model law. See table 3.1 for typical relationships and Hughes (1993) for a detailed description. Flow characteristics can be modeled sufficiently correctly in that case.

When however applying the approach to a direct (length) scaling of natural bed material of the sea bed, this typically results in extremely small grain sizes

and thus large influences of cohesion, which should be avoided. As far as natural, cohesionless sediments with grain sizes larger than theoretically given by a geometric scaling should however be used in the model, possible scaling effects are evident and should therefore be kept in mind. Alternatively, bed material can be scaled based on the Shields parameter as given by equation (2.19). This approach has the advantage of giving two scaling parameters instead of one: the grain size d and the density ρ_o of the material. Thus, alternative materials with varying relationships of grain size and density can be applied in the experiments. In practice, typically natural lightweight or artificial material is used, e.g. Polystyrene, Bakelite, PVC or coal, see e.g. Bettess (1990) for an analysis of material parameters and Ettmer (2007) for a lightweight-material scaling approach.

3.4.3 Model Result Comparison

From a direct comparison of scour pattern and depths derived from the small-scale (1:40) WKS wave flume and the large-scale (1:12) GWK wave flume experiments using equal but scaled wave boundary conditions and after reaching an (almost) equilibrium state, two general conclusions can be drawn. On the one hand, overall scour patterns are equal in both model scales, giving local maximum scours at the piles and under the main column of the tripod structure, as well as a global scour formation around the entire structure. The latter is thereby more pronounced in the large-scale tests. On the other hand, certain discrepancy was observed regarding the absolute or relative S/D local scour depths, as scours were partly significantly deeper in the large-scale experiments. As fine sand with a median diameter of $d_{50} = 0.148\text{mm}$ was used as model sediment in both setups, resulting differences can thus be mainly attributed to general scaling effects of the bed material.

It was already given in §3.3.3 that the local wave heights measured in front of the tripod section were slightly increased by 5-10% compared to the generated waves at the wave maker, in turn directly scaled from the WKS flume test conditions. Furthermore, the blockage ratio in the GWK wave flume ($r_t \approx 0.20$) was increased compared to the small-scale tests ($r_t \approx 0.14$), thus leading to the assumption that these differences might have an effect on both the overall sediment transport rates and the local, developing scour depths.

A further analysis and quantification of these possible effects was therefore carried out in terms of numerical investigations, see §5.3.3 for a discussion. As a short preview on the results, it can be stated that the combination of increased wave height and reduced flume width results in enhanced bed shear stresses in the near-field of the structure, while the major part however comes from the wave height increase. At the rear piles and the lower braces in 0° tripod installation, which is the location for highest shear stresses in the rigid-bed simulations, local bed stresses are increased

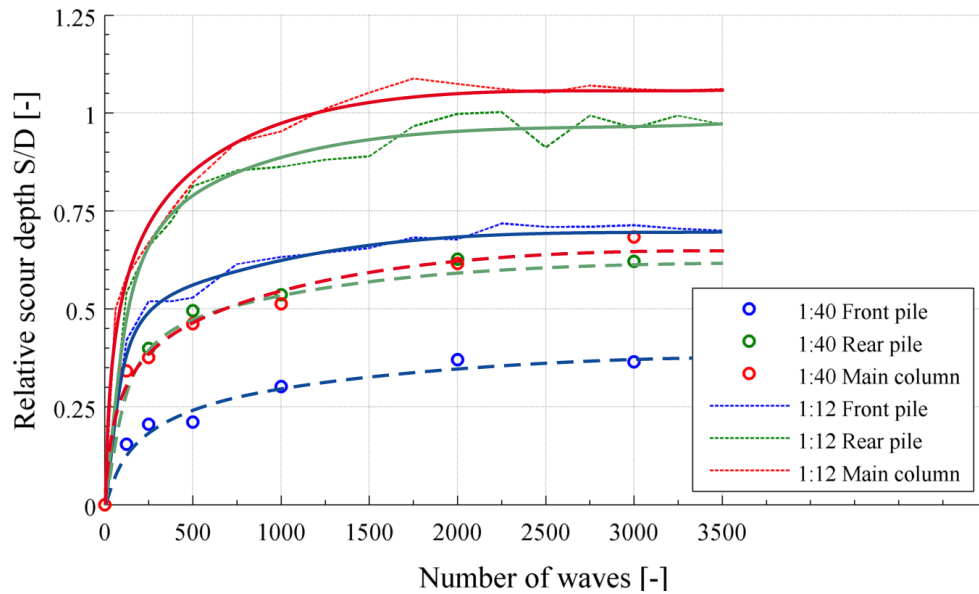


Figure 3.28: Comparison of local relative scour depths S/D over time for test series r2130-01 and r7655-01 (reduced by 13%), given as local values over number of wave cycles. Symbols: dots: 1:40 test records; light dashed lines: 1:12 test records; thick lines: trends of scour evolution.

by about 13% ($\tau_{1:40} = 8.65\text{N/m}^2$). Results were obtained from a 1:40 model scale in the simulations. Furthermore, bed shear stresses were determined for a 1:12 model scale simulation using wave parameters of test series r7655-01, resulting in maximum bed stress values at the rear piles of $\tau_{1:12} = 22.5\text{N/m}^2$, which is a local increase with a factor of around 2.6 compared to the small-scale runs.

A comparison of local scour depths from both the WKS and GWK flume experiments is given in figure 3.28. Values are given as relative scour depths S/D , where D is the diameter of the piles, for locations of front and rear piles and the section under the main column. It should be noted that depths for the 1:40 tests are given as local mean values here in order to reduce local influences from bed ripples. It was stated before that the increase of wave height and reduction of flume width results in slightly increased shear stresses for the GWK tests. In order to however draw a comparison using almost equal boundary conditions and setups, depths in the plot are reduced by 13%, making a first, simplified assumption of linear reduction.

It is obvious to see that local scour depths in the large-scale (1:12) experiments are larger compared to the 1:40 tests, mainly resulting from significantly enlarged local bed shear stress values. A direct comparison leads to mean depth-increase factors of 1.9 for the front pile, 1.6 for the rear piles and 1.7 for the main column, giving an overall mean local scour depth increase of about 70% for the 1:12 flume experiments. This effect is however not astonishing, as the same sediment was used in both model scales, therefore resulting in a higher bed resistance to the given wave load conditions in the small-scale model. Besides this, it can however be stated that

both the time-development of scour and the relative scour depth values between the single measuring locations, i.e. depth differences between front piles, rear piles and main column section are almost equal in both model scales.

A possible circumvention of this scale behavior was already given above in §3.4.2, i.e. scaling the model sediment not directly, but based on the Shields parameter by varying both the diameter and the density, finally resulting in lightweight, artificial materials. Ettmer (2007) gives a direct scaling approach for artificial model sediments based on both geometric and density consideration for current flow situations. The given approach was applied in some first, preliminary tests which were carried out before the final test conduction in the WKS wave flume. Unfortunately, no satisfactory results could however be achieved when applying it to the given wave motion flow situation.

As the main intention of conducted tests however was to gain general knowledge on scour development around a tripod structure, no further action was finally carried out on this topic as part of the present investigations. Therefore, given scour depth results, especially those from the 1:40 WKS flume experiments can only be seen as a guidance here.

3.5 Conclusions

In order to gain both general and detailed knowledge of physical processes under wave load conditions, local and global scour development as well as local flow pattern leading to scour, physical model tests were carried out in wave flumes on two different model scales of $\lambda = 40$ and $\lambda = 12$. The choice of two scales was thereby due to following reasons: Small-scale laboratory tests were carried out mainly in order to investigate the general scouring phenomena, having the advantage of easier model setups, test repeating and variations; they further served as kind of feasibility studies for the large scale tests, as well as for the generation of data sets for the numerical model validation. Large-scale tests were then conducted for selected test conditions under minimized laboratory model scaling effects, especially with regard to scaling of the sediment.

As boundary conditions for both model scale test series, different regular wave and wave spectra combinations were tested, while the tripod foundations were installed with varying wave-encounter angles in the flumes. Measurement of scour development was carried out by means of point-wise and areal recording techniques. Furthermore, flow patterns in the small-scale tests around the tripod were measured for a validation of numerical flow simulations.

As a result of the small- and large-scale tests, three main regions of scour formation could be determined for a tripod structure under the given load conditions: 1. around the single piles, while larger depths could be found at the rear piles, 2.

under the main column giving maximum depth values as well as the lower braces connected to the rear pile sleeves, 3. a global scour formation around the entire structure. Suspended sediment transport could be determined as the dominant transport process for the given cases. Generally, the overall scour pattern shows a combination of local and global scour formation, which was however found to be more distinct in the large-scale tests. Furthermore, the characteristics of scour development at the structure depends significantly on the incoming wave direction with respect to the pile locations, as scour patterns differ depending on the wave-encounter angles. Comparison of local scours at the structure showed larger depths in the large-scale tests when applying equal, scaled boundary conditions, with a local depth-increase factor found to be around 1.7. This is mainly resulting from the fact that equal fine sediments with $d_{50} = 0.148\text{mm}$ were used as model sediment in both setups. Results from small scale tests can therefore generally be seen as a guidance to the overall sediment behavior and scour patterns.

As a further main result of the investigations it can be concluded that scour formation around the tripod structure differs significantly from typical scour patterns that can be observed at single vertical pile structures, i.e. cylinders and monopiles, for which typically detailed knowledge on flow pattern and numerous scour depth design formulas exist. Due to the complexity of tripod scour patterns being directly depending on boundary conditions like wave types and parameters, encounter angles, water depth and structural dimensions of the tripod itself, existing design formulas for cylindrical structures are not applicable here. Even more, also geometrically similar tripod foundations however with variations in the structural dimensions, e.g. regarding piles, main column, brace diameters and angles as well as soil distances of structural elements might result in different scour pattern than given for the present type.

A generation of detailed knowledge on scour and flow patterns including all these relevant parameter variations would result in tremendous effort, costs and time when conducting physical model tests, especially in large scale. A step to partly circumvent this drawback could therefore be the implementation of an appropriate numerical flow and scour model, which is then applied to parameter studies on scouring effects.

4 Numerical Model of Flow and Scour

4.1 Introduction

Investigations on local scour development by use of numerical methods have been carried out in numerous studies. As the flow pattern in the near-field of a structure is complex and predominantly three-dimensional, a suitable three-dimensional numerical flow model including turbulence modeling capabilities has to be chosen in order to correctly simulate flow processes. Widely used models with hydrostatic pressure assumption are therefore no longer valid here, as an acceleration of fluid particles in the near-field of a structure subsequently results in additional dynamic pressure components which have to be accounted for in the numerical model. When modeling scour processes at offshore wind turbine foundations or any other foundation type in the marine environment, the model further has to be able to capture all relevant load conditions, i.e. wave and current processes on the one hand, and the relevant sediment transport processes, i.e. bed load and suspended load on the other hand. Besides questions regarding scour development which are analyzed in detail here, further typical questions and problems in an engineering context might deal with dynamic loads at structures, oscillations and vibrations or general installation processes of the foundations. In this context, hydrodynamic numerical modeling is widely used, but sediment transport processes are typically not incorporated then.

In order to deal with the requirements mentioned above, a fully three-dimensional numerical model using the Volume of Fluid (VOF) method has been applied within the OpenFOAM software framework in the present setup, solving Reynolds Averaged Navier-Stokes (RANS) equations in combination with a $k - \omega SST$ turbulence closure model. Wave and current load conditions with free-surface modeling have been adopted using appropriate boundary conditions and wave damping at the domain outlet. In order to capture the relevant sediment transport processes, a new transport model including bed load and suspended load has been implemented, with additional treatment of local scouring problems and a moving mesh approach. As sediment transport and local scouring processes typically need long-term simulations and are therefore very time-consuming, parallel computations have been used throughout. Details of both the flow and sediment transport model implementations are given in the following sections.

4.1.1 OpenFOAM Software Toolbox

OpenFOAM®¹ is a software toolbox which was designed for the simulation of various physical phenomena, ranging from complex flows in fluids and gases including

¹OpenFOAM is a registered trademark of OpenCFD Ltd.

turbulence, heat transfer and chemical reaction to solid dynamics and electromagnetic applications. The toolbox is a collection of different solvers and libraries for simulation as well as pre- and post-processing of model domains and data, written in C++ programming language. Although some Finite Element Method (FEM) functionalities are partly used in the code, it is mainly based on Volume of Fluid method with generally unstructured meshes in order to solve systems of partial differential equations. Unstructured meshes in this case means that typical mesh constellations of block meshes, tetrahedra meshes and general polyhedra meshes as well as combined mesh approaches can be used. A detailed description of the implementation and discretization methods can e.g. be found in Jasak (1996) or Weller et al. (1998). OpenFOAM is published under the GNU General Public License (GNU GPL 3) and its source code is therefore freely available, which allows a flexible modification and extension of the code. In the present setup, OpenFOAM version 1.6-ext has primarily been used, but with some modifications based on version 1.7.x. In addition to the standard releases by OpenCFD and OpenFOAM® Foundation, respectively, version 1.6-ext is a community-driven release by the OpenFOAM® extend project², including several extensions over the official versions. The OpenFOAM toolbox has been chosen for the present investigations mainly due to free availability of its source code, which therefore allows any kind of modification and expansion. In contrast to open source software, commercial CFD packages have the drawback of mainly being a black box system to the user. Although code structures and equations are mainly given in manuals, possible assumptions and simplifications in the implementation and their influence on simulation results can however not be fully quantified then.

It has to be noted that for the present investigations, all modifications and expansions of the code have been made by use of standard OpenFOAM libraries as well as by general C++ programming language. All relevant solvers have been coded for parallel computation, i.e. by use of inter-processor communication using OpenFOAMs build on MPI (Message Passing Interface) protocol. The use of parallel computations was thereby found to be essential for the simulation of complex flow phenomena and scour investigations with moderate computational times.

4.2 Two-Phase Flow Model

Modeling of surface water waves around offshore structures or any other objects using a two-phase flow model is a typical scientific and engineering topic. Flow models can generally be classified by two categories, Lagrangian and Eulerian approaches. The latter has been applied for the present work.

²More information can be collected at www.extend-project.de

4.2.1 Fluid Flow Solver and Governing Equations

In the mathematical descriptions of turbulent flows, different approaches are used, while in many cases a solution of the RANS equations in combination with an appropriate turbulence closure model, Large Eddy Simulations (LES) or combined approaches like Detached Eddy Simulations (DES) are used in practical applications. A general description of the mathematical background, applications and comparisons can e.g. be found in Rodi (1997), Rodi et al. (1997) or Wilcox (2006).

Although LES generally aims to give better results in the description of turbulent quantities, it has a high demand on mesh resolution and computational loads. Due to the complexity of foundation structures and therefore complex flow situations modeled here on the one hand and the generally large computational times in sediment transport simulations on the other hand, an application of the RANS equations in combination with the $k-\omega$ SST turbulence closure model was therefore chosen in the present setup.

The governing equations for the fluid flow model therefore are the continuity equation for incompressible fluid

$$\nabla \cdot u = 0 \quad (4.1)$$

and the Reynolds Averaged Navier-Stokes equations (RANS) given as

$$\frac{\partial \rho \vec{u}}{\partial t} + \nabla \cdot (\rho \vec{u} \vec{u}) = -\nabla p + \nabla \cdot [\mu \nabla \vec{u} + \rho \tau] + \rho \vec{g} + \sigma K_\alpha \nabla \alpha \quad (4.2)$$

with \vec{u} being the fluid flow vector in Cartesian coordinates, ρ the fluid density, p the pressure field, μ the dynamic viscosity, \vec{g} the acceleration vector due to gravity and $\tau = -\overline{u'u'^T}$ the Reynolds stress tensor. Furthermore, σ gives the surface tension and K_α the interface curvature.

Volume of Fluid Method The representation of the water-air interface was modeled using the Volume of Fluid (VOF) method, i.e. an Eulerian approach. The general concept of volume fractions was first introduced by Noh and Woodward (1976) and later by Hirt and Nichols (1981) giving the name of the well-known VOF method. In this *interface-capturing* technique for two-fluid flows, the free-surface is directly resolved within the spatial model domain by use of volume fractions of the two fluids in each computational cell, i.e. a mixture of the two fluids, out of which the interface position can be reconstructed by interpolation. In the present setup, scalar values of α_r representing the volume fractions of the two fluids have been taken as

$$\alpha_r = \begin{cases} 0 & \text{for air} \\ 1 & \text{for water} \end{cases} \quad (4.3)$$

where α_r is modeled as being passively transported by the fluid flow, giving the advection transport equation

$$\frac{\partial \alpha_r}{\partial t} + \nabla \cdot (\alpha_r \vec{u}) = 0 \quad (4.4)$$

This approach is therefore different from an *interface tracking* approach, in which the interface is captured directly by a tracking mesh that needs to be moved and updated as the flow evolves. A drawback of the interface-capturing technique using the VOF method is numerical diffusion taking place at the interface between the two fluids which can, esp. in case of wave modeling, have a damping and truncating effect on wave heights. It was however shown by Ubbink (1997) and later in Ubbink and Issa (1999) that due to a proper selection of the differencing scheme (in their case the CICSAM scheme) in VOF, numerical diffusion can be minimized. In the OpenFOAM version used for the present setup, a different interface-compression method is however used, which replaces the formerly implemented CICSAM scheme due to its better performance. Modifications like relaxation of the velocity in the air phase in order to reduce computational times as given in Liu (2008) who made use of the CICSAM scheme have been tested here as well, but have been found unessential for the presently implemented numerical scheme.

The use of a two-phase model and therefore free surface flow is especially necessary for wave modeling cases. In contrast, widely used rigid lid approaches are only valid for flow conditions without large surface disturbances e.g. due to flow separation and pile-up at structures, as otherwise pressure and flow pattern might be artificially changed, introducing nonphysical errors in the computations.

Besides the free surface capturing, fluid mixture properties are further assigned using α_r fraction values. Therefore, density ρ and viscosity μ are calculated within the domain as

$$\rho = \rho_0 \alpha_r + (1 - \alpha_r) \rho_1 \quad (4.5)$$

$$\mu = \mu_0 \alpha_r + (1 - \alpha_r) \mu_1 \quad (4.6)$$

where subscripts 0 and 1 give the fluid-specific values assigned after equation (4.3).

As the investigations carried out here represent unsteady problems throughout, the Navier Stokes equations are solved using the PISO (Pressure Implicit with Splitting of Operators) algorithm in OpenFOAM, see Issa (1986) for further information.

4.2.2 Turbulence Model

According to Wilcox (2006), “virtually all flows of practical engineering interest are turbulent.” Turbulence thereby occurs in fluid flows at larger Reynolds numbers, when the “fluid’s inertia overcomes the viscous stresses, and the laminar motion becomes unstable. Rapid velocity and pressure fluctuations appear and the motion

becomes inherently three dimensional and unsteady.”

For the determination of additional flow resistance due to turbulent behavior of the local flow field, the concept of eddy viscosity is widely used in numerical implementations. It follows the general idea of simulating turbulent fluctuations taking place under natural flow conditions by use of artificial viscosity to locally inhibit the flow process and simultaneously ensures moderate computational times. The turbulent viscosity ν_t is thereby modeled by use of an adequate turbulence model, which further calculates turbulent kinetic energy k and turbulence dissipation ω or ε , depending in the model, see e.g. Wilcox (2006).

The latter mentioned turbulence parameters are thereby given as boundary conditions for the turbulence model, while their implementation depends, amongst others, on the type of boundary layer resolution, see §4.2.4. If the viscous sublayer is directly resolved by the model, the viscous terms are integrated into the turbulence equations. Boundary conditions can then be formulated in a rather simple way, e.g. $k = \varepsilon = 0$, see Schlichting and Gersten (2006), p. 603. The grid resolution in this case is fine enough to fulfill the criterion of a low-Reynolds model, i.e. the turbulent Reynolds number defined as $Re_t = k^2 / (\varepsilon \nu)$ becomes very small, as given by Menter (2009). The counterpart of this type of direct modeling is given by the high-Reynolds model formulation. In practical and especially in industrial applications, wall function approaches are then used mainly in order to save computational times, as boundary layer grid resolutions are significantly reduced. In wall function approaches, direct resolving of the near-wall boundary layers is resigned. Near-wall values are constructed from functional relations and the wall-nearest cell values instead. A requirement for the application of wall functions is a near-wall grid resolution in which the first grid point is located within the logarithmic boundary layer, see table 2.1 for a classification. Regarding the accuracy of low-Re and high-Re formulations, Schlichting and Gersten (2006) state that both approaches give results having equal magnitudes, while Menter (2009) states that wall function approaches are generally less accurate.

Following Wilcox (2006), “an ideal model should introduce the minimum amount of complexity while capturing the essence of the relevant physics.” Typically, two-equation turbulence models are used, like $k - \omega$ or $k - \varepsilon$ models. Following Wilcox (1998), an advantage of the $k - \omega$ over the $k - \varepsilon$ model thereby lies in giving better results especially for flows with adverse pressure gradients. A further advantage of the $k - \omega$ models is the fact that they can easily be adjusted to account for surface roughness, which is indispensable for sediment transport modeling as given in the present case. Following Wilcox (2006), the “omega-oriented equations possesses solutions in which the value of omega may be arbitrarily specified at the surface. This is an advantage because it provides a natural way to incorporate effects of surface roughness through surface boundary conditions”.

In addition to strict low-Re and high-Re formulations given above, OpenFOAM provides continuous wall function approaches using Spaldings law of the wall, which allows modeling over wider y^+ ranges. Further information can e.g. be found in Shih et al. (1999) or Kalitzin et al. (2005). In the present setup, the $k - \omega SST$ (k-omega Shear-Stress-Transport) model of Menter (2009) has been applied, originally implemented in a way to be used with such continuous wall functions for k , ω and ν_t . To account for the effect of surface roughness on the near-wall flow and turbulence characteristics, a direct modification of the ω boundary values at smooth, rough and semi-rough boundaries has further been implemented in addition to the standard implementations within this work, see §4.2.4 for its details and usage.

A description of the $k - \omega SST$ turbulence closure model is given in the following, where the equations are given in the forms as implemented. It has to be noted that there are certain differences to the original formulations, which however result from the general OpenFOAM framework. For instance, the fluid density ρ is excluded from the equations, even for the two-phase incompressible flow cases. This results in turbulent diffusion in case of free surface waves where $\nu_{t,air} \gg \nu_{t,water}$, as it was already stated by Jacobsen (2011).

The turbulent kinetic energy is modeled solving for k as

$$\frac{\partial k}{\partial t} + \nabla \cdot (\phi k) - \nabla \cdot (\phi) k - \nabla \cdot [D_{k,b}(F_1) \nabla k] = P_k - \beta^* \omega k \quad (4.7)$$

with ϕ as the flux, $D_{k,b}(F_1)$ the effective viscosity, P_k the production term of k and β^* a model constant which takes a value of 0.09 as given in the standard model. In this form, the production term is calculated as

$$P_k = \min(G, 10\beta^* k \omega) \quad (4.8)$$

where G takes the form

$$G = 2S_r^2 \nu_t = 2 |(\nabla \vec{u})|^2 \nu_t \quad (4.9)$$

with S_r^2 being related to the strain rate. The effective viscosity $D_{k,b}(F_1)$ is calculated as the sum of kinematic viscosity ν and turbulent viscosity ν_t , where the latter is modified as $\alpha_k(F_1) \nu_t$ using blending functions of the general form $\psi = F_1(\psi_1 - \psi_2) + \psi_2$ to blend between the wall region and outer region model formulations and related constants. Here, $\alpha_{k1} = \psi_1 = 0.85034$ and $\alpha_{k2} = \psi_2 = 1.0$, leading to $\psi = \alpha_k$. Unlike in the standard model, the third term on the left hand side in equation (4.7) is additionally incorporated here to account for implicit or explicit calculation depending on variable sign and to further ensure boundedness.

The specific dissipation rate is modeled solving for ω as

$$\frac{\partial \omega}{\partial t} + \nabla \cdot (\phi \omega) - \nabla \cdot (\phi) \omega - \nabla \cdot [D_{\omega,b}(F_1) \nabla \omega] = P_\omega - \beta(F_1) \omega^2 - \frac{(F_1 - 1) CD_{k\omega}}{\omega} \omega \quad (4.10)$$

with P_ω the production term of ω and β a model variable modified using blending functions given above, which is calculated using $\beta_1 = \psi_1 = 0.075$ and $\beta_2 = \psi_2 = 0.0828$. $CD_{k\omega}$ is a model variable further calculated as

$$CD_{k\omega} = 2\alpha_{\omega 2} \frac{\nabla k \cdot \nabla \omega}{\omega} \quad (4.11)$$

Similar to the approach presented above, $D_{\omega,b}(F_1)$ is calculated as the sum of kinematic and turbulent viscosity including a blended modification of the latter, which is calculated as $\alpha_\omega(F_1)\nu_t$. However, $\alpha_{\omega 1} = \psi_1 = 0.5$ and $\alpha_{\omega 2} = \psi_2 = 0.85616$ here, leading to $\psi = \alpha_\omega$. Again, the third term on the left hand side is added for implicit/explicit calculation. The production term for ω is calculated as

$$P_\omega = 2|(\nabla \vec{u})|^2 \gamma_\omega(F_1) \quad (4.12)$$

with γ_ω being modified using blending functions and values of $\gamma_1 = \psi_1 = 0.5532$ and $\gamma_2 = \psi_2 = 0.4403$.

The above given blending function for F_1 and F_2 for the calculation of final ν_t are given as

$$F_1 = \tanh \left\{ \left(\min \left(\min \left(\max \left(\frac{1}{\beta^*} \frac{k^{0.5}}{\omega y}, \frac{500\nu}{\omega y^2} \right), \frac{4\alpha_{\omega 2} k}{CD_{k\omega}^+ y^2} \right), 10 \right) \right)^4 \right\} \quad (4.13)$$

and

$$F_2 = \tanh \left\{ \left(\min \left(\max \left(\frac{2}{\beta^*} \frac{k^{0.5}}{\omega y}, \frac{500\nu}{\omega y^2} \right), 100 \right) \right)^2 \right\} \quad (4.14)$$

with $CD_{k\omega}^+ = \max(CD_{k\omega}, 1e^{-10})$ and y being the distance to the nearest wall boundary patch.

Finally, the turbulent viscosity is calculated as

$$\nu_t = \frac{\alpha_\nu k}{\max(\alpha_\nu \omega, F_2 \sqrt{2S_{ij}^2})} \quad (4.15)$$

where α_ν holds a value of 0.31 in the present setup.

4.2.3 Model Domain and Grid Generation

The main objective of present investigations, esp. in terms of model verification, is to show the general capability of the present numerical flow and sediment transport model to reproduce results obtained from laboratory tests as given in §3.2. For this reason, the general numerical model domain setup is, in terms of physical dimensions and load conditions, primarily based on these tests if not otherwise stated in this work.

A sketch of the numerical model domain is given in figure 4.1, showing the general model zones and domain boundaries. The latter are further discussed below in §4.2.4.

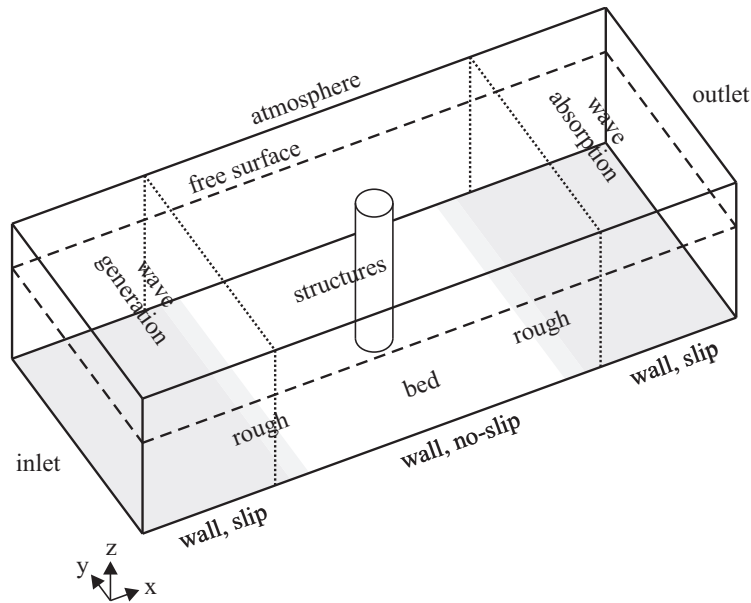


Figure 4.1: Sketch of the numerical model domain including wave generation and absorption zones. The location of foundation structure is represented by a vertical pile for simplicity.

It has to be noted that the setup of the laboratory tests is not fully represented in the numerical model domain, as the areas of connection between the original laboratory flume bottom and the elevated model section using ramps as sketched in figure 3.1 are given with a horizontal bed layer here. As these zones are however completely covered by the wave generation zone, influences on the results are supposed to be negligible.

For the final generation of the computational grid, different mesh generation techniques were combined in the present setup by use of OpenFOAMs build-in grid generation mechanisms as well as third-party software as given in the following:

1. In case of investigations on flow and scour around objects, the particular three-dimensional surfaces of the structures were generated and modeled using open source pre- and post-processing software SALOME³. For further usage in OpenFOAM meshing algorithms, objects were then exported using STL (Standard Tessellation Language) file format, a native CAD software file format describing object surfaces by its vertices and unit normals after surface triangulation in Cartesian coordinates.

³See <http://www.salome-platform.org> for further information.

2. In a second step, the overall model domain, without representation of the object surface, was generated using OpenFOAMs *blockMesh* grid generator while producing quadrilaterally-faced hexahedra meshes. Afterwards, areas around the location of objects were further refined using general splitting techniques of the computational cells from the ambient model domain, in either two or three dimensions.
3. Finally, any objects generated in the first step were included into the overall model domain using OpenFOAMs *snappyHexMesh* grid modifier. Generally said, the method is capable of incorporating object surfaces in STL file format by removing grid cells inside an object from the ambient model domain grid while producing iteratively-refined and surface-aligned hexahedra as well as split-hexahedra meshes around the object surface.

It however has to be noted that the utility does not necessarily produce smooth grids and object surface alignments, especially in regions with sharp corners between particular object components, e.g. at brace-pile sleeve connections in case of the tripod structure. Certain effort is therefore required to adapt refinement and surface snapping options to the specific object requirements.

In addition to this procedure, simple objects like vertical cylinders can however be incorporated into the model domain using step two from the procedure described above along with a modified grid generation setup, which bears the advantage of computationally smoother grids. Due to a comparison between model domains including cylindrical structures generated with both techniques, it was however found that there is no outstanding advantage of a direct object inclusion. For this reason, the combined domain generation approach was mainly applied in the present investigations, as it further makes the complete simulation process more general and applicable to different complex objects, i.e. foundation structures.

For the investigations presented here, it was generally found preferable to use OpenFOAMs build-in grid generation mechanism as described above, although several mesh converters are available in the releases, making it possible to use computational grids generated from third-party meshers. It has however been discovered that especially converted tetrahedra meshes, which were used in the first stages of the work, led to numerous computational instabilities in the area of the water surface at the inlet boundary when using wave generation techniques, as well as at vertical object surfaces during pile-up, i.e. in situations and locations with high flow velocities occurring at the water-air interface.

Grid Composition Regarding the spatial grid composition and resolution, the overall mesh consists of a multilevel grid, see figures 4.2 and 4.3. In the following, both composition and resolution are given for the case of tripod flow and scour

investigations with free surface, which is the main focus of the present work. For additional cylinder scour investigations under steady current load (see §5.4.2), the applied grid however differs from the given setup.

In areas without structural influence, the grid cells (hexahedra) have a resolution Δ_c , i.e. the edge length of a hexahedron of mainly 5cm in horizontal (x, y) direction. In the wave absorption zone, grid cells are however expanded in x direction. In vertical (z) direction, the grid is further resolved with $\Delta_c = 1.25\text{cm}$ in the region of maximum wave amplitude and a vertically graded mesh at the bottom boundary with lowermost cells in the range of $y^+ \approx 1 - 25$. Ideally, one would resolve the domain in the remaining area with a similar resolution as given for the wave and near-bed region. This however would result in tremendous computational times and is therefore not applicable for the present investigations. Through comparison with finer grid resolutions, it has been found sufficient to coarsen the vertical mesh resolution in the remaining water column to a grid resolution of $\Delta_c \approx 5\text{cm}$. In the near-field of an object, i.e. the tripod foundation structure, grid cells are then gradually refined by splitting each computational cell by a factor of 1-4 in all directions based on the fundamental model grid, giving a main resolution of $\Delta_c \approx 0.6\text{cm}$ around the main structure and $\sim 0.2\text{cm}$ at the piles, where the vertical resolution of the lowermost cells at the bottom boundary was kept with the y^+ range given above.

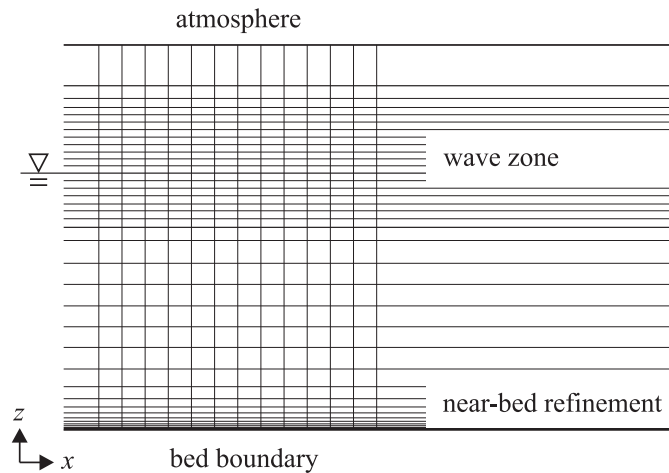


Figure 4.2: Schematic diagram of the numerical model domain as vertical slice in an area without foundation structure, giving the horizontal layering method of the model grid.

4.2.4 General Boundary Conditions

As a numerical model domain typically represents only a small part of the reality including the area of main interest, the domain is finite and therefore needs appropriate boundary conditions that either model physical behavior like fluid-structure

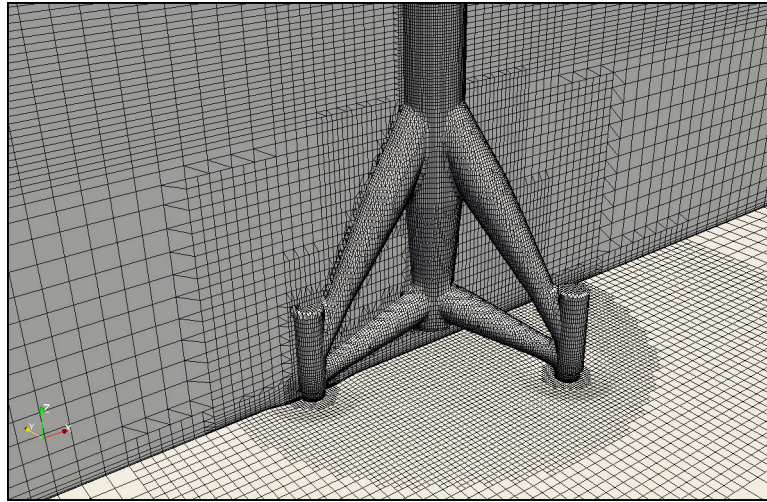


Figure 4.3: Detail of the OpenFOAM computational grid for flow and scour simulations for the tripod structure. Grid given as slice trough vertical as well as bottom and tripod structure boundary mesh.

interaction at walls or aim to simulate the imaginary boundary at the numerical domain that would normally interact with the fluid body outside the model domain.

For the present setups, boundary conditions at inlet, outlet, solid side walls (if present), atmosphere, bottom boundary and model structures had to be specified, as given in figure 4.1. Special attention had to be drawn to the wave modeling and turbulence modeling part, which is however given in §4.2.5 and §4.2.6 due to their specific implementations. Furthermore, boundary conditions for bed load and suspended load transport had to be prescribed, which are further specified in §4.3.4. Generally, all boundary conditions are applied to the faces of the boundary-connected cells of the computational domain in the present model.

Inlet and Outlet For the inlet boundary, the velocity components \vec{u} are either specified by a logarithmic velocity profile using equation (2.7) in case of pure current flow, or are indirectly set by the wave generation and absorption method if wave or wave-current flow is applied, see §4.2.6. Similarly, the surface elevation given by the volume fraction α_r is either set directly based on still water level in case of pure flow, or by the wave generation method in the other cases. The pressure is set as zero normal gradient, i.e. as Neumann boundary condition giving $\partial p / \partial \vec{n} = 0$. Turbulence quantities for k and ω are explicitly set as fixed values, i.e. a Dirichlet boundary condition.

At domain outlets, there is typically no direct information available on variable values a priori, for which reason time-dependent values are calculated from within the model domain. Therefore, zero normal gradient is specified for all quantities at the outlet, except for the pressure. The latter is set as total pressure by $p_0 = p + 0.5\rho [\vec{u}]^2$,

i.e. adjusted with changing velocity field.

Atmosphere At the atmosphere patch, which represents the uppermost boundary of the computational domain, turbulence quantities as well as pressure are set as zero gradient. Regarding the flow velocity, a flow direction-dependent boundary condition is applied, which either serves as a Neumann boundary condition for flow out of the domain or as a fixed value boundary condition with zero tangential components for inflow, i.e. backflow cases. Similar to this, the volume fraction is further specified depending on the flow direction, while allowing outflow from the domain but suppressing any backflow.

Bottom Boundaries In the present setup, the general bottom boundary representing the lowermost patches of the numerical domain are split into three categories: the movable bed section, concrete zones and roughness element zones as given in the laboratory flume experiments. As the concrete bottom parts can generally be regarded as hydraulically smooth in the present setup and are furthermore not in the focus of main interest, a continuous wall function approach is applied to the turbulence properties.

For the movable bed and roughness element sections, turbulent quantities are however calculated by use of an explicit treatment, which is further described below in §4.2.5. Independent from this, volume fractions as well as pressure are set as zero gradient for all bottom boundaries, where the velocity is specified with a no-slip condition, i.e. $\vec{u} = 0$.

Side Walls and Object Surfaces Generally, no-slip conditions for the flow are applied to any solid walls. In the wave generation and wave damping zones, slip conditions are however used in these regions at the side walls in order to avoid high flow velocities otherwise occurring at the water-air interface due to the direct value manipulation technique. For a thorough description of the latter, see Jacobsen (2011). Regarding the turbulence model quantities, zero gradient conditions are applied at slip walls. The remaining solid wall boundaries, i.e. flume walls and object surfaces are modeled using wall function approaches, i.e. the way quantities are modeled at concrete bottom boundaries as described before. Finally, surface elevation and pressure are set as zero gradient for all wall boundaries.

4.2.5 Turbulence Boundary Conditions

Generally, two types of turbulence boundary treatments have been used in the present setup: An explicit treatment of the turbulence characteristics has been applied for domain boundaries representing sediment and roughness element interfaces

on the one hand, while wall function approaches using blending functions have been applied for smooth wall boundaries, i.e. flume walls, rigid bed elements and foundation structures on the other hand, further described below.

Explicit Treatment As already stated in §4.2.2, the turbulence characteristics of the flow near the wall boundary can be directly controlled in the $k - \omega$ type turbulence models by a modification of the specific dissipation of turbulent kinetic energy at the boundary in order to account for surface roughness effects, which therefore serves as a Dirichlet type boundary condition. In this case, large values of ω lead to a reduction of turbulence at the wall due to turbulent energy dissipation, whereas generally, ω decreases with increasing roughness height.

In the original turbulence model formulation of Wilcox (2006), the wall boundary condition for ω is given as

$$\omega = \frac{u_f^2}{\nu} S_r \quad (4.16)$$

where S_r is a model variable which is calculated depending on the surface roughness k_s^+ , which thereby covers the full roughness range from smooth to rough wall cases. Recalibrations of S_r have been carried out by Roulund et al. (2005) and Fuhrmann et al. (2010) due to modifications in the boundary value formulation for k , where the latter formulation has been applied in the present work, giving

$$S_r = \begin{cases} \left(\frac{200}{k_s^+}\right)^2 & \text{for } k_s^+ \leq 5 \\ \frac{180}{k_s^+} + \left(\frac{200}{k_s^+}\right)^2 - \frac{180}{k_s^+} \exp(5 - k_s^+) & \text{for } k_s^+ > 5 \end{cases} \quad (4.17)$$

Roulund et al. (2005) identified that the determination of the friction velocity u_f , generally and esp. for modeling of equation (4.16) is very sensitive to grid resolution and surface roughness values. The traditional form of calculating wall shear stress and friction velocity by use of the near-wall velocity gradient $\partial u / \partial y$ is only valid for a limited range of small y^+ values, see §2.2.1, which results in very fine near-wall grid spacings and therefore tremendous computational costs in order to fulfill this requirement. To circumvent this restriction, the friction velocity has been calculated by use of the van Driest (1956) velocity profile in the present implementation, which is similar to the method given in Roulund et al. (2005).

van Driest (1956) developed a theory providing a “continuous velocity and shear distribution for turbulent flow near a smooth wall” and a further basis of its calculation for rough wall cases, which was proven to be valid in the viscous sublayer, the buffer layer and the logarithmic layer following table 2.1. The original formulation of the velocity profile has been further modified by Cebeci and Chang (1978) in order to account for surface roughness by coordinate shift method.

By use of this formulation, the friction velocity has been calculated by iteration from the near-wall velocity in the first computational cell above the wall boundary. Here, the dimensionless near-wall velocity using the van Driest velocity profile including roughness coordinate shift is calculated as

$$u^+ = \frac{u_\tau}{u_f} = \int_0^{y^+} \frac{2dy^+}{1 + \sqrt{1 + 4\kappa^2 (y^+ + \Delta y^+)^2 \left[1 - \exp\left(-\frac{y^+ + \Delta y^+}{A}\right) \right]}} \quad (4.18)$$

with u_τ being the tangential component of the near-wall velocity, $\kappa = 0.41$ the van Karman constant, A the van Driest damping factor holding a value of 25 and Δy^+ the coordinate shift due to roughness, which takes values of

$$\Delta y^+ = \begin{cases} 0 & \text{for } k_s^+ \leq 5 \\ 0.9 \left[\sqrt{k_s^+} - k_s^+ \exp\left(-\frac{k_s^+}{6}\right) \right] & \text{for } 5 < k_s^+ < 2000 \end{cases} \quad (4.19)$$

For integration of equation (4.18), the trapezoidal rule has been applied, given in the general form as

$$\int_a^b f(x) dx \approx (b - a) \frac{f(a) + f(b)}{2} \quad (4.20)$$

where uniform discretization has been chosen with $N = \lfloor y^+ + 1 \rfloor$ as the number of equally spaced panels.

Regarding the boundary formulation for turbulent kinetic energy k , it has been found by several others in the course of physical and numerical investigations, e.g. Nezu (1977), Sumer et al. (2003) or Fuhrmann et al. (2010) that the original formulation and near-wall treatment e.g. given in Wilcox (2006) by assuming $k = 0$ at the boundary independent of the surface roughness and in combination with equation (4.16) forces the development of a viscous sublayer in both smooth and rough bed conditions in the model, which is not physically correct for the latter case. In contrast, $\partial k / \partial y = 0$ serving as a Neumann boundary condition is proposed by the authors as it is more consistent with the near-wall physics. It allows the development of a viscous sublayer in smooth bed conditions, but however avoids this in rough bed cases. Numerical model results in Fuhrmann et al. (2010) have further shown that no significant difference could be determined for hydraulically smooth conditions, depending on whether $k = 0$ or $\partial k / \partial y = 0$ is used. The latter formulation using Neumann boundary condition has therefore been chosen in the present work.

Finally ν_t at the wall boundary is calculated based on the internal calculation of the turbulence model following equation (4.15).

Wall Function Approach As domain boundaries like flume walls, rid bed areas or foundation structure models can typically be regarded as hydraulically smooth in the present setup, it has been found unessential to explicitly treat the turbulence characteristics at the wall boundaries following the procedure described above. Furthermore, domain areas not being directly in the focus of investigations can be modeled using a simpler and therefore time-saving but still computationally valid method. Therefore, continuous wall function approaches as implemented in the standard OpenFOAM release have been chosen here, which are still working well in a wider range of y^+ values, i.e. in ranges of $y^+ \approx 1 - 300$ due to the application of blending functionality.

The wall boundary condition for ω is implemented following Menter and Esch (2001) as

$$\omega = \sqrt{\omega_{vis}^2 + \omega_{log}^2} \quad (4.21)$$

where the viscous part is modeled applying

$$\omega_{vis} = \frac{6\nu}{\beta_1 y^2} \quad (4.22)$$

and the logarithmic part as

$$\omega_{log} = \frac{\sqrt{k}}{C_\mu^{0.25} \kappa y} \quad (4.23)$$

The model constant β_1 holds a value of 0.075. The friction velocity in the original formulation has been replaced here by the expression $u_f = C_\mu^{0.25} \sqrt{k}$ following Ferziger and Peric (2008), where C_μ has a value of 0.09.

The wall condition for the turbulent kinetic energy k again serves as a Neumann boundary condition here, i.e. $\partial k / \partial y = 0$ over the complete y^+ range.

4.2.6 Surface Wave Modeling

Several techniques have been developed and used to generate waves in numerical free-surface models. Generally, the technique is to either simulate and reproduce the motion of a wave maker in physical modeling by modifying and moving the computational boundary mesh at the wave inlet, or to set surface elevations and velocity components directly at or near the wave boundary, using either components from wave theory or from measurements in physical models. Both techniques have successfully been used and have provided correspondence between both theory and experimental data: flap or piston type wave maker boundary motions have e.g. been used by Huang et al. (1998) and Lal and Elangovan (2008); prescribing velocity components and surface elevation over time using wave theory has been used by Park et al. (1999), Ryu et al. (2003), Smith (2009), Afshar (2010), Morgan et al. (2010) and Jacobsen et al. (2012) in order to simulate wave propagation.

In the present model setup, two different boundary condition approaches were investigated:

1. direct, time-varying prescription of surface elevation and flow velocities at the inlet boundary
2. wave generation at the inlet zone in combination with a wave absorber using blending functionality

At the beginning of the model setup, the inlet boundary quantities of surface elevation η and velocity components \vec{u} were prescribed directly at the boundary (1.), i.e. the computational faces of the model domain at the inlet section. Therefore, quantities were implemented using both Airy and 2nd order Stokes wave theory. In case of additional current load, the velocity components in horizontal direction were furthermore superimposed to the wave load components using a logarithmic velocity profile. The advantage of this setup lies in the omission of an additional wave generation zone, which generally reduces computational costs. It however has the drawback that the implementation acts as a wave generation boundary condition only, i.e. no wave absorption mechanism is implemented here.

Due to this, the second approach (2.) was therefore chosen for the final model setup. The wave generation mechanism described in Jacobsen et al. (2012) was applied⁴. In the general implementation, different wave types using Airy, 2nd and 5th order Stokes, Stream Function theory, irregular waves and wave combinations can be generated based on wave theory in a defined wave generation zone at the inlet by use of blending functions. The general description of the blending mechanism is further described below in the outlet boundary section. It is an advantage of this approach that reflected waves e.g. from a structure placed in the model domain, which enter the wave generation zone, can successfully be removed at the same time the waves are generated, i.e. the functionality is similar to the one of a wave absorber. However, an additional part of the computational domain is necessary for the mechanism to act.

4.2.7 Non-reflecting Outlet Boundaries

When modeling surface water waves in a finite model domain, appropriate outlet boundary conditions are required, which allow waves to leave the domain without unphysical reflections at the boundaries. Typical outlet boundary conditions like zero gradient Neumann condition suitable for unidirectional flow do not fulfill these requirements as parts of the velocity components are reflected back. Due to wave-structure interactions and typical wave effects like diffraction, shoaling or

⁴For further information, see <http://openfoamwiki.net/index.php/Contrib/waves2Foam>.

wave breaking within the model domain, periodic boundary conditions cannot be used here, as waves at the outlet might be different from the waves triggered at the inlet. Especially when simulating wave conditions for long-term sediment transport processes, eliminating or at least minimizing wave reflection is however essential.

One way of prescribing non-reflective boundaries is to use the Sommerfeld condition acting as a kind of high-pass filter, e.g. described and discussed in Romate (1992) and Durrán (2001). It unfortunately has the drawback that an accurate estimation of wave celerity near the outlet is necessary, which is difficult or even impossible to derive for complex cases. A method to calculate wave celerity is nevertheless given in Orlanski (1976), where the flow field inside the domain near the outlet boundary is used to calculate the desired quantity.

Another method used quite often is the implementation of a so-called sponge layer or numerical beach in a damping zone of the model domain. Internally, two major different methods are used for wave damping. In the first case, an additional (artificial) viscosity term $\nu_d(x, y, z)$ is added to the momentum equation in order to dissipate energy in the damping zone. This artificial viscosity is a function of space and is non-zero in the damping zone only, where it is smoothly ramped from the start location of the zone to its final value at the outlet boundary. A sufficiently smooth ramping is necessary in order to prevent unwanted reflections directly at the zone starting point. Implementations of this viscosity method can e.g. be found in Cao et al. (1993), Wang et al. (2007) and Smith (2009). The fact that it can be used for wave damping only until still water level and zero velocities are reached is a drawback of this method; it can not be used if an additional current velocity like in wave-current interaction cases is required to be prescribed at the outlet.

In the second case, surface elevations and velocity components along the damping zone are directly modified using blending functions to blend between the actual, computed values from the model and target values, e.g. still water level and zero velocity or a current velocity function. The blending is again implemented as a smooth function, where the computed values have a weight of one at the damping zone starting location and the target values have zero weight, respectively, while this function is reverted at the outlet boundary. Implementations of this method are e.g. used in Afshar (2010) and Jacobsen et al. (2012). Several, different implementations for the viscosity damping and blending coefficients can be found in literature, using mainly quadratic, cubic, hyperbolic, polynomial or cosine functions in order to smoothly increase their value over the zone length.

Other approaches are the use of damping zones with artificial porous media or the extension and expansion of the model domain, using numerical damping due to wave dissipation and interface smearing.

Combined approaches can further be found in literature. An approach of the aforementioned damping methods is given in Clément (1996), using an artificial

viscosity damping as a low-pass filter in combination with a high-pass filter outlet boundary condition; further combinations have e.g. been investigated in Morgan et al. (2010).

Present Wave Absorption Mechanism For the present setup, two approaches have been investigated, which are however based on a similar approach: In the beginning, a wave damping zone was implemented at the rear part of the model domain using blending functionality, as it was generally described before. The blending function used takes the form

$$\eta_b = 1 - \left(\frac{x - x_0}{x_{dist}} \right)^6 \quad (4.24)$$

in which x gives the actual position, x_0 the start coordinate and x_{dist} the overall length of the damping zone, leading to values $\eta_b = 0$ at the domain boundary and $\eta_b = 1$ at the zone end position within the model domain. The blend between actual solutions and target solutions is then calculated as

$$\psi = \eta_b \psi_{actual} + (1 - \eta_b) \psi_{target} \quad (4.25)$$

The second approach is the one given in Jacobsen (2011) and implemented in the wave generation and absorption toolbox described above. In this case, the blending function after Fuhrmann et al. (2006) is applied, taking the form

$$\eta_b = 1 - \frac{\exp(\chi_b^{3.5}) - 1}{\exp(1) - 1} \quad (4.26)$$

where $\chi_b \in [0, 1]$ similarly is a function giving the actual, spatial position within the blending zone, in which η_b again holds a value of zero at the domain boundary and a value of one at its end position, see figure 4.4. The blend between actual and target solutions is then calculated using equation (4.25) for every position within the zone at every time step of the computation, where ψ is applied to the fluid velocity vector \vec{u} and the volume fraction α_r .

It has to be noted that the wave generation and absorption toolbox given in Jacobsen et al. (2012) has been released after implementation of the first approach. Generally, a comparison of the efficiency between the two approaches led to similar results for the wave parameters investigated here. Due to better consistency in combination with the wave generation mechanism, the second approach has finally been applied for the present work.

As an extension of the package, a logarithmic current velocity profile using equation (2.7) was implemented. In the absorption zone, the target function takes the form of the current profile in case of a current or combined wave-current load case. In

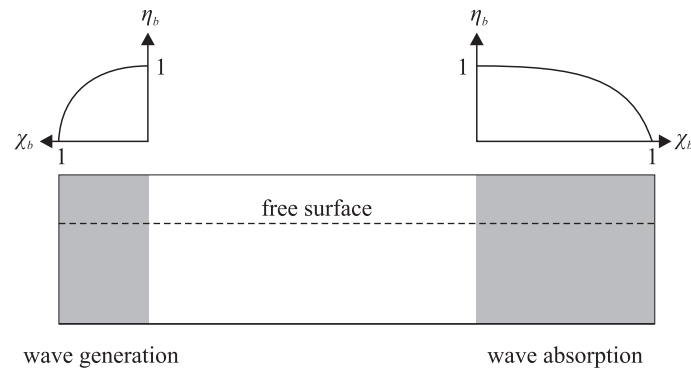


Figure 4.4: Sketch of the η_b blending function variation in the wave generation and absorption zones. Modified after Jacobsen (2011).

the wave generation zone, the current profile then either serves as the target function alone, or its horizontal velocity components are superimposed onto the horizontal orbital motion velocity profiles to form the target function.

4.3 Sediment Transport Model

The classical approach of modeling sediment transport processes using numerical methods is to divide the physical processes into two phases: the near-bottom (bed load) transport and the transport in the water column (suspended load), which therefore follows the general classification as given in §2.3.3. Depending on the load conditions, sediment properties and crucial physical processes, the suspended load processes can be neglected while still achieving reasonable results, especially when modeling coarse bed materials. The problem is then reduced to the choice of a proper bed load transport formulation, see e.g. the works in Weillbeer (2001), Roulund et al. (2005) or Göthel (2008). The modeling process can be further reduced when assuming uniform sediments, i.e. without modeling each sediment fraction separately, which is valid for most laboratory experiments with well-defined grain distributions, but also for natural, narrow distributed sediments that can be found in many parts of the North Sea area.

Regarding sediment transport formulations, most approaches are based on the assumption that a certain threshold value has to be exceeded in order to set particles in motion. The beginning of sediment motion is generally given by the condition $\theta > \theta_c$. This means that a strict criterion for the beginning of sediment motion is typically given in the numerical model, while such a strict cut-off is not necessarily given in natural applications.

In the present implementation, the transport process is divided into bed load and suspended load, where both parts are modeled separately, see §4.3.2 and §4.3.3. As it could already be seen from the laboratory tests, the latter process cannot be neglected here, as a major transportation of particles is carried out in suspension for

the present cases under the influence of wave load. The Exner equation for sediment continuity is finally applied for calculation of bed elevation changes, see §4.3.5. Only uniform sediments are modeled here, which is a valid assumption when regarding the sediment properties used in physical modeling as given in §3.2.1.

4.3.1 Shear Stress Determination

In sediment transport modeling, the bed shear stress serves as the main input parameter for the bed load and suspended load transport formulations and thereby connects the quantities from the hydrodynamic flow model to the sediment transport models. Therefore, a proper choice of shear stress determination is necessary. Different approaches for its calculation exist, which are however strictly valid only under specific conditions. In case of low-Re formulations, i.e. when the near-boundary flow is directly resolved by the computational grid or slightly above, the wall shear stress can be determined using the velocity gradient at the wall as

$$\tau_w \equiv \tau(y=0) = \mu \frac{\partial u}{\partial y} \quad (4.27)$$

In a second approach, the wall shear stress is taken as the inner fluid stress at the wall boundary by use of the Reynolds stress due to velocity fluctuations calculated by the turbulence model in case of turbulent flow conditions, given as

$$\tau_w \approx R_{ij} \equiv \rho \overline{u'_i u'_j} \quad (4.28)$$

It however has to be noticed that only the tangential component of the Reynolds stress value is taken then.

Another approach, which is used in the present setup, is to calculate the wall shear stress from the friction velocity u_f determined using the van Driest velocity profile given by equation (4.18), which relates u_f to the near-bed flow velocity u_τ . This formulation has the advantage of directly taking into account the effect of surface roughness and is further valid over a larger range of y^+ values. The shear stress is then simply calculated from given quantities as

$$\tau_w = u_f^2 \rho \quad (4.29)$$

4.3.2 Bed Load Transport

General Calculation Procedure Following the definitions in §2.3.3, bed load generally takes place directly at or slightly above the bed surface. Therefore, a calculation of the bed load transport rates q_b is carried out directly at the lower bottom boundary of the computational domain. In the present implementation, a separate mesh representing the generally two-dimensional bed boundary grid with

curved surface is constructed for bed load calculation. The particular computational nodes and cell faces of the three-dimensional fluid volume grid and the bed boundary grid are thereby equal in space, which means that a direct projection or mapping of quantities is carried out between the meshes. Details on the present mapping procedure are given in §4.5 and are sketched in figure 4.5.

For calculations and value mapping, the finite area method (FAM) is used, which is implemented in the framework of the OpenFOAM 1.6-ext version. The FAM was thereby generally designed for solving partial differential equations using the finite volume approach for curved surfaces in three-dimensional space. Further information on the FAM can be found in Tukovic (2005) and the particular OpenFOAM source code.

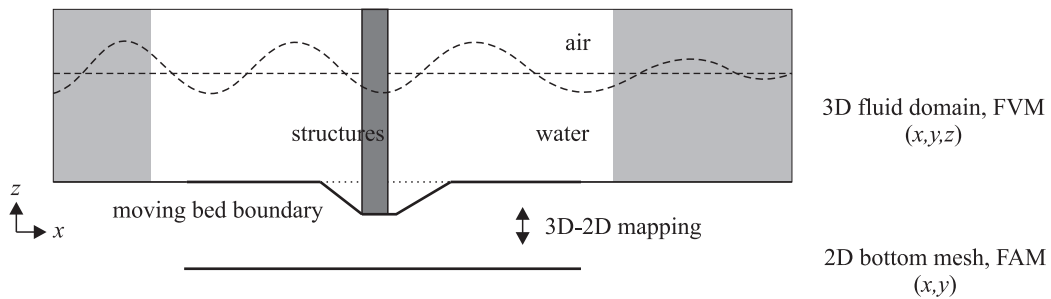


Figure 4.5: Sketch of the mapping procedure between 3D FVM flow model domain and 2D FAM bottom boundary mesh.

Implementation of Forces in Vectorial Form The calculation of q_b as the bed load transport rate from given hydrodynamic and external forces is implemented in vectorial form here, see figure 4.6. The general concept taking into account any slope-dependent modifications follows the idea given in Roulund et al. (2005), which was designed as an extension of the bed-load transport formulation of Engelund and Fredsøe (1976) to the three-dimensional space for sloping beds and which is in turn based on the vectorial approach given in Kovacs and Parker (1994). A system of equations can be derived from particular componential formulations of external forces acting on the single grains during flow, from which the transport direction \vec{u}_b can be derived. Similar to Jacobsen (2011), the OpenFOAM grid representation of computational cells, faces and normal vectors \vec{N} is used in order to reduce the problem of originally four non-linear coupled algebraic equations to a set of three equations that need to be solved.

In case of sloping beds, there are several forces acting on the single sediment grains as given in §2.3.4, namely the gravity force \vec{F}_g , trying to move sediment from higher to lower levels and the combined lift and drag force \vec{F}_{drag} due to the absolute motion of the grains relative to the surrounding fluid flow field. Here, the force of

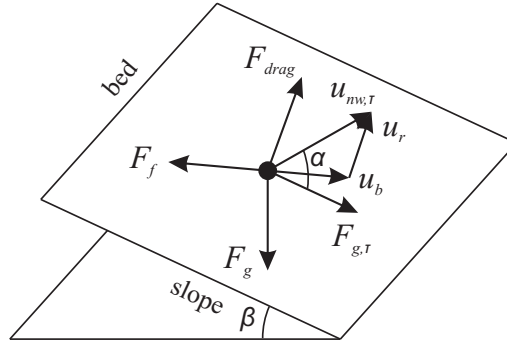


Figure 4.6: Sketch of forces acting on the particle on a sloping bed.

gravity (and buoyancy) is split into a friction force trying to withstand the sediment grain movement

$$\vec{F}_{fric} = - \left| \vec{F}_g \right| \cos \beta \cdot \mu_d \frac{\vec{u}_b}{|\vec{u}_b|} \quad (4.30)$$

with μ_d being the dynamic friction coefficient corresponding to the dynamic friction angle ϕ_d of the sediment and an acting force in the direction of the steepest point of local bed slope giving

$$\vec{F}_{g,\tau} = \vec{N} \times \left(\vec{F}_g \times \vec{N} / |\vec{N}| \right) / |\vec{N}| \quad (4.31)$$

As mentioned above, the normal vector \vec{N} is used here in order to get the vectorial components of the direction of the bed slope. The force of lift and drag is further calculated by

$$\vec{F}_{drag} = \frac{1}{2} \rho c_d \frac{\pi}{4} d^2 |\vec{u}_r| \vec{u}_r \quad (4.32)$$

with c_d as a constant factor accounting for the drag and lift force modifications based on experimental results by Fernandez Luque (1974) and discussed in Engelund and Fredsøe (1976), given as

$$c_d = \frac{4\mu_d}{\frac{3}{2} a^2 \theta_{cr,0}} \quad (4.33)$$

in which $\theta_{cr,0}$ gives the critical Shields parameter for horizontal bed.

As sketched in figure 4.6, the relative velocity \vec{u}_r given in vectorial form is related to the near-wall flow velocity \vec{u}_{nw} and the bed-load transport velocity \vec{u}_b by

$$\vec{u}_r = \vec{u}_{nw,\tau} - \vec{u}_b \quad (4.34)$$

Although it might be obvious to simply take \vec{u}_{nw} from \vec{u} as the flow velocity vector in the first computational cell above the bed, this would lead to highly grid-dependent results, as the velocity magnitude varies with varying cell height, which is typically not constant in case of scour deformation on the grid. Therefore, the near-wall

velocity is calculated from the friction velocity as

$$\vec{u}_{nw} = au_f \frac{\vec{u}}{|\vec{u}|} \quad (4.35)$$

instead, with a taken as $\mathcal{O}(10)$ here, see §2.3.4. As \vec{u}_{nw} might further contain normal portions of the flow quantity and only bed-parallel portions should be considered here, a projection onto the bed is required, reading

$$\vec{u}_{nw,\tau} = \vec{N} \times \left(\vec{u}_{nw} \times \vec{N} / |\vec{N}| \right) / |\vec{N}| \quad (4.36)$$

Under the assumption of steady motion of the sediment, the resulting bed-load transport velocity \vec{u}_b can then be found from aforementioned, external forces as

$$\vec{F}_{fric} + \vec{F}_{g,\tau} + \vec{F}_{drag} = 0 \quad (4.37)$$

When taking eqs. (4.30), (4.31) and (4.32) and inserting into equation (4.37), a nonlinear system of coupled equations is finally derived, which can be applied to solving for the three vectorial components of \vec{u}_b using multidimensional root-finding algorithms, i.e. solving a nonlinear system with n equations in n unknowns. In the present implementation, the root-finding problem is solved numerically by use of the GNU Scientific Library (GSL), which generally gives a collection of numerical routines for scientific computing, see Galassi et al. (2011). By inclusion of the corresponding libraries, the necessary parts of the GSL framework have been fully integrated into OpenFOAM source code in order to solve for \vec{u}_b at run time, while the Newton-Raphson iteration technique has been applied here.

Slope-dependent Shear Stress Modification Following §2.3.6, the Shields parameter has to be modified to account for the effect of sloping beds. Based on the idea given in Roulund et al. (2005), which generally uses the flow velocity vector and the steepest slope direction after figure 4.6 in order to adjust the critical Shields parameter as suggested by Engelund and Fredsøe (1976), the modification is calculated as

$$\theta_{cr} = \theta_{cr,0} \left(\cos \beta \sqrt{1 - \frac{\sin^2 \alpha \cdot \tan^2 \beta}{\mu_s^2}} - \frac{\cos \alpha \cdot \sin \beta}{\mu_s} \right) \quad (4.38)$$

with α being the angle between the near-bed flow velocity vector $\vec{u}_{nw,\tau}$ and the direction of the steepest slope, β the slope angle, $\theta_{cr,0}$ the critical Shields parameter in case of horizontal bed and μ_s the static friction coefficient of the sediment.

As the slope angle in the present model implementation is allowed to exceed the angle of repose by a few degrees before a sand sliding procedure starts as given in §4.3.6, the slope angle in equation (4.38) however had to be bounded to $0 \leq \beta \leq \phi$,

i.e. only positive values up to the angle of repose are allowed, as otherwise unrealistic values for the modified critical Shields parameter occur.

Bed Load Model Formulation In the present setup, the bed load transport formulation of Engelund and Fredsøe (1976) has been chosen, which can generally be given as a semi-empirical model law relating the bed load flux q_b to the mean transport velocity \vec{u}_b of a particle moving as bed load while taking into account the probability of movement under the given load conditions. The formulation has already been applied in works of Roulund et al. (2005), Liu (2008), Göthel (2008) and Jacobsen (2011), where all in all good results were achieved.

When applying the transport formulation, the bed load rate is calculated as

$$\vec{q}_b = \frac{\pi}{6} d p_{EF} \vec{u}_b \quad (4.39)$$

with p_{EF} being the probability of occurrence of particles moving near the bed, given by

$$p_{EF} = \left[1 + \left(\frac{\frac{\pi}{6} \mu_d}{\theta - \theta_{cr}} \right)^4 \right]^{-1/4} \quad (4.40)$$

As an alternative of calculating the near-bed velocity \vec{u}_b in a different way than applied here and given in the procedure described above, a semi-empirical equation after Engelund and Fredsøe (1976) might be taken as simplification, giving

$$\vec{u}_b = a \vec{u}_f \left(1 - 0.7 \sqrt{\frac{\theta_{cr}}{\theta}} \right) \quad (4.41)$$

in which the vector components of friction velocity \vec{u}_f might be taken from the flow velocity vector in the first computational cell above the bed, however having in mind that it does not include any effects of slope-dependencies or vectorial force and flow components.

4.3.3 Suspended Load Transport

Suspended sediment can be described as part of the total sediment load that moves without a continuous contact to the bed as given in §2.3.3. Due to enhanced shear stresses caused by the near-bed flow, individual particles are picked up and entrained into the water column, which are then accelerated by the flow field and might interact with other particles. The fluid turbulence is relatively small near the bottom of the bed load layer and therefore inter-granular interaction of particles can be identified as the dominant mechanism for suspended transport. In contrast, inter-granular interaction diminishes and turbulence becomes stronger at the upper end of the bed load region, where the concentration rapidly decreases with increasing distance from

the bed and turbulent suspension becomes the dominant transport mechanism, see Amoudry et al. (2005).

In the undisturbed case, suspended load is mainly carried in the lower to middle part of the water column and moves with the flow field. In this case a typical sediment concentration distribution can be described by means of the Rouse (1938) profile, which was developed under the assumption of uniform equilibrium suspension in the water column and a balance of upward directed sediment fluxes due to turbulence and downward directed sediment settling:

$$c = c_a \left[\left(\frac{h-z}{z} \right) \left(\frac{a}{h-a} \right) \right]^N \quad (4.42)$$

in which

$$N = \frac{w_s}{\kappa u_f} \quad (4.43)$$

with c as the local, fractional volumetric suspended sediment concentration, c_a as the concentration at the reference level a above the bed, h the water depth, z the vertical coordinate and $\kappa = 0.41$ the van Karman constant. In case of non-uniform, transient flow due to waves or around structures, such an idealized description is nevertheless not sufficient, which is why the suspended load transport and concentrations have to be modeled directly by solving a concentration-balance equation resulting from mass conservation law.

In the present setup, the transport of suspended sediment particles in the fluid domain is solved using the advection-diffusion equation

$$\frac{\partial c}{\partial t} + \nabla \cdot [(\alpha_r \vec{u} + \vec{w}_s) c] = \nabla \cdot (D_\nu \nabla c) + S_c \quad (4.44)$$

with α_r being the VOF ratio coefficient (see §4.2.1), \vec{u} and \vec{w}_s the fluid velocity and sediment settling velocity vectors, D_ν the diffusivity and S_c a source/sink term for entrainment and deposition further discussed below.

The diffusivity in the present implementation is calculated taking into account the concentration-dependent turbulent Schmidt number σ_c , which describes the ratio of viscosity and mass diffusivity as

$$D_\nu = \frac{\nu_t}{\sigma_c} \quad (4.45)$$

Regarding this number, Amoudry et al. (2005) (and van Rijn (1984c) therein) estimate a reasonable value range of 0.3 to 1.0. In their investigations, typical values of 0.7 close to and 0.5 far from the bed could be found. As a similar, bed-distance dependency is typically found in the concentration distribution, this led to the formulation of a concentration-dependent (and therefore distance-dependent) Schmidt

number. According to the authors, the “Schmidt number is expected to increase with the concentration because of the dynamic effect of the sediment itself, making it more difficult for sediment to be diffused”, and might therefore be calculated using the approach

$$\sigma_c = \sigma_{c0} \left(1 - \frac{c}{c_0}\right) + \left(\frac{c}{c_0}\right)^{q_c} \quad (4.46)$$

where c_0 is the maximum possible sediment concentration, q_c a power law coefficient and σ_{c0} an empirical constant. The authors propose a value of 0.5 for q_c and 0.39 or 0.40 for σ_{c0} , depending on if either the reference concentration approach or the pick-up function approach is chosen, see §4.3.3 below. According to the authors and Fredsøe and Deigaard (1995), the maximum possible sediment concentration in the fluid is taken as 0.65, corresponding to firm packing of the particles which suppressed free motion.

The equation (4.44) is a passive scalar transport equation, i.e. the sediment suspension is modeled as being passively transported by the flow without further interaction. It is therefore assumed that the development of the flow field itself is not influenced by the suspended sediment particles in the water column. According to Wu (2004), this is an assumption made in most of the existing sediment transport models, which is generally valid as the suspended sediment concentration is typically low and the bed load layer containing these concentrations typically stays very thin. Depending on the erosion, transportation and deposition processes and therefore changes in the bed surface, suspended particles may nevertheless have an influence on the flow field due to the formation of ripples and dunes, or generally roughness elements. Such effects are typically taken into account through the bed boundary conditions or, as in the current setup, through the topological changes from the overall sediment transport model.

Sediment Settling Velocity Besides the transport of suspended sediment particles with the flow field itself, the sediment settling velocity due to gravity action is one of the key parameters influencing the transport process. Following e.g. Jiménez and Madsen (2003), a wrong estimation of the settling velocity may result in an error with a magnitude of factor three or more regarding the suspended load transport computation, which shows the importance of choosing a reasonable value. Therefore, numerous investigations have been carried out by different researchers over the past decades, describing and quantifying the settling velocity of sediment particles, like Rubey (1933), Zanke (1977), Dietrich (1982), Graf (1984), van Rijn (1984c), Soulsby (1997), Jiménez and Madsen (2003), Camenen (2007). Formulas have mainly been developed based on laboratory experiments and as (semi-) empirical approaches, as in-situ data are generally difficult to collect and are therefore scarce. In earlier works, the assumption has been made to take the single grains as spheres and de-

rive a formulation for this ideal situation. However, settling velocities for natural sediments, which in most cases clearly differ in their shape from ideal spheres, are mainly lower due to higher resisting forces.

Under the assumption of a single sediment particle under equilibrium conditions, i.e. being at rest in the flow field, agitating and stabilizing forces due to gravity and buoyancy must be balanced, therefore leading to the general formulation

$$s_{sg}\rho g \frac{\pi}{6}d^3 = \frac{1}{2}\rho c_D \frac{\pi}{4}d^2 w_{s0}^2 \quad (4.47)$$

from which the settling velocity of a single particle may be derived as

$$w_{s0} = \sqrt{\frac{4s_{sg}gd}{3c_D}} \quad (4.48)$$

with c_D being the drag coefficient depending on the grain Reynolds number Re_s given as $Re_s = w_{s0}d/\nu$. For natural sediment grains, the relationship between c_D and Re_s is effected by the shape and roundness of the particle, which might be described as the relationship between the lengths of the particle along its axes.

In the present model, the formulation of Jiménez and Madsen (2003) for the calculation of the (single grain) settling velocity has been chosen. It was mainly derived from previous investigations of Dietrich (1982) by reformulation and fitting of the data, taking into account the sediment diameter and density, the shape factor and the roundness of the particles as input parameters. The formulation has been developed for grain sizes between 0.063 and 1.0mm and is therefore only strictly valid in this range. It was however shown by the authors that it might be applicable for grain sizes up to 2mm as well, giving better or at least comparable results than other, simpler settling velocity formulations.

The dimensionless sediment settling velocity W_* , out of which the settling velocity w_{s0} might be derived is then calculated as

$$W_* = \frac{w_{s0}}{\sqrt{s_{sg}gd_N}} = \left(A_w + \frac{B_w}{S_*} \right)^{-1} \quad (4.49)$$

with

$$S_* = \frac{d_N}{4\nu} \sqrt{s_{sg}gd_N} \quad (4.50)$$

being the dimensionless particle diameter, d_N the nominal diameter of the particle (diameter of a sphere with equal volume) and A_w and B_w being some dimensionless formula coefficients as functions of the shape and roundness factors according to Dietrich (1982). For naturally worn quartz sands, typical values of $A_w=0.954$ and $B_w=5.12$ are proposed, corresponding to a shape factor of 0.7 and a particle roundness factor of 3.5. For the determination of the nominal diameter d_N from

the commonly used sieve diameter d_s , the relationship $d_s/d_N \approx 0.9$ according to Raudkivi (1990) can be applied.

Concentration- and Fluid-Dependencies When regarding suspended sediment transport processes with higher sediment concentrations in the water column and in the near-bed region, particles counteract and influence each other, leading to reduced settling velocities compared to single particles. Following the experimental work of Richardson and Zaki (1954), the relationship between the single and 'group' settling velocities due to the local concentration can be taken as

$$\frac{w_s}{w_{s0}} = (1 - c)^{n_c} \quad (4.51)$$

with w_s and w_{s0} being the concentration-dependent and single grain settling velocities, respectively, c the fractional volumetric concentration and n_c being a power coefficient depending on the grain Reynolds number:

$$\begin{aligned} n_c &= 4.35Re_s^{-0.03} & Re_s < 1 \\ n_c &= 4.45Re_s^{-0.10} & 1 \leq Re_s < 500 \\ n_c &= 2.39 & 500 \leq Re_s \end{aligned} \quad (4.52)$$

It has to be noted that in the original formulation of Richardson and Zaki (1954), equation (4.52) is limited to $Re_s > 0.2$ as the lower boundary, but was further extended for the present implementation.

In the two-phase VOF approach, the local sediment settling velocity differs depending on the fluid properties, i.e. density and viscosity, where the two phases are identified by the VOF ratio coefficient α_r . As no sharp interface between the two fluids is existent due to the VOF model approach as given in §4.2.1, a blending approach has been chosen to calculate the local, fluid-dependent settling velocity:

$$\vec{w}_s = \alpha_r \vec{w}_{s,w} + (1 - \alpha_r) \vec{w}_{s,a} \quad (4.53)$$

with $\vec{w}_{s,w}$ and $\vec{w}_{s,a}$ being the local settling velocities in water and air, respectively. Although it has been discussed in Jacobsen (2011) that the above, linear dependency of the settling velocity from the VOF ratio coefficient might result in rather large changes of \vec{w}_s even for small changes in α_1 , the chosen approach nevertheless gives reasonable results for the present investigations. In the modeled scouring and transport processes, no significant fluid mixture takes place in the water column and esp. in the bed boundary area with high suspended sediment concentrations, where in the 'mixing zone', i.e. at the water surface $c \approx 0$ and therefore a resulting divergence is negligible.

In the present implementation, the concentration- and fluid-dependent settling

velocities \vec{w}_s are calculated within the hydrodynamic module using eqs. (4.51) to (4.53) every single time step and for every fluid domain cell, with explicit treatment for equation (4.51).

Entrainment and Deposition As the sediment transport is modeled on different parts of the computational domain due to process splitting, an interface between the two components is needed. This is achieved by specifying quantities of the total flux of suspended sediments from the bed into the fluid domain and vice versa using appropriate near-bed boundary conditions. Different approaches for the calculation of entrainment and deposition of particles have been developed by different authors over the past years and can be found in literature.

They mainly describe the particle exchange as the flux over the boundary between the hydrodynamic model domain and the bed, i.e. where suspended transport and bed load transport takes place, respectively. A slightly different approach which is used in the present setup is to consider the exchange of particles using a source/sink term at the lowermost computational cells of the fluid model domain, which is located just above the bed boundary then. The source/sink term S_c in equation (4.44) therefore describes the difference between entrainment fluxes E and deposition fluxes D of suspended sediment as

$$S_c = E - D \quad (4.54)$$

Similar approaches have successfully been used e.g. in Lesser et al. (2004), Wu (2004) and Warner et al. (2008).

Boundary Location As the sediment concentration near the bed rapidly decreases with distance from the bed, a proper choice of the boundary location is needed. In empirical approaches, the boundary is typically located directly at the interface between the bed and the inner nodes, i.e. the lowermost faces of the computational cells or at some particle-related distance above, while typically values around $2 \cdot d_{50}$ are taken then. This approach may however not be completely correct in cases of high shear stresses when sheet-flow occurs, as a layer of bed material with a thickness of several grain diameters then moves with the flow. According to Wilson (1966) and Wilson (1977), this layer thickness depends linearly on the value of θ , which makes it difficult to define a concrete reference level in that case. According to the author, sheet-flow might occur at values of $\theta > 0.8$. As will be seen in the numerical scour simulations given later, this critical value will be locally exceeded under certain conditions. In addition, the Shields parameter will strongly vary in space and time under non-uniform flow conditions and especially in case of scouring processes. For the present setup, it has therefore been chosen not to

determine a concrete reference level or boundary location, but to assume one with a certain thickness that coincides with the location of the source/sink term in the model domain given above.

Reference Concentration Approaches The predominant number of existing approaches for suspended sediment entrainment from the bed into the flow give an estimation of the so-called reference concentration c_b at the reference level z_b , i.e. the boundary location above the initially undisturbed bed. The entrainment rate is then calculated under the assumption of equilibrium conditions under upward and downward directed fluxes due to erosion and deposition. Empirical approaches have e.g. been developed by Einstein (1950), Engelund and Fredsøe (1976), Smith and McLean (1977), van Rijn (1984c) or Zyserman and Fredsøe (1994).

In model implementations, mainly two different approaches for the calculation of the final entrainment rate E can be found:

- The first one uses the concept of turbulence diffusivity and therefore sets the flux as $E = \nu_t \partial c / \partial y$ with ν_t as either the turbulent viscosity or the sum of turbulent and kinematic viscosity, e.g. found in Brørs (1999), Liang et al. (2005) and Jacobsen (2011).
- The second one sets the flux as $E = c_b w_s$ under the assumption of equilibrium conditions, e.g. given in Garcia and Parker (1991).

The latter approach has been chosen for the present implementation, where w_s is the group settling velocity given in eq. equation (4.51).

Sediment Pickup Approach A different approach, where the entrainment flux E can be directly calculated from given quantities without knowledge of a reference concentration is the one given in Nielsen (1992). It is based on the approach of van Rijn (1984a) but has been modified for unsteady flow conditions, as Nielsen (1992) states that an equilibrium concentration as originally assumed is typically not given when regarding scour formation processes or unsteady flow situations. A drawback of the pickup approach is however the fact that it is not bounded in the upper flux region. In cases of very high local shear stresses, this might result in unphysical and unreasonable, enhanced sediment pickup rates. For the present investigations, the maximum sediment flux has therefore been bounded: for the reference concentration approach, Fredsøe and Deigaard (1995) give a value of $c_b = 0.35$ as a reasonable maximum concentration. The maximum sediment pickup is consequently bounded to $0.35w_s$ in the current setup in case of larger flux values.

Survey of Approaches A survey of several reference concentration and pickup approaches for sediment entrainment, which can be found in various numerical model

applications in literature, is given in the following:

- Fredsøe and Deigaard (1995):

$$c_b = \frac{0.65}{(1 + 1/\lambda)^3} \quad (4.55)$$

$$\text{with } \lambda = \left[\kappa^2 a^2 \frac{(\theta - \theta_c - \frac{\pi}{6} \mu_d p_{EF})}{0.013 s \theta} \right]^{0.5}, \quad a = 2, \quad p_{EF} \text{ given by equation (4.40).}$$

- Zyserman and Fredsøe (1994):

$$c_b = \frac{A (\theta - \theta_c)^n}{1 + \frac{A}{c_m} (\theta - \theta_c)^n} \quad (4.56)$$

$$\text{with } A = 0.331, \quad n = 1.75, \quad c_m = 0.46$$

- Nielsen (1992):

$$E = p(t) = 0.0033 \left(\frac{\theta - \theta_c}{\theta_c} \right)^{1.5} \frac{s_{sg}^{0.6} g^{0.6} d_{50}^{0.8}}{\nu^{0.2}} \quad (4.57)$$

- van Rijn (1984c):

$$c_b = 0.18 c_m \frac{S_0}{D_*} \quad (4.58)$$

$$\text{with } c_m = 0.65, \quad S_0 = \frac{\theta}{\theta_c} - 1, \quad D_* = d_{50} \left[\frac{s_{sg} g}{\nu^2} \right]^{1/3}$$

The single, empirical approaches have mainly been developed using different data sets for compilation and fitting, for which reason certain deviance in a direct application can be expected. It finally has to be mentioned that the approaches have been developed for non-cohesive sediments only. Approaches for cohesive sediments can e.g. be found in Amoudry (2008).

Regarding the different approaches, neither reference concentration nor pickup approaches have generally been found to give better results in suspended sediment concentration prediction, see the works in Davies and Li (1997). For this reason, a direct comparison of several approaches with regard to scour development in the present numerical model has been carried out and will be discussed later in §5.4.1.

Deposition of Suspended Load The deposition of suspended particles is calculated by $D = c(\vec{u} + \vec{w}_s) \vec{N}$ in the present model, i.e. taking only the face normal components of the fluid flow and sediment settling velocity vectors into account. For determination of D , knowledge of the concentration at the bottom boundary is needed. For the present model setup, c is taken as the concentration in the low-

ermost computational cells above the bed boundary, corresponding to an interface location within the computational cell.

Upper Boundary Conditions Regarding the boundary condition at the free surface, the total flux must be zero here. In the present setup, there is however no clear interface due to changing wave surface profiles and the applied VOF approach. Therefore, no direct no-flux boundary condition can be prescribed. The criterion of zero flux is however fulfilled, as $w_{s,0} \gg w_{s,1}$, i.e. the particle settling velocity in air is typically much larger than in water, preventing particles to be raised from the water column. At the atmospheric domain boundary, the sediment concentration is however defined as zero using Dirichlet boundary condition.

Time Stepping Approach The equation (4.44) is solved using a smaller, inner time step compared to the time step of the global hydrodynamic model calculation. Due to relatively large sediment settling velocities with their component in vertical downward direction and therefore mainly perpendicular to the bed boundary with comparatively flat cells in this region, taking the time step from the hydrodynamic model would typically result in Co numbers $\gg 1$. Therefore a time stepping approach is used, where equation (4.44) is solved with an (inner) time step several times per (outer) time step from the hydrodynamic model, with inner Co being < 0.75 . This approach is feasible, as the sediment settling velocity is independent of the flow field itself, i.e. there is no strict dependency from the quantities.

4.3.4 Sediment Boundary Conditions

In addition to the general boundary conditions associated with the fluid flow model, boundary conditions for both bed load q_b and suspended load c have to be specified for the 2D and 3D domain, respectively. At the inlet, both quantities are typically set to zero, which corresponds to clear water conditions and flow over fixed ground. None-zero conditions can however be specified if a sediment feeding rate is given and known. Both quantities are set as zero gradient at the outlet and c is further set to zero at the atmosphere boundary. At solid walls, i.e. flume walls and objects, both q_b and c are set as zero flux conditions. The boundary conditions for the bed are directly described by the entrainment and transport approaches given above.

4.3.5 Morphological Update

The sediment transport processes lead to morphological changes in the bed level in case of a local imbalance between erosion and deposition of material. Therefore, a bottom evolution equation describing sediment continuity is solved over the bottom domain. The bottom evolution equation generally describes the mass conservation

of sediment in an arbitrary control volume, in this case the computational faces of the bottom bed domain. If more sediment is going into the control volume due to sediment fluxes, the geodetic height is rising and vice versa. In the present setup, the Exner equation for sediment continuity is solved, see Exner (1925), which is given here as

$$\frac{\partial h}{\partial t} = -\frac{1}{1-n} [\nabla \cdot \vec{q}_b - E + D] \quad (4.59)$$

with h as the local geodetic bed level height, n the bed porosity taken as 0.4 in the present setup, \vec{q}_b the bed load transport flux and E and D the fluxes from the suspended transport model. The input therefore results exclusively from the divergence term and the source terms on the right-hand side.

It has to be noted that the general limitation of the equation to continuous sediments neglects the natural characteristics of single grains, as discrete masses (grains) are regarded as a continuum here. It might therefore happen that local height changes occur, which are even smaller than the available grain sizes, however giving a mean change of the regarded bed area. As every single change in mass directly results in a change of geodetic height, direct consideration of firm packing of sediments is neglected. This is nevertheless somehow accounted for using the bed porosity factor n . It is further assumed that there is always sufficient material available in the bed layer to fulfill the prescribed sediment mass transport.

Other model implementations not applying equation (4.59) are generally available, which include additional terms to account for changes in grain fractions due to disaggregation, which are then considered using sink terms, see e.g. Li et al. (2008).

Filtering of Bed Elevation Changes As the Exner equation takes the form of a nonlinear hyperbolic scalar equation accounting for the effect of bed formation and migration processes, numerical instability issues may occur. Investigations on this issue have e.g. been carried out by Jensen et al. (1999), Callaghan et al. (2006), Kubatko and Westerink (2007) and Long et al. (2008), where countermeasures mainly consist of either numerical filtering of the solution or the choice of a proper numerical solution scheme in order to suppress spurious oscillations.

In order to minimize numerical errors in the bed evolution, a numerical filter approach similar to the idea given in Jensen et al. (1999) has been incorporated here in between solving of equation (4.59) and finally applying the moving mesh procedure to the bottom bed geometry. The filter works as a smoothing of the local bed elevation changes, spatially in the order of the grid size, by applying a filter operator of the general form

$$\tilde{z}_i = k \cdot z_i + m \cdot z_{j\dots n} \quad (4.60)$$

and finally taking differential values, while in the above equation, k and m are variable factors with the restriction that $k + m = 1$, z_i is the geodetic height of point i and $z_{j\dots n}$ gives the mean value of the direct neighbor points $j\dots n$ of point i . In detail, the filter procedure for every mesh point of the bed boundary grid to filter bed elevation changes $h_i \rightarrow \hat{h}_i$ is implemented as:

1. In a first filter step, the filtered value of the new (temporary) point coordinate including local bed elevation change after equation (4.59) is calculated as

$$\tilde{z}_i = 0.65(z_i + h_i) + 0.35(z_{j\dots n} + h_{j\dots n}) \quad (4.61)$$

2. In a second filter step, results from 1. are again filtered with the (temporary) point coordinates from neighboring points by taking

$$\bar{z}_i = 1.35\tilde{z}_i - 0.35\tilde{z}_{j\dots n} \quad (4.62)$$

3. Afterwards, the bed elevation change \hat{h}_i as the result of the filtering procedure is finally calculated by taking differential values of the form

$$\hat{h}_i = \bar{z}_i - z_i \quad (4.63)$$

however only in the case of

$$|(z_{j\dots n} + h_{j\dots n}) - z_i| > \frac{1}{8}\bar{d}_{xy} \quad (4.64)$$

where \bar{d}_{xy} gives the mean value of distances from point i to the neighbor points $j\dots n$ in x, y coordinates. This further restriction is incorporated in order to filter only bed elevation changes above a certain, grid-dependent threshold, as otherwise local effects of bed changes get smeared out.

The limitation of the filter to the direct neighbors of each point ensures that only local disturbances of the order of the grid size are filtered here, without additional effects from further points of the bottom bed grid. It however has to be noted that the given method is only strictly valid in terms of mass conservation when equally spaced bed grids are used.

4.3.6 Sediment Sliding on Large Bed Slope

Due to bed load and suspended load processes, changes in the local bed slopes are evident and might reach large values especially in the case of local scour formation. When the local slope angle becomes that large that the inner frictional forces of the sediment particles cannot withstand the outer force of gravity acting on the

particles, sediment sliding occurs while shifting single particles or conglomerations from higher to lower locations of the bed.

This is typically the case when the angle of repose is exceeded, which can therefore be taken as the threshold value of sediment sliding. Experimental works on cylinder scours given in Roulund et al. (2005) however show that a slight exceedance $\Delta\varphi$ of the friction angle by about 2° typically occurs before a sliding begins. The procedure finally stops at angles of 2° below the friction angle afterwards. Experimental investigations on cylinder scour in Zanke (1982b) and later given in Zanke et al. (2011) have furthermore shown that the friction angle might even be exceeded by further few degrees in case of high flow velocities and with a flow direction opposite to the slope direction in a scour hole in front of a vertical cylinder as a stabilization of the sediment occurs here.

In numerical scour models, the implementation of a slope limiter and an appropriate sediment sliding procedure is mandatory, as a quickly growing slope angle in case of scour hole formation otherwise leads to unphysically large values of sediment transport fluxes due to the absence of limiting parameters in the original transport formulations. The latter is due to the fact that the majority of formulations has been developed for horizontal beds only.

A number of different ways have been introduced and can be found in literature to model the sediment sliding procedure, i.e. transport from higher to lower points down the bed slope while ensuring mass conservation. Model implementations are mainly based either on rising and lowering neighboring mesh points, e.g. Niemann et al. (2011), solving the bottom evolution equation based on iterative shifting, e.g. Göthel (2008) or using artificial transport rates while solving the bottom evolution equation, e.g. Roulund et al. (2005).

For the present setup, a method based on the approach of an artificial transport rate formulation has been implemented, where the procedure of iterative shifting is as follows:

1. For all faces of the computational bottom boundary grid, the actual slope angle β is calculated.
2. If β exceeds
 - (a) the value of maximum slope, i.e. the angle of repose $+2^\circ$ or
 - (b) the angle of repose -2° and the computation face has been marked as 'sliding' in the previous iteration,

the current bed face gets a marking flag identifying that a sliding procedure is currently taking place.

3. For all faces marked as 'sliding', the bed slope direction \vec{s}_d is calculated in vectorial form. Afterwards, an artificial sliding parameter in terms of bed load flux is calculated as

$$\vec{q}_{b,s} = \frac{\vec{s}_d}{|\vec{s}_d|} s_f \cos \beta \quad (4.65)$$

in which s_f is an artificial sliding increase factor taken in the order of $\mathcal{O}(3.5)$ in the present setup. The term $\cos \beta$ is further incorporated to account for grid-dependency of the solution.

4. By incorporation of $\vec{q}_{b,s}$ into the bottom evolution equation and solving over the entire bottom bed domain, the local changes in bed level are finally calculated using the formulation of

$$\frac{\partial h}{\partial t} = -\frac{1}{1-n} [\nabla \cdot \vec{q}_{b,s}] \quad (4.66)$$

5. The aforementioned procedure is repeated until either none of the bottom bed faces holds a 'sliding' flag or the maximum number of iteration steps $n_{s,max}$ is reached, where a value of 50 has been chosen for the latter. In practical application, the number of iteration steps however is in a range of $\mathcal{O}(10)$.

The sediment sliding procedure is carried out in steps of $T = [0.5, 1]$, where T is the period of flow repeating as given in §4.5.

In addition to the aforementioned procedure, other methodologies have been further investigated in the present work, mainly based on the concept of incorporating external forces from the flow field into the formulation of the sediment sliding direction. This was carried out under the assumption that in case of strong flow effects, a modification of the sliding direction different from a simple downward-directed shifting is more realistic. Furthermore, the sediment sliding procedure typically takes more time than its is modeled with instantaneous shifting in numerical model time steps. As these implementations however did not stay completely numerically stable for all cases, the slightly simpler approach given above was finally chosen.

4.4 Moving Mesh Approaches

The feedback from local bed elevation changes due to scouring to the surrounding flow field and hence resulting changes in the flow situation is carried out by means of moving mesh approaches in the present model implementation. Thereby, $\partial h / \partial k$ (k as a time fragment, see §4.5 for the notation or $\partial h / \partial t$ in the general form) derived by solving of the Exner equation (4.59) serves as a direct input for movement of the bottom bed grid. Based on this as a boundary condition, the inner nodes of the computational domain are moved accordingly.

For the final setup of the present model, two different approaches have been implemented, which will extensively be described below:

1. A distance-based mesh motion function for selectable grid points
2. A mesh motion function based on Laplacian operator smoothing

Both methods have in common that the mesh motion is carried out in vertical direction only, which is a valid simplification for topological changes due to local scouring.

4.4.1 Distance-based Mesh Motion Function

In the first approach, the motion of bed boundary grid points and inner nodes of the computational domain is performed based on their particular distances to a defined distance surface patch in vertical (z) direction, see figure 4.7 for the definitions, i.e. a point displacement technique. In this manner, only those grid points located underneath the distance surface patch are selected for movement, which reduces computational costs on the one hand and ensures no mesh modification in upper regions, e.g. in the zone of wave amplitude. Furthermore, a selection of the movement region can be expanded to the horizontal direction (x, y).

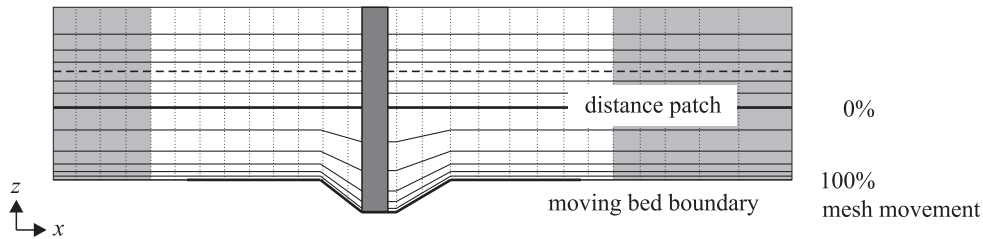


Figure 4.7: Sketch of the distance-based mesh motion functionality.

For every single grid point selected for movement, its modified vertical position z_p at time $k + 1$ (see §4.5) is calculated by use of a moving coefficient similar to the approach given in §4.2.7 as

$$\eta_m = \frac{z_p - z_b}{z_{max} - z_b} \quad (4.67)$$

with z_p as the actual vertical point position, z_b a corresponding point on the bed boundary grid and z_{max} the corresponding maximum value at the distance surface patch, both found by vertical projection of z_p coordinates. In equation (4.67), $\eta_m \in [0, 1]$. Finally, the new value is found by

$$z_p^{k+1} = z_p \eta_m + (1 - \eta_m) (z_p + \partial h) \quad (4.68)$$

In this manner, a complete mesh motion is achieved at the bed boundary grid, where no motion occurs at the distance surface patch.

As the mesh motion algorithm was intended to work with any unstructured grids, interpolation algorithms for projection of z_p onto bed boundary grid and distance surface patch, i.e. the procedure of determining z_b and z_{max} had to be found. Implemented algorithms are thereby mainly based on inverse distance weighted interpolation, i.e. Shepard's method as given in Shepard (1968).

The distance surface sketched in figure 4.7 does not necessarily have to be a horizontal plane, but can adopt any complex shape as long as the requirement of continuity of the surface is fulfilled. In this manner, more complex distance patch surfaces could be achieved by use of motion point searching functionality implemented for this purpose. Regarding the investigated tripod foundation structure, the distance patch surface e.g. follows the area under the braces and the main column as a selection of mesh motion points with maximum vertical position within the domain.

4.4.2 Mesh Motion Function based on Laplace Equation

In the second approach implemented here, the automatic mesh motion is based on Laplacian operator smoothing, i.e. a motion velocity approach. The concept is similar to that given in Liu (2008) and Jasak and Tukovic (2007), where the latter generally works for mesh motions in three-dimensional space and additionally uses a mesh decomposition technique. However, the motion is solely carried out in vertical direction here. The equation to solve for mesh motion in the entire model domain can therefore be simplified as

$$\nabla \cdot (\gamma \nabla v_z) = 0 \quad (4.69)$$

where v_z is a scalar quantity giving the vertical motion of the cells and γ is the diffusion coefficient. Mesh motion is generally solved at the cell centers and finally interpolated onto the grid points to determine the new positions. Solving of equation (4.69) at every time step k (see §4.5) needs some model boundary conditions, which are again given by $\partial h / \partial k$. Finally, the new grid cell and therefore the grid point positions z_p^{k+1} can be determined as

$$z_p^{k+1} = z_p + v_z \Delta k \quad (4.70)$$

Unlike in the work of Liu (2008), γ can be chosen as a spatially-variable and distance-based parameter used to control mesh motion especially in the area around objects.

4.4.3 General Remarks and Model Choice

It has to be noted that several built-in mesh motion algorithms are available in the OpenFOAM package, which are generally based on point displacement, point ve-

locity displacement or complex Laplacian operator methods. A comparison of such strategies can be found in Kassiotis (2008). Through thorough testing of available motion solvers, it was however found that none of the available strategies were capable of generating distortion-free meshes during scour simulation for the present investigations, as finally all methods led to simulation breakdowns. Therefore, the implementation of motion methods given above was inevitable for the present simulations.

A drawback of the approaches, which is however given in any other mesh motion technique, is the fact that the maximum vertical movement of the bottom bed grid is limited by the presence of any horizontal object, e.g. the lower braces in case of the tripod structure. Therefore no further mesh motion in positive vertical direction ($+z$) is allowed to take place after a certain distance threshold between actual bed position and lower surface locations of an object has been reached. In this case, the motion solver stops in order to avoid any mesh distortion occurring otherwise. Due to this procedure, the criterion of sediment mass conservation is however not fulfilled in that case. As a circumvention, the mesh motion procedure could be coupled with a sediment sliding procedure in that special case in order to fully ensure mass conservation. For the present investigations, such situations could however only be recorded in very special and extremely rare cases at the beginning of a scour development process for the tripod structure, for which reason no further countermeasures were directly investigated here.

In terms of setting up the numerical model, the mesh motion based on Laplacian operator smoothing has been found preferable over the first approach, which needs a certain higher amount of manual interaction. As the method as presently implemented in the code has however been found not to behave fully stable in parallel computations, the first strategy as given in §4.4.1 was finally applied for the present calculations.

4.5 Model Coupling

In the natural environment, a direct and continuous interaction takes place between hydro- and morphodynamic components. In numerical models, such a strict and direct coupling would however result in tremendous computational effort, which is why certain model simplifications might be required.

Typically, the hydrodynamic and morphological time scales differ in magnitudes, as overall bed elevation changes take place rather slowly in comparison to the natural, hydrodynamic flow behavior, especially in situations with high turbulence. Therefore, both processes are often modeled independently with only temporal interaction. Different types of couplings for morphodynamic models can be found in numerical transport models, ranging from weak coupling in terms of fluid vis-

cosity modifications, bed roughness changes and up to strong coupling in terms of computational bed and grid modifications with direct influence on the flow.

4.5.1 Present Coupling Procedure

In the present implementation, the hydro- and morphodynamic model coupling is carried out by means of a 'semi-strong' coupling procedure using computational domain grid changes as described in the previous sections. In contrast to a fully strong coupling procedure, where both hydrodynamic and morphodynamic equations are solved simultaneously within one solver at every single time step, the present coupling has some simplifications. Here, the hydrodynamic quantities serve as an input condition for the morphodynamic calculations, which then in turn evoke an update of the hydrodynamic field due to domain changes, while both sets of equations are solved in different solvers. A 'semi-strong' procedure was chosen here mainly in order to save computational time in long-term morphodynamic calculations. In contrast, a fully strong coupling leads to extensive computational costs and storage requirements. Furthermore, it is assumed that any uncertainties related to the choice of the sediment transport model (bed load and suspended load) are typically much larger than those caused by a simplified, semi-strong coupling method.

The present coupling procedure is as follows:

1. For a time span equal to a chosen flow period, i.e. the wave period in case of regular wave load or the period of flow separation around an object in case of steady current load generally described by the Strouhal number St , denoted as T in the diagram in figure 4.8, the hydrodynamic and turbulent quantities are solved within the two-phase flow solver using an adjustable time-stepping approach based on general Co criterion. At the same time, the suspended sediment transport taking place within the hydrodynamic model domain is solved at every single time step i , as required quantities for calculation of sediment entrainment and deposition are given by the hydrodynamic model.

For every time step i , quantities of $\vec{u}_{nw,\tau}$, E , D and τ_w are then stored in a time-averaged manner as fragments k of the wave period. Typically, fragment lengths of 0.05-0.1s have been chosen in the present work in order to capture all relevant processes in terms of maximum and peak values.

2. Afterwards, the bed load sediment transport \vec{q}_b is calculated for every time fragment k of the flow period. Results are mapped from the 3D fluid domain to the 2D bottom boundary grid and the Exner equation is solved.
3. Finally, results are mapped back from 2D to 3D and the mesh movement algorithm is applied for every single time fragment k over the entire flow period

T using the local bed elevation changes from the Exner equation as input boundary conditions.

Modifications in the flow field due to topological changes are afterwards calculated by repeating the calculation procedure starting with step 1.

As local bed elevation changes between the single flow periods have generally been found to be comparatively small, the calculations in steps 2. and 3. are typically carried out several times using the pre-calculated hydrodynamic and morphological quantities from 1., i.e. the hydrodynamic quantities are updated after the final mesh movement procedure in the present setup. So far, the number of such ‘repeating loops’ n has been manually chosen here, with typical values of 5 for steady current flow and 10-20 for wave load cases, while smaller values of 2-5 are chosen at the beginning of the simulations when local scours increase rapidly. If no such repeating is desired, the mechanism can however be circumvented by choosing appropriately small values for T and k . Finally, the calculation procedure is completed when an equilibrium stage of scour development is reached. So far, no direct criterion for an automatic determination has however been found, for which reason this situation is controlled manually by observation of the simulation results.

It has to be noted that before the complete sediment transport calculation starts, the hydrodynamic model is however run alone for a certain time span in order to achieve a stable flow situation first. For wave load cases, a time span of typically 10 wave cycles is chosen, while for current load cases, 20-30 periods of wake separation are taken.

4.6 Conclusions

For numerical investigations on flow and scour processes around offshore structures, a fully three-dimensional numerical model was developed and applied within the OpenFOAM software framework in the present setup, solving the Reynolds Averaged Navier-Stokes equations in combination with a $k-\omega SST$ turbulence closure model, while the free surface representation of water waves is ensured using the Volume of Fluid method. Wave, current and combined load conditions in the model domain can be generated on the basis of appropriate boundary conditions at the domain inlet and by wave damping at the outlet. Thereby, different types of regular waves, e.g. 2nd and 5th order Stokes wave theory can be simulated, while a wave generation and damping zone technique as given by Jacobsen et al. (2012) was finally applied. For wave spectra considerations, representative regular wave parameters were generated, while the corresponding translation coefficients result from scour considerations derived from the laboratory experiments in the WKS wave flume on scour investigations around the tripod structure.

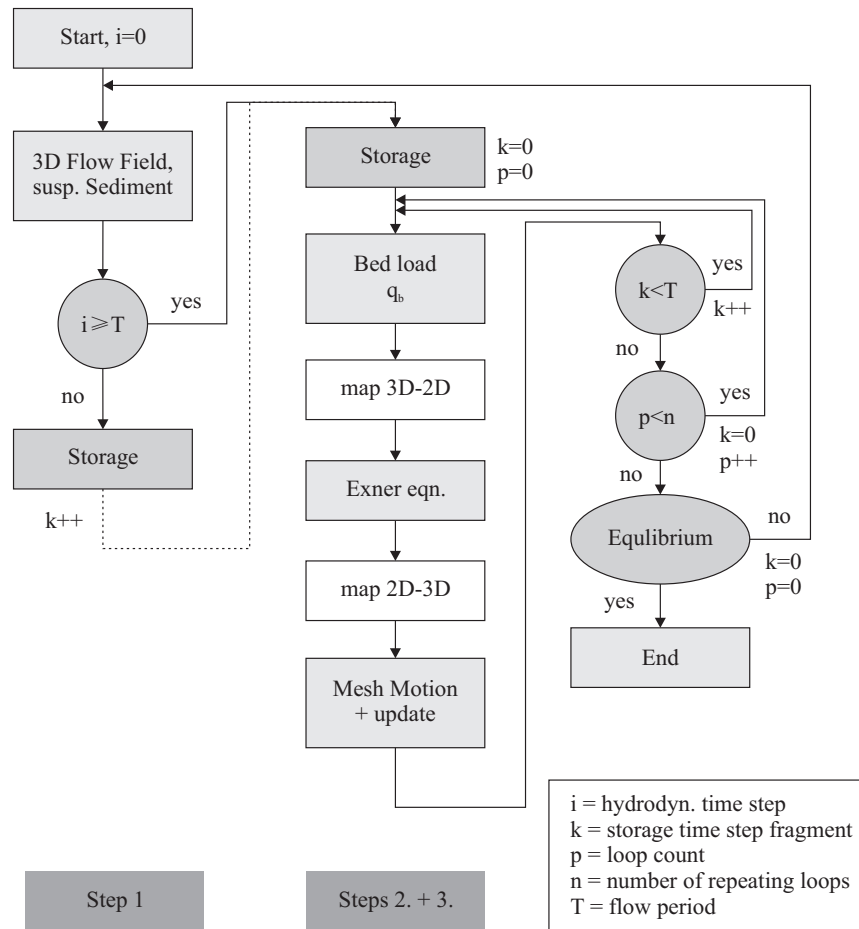


Figure 4.8: Flow chart of the flow field and sediment transport model coupling procedure during scour simulation process.

In order to capture the relevant sediment transport processes leading to local scour, a sediment transport model including both bed load and suspended load was implemented in the code. The description of acting forces on bed particles was carried out in vectorial form, including slope-dependent parameter modifications and a sediment sliding procedure to account for steep slope processes. For the bed load part, the approach of Engelund and Fredsøe (1976) was applied, while a new model approach for the suspended load part is chosen, see §5.4.1. Furthermore, new moving mesh approaches for inner domain grid motion were implemented in order to ensure numerical stability for investigations on complex foundation structure geometries. The hydro- and morphodynamic model coupling is carried out by means of a 'semi-strong' coupling procedure. As sediment transport and local scour processes typically need long-term simulations and are therefore very time-consuming, parallel code implementations and computations were applied throughout.

5 Numerical Model Application

5.1 General considerations

Results of different numerical simulations on hydrodynamic parameters, shear stress and final scour development are given and discussed in the following sections. Numerical results of the flow model are validated against both theoretical and experimental data on wave parameters and measured flow patterns around the tripod structure. As an application, shear stress distributions at the tripod for different load conditions are investigated. The implemented sediment transport model approach is finally applied to the simulation of scour development for different structures under wave and current flow. In a first step, the model is validated against experimental and numerical data for a vertical cylinder under steady current load. In a second step, scour development around the tripod structure under waves is simulated.

5.2 Model Verification

5.2.1 Wave Modeling

When modeling wave conditions as load parameters on foundation structures, in turn resulting in local scour formation, a sufficiently correct numerical wave model is one of the input requirements for present investigations. In the present numerical setup, waves are generated using a generation zone approach as given in §4.2.6, while the domain inlet boundary is located at $x = -6.0\text{m}$, with $x = 0.0\text{m}$ being the location of the tripod structure.

Results of numerical simulations given in the following are based on wave parameters equal to the experimental setup in test case r2130-01 (table 3.4), i.e. using wave parameters of $H_m = 0.205\text{m}$, $T_m = 3.0\text{s}$ and $d = 0.75\text{m}$ as regular waves, using a wave theory of type 5th order Stokes. A time period of ten wave cycles was run before data were compared in order to ensure fully developed flow conditions.

Determination of Free Surface Location In numerical modeling using the VOF method, there is typically no sharp interface between the two modeled, immiscible fluids as it is for the physical nature. The location of the free surface therefore lies between two points (cell mid points) holding values of $\alpha_r = 0$ and $\alpha_r = 1$. Due to the surface capturing method used in the present OpenFOAM setup, see §4.2.1, diffusion and therefore smearing of the interface occurs, which results in several cells around the fluid interface η holding values in the range of $\alpha_r \in]0, 1[$. The amount of cells depends on the chosen surface compression factor and typically lies in a range of three cells holding values of $0.9 \geq \alpha_r \geq 0.1$ for the present setups. The location of the interface is found using linear, distance-based interpolation between

two neighboring points (cell values) found at the locations of $\alpha_{r,0}$ and $\alpha_{r,1}$ with $\alpha_{r,0} \leq \alpha_{r,\eta} \leq \alpha_{r,1}$. For the present setup, a value of $\alpha_{r,\eta} = 0.45$ has been chosen due to best agreement of surface wave profile locations with theoretical locations.

Surface Elevation A comparison between numerical model data and experimental wave parameters depicts whether equal load conditions are generated in both setups. This is particularly essential for the present case, as wave load conditions in the numerical model are generated using surface elevation and velocity components based on wave theory instead of experimental data due to an absence of the latter in detailed form. Surface wave profiles in the WKS flume experiments were conducted using wave gauges at different locations as given in §3.2.1.

For comparison, a representative surface profile for one wave cycle, i.e. $T = 3.0$ s in the present case was generated by averaging over more than 200 measured wave cycles for wave gauge No. 3 (see figure 3.1), which is located at $x = -4.0$ m in front of the tripod location. Averaging of data was necessary as waves generated in numerical models ideally are not subject to any fluctuations. Under the assumption that the wave profile in the experiments is not influenced by the tripod itself and no significant profile transformation takes place over the distance of 4m, the representative surface profile is compared to numerical results at the location $x = 0.0$ m (main column axis) without tripod installation in the model, i.e. in the undisturbed case. Results are given in figure 5.1.

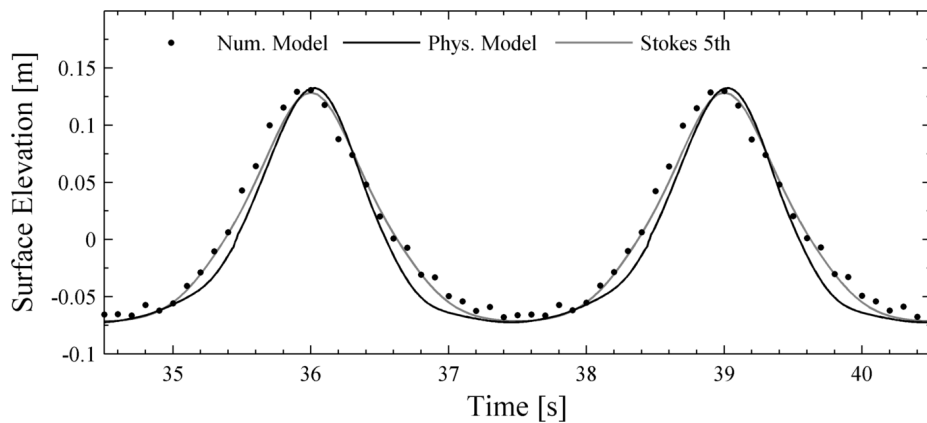


Figure 5.1: Comparison of surface elevation between model results, laboratory experiments and wave theory at location $x = 0.0$ m (main column axis).

The comparison shows that an overall good agreement between experimental data and numerical results could be obtained, especially regarding maximum and minimum surface displacements. Moreover, wave asymmetry is reproduced well in the model. Certain discrepancy can however be observed regarding the wave troughs, as profiles are steeper in the numerical model, which however results from the direct representation using Stokes 5th order wave theory. It should finally be

noted that surface fluctuations at the wave troughs in the numerical model are due to the determination procedure of the free surface location.

Velocity Distribution No direct orbital velocity measurements in the undisturbed case are available from the laboratory WKS experiments. Therefore, comparison of velocity components is carried out based on theoretical values in order to investigate wave propagation in the model. Profiles are given for horizontal components u in figure 5.2 for five different time steps 0.5s, 1.5s, 2.25s, 2.7s and 3.0s, in which the latter is the moment of wave crest passage at location $x = 0.0\text{m}$ (main column axis) without tripod installation. As input, regular waves of type 5th order Stokes were generated as given before.

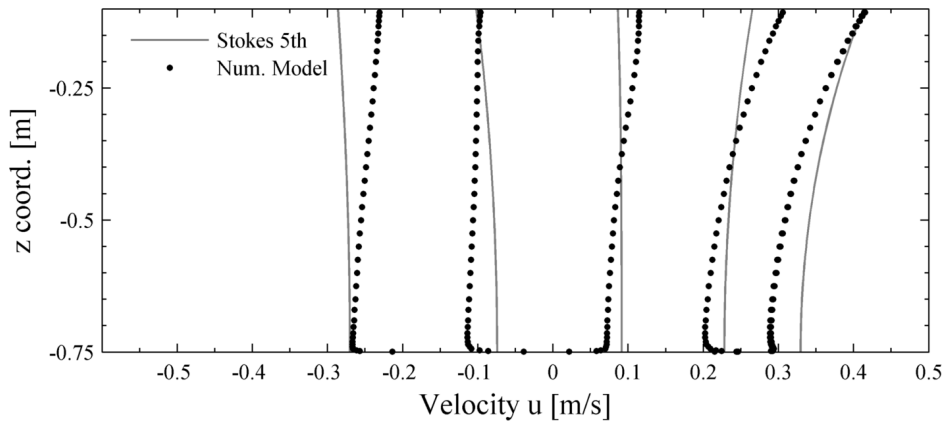


Figure 5.2: Comparison of theoretical and modeled horizontal velocity profiles at location $x = 0.0\text{m}$ (main column axis) for one wave passage. Times from left to right: 1.5s (wave trough), 2.25s (zero-crossing), 0.5s, 2.7s and 3.0s (wave crest).

The overall velocity distribution of modeled waves follows the theoretical profiles very well. Differences between modeled and theoretical profiles are in a range of 1-12% in the lower region, partly up to 30% at flow reversal, which however results from a certain phase shift that could be observed in the given case. The general wave asymmetry is clearly shown in the velocity distribution, resulting in larger flow velocities under the wave crest.

Near the bottom, wave profile shapes differ from theoretical considerations giving high velocity gradients at the wall, which could however be expected due to formation of the wave boundary layer. Some discrepancy can be observed at greater distances from the bed, i.e. reaching the free surface, where a general forward-directed flow acceleration is given. This mainly results from the applied combination of turbulence modeling and given VOF approach implementation, where the latter leads to high flow velocities at the free surface interface and could not be fully avoided in the present setup. The shear stress under the wave crest is calculated as 0.57N/m^2 , which gives a difference of 6% compared to the theoretical one after §2.3.1.

5.2.2 Local Flow Characteristics around Tripod Structure

The local flow characteristics around the tripod structure have been recorded by means of ADV measuring data in the laboratory WKS experiments as given in §3.2. It is therefore obvious to compare those experimental data with numerical results derived from the two-phase flow model in order to analyze the general validity of the model in terms of local flow characteristics.

As the amount of recorded data is not large enough to derive surface plots from given measuring points, results are compared for single point locations 1, 3, 7, 9, 11 and 14 (see figure 3.5, crosses) around the tripod structure over one wave period instead, given for each velocity direction u, v, w (x, y, z) in figures 5.3 to 5.5 and C.1 to C.3, respectively. For reason of clarity, velocity profiles are given at the two vertical positions $z_1 = -0.74\text{m}$ and $z_2 = -0.25\text{m}$ only, i.e. over ground and under the wave surface profile, which give the lowermost and uppermost positions available in the data sets.

Position 3 is located in the flume x axis directly behind the tripod main column, holding coordinates of $x = 0.13\text{m}$ ($0.87D_{mc}$ with $D_{mc} = 0.15\text{m}$ as the main column diameter) and $y = 0.0\text{m}$. At this position, formation of large eddies due to flow separation and following flow merging in the rear of the main column takes place near the surface at the time right after wave crest passage (36s), resulting in maximum velocities up to $0.4 - 0.5\text{m/s}$. Velocities in vertical downward direction are slightly higher than in the undisturbed case. Near the bottom, reverse directed flow in u direction can be observed at the same time. As expected, flow velocities in the direction perpendicular to the direction of wave progression are around zero due to flume and structure symmetry.

Position 7 is located directly behind the rear pile, at coordinates of $x = 0.27\text{m}$ ($1.8D_{mc}$) and $y = 0.21\text{m}$ ($1.4D_{mc}$). Flow separation and consolidation therefore occurs here, resulting in increased v velocity values up to 0.3m/s and damping in x direction for the near-bed flow.

Furthermore, measuring position 14 is located near the front pile at $x = -0.35\text{m}$ ($-2.3D_{mc}$) and $y = 0.09\text{m}$ ($0.6D_{mc}$). As can be seen from given velocities in u direction, curves are nearly congruent for both vertical positions, i.e. the near-bed velocity is nearly uninfluenced by the structure at the time of wave crest passage. Certain increase of flow velocity is however given at the passage of wave crest due to flow separation and acceleration at the pile. This pattern can further be observed when regarding the velocity component in v direction.

As can be seen from the figures, the overall agreement between experimental data and numerical model results is clearly good. Regarding absolute values, some minor deviation can be observed for maximum values esp. at position 3 and due to certain phase shift. Furthermore, velocity fluctuations as can still be found in

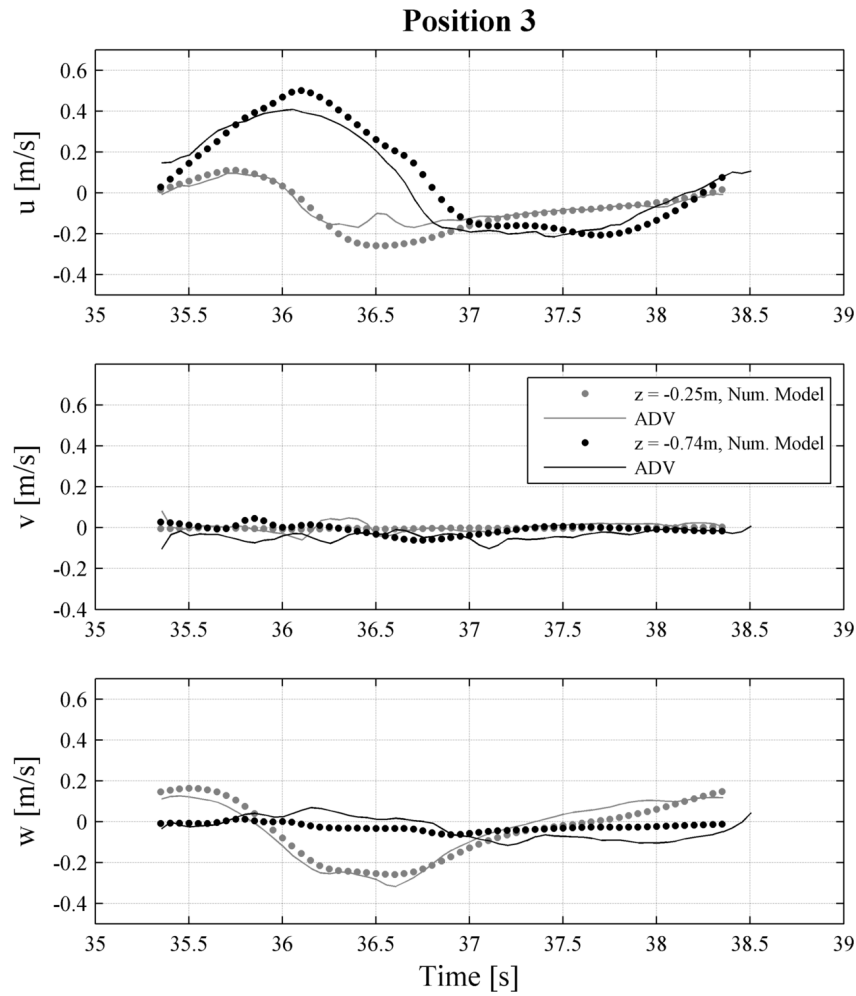


Figure 5.3: Comparison of local flow components in numerical model and experiment at position 3 around tripod structure.

the ADV data are not given in the model, which however results from the applied turbulence formulation itself. Despite this, the model is capable of capturing all relevant flow processes near the free surface and, which is of even more importance, in the near-bed region.

5.3 Results of Flow and Shear Stress Calculations

The final application of the present flow and scour model is given in the following sections. First, the flow patterns around the tripod structure under waves are investigated and resulting shear stress calculations for different load combinations are given. Finally, the model is applied to the numerical simulation of scouring processes. Boundary condition parameters for the tripod investigations thereby used are given in table 5.1.

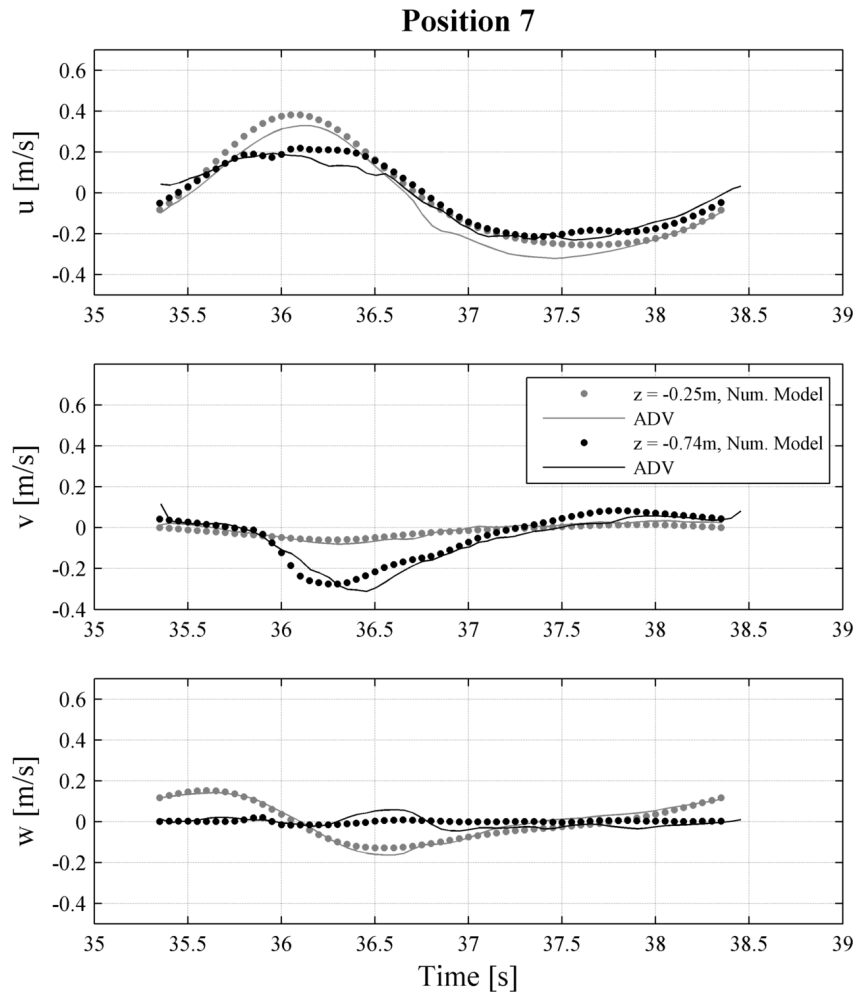


Figure 5.4: Comparison of local flow components in numerical model and experiment at position 7 around tripod structure.

5.3.1 Flow Field around Tripod under Waves

In addition to the general description of the flow characteristics around the tripod foundation under wave load as given in the context of the laboratory experiments in §3.2.4, the complex flow field was further analyzed in terms of numerical methods. In contrast to the laboratory tests, where information was gained in temporally and spatially limited form only, the numerical flow model has the advantage of giving an entire flow field description, which makes it possible to further analyze locations that could not be measured in the experimental setup.

To determine the local flow processes around the structure and especially in the near-bottom region finally leading to erosion and deposition processes, load conditions for test series r2130-01 given in the WKS flume experiments were simulated in the model, denoted as w2130-01 in the following. Wave parameters are given in table 5.1, the water depth was 0.75m. Snapshots of the local flow field as cross

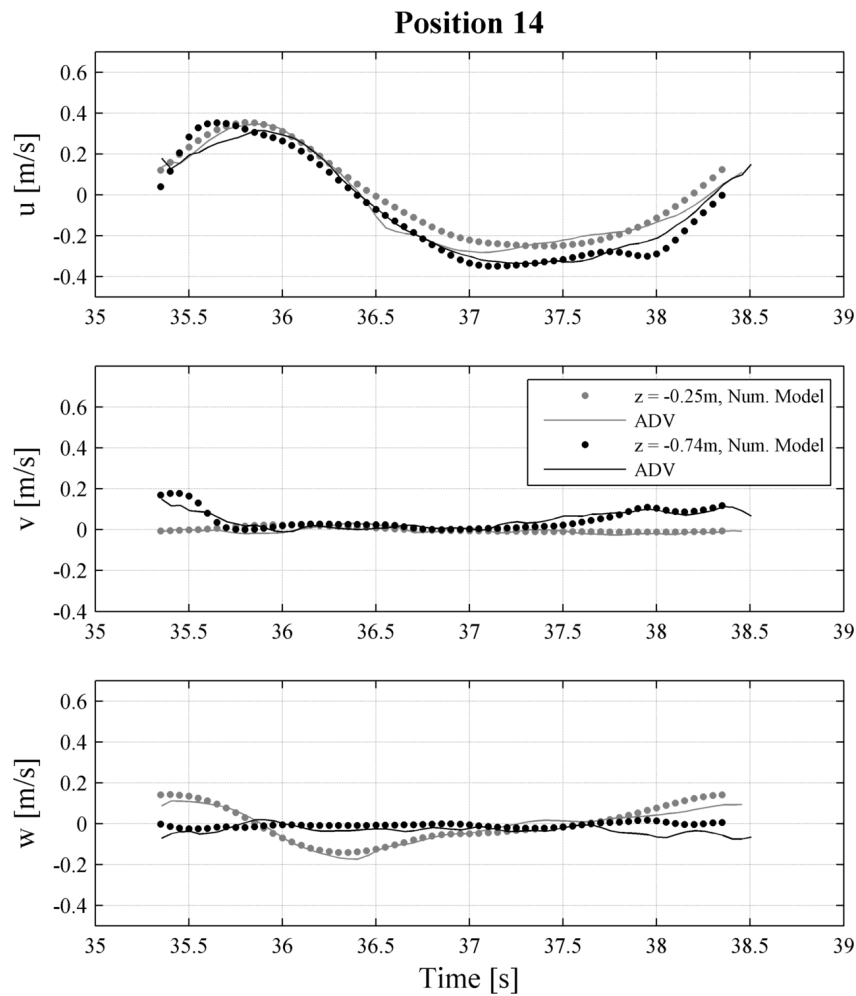


Figure 5.5: Comparison of local flow components in numerical model and experiment at position 14 around tripod structure.

sections through both the numerical flume and the structure are given in figures 5.6 to 5.9 for the moments of wave crest (0.0s), zero crossing (0.75s), wave trough (1.5s) and following zero crossing (2.25s) passage at the tripod center. Cross sections are given at positions (a) $z = -0.74\text{m}$ and (b) $z = -0.70\text{m}$ in x, y plane, (c) $y = 0.0\text{m}$ in x, z plane and (d) $x = 0.15\text{m}$ in y, z plane; velocities are plotted as magnitudes $|\vec{u}|$. It has to be mentioned that the velocity range in the plots is limited for clarity to a maximum value of 0.6m/s in all plots, although local peak velocities up to 0.9m/s were observed; points of occurrence are given in the following.

At the moment of wave crest passage, the flow resistance of the structure due to blockage leads to local accelerations, flow around the structural elements and thus enhanced flow velocities. This can especially be observed at the locations of triangular sections between lower and upper braces, main column and pile sleeves as well as in the corner section between the lower braces, pile sleeves and the bed boundary,

Table 5.1: Wave and current condition test parameters for numerical investigations.

Name	type	wave height H [m]	wave period T [s]	angle [$^{\circ}$]	u [m/s]	flume width [m]
w2130-01	wave	0.205	3.0	0	-	2.2
w2130-02	wave	0.205	3.0	0	-	4.0
w2130-03	wave	0.205	3.0	0	-	1.5
w2130-04	wave	0.205	3.0	180	-	2.2
w2130-05	wave	0.205	3.0	90	-	2.2
c0206-01	current	-	-	0	0.206	2.2
w2319-01	wave	0.234	1.94	0	-	2.2
w2319-02	wave+current	0.234	1.94	0	0.206	2.2
w2330-01	wave	0.228	3.0	0	-	1.5
w7655-01	wave	0.760	5.48	0	-	5.0

where maximum flow velocities of up to 0.9m/s were observed, subsequently leading to sediment mobilization in this area, see figure 5.6(d). The second, near-bed region of enhanced flow velocities is given in the area directly under the column, again resulting from blockage of the structure. The region is however not locally limited to the lower main column, but accretes to the section of the pile sleeves, thereby forming a larger area of enhanced near-bed flow velocities under the lower braces reaching to both end sides. Regarding the flow field near the free surface in the rear part of the main column, certain vortex formation and downstream-directed flow can be observed due to water converging behind the structure right at the moment of wave crest passage, as it was already observed in the laboratory experiments (figure 3.8a).

Expectedly, flow velocities are generally much lower at the subsequent flow reversal (during zero crossing at the tripod main column), reaching values up to 0.35m/s in the near-field. Due to natural wave asymmetry, the time step of $t = 0.75$ s given in figure 5.7 does however show the moment shortly after the flow reversal started at the tripod center section. At that moment, water starts moving back and is downward directed in the rear part of the main column due to blockage of the structure. At locations where the water is still flowing in positive forward (x) direction, vortex formation can be observed, e.g. in areas behind the lower braces and the near-bottom part of the main column. Flow furthermore starts to move around the lower sections of the pile sleeves, resulting in near-bed turbulence in these areas.

During wave trough passage, areas of high near-bed flow velocities are similar to those at the moment of wave crest passage, resulting in locally increased velocities under the main column and the lower braces. All in all, flow velocities are however considerably lower, again resulting from the natural wave asymmetry. This can

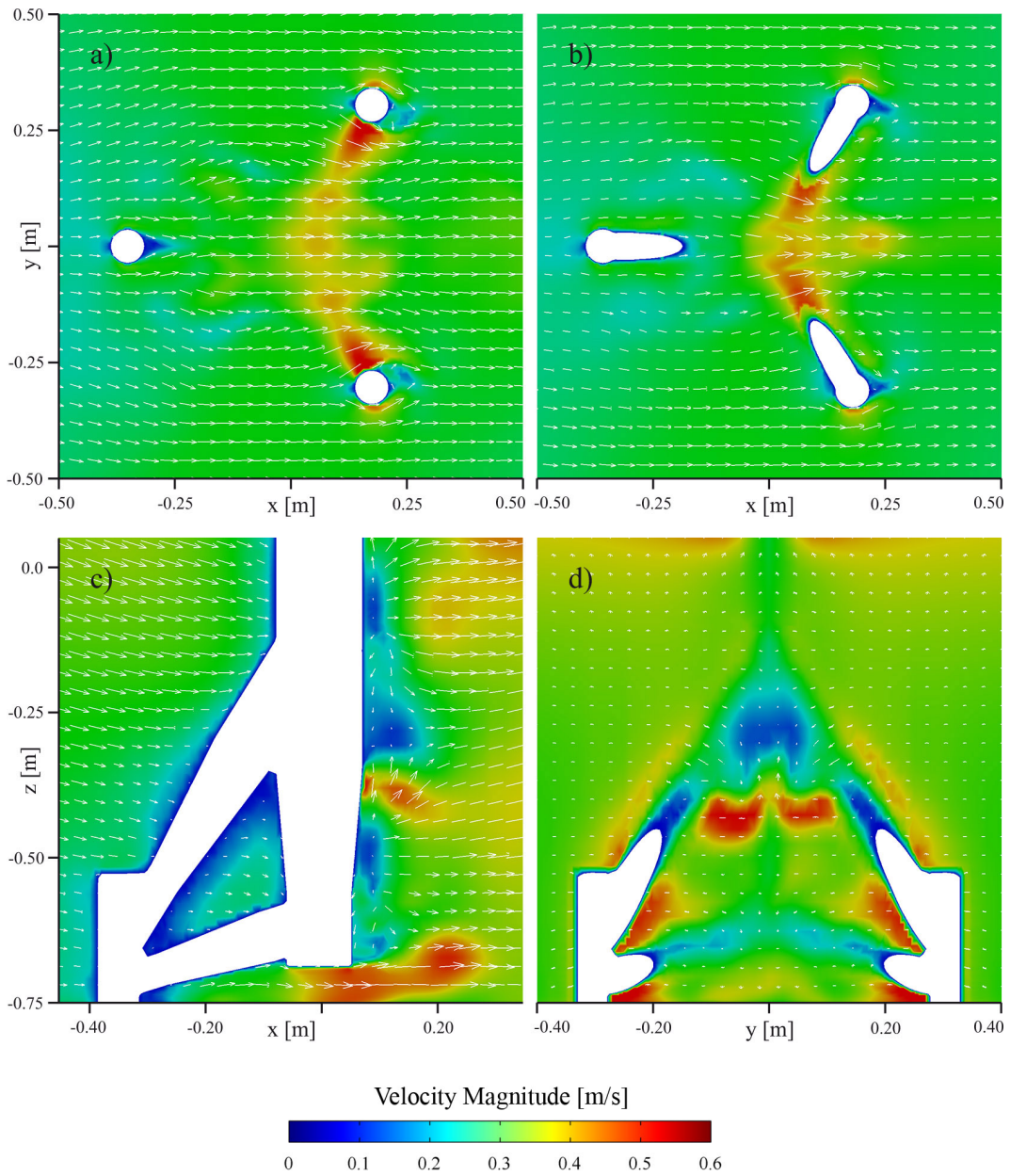


Figure 5.6: Calculated flow pattern around tripod at $t = 0$ s (wave crest passage) for test series w2130-01 as cross sections for (a) x, y plane at $z = -0.74$ m, (b) x, y plane at $z = -0.70$ m, (c) x, z plane at $y = 0.0$ m and (d) y, z plane at $x = 0.15$ m. Velocities are given as magnitudes $|\vec{u}|$.

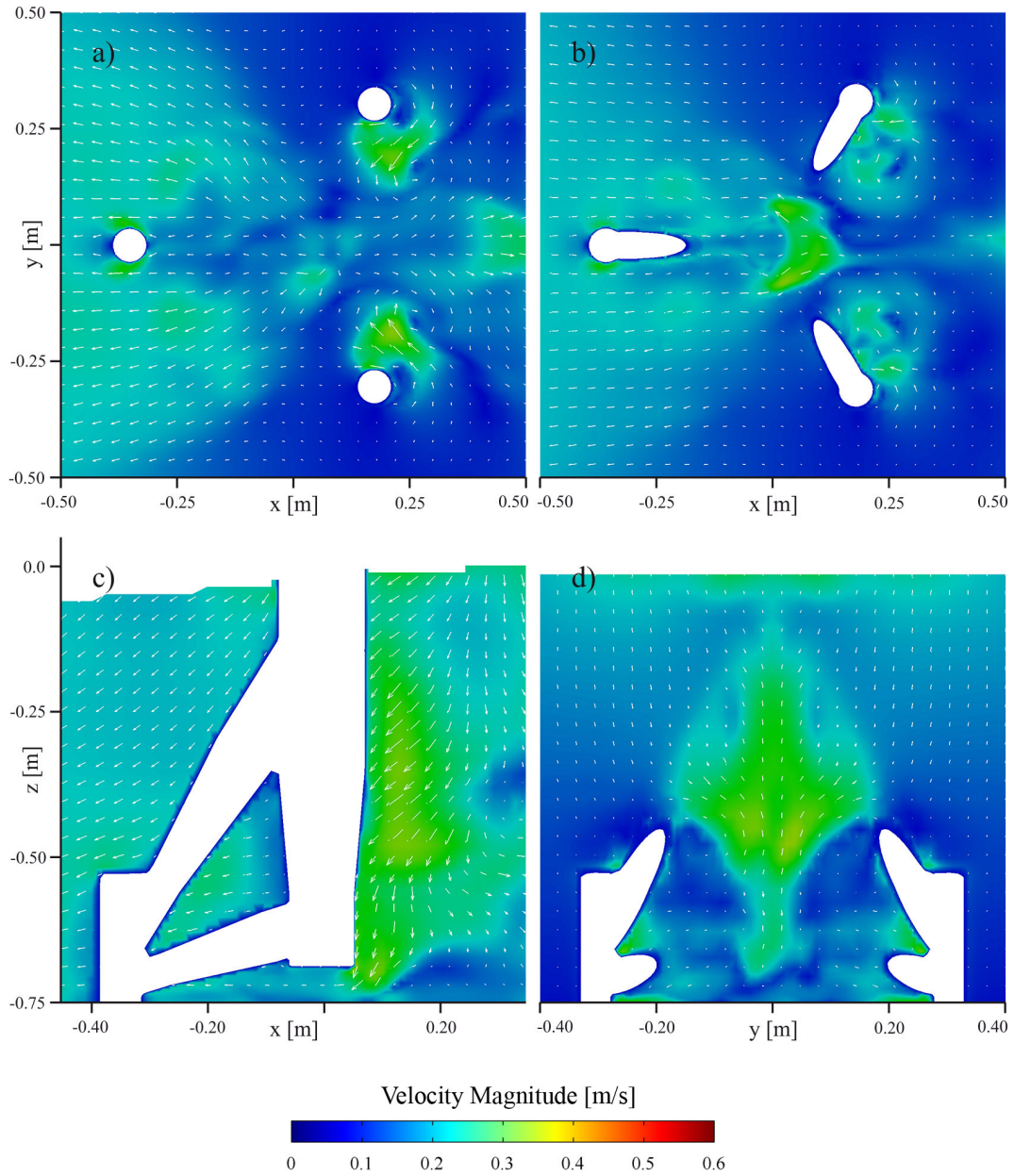


Figure 5.7: Calculated flow pattern around tripod at $t = 0.75\text{s}$ (zero crossing) for test series w2130-01 as cross sections for (a) x, y plane at $z = -0.74\text{m}$, (b) x, y plane at $z = -0.70\text{m}$, (c) x, z plane at $y = 0.0\text{m}$ and (d) y, z plane at $x = 0.15\text{m}$. Velocities are given as magnitudes $|\vec{u}|$.

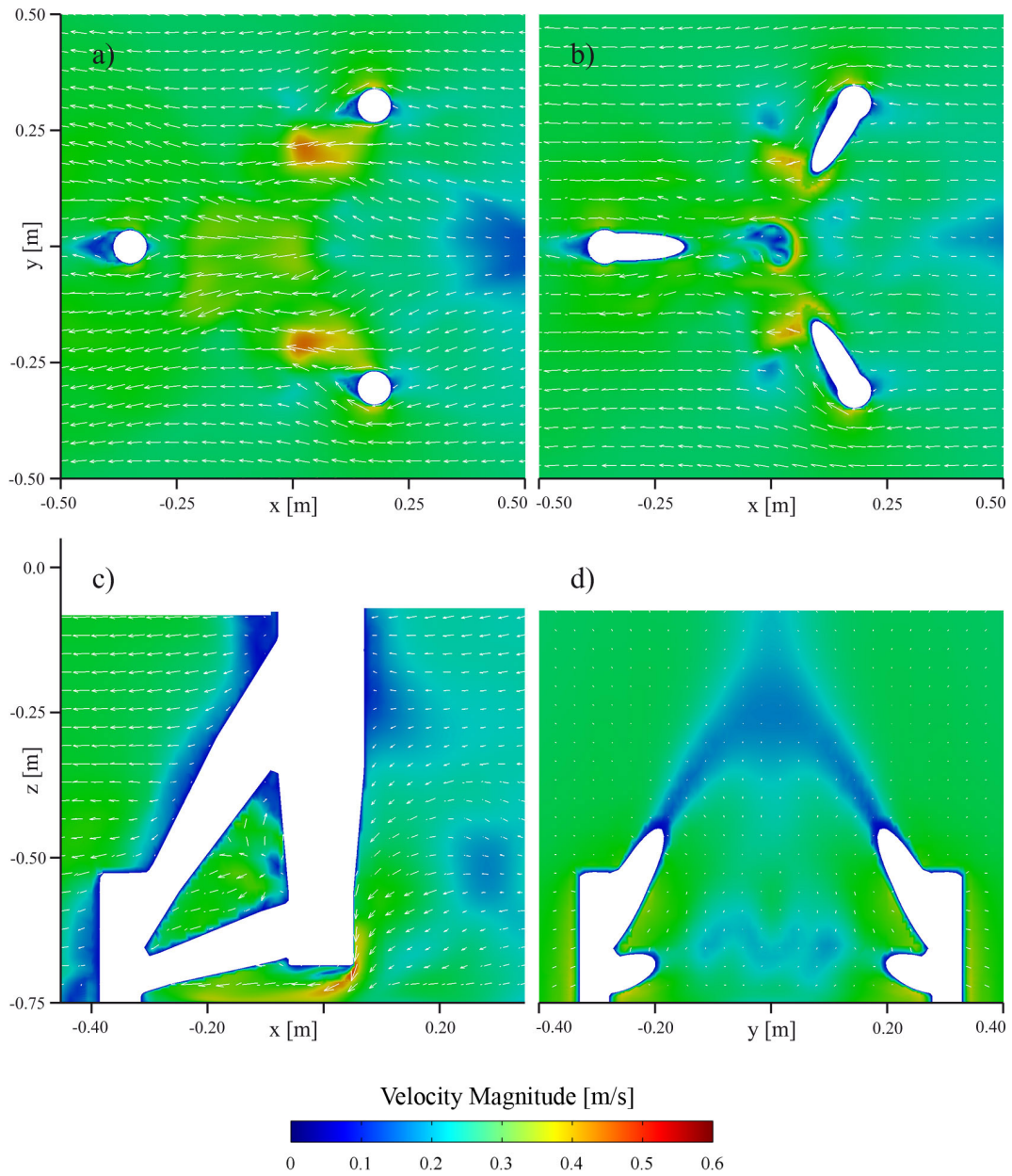


Figure 5.8: Calculated flow pattern around tripod at $t = 1.5$ s (wave trough passage) for test series w2130-01 as cross sections for (a) x, y plane at $z = -0.74$ m, (b) x, y plane at $z = -0.70$ m, (c) x, z plane at $y = 0.0$ m and (d) y, z plane at $x = 0.15$ m. Velocities are given as magnitudes $|\vec{u}|$.

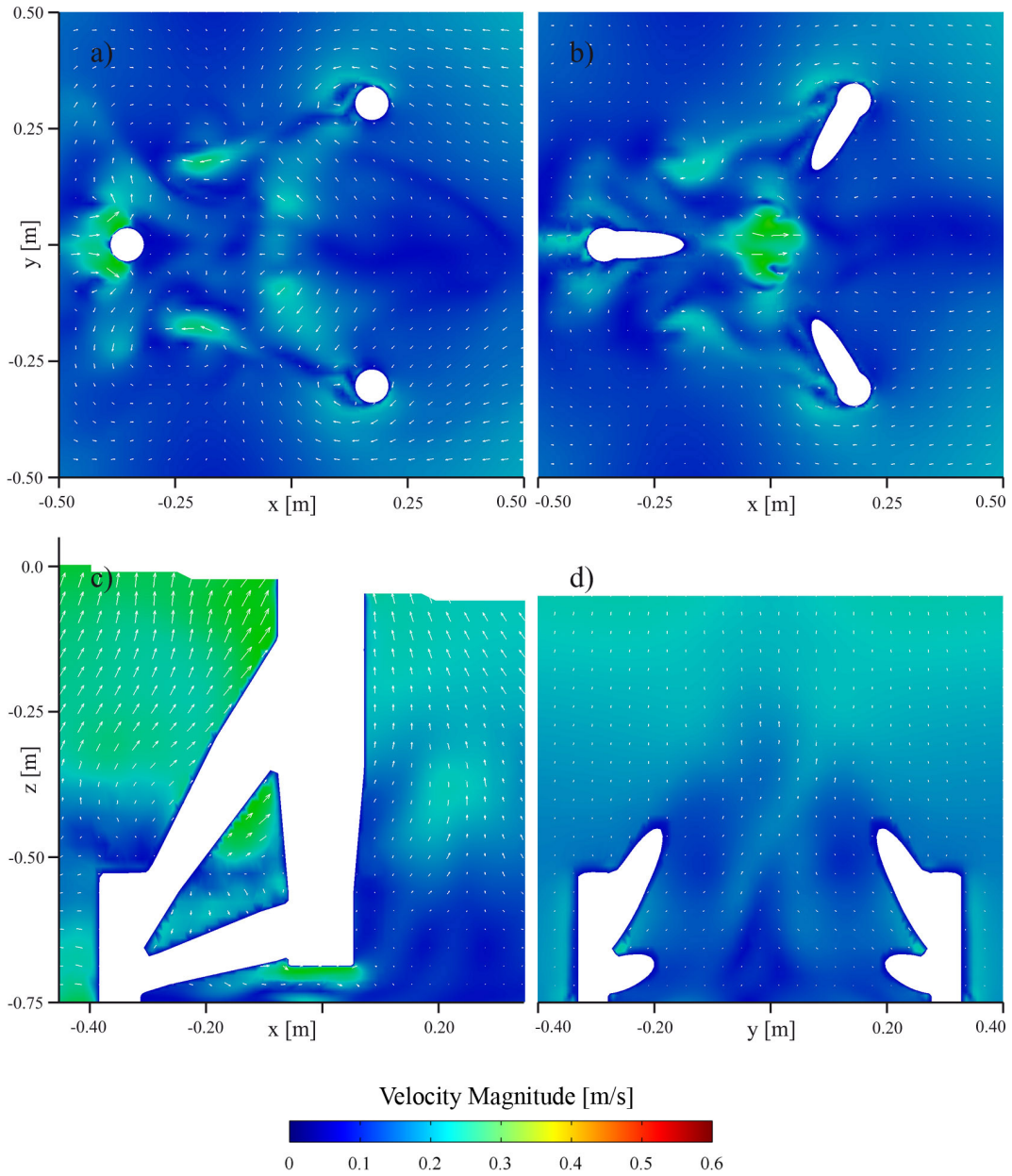


Figure 5.9: Calculated flow pattern around tripod at $t = 2.25$ s (zero crossing) for test series w2130-01 as cross sections for (a) x, y plane at $z = -0.74$ m, (b) x, y plane at $z = -0.70$ m, (c) x, z plane at $y = 0.0$ m and (d) y, z plane at $x = 0.15$ m. Velocities are given as magnitudes $|\vec{u}|$.

especially be observed in the near-bed areas at the rear pile sleeves. Finally, at the moment of subsequent zero crossing, flow stagnation can be observed in the rear-part of the lower main column section. In the front part, flow velocities however start to enhance due to the approaching wave crest. The flow field around the near-bottom part of the pile-sleeves is thereby opposite-directed to the former moment of zero crossing, which can be observed by comparing figures 5.7(a) and 5.9(a).

It can generally be concluded that the locations of maximum flow velocities and the flow processes during one wave cycle passage correspond well to local scour formations observed in the WKS flume experiments, in which largest scour depths were recorded at the piles and especially at the inner sections of the rear piles as well as in the area under the main column.

Due to generally larger near-bed flow velocities during wave crest passage, the global transport of sediment could be assumed to occur in the (positive) direction of wave propagation. This however stands in contrast to the local observations from the laboratory experiments, see §3.2.4, where areal erosion was observed in the rear part of the structure, while slight accumulation areas could be found in the front section. An explanation might however be given by the local flow characteristics: The near-bed flow velocities are generally larger in the rear part of the structure, as it can be observed by a direct comparison of the two moments of wave crest and trough passage. This leads to an enhanced erosion of bed material in the area of the bend between rear pile sleeves and the main column of the tripod, while the eroded material is then transported away by the flow field, mainly in the direction of wave propagation.

5.3.2 Shear Stress Distributions

Shear Stress under Regular Waves The velocity fields for flow around the tripod structure under regular waves, denoted as test series w2130-01, were given above in §5.3.1. The corresponding shear stress distributions at the bed boundary around the structure are now given in the following. In addition to the previously regarded 0° wave-encounter angle, shear stress distributions for angles of 180° and 90° (w2130-04 and w2130-05) are given, which correspond to tests r2130-04 and r2130-05 from the WKS wave flume experiments, see table 3.4.

The stresses are given for the two moments of wave crest and wave trough passage at the tripod main section, as maximum loads and resulting stresses occur at these moments. This corresponds well to the former observations on flow pattern. It however has to be mentioned that maximum bed shear stress values in the undisturbed case, i.e. without structure installation occur slightly before wave crest and trough passage at the tripod center position, resulting in a time shift of -0.2s and -0.3s, respectively. For the given wave conditions, stress values τ_0 in the undisturbed

case are 0.63N/m^2 (wave crest) and 0.38N/m^2 (wave trough), taken from the numerical model calculations, while the difference results from wave asymmetry. The critical shear stress for the sediment modeled here is 0.14N/m^2 , which is therefore exceeded under maximum conditions, meaning that life-bed conditions are present.

The definition of maximum stress values in the undisturbed case is useful for the determination of the direct influence by the structure at the particular position, further described by the shear stress amplification factor

$$\alpha_\tau = \frac{\tau}{\tau_0} \quad (5.1)$$

where τ gives the local shear stress and τ_0 the value without structural influence at the same position.

Shear stress distributions for wave-encounter angles 0° , 180° and 90° are given in figure 5.10 for the moments of wave crest and wave trough passage at the center position of the tripod. Corresponding amplification factors are further given in figures 5.11, C.4 and C.5, where τ_0 is 0.63N/m^2 , i.e. the shear stress during wave crest passage giving the maximum value without structural influence. It should be noted that the particular color bars have been adapted for clarity to the respective cases, resulting in maximum value representations (red) covering a larger value range without linear scaling. These peaks however occur only very locally limited, as will be given in the following. White areas in the figures depict the positions of the tripod pile-sleeves.

The global influence of the structure on the shear stress distribution in its near-field is rather limited under wave conditions and reaches about one meter in the direction of wave propagation and about 0.75m perpendicular to it.

Test case w2130-01 (0°) Not surprisingly, the areas of high shear stresses for case 0° correspond directly to the observed near-bed flow velocities. For figure 5.10a, this results in areas of locally high shear stress in the sections under the braces and the main column, with highest values up to 7.2N/m^2 (wave crest) at the inner part of the pile-sleeves. This maximum value is therefore around twelve-fold above the local shear stress under the wave crest in the undisturbed case (see figure 5.11), which again illustrates the high influence of the near-bed structural elements on the local bed shear stress development. At the moment of wave trough passage, global shear stress distributions and hot spots are similar. Local values, also in the near-field of the structure are however comparatively lower (up to 2.9N/m^2), resulting from generally lower flow velocities under the wave trough during wave passage.

Test cases w2130-04 (180°) and w2130-05 (90°) Under a wave-encounter angle of 180° , shear stress values and local distributions are altogether similar to what

could be observed in the 0° constellation, however turned 180° like the structure, see figure 5.10b. During wave crest passage, maximum values reach up to 6.2N/m^2 , again at the inner parts of the pile-sleeves, giving an amplification of $\alpha_\tau = 10$. During wave trough passage, maximum bed shear stresses at the piles are locally higher than given in 0° constellation. No distinct, increased shear stress can be observed in the area under the main column. The latter results from a different flow pattern during backflow, in which no distinct downward- and reverse-directed flow alignment takes place in the back of the main column due to the presence of the rear braces.

In 90° constellation, an asymmetric shear stress pattern can be observed, where largest values up to 5.5 N/m^2 occur at the single pile during wave crest and up to 3.8 N/m^2 during wave trough passage, respectively. At this exposed location, flow resistance due to structural blockage is largest for this setup. Regarding the remaining two pile-sleeves, slightly lower shear stresses are given at the respective rear ones due to shadowing effects. It can be stated that the global as well as local shear stress distribution is equal to the scour formation that could be observed in the WKS flume experiments, see figure 3.14.

Influence of Single Load Components in Combined Case In addition to pure wave load as it was investigated before, the influence of the single load components in a combined wave-current climate is further investigated in the following. Numerical simulations were carried out for load conditions based on extreme event parameters as given in §3.1.1. Shear stress plots for test cases c0206-01, w2319-01 and w2319-02 (table 5.1) are given in figure 5.12. Corresponding amplification factors can further be found in figures C.6 to C.8. It should again be noticed that the numerical model was run on a model scale of 1:40 here. Wave load parameters given as wave spectra values were further converted to representative regular wave conditions following equation (3.1). Furthermore, tidal flow is given as time-invariant current flow here, therefore representing the maximum condition in the combined wave-current load case only. It should be noticed that similar investigations were previously published in Stahlmann and Schlurmann (2012a) and Stahlmann and Schlurmann (2012b). Results however slightly differ from the published ones, as on the one hand, no bed roughness was previously included and stresses were determined by use of the Reynolds stress tensor on the other hand. Furthermore, waves were generated as 2nd order Stokes waves instead of 5th order as given here.

The magnitudes of bed shear stresses in the undisturbed case were again determined from the numerical model, given as 0.067N/m^2 for current flow (theoretically 0.051N/m^2 after §2.3.1), 0.556N/m^2 for the maximum value under the wave crest (theoretically 0.54N/m^2) for pure wave load (trough 0.548N/m^2) and 0.626N/m^2 for the combined wave-current load case (theoretically 0.64N/m^2) under the wave

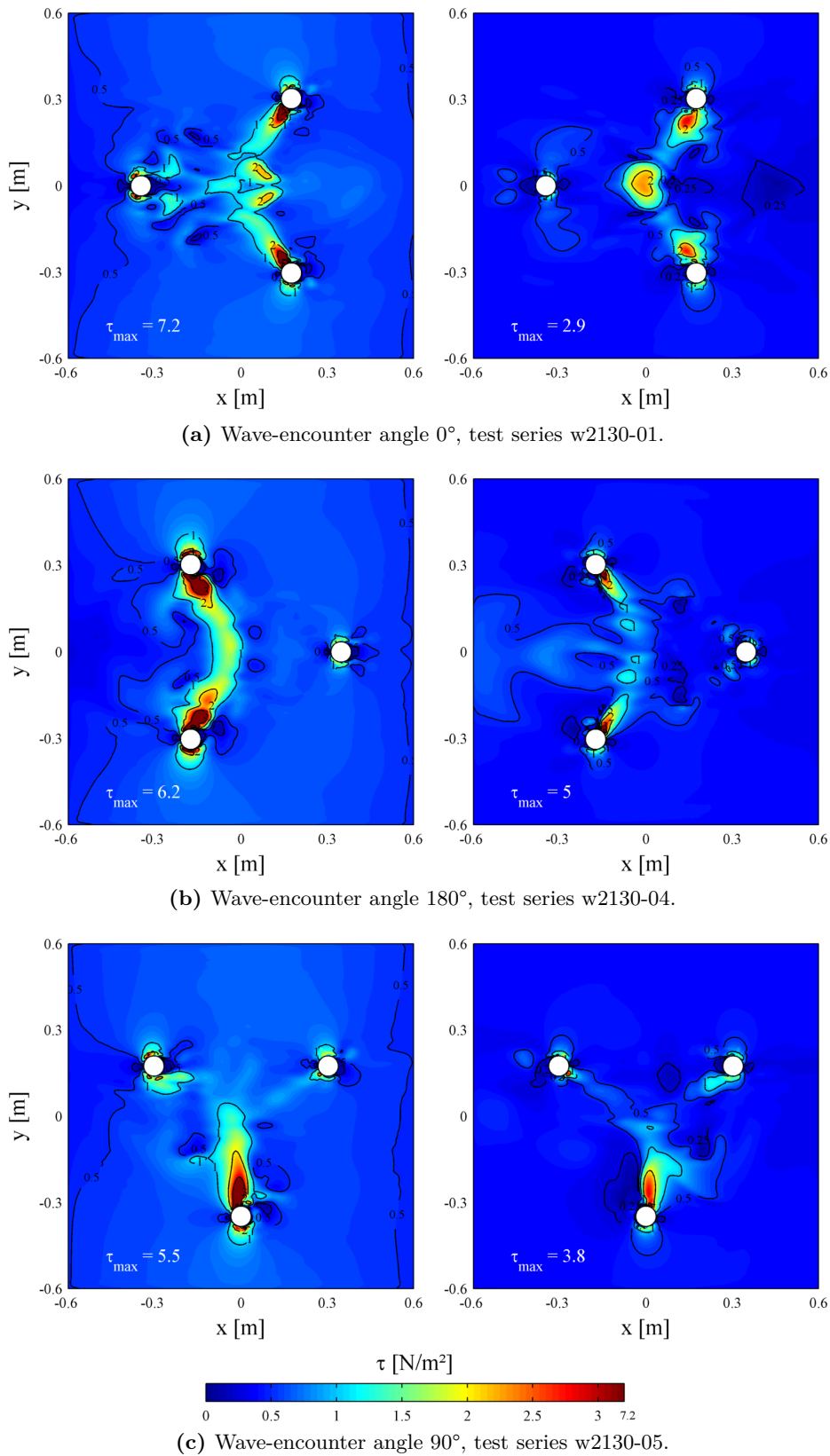


Figure 5.10: Bed shear stress distributions for wave-encounter angles (a) 0° , (b) 180° and (c) 90° . Moments of wave crest (left) and wave trough (right) passage at centre of structure.

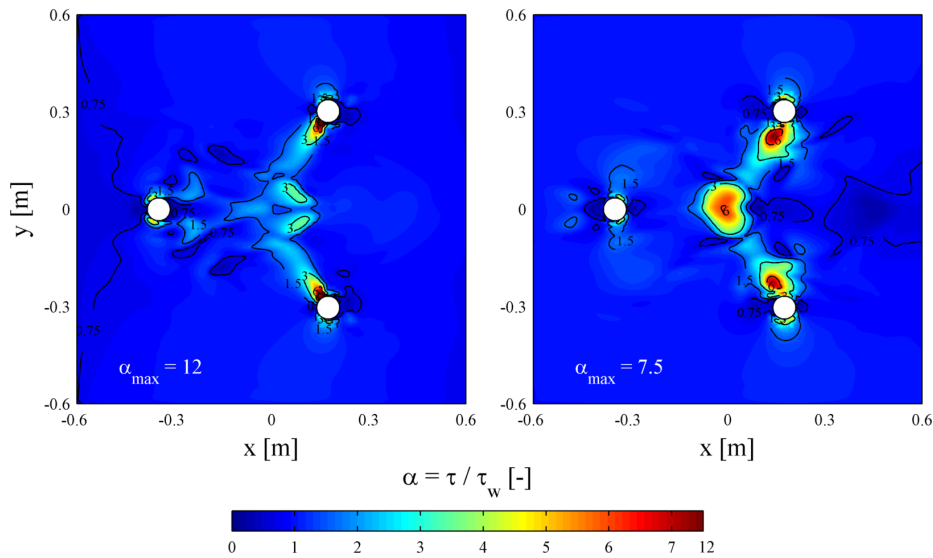
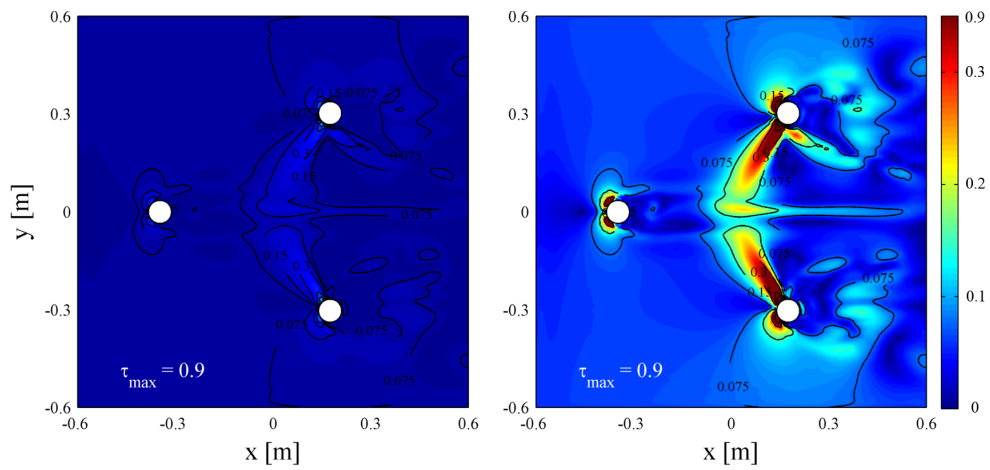


Figure 5.11: Amplification factors for figure 5.10a, test series w2130-01. Moments of wave crest (left) and wave trough (right) passage at centre of structure. Shear stress τ_0 corresponds to wave crest passage in undisturbed case.

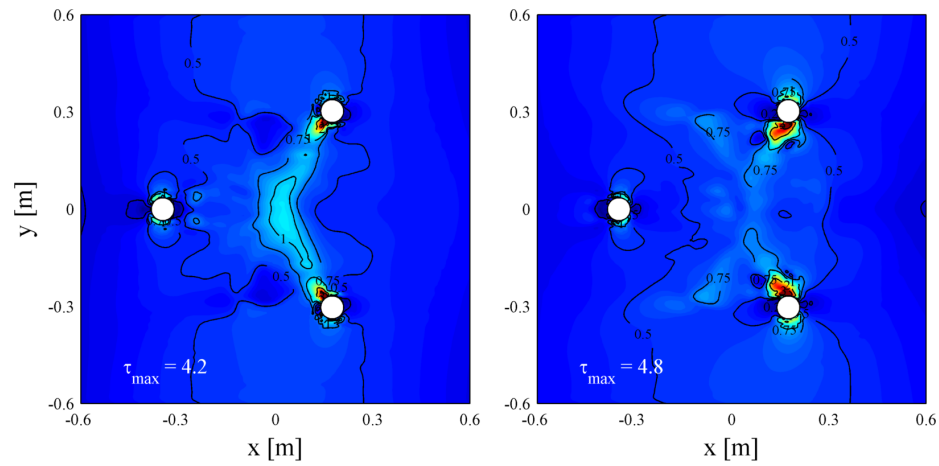
crest (trough 0.382N/m^2). It can already be seen that even in the undisturbed case, resulting shear stresses under waves due to an extreme event are around a factor of 8 higher than under pure current flow investigated here. Similar to what could previously be observed in §5.3.2, maximum shear stresses under waved and wave-current cases occur slightly before the maximum wave amplitude is reached, therefore again resulting in a time shift of -0.15 to -0.30s for the given cases.

Regarding the latter (figure 5.12a), shear stresses locally increase by a factor of up to 13 due to the presence of the structure compared to the undisturbed case and result in shear stresses up to 0.9N/m^2 , where the maximum values occur at the sides of the rear piles and below the lower braces due to the concentration of the flow field. Beneath the center tube, shear stresses are still increased by a factor of 2-3, while shadowing effects lead to reduced shear stresses behind the rear piles. It should be noted that shear stress plots in figure 5.12a give the same situation in both left and right plots; the right plot has however been adjusted in terms of color coding, while the color coding in the left plot is the same for the remaining load conditions.

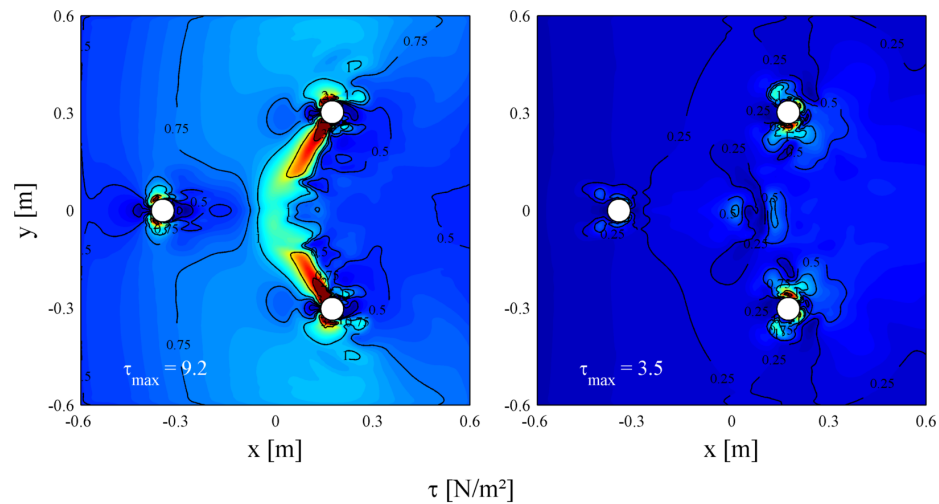
Under wave load (figure 5.12b), shear stress distributions are similar to those observed in test case w2130-01. Maximum bed shear stresses again occur at the sides of the piles and below the lower braces, with values locally increased by a factor of up to 7.7 (wave crest) and 8.7 (wave trough) compared to the undisturbed case, leading to maximum shear stresses of 4.2N/m^2 and 4.8N/m^2 , respectively. The stress distribution at the time of passing wave crest is generally similar to the one under current conditions; the influencing area of the structure is however substantially smaller than under constant flow due to changing flow directions under



(a) Current load, test series c0206-01. Left and right moments are equal.



(b) Wave load, test series w2319-01.



(c) Combined wave-current load, test series w2319-02.

Figure 5.12: Bed shear stress distributions for (a) current, (b) wave and (c) wave-current load. Moments of wave crest (left) and wave trough (right) passage at centre of structure. In plot (a), right is same as left, but using different color coding.

waves, which leads to a local (temporal) limitation of the increased shear stresses. Due to increased flow velocities under such extreme conditions as given here, bed shear stresses are generally larger than under considered current flow.

Under combined load (figure 5.12c), the constant current flow obviously leads to an increase in flow velocities and bed shear stress compared to pure wave load. Maximum stresses appear at the piles due to constriction and acceleration effects, reaching local values of up to 9.2N/m^2 under the wave crest and $\alpha_\tau = 11 - 12$. Typical constant-flow phenomena such as periodic vortex shedding behind the structure cannot be found here. Below the center tube, the shear stress rises up to 1.3N/m^2 and is therefore slightly higher than compared to a linear addition of the individual load components. This effect increases with reduced distance in the direction of the piles-sleeves below the braces.

For the given event, local shear stresses at the foundation under combined wave-current load are up to a factor of 5 higher than calculated by a simple addition of the single load component results, leading to the assumption that the maximum scour depths will be reached here. This is further confirmed by Soulsby (1997), stating that for combined wave-current flow, sediment is stirred up and suspended within the boundary layer first and is then transported away through the turbulent behavior of the current flow.

5.3.3 Influence of Model Scales

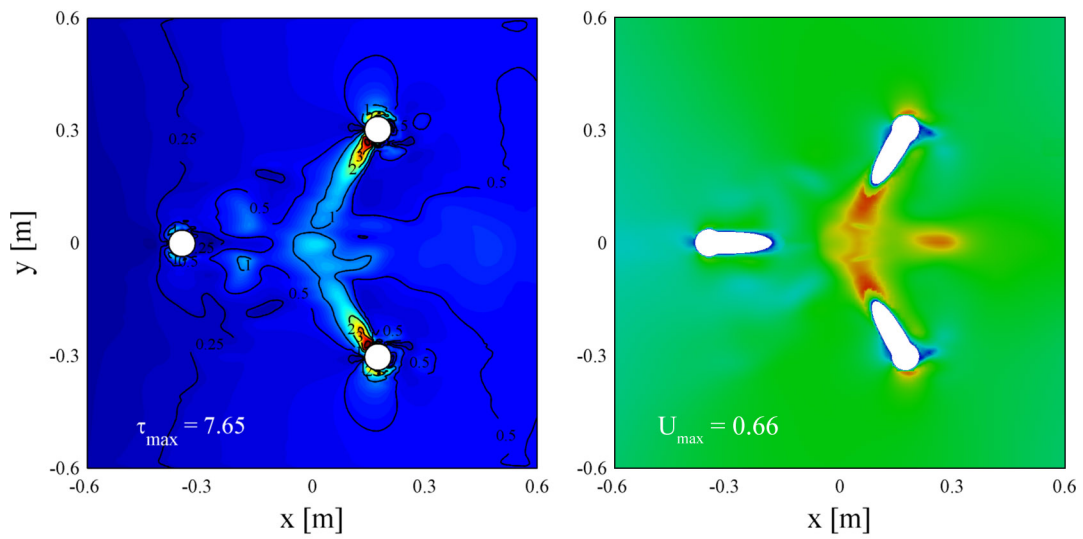
Experimental investigations on wave-induced scour development for a tripod foundation were carried out on different model scales of 1:40 and 1:12 in the WKS wave flume of the Franzius-Institute and the Large Wave Flume (GWK), as given in §3. The different wave flume installations resulted in different blockage ratios of $r_{t,1:40} \approx 0.14$ (WKS, $\lambda = 40$) and $r_{t,1:12} \approx 0.20$ (GWK, $\lambda = 12$), see §3.4.3. Furthermore, wave heights in the large-scale experiments were slightly increased by about 10% for the regular waves tests compared to the small-scale ones. The influence of given deviations on the local bed shear stress results and flow pattern were therefore investigated by use of numerical model calculations for regular waves and 0° wave-encounter angle on a model scale of 1:40. Large-scale wave parameters and flume dimensions were scaled down for comparison, resulting in a regular wave height of $H = 0.228\text{m}$ as given by test series w2330-01 and a flume width of 1.5m, see table 5.1.

In addition to these simulations regarding the given flume installations, the general blockage ratio effect was investigated in a first step. Although the blockage ratio in the small-scale experiments, i.e. the WKS wave flume having a value of $r_{t,1:40} \approx 0.14$ is below the critical value of $r_b = 1/6 \approx 0.167$ after Whitehouse (1998) for influences on the results, certain blockage effects could be expected. In order to

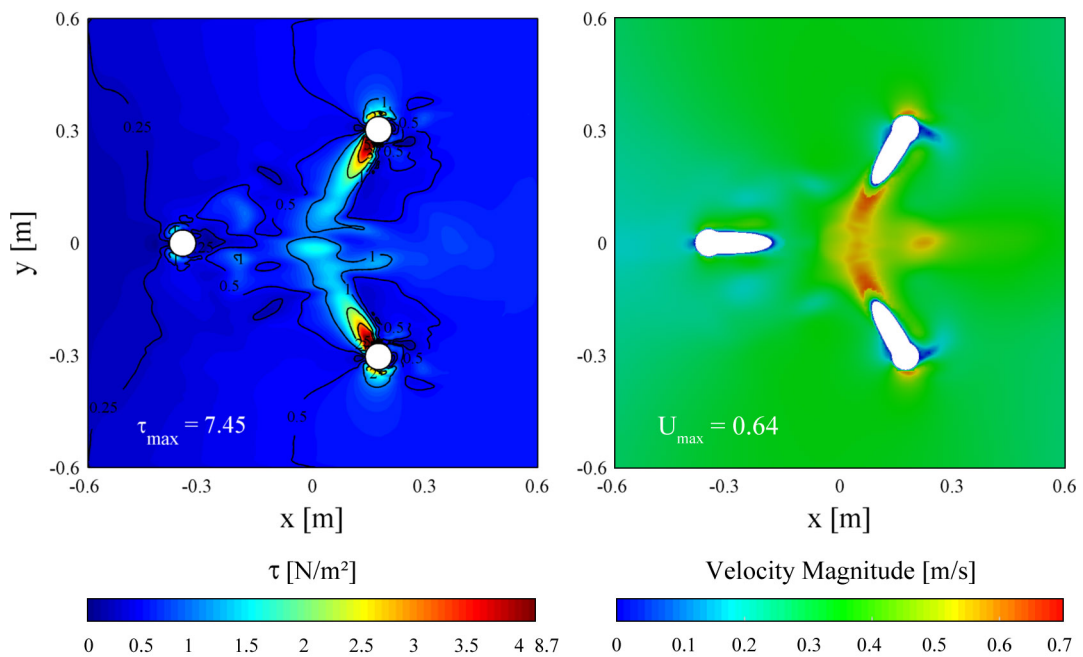
estimate a magnitude of blockage error, results of the 2.2m 'original' flume width (test series w2130-01) were compared with an artificial 4.0m flume width installation (w2130-02) in the numerical model in a first step, see table 5.1 for the parameters. It is thereby assumed that the 4.0m flume width results in negligible blockage effects for the investigated tripod structure, as the blockage ratio holds a value of $r_{t,1:40} \approx 0.08$ for this case. Results of the respective calculated bed shear stress distributions (bed boundary) and flow pattern given as cross section in x, y plane at $z = -0.70\text{m}$ for test series w2130-01 and w2130-02 are given in figure 5.13. All in all, global and especially local bed shear stress distributions as well as flow pattern are very similar for both cases. Maximum flow velocities given as velocity magnitudes $|\vec{u}|$ in the figures hold values of 0.66m/s for test series w2130-01 (2.2m) and 0.64m/s for test series w2130-02 (4.0m), respectively, while bed shear stresses result in a maximum of 7.65N/m^2 and 7.45N/m^2 , respectively at the single rear piles. It can thus be assumed that the 2.2m 'original' WKS wave flume installation overall results in negligible blockage errors regarding both the flow field and the resulting sediment transport.

In a second step, simulations regarding the (scaled down) 1.5m flume width installation were carried out, while regular wave parameters were kept with $H = 0.205\text{m}$ and $T = 3.0\text{s}$ as given by test series w2130-03. Results are given in figure 5.14a for the bed shear stresses and flow pattern in x, y plane. Again, both flow pattern and bed shear stresses are nearly equal to the 'original' flume installation, however resulting in slightly increased maximum flow velocities of 0.70m/s and bed shear stresses of 7.67N/m^2 for the given wave load cycle. Thus, deviations in the large-scale GWK experiments due to the given increased blockage ratio of $r_t \approx 0.20$ alone can be regarded as minor here.

A factor, which however results in certain deviation between large-scale GWK experiments and the small-scale WKS tests is given by the about 10% increase in wave height in the GWK experiments. Results of simulated flow pattern and bed shear stresses for an increased wave height, resulting in $H = 0.228\text{m}$ in test series w2330-01 (scaled down to 1:40 model scale) are given in figure 5.14b. Global as well as local bed shear stress distributions are again similar for the two different wave height cases. Maximum bed shear stresses especially around the single rear piles for the increased wave height case are however slightly higher, resulting in a maximum value of 8.65N/m^2 for the moment of wave crest passage, compared to 7.65N/m^2 for the 'original' case as given in figure 5.13a. The circumference of enhanced shear stresses around the rear piles is furthermore slightly larger. Maximum flow velocities reach a value of 0.81m/s for the given parameters. Compared to the WKS wave flume experiments and the respective simulation, this overall results in a maximum local bed shear stress enhanced by about 13%, while the major part is resulting from the increased wave height alone.

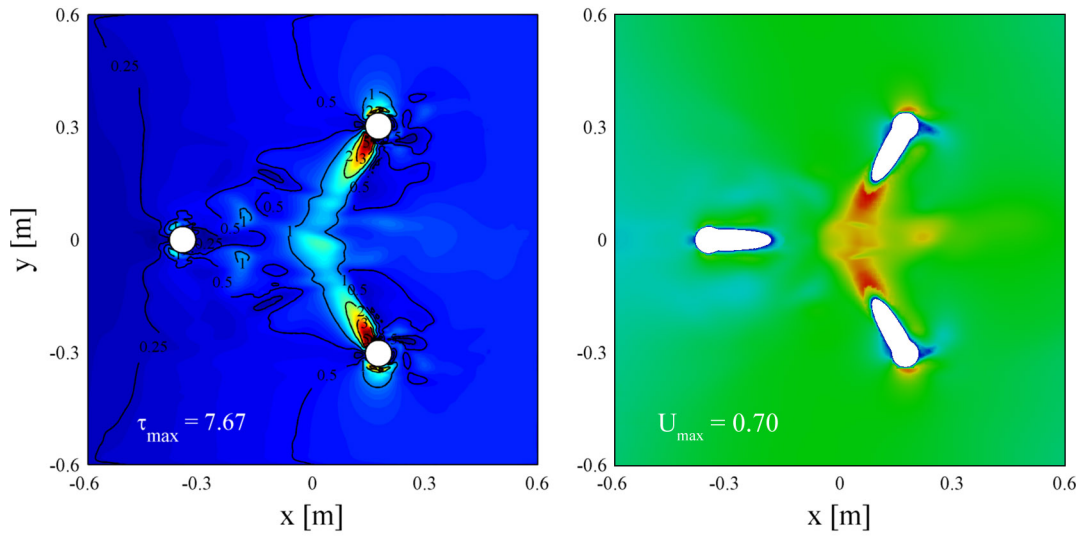


(a) Test series w2130-01. $H = 0.205\text{m}$, flume width 2.2m, 1:40 scale.

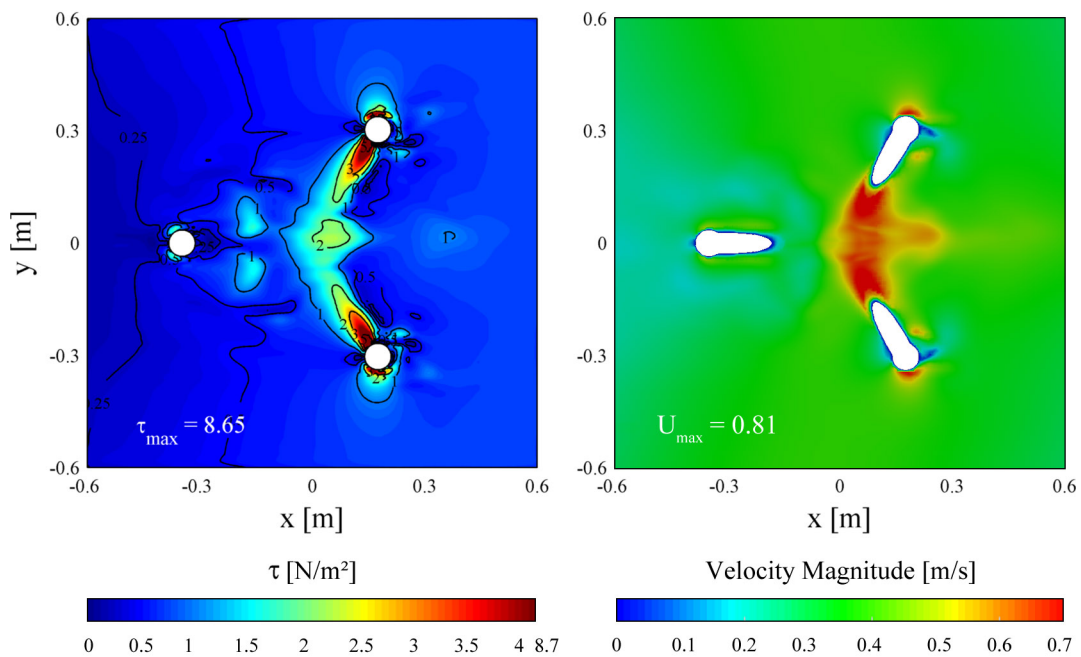


(b) Test series w2130-02. $H = 0.205\text{m}$, flume width 4.0m, 1:40 scale.

Figure 5.13: Calculated bed shear stress distributions (left) and flow pattern (right) for wave load cases w2130-01 (a) and w2130-02 (b), 1:40 model scale, given at moments of wave crest passage at centre of structure. Shear stress given at bed boundary; flow field given as cross section in x, y plane at $z = -0.70\text{m}$ as magnitude $|\vec{u}|$. Max. values depicted in the figures.



(a) Test series w2130-03. $H = 0.205\text{m}$, flume width 1.5m, 1:40 scale.



(b) Test series w2330-01. $H = 0.228\text{m}$, flume width 1.5m, 1:40 scale.

Figure 5.14: Calculated bed shear stress distributions (left) and flow pattern (right) for wave load cases w2130-03 (a) and w2330-01 (b), 1:40 model scale, given at moments of wave crest passage at centre of structure. Shear stress given at bed boundary; flow field given as cross section in x, y plane at $z = -0.70\text{m}$ as magnitude $|\vec{u}|$. Max. values depicted in the figures.

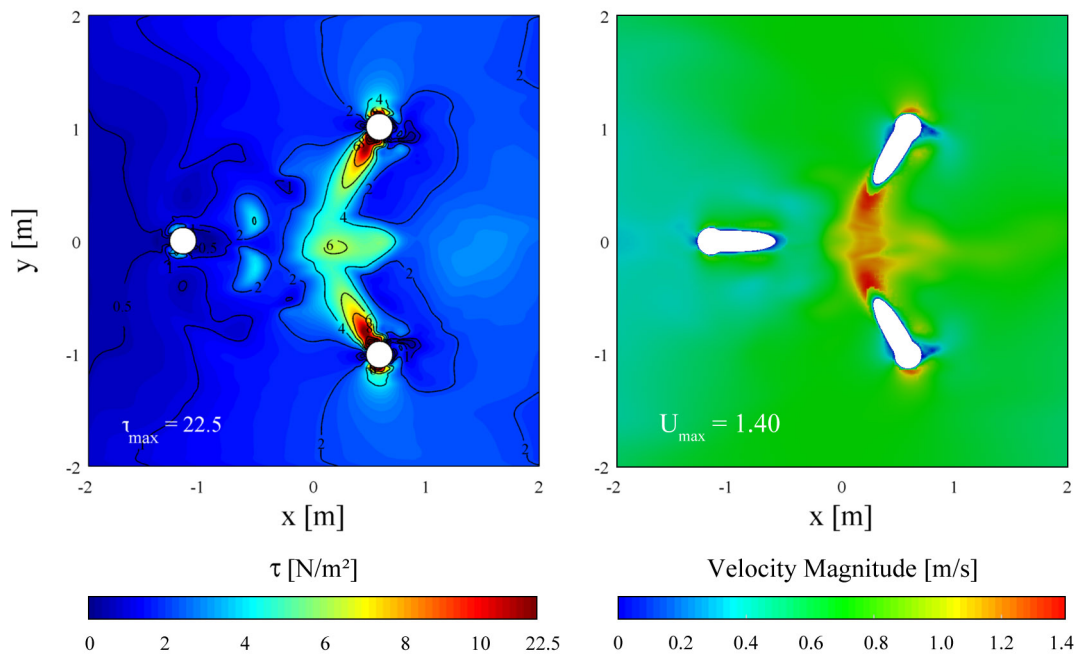


Figure 5.15: Calculated bed shear stress distribution (left) and flow pattern (right) for wave load case w7655-01, 1:12 model scale, given at moment of wave crest passage at centre of structure. Shear stress given at bed boundary; flow field given as cross section in x, y plane at $z = -2.33\text{m}$ as magnitude $|\vec{u}|$. Max. values depicted in the figures.

In order to investigate the influence of the model scales itself on flow pattern and bed shear stresses, thus resulting in deviations regarding the sediment transport, these parameters were finally calculated for a length scale of 1:12 in the numerical model. Wave parameters, directly coming from the GWK large-scale experiments, are given by test series w7665-01, see table 5.1. Compared to the 1:40 small-scale simulation given by test series w2130-01 (and all remaining tests given above), the bed roughness in the simulation resulting from the given sediment parameters was kept the same. Results are given in figure 5.15, again for bed shear stresses and flow pattern in x, y plane for the moment of wave crest passage in the plots.

For the 1:12 model scale and the given wave conditions, bed shear stresses reach maximum values of up to 22.5N/m^2 in local areas around the rear piles and under the braces sections, while around 6N/m^2 are calculated in the area underneath the main column. The overall shear stress distribution is nearly equal to the one determined for the w2330-01 test series calculations. Deviations in the plots thereby mainly result from the given color coding. Compared to the 1:40 tests, an increase of maximum, local bed shear stresses with a factor of around 2.6 is given, while the factor of maximum flow velocity increase is around 1.7.

This increase especially in bed shear stresses clearly constitutes the observed differences in global and local scour depths at the single piles as well as under the

main column in the WKS and GWK wave flume experiments as discussed in §3.4.3, where equal model sediments with $d_{50} = 0.148\text{mm}$ and therefore equal resistance parameters were used in the two different model scales.

5.4 Scour Simulations

For the scour simulations, the inclusion of both bed load and suspended load transport processes was considered. The final choice of the suspended sediment entrainment approach is thereby given in §5.4.1. It was evident to activate the sand sliding procedure in the numerical simulation of local scour development, as otherwise unphysically large bed slopes would occur. Other works using numerical methods e.g. in Weilbeer (2001) or Link (2006) have investigated this topic, for which reason no further comparison was carried out here. It is however supposed that an exclusion of numerical sand sliding does not lead to such distinctive errors for wave load cases due to the given periodic flow reversal as it is the case for pure current flow around objects.

5.4.1 Choice of Sediment Entrainment Approach

Several existing approaches for the calculation of the reference concentration c_b for the entrainment function of suspended sediment particles into the flow are given in §4.3.3. A comparison of the approaches by van Rijn (1984c), Nielsen (1992), Zyserman and Fredsøe (1994) and Fredsøe and Deigaard (1995) is given in figure 5.16 for a sediment with a grain diameter of $d_{50} = 0.148\text{mm}$, while the respectively calculated reference concentrations c_b are plotted over the Shields parameter θ . Furthermore, experimental data on particle entrainment summarized by Guy et al. (1966) are given in the plot. It should be noticed that for the Nielsen (1992) approach, the reference concentration was calculated as $c_b = E/w_s$ for comparison.

It is obvious to see that a scatter of calculated reference concentrations by the different approaches is given, hence resulting in variations of calculated transport processes and scour development. The scatter mainly results from the fact that different experimental data were used to derive the respective approaches. Data from Guy et al. (1966), which are plotted here in figure 5.16 were used to derive the Zyserman and Fredsøe (1994) approach only. Furthermore, scatter of the single results within one experimental data set is clearly given.

Through comparison of different approaches in terms of numerical scour simulations for the tripod structure, it was found that the formulas of Nielsen (1992) and Zyserman and Fredsøe (1994) all in all resulted in too little scour formation for the present cases, while the approaches of van Rijn (1984c) and Fredsøe and Deigaard (1995) led to a certain over prediction of scours. Therefore, a different reference concentration approach was developed and finally applied in the present

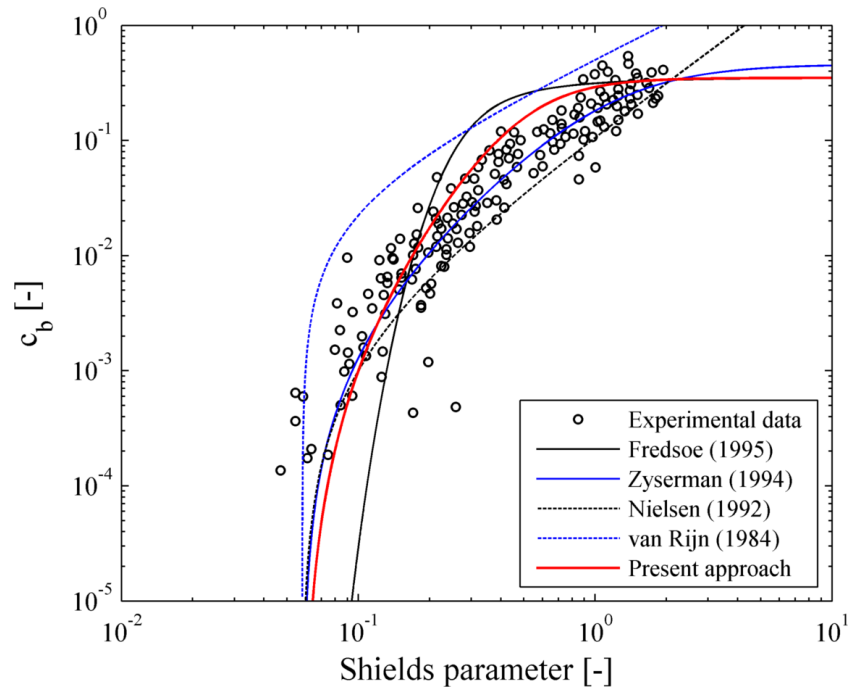


Figure 5.16: Present suspended sediment reference concentration (c_b) approach (red line) in comparison with existing approaches and data from literature.

model calculations, giving all in all averaged c_b quantities with regard to compared formulations.

The present approach thereby, equal to the method given in Zyserman and Fredsøe (1994) takes the general form

$$c_b = \frac{A(\theta - \theta_c)^n}{1 + \frac{A}{c_m}(\theta - \theta_c)^n} \quad (5.2)$$

Different from the Zyserman and Fredsøe (1994) formulation, in which coefficients of $A = 0.331$, $n = 1.75$ and $c_m = 0.46$ were applied to fit the applied experimental data, the present model formulation holds coefficients of $A = 0.9$, $n = 1.9$ and $c_m = 0.45$, leading to a value fitting as plotted by the red line in figure 5.16.

5.4.2 Scour around Vertical Cylinder under Steady Current

Scour around objects like cylinders have been investigated in several numerical studies over the past years. Some of the model applications are listed in §2.5.2. From the given studies, the investigations of Roulund (2000) and later published in Roulund et al. (2005) are the only works in which own experimental studies were carried out for a verification of the numerical model results. The author therefore draw a comparison between modeled and simulated scour developments, which were further used for a validation of numerical models in Weilbeer (2001) and Göthel (2008). Due

to an appropriate availability of data, both the experimental and numerical results were again used for a comparison with the present model implementation.

Model Setup A description of the model setup is briefly given in the following. For the experiments, a vertical cylinder with a diameter of $D = 0.1\text{m}$ was placed in a movable bed test section in a current flume. The flume had dimensions of 3.86m in width and 9.90m in length, while the movable bed test section was 5.65m long and 3.60m wide, see figure 5.17. The water depth in the experiments on scour development was 0.40m . The cylinder was subjected to a steady current, having a depth-averaged flow velocity of 0.46m/s .

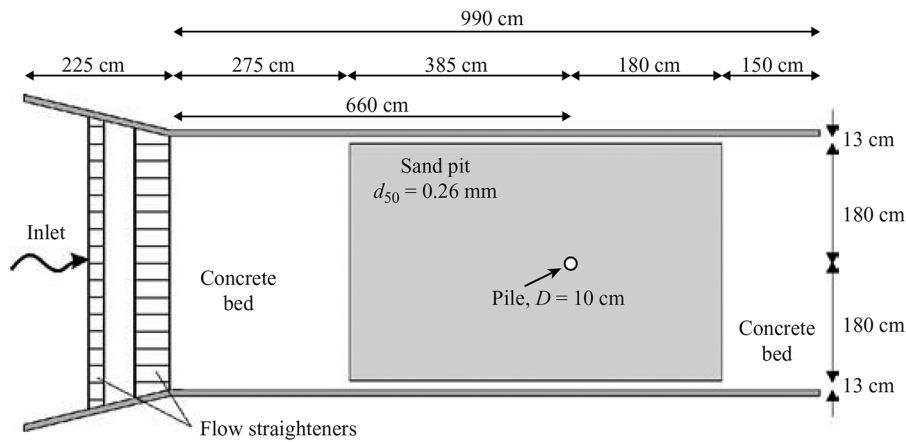


Figure 5.17: Test setup for cylinder scour experiments, from Roulund et al. (2005).

Regarding the numerical model in Roulund et al. (2005), it should be noted that only a water depth of 0.20m was simulated here, using a rigid lid approach instead of a free surface; the numerical model further used a steady-flow approach. The reduced water depth was assumed to correspond with the logarithmic part of the boundary layer.

For comparison with the existing data, the present model was likewise run with a water depth of 0.20m . The rigid lid was simulated using a symmetry boundary approach at the upper domain boundary. The model was however run using a transient flow approach, further including both bed load and suspended load sediment transport processes as given in §4. Model parameters with regard to the sediment properties for both the Roulund et al. (2005) experiment and the present numerical simulations as well as the present model coupling are given in table 5.2. Here, $T = 1.087$ is resulting from the St number. For the number of repeating loops n , a value of 10 is chosen here for the larger part of the simulation time, however gradually increased from $n = 2$ at simulation start due to a rapidly evolving scour hole around the cylinder.

The model domain has a length of $27.5D$ with D as the pile diameter and a width

Table 5.2: Model parameters for flow-induced scour simulation.

d_{50} [mm]	w_{so} [m/s]	θ_c [-]	μ_s [-]	μ_d [-]	φ [°]	$\Delta\varphi$ [°]	T [s]	n [-]
0.26	0.034	0.05	0.63	0.51	33	2.5	1.087	2-10

of $15D$, see figure 5.18. The overall number of cells in the computational domain is approx. 152k. Cell dimensions are in a range of 2.5-5mm around the cylinder (horizontal) and approx. 0.5mm at the bottom (vertical) at simulation start.

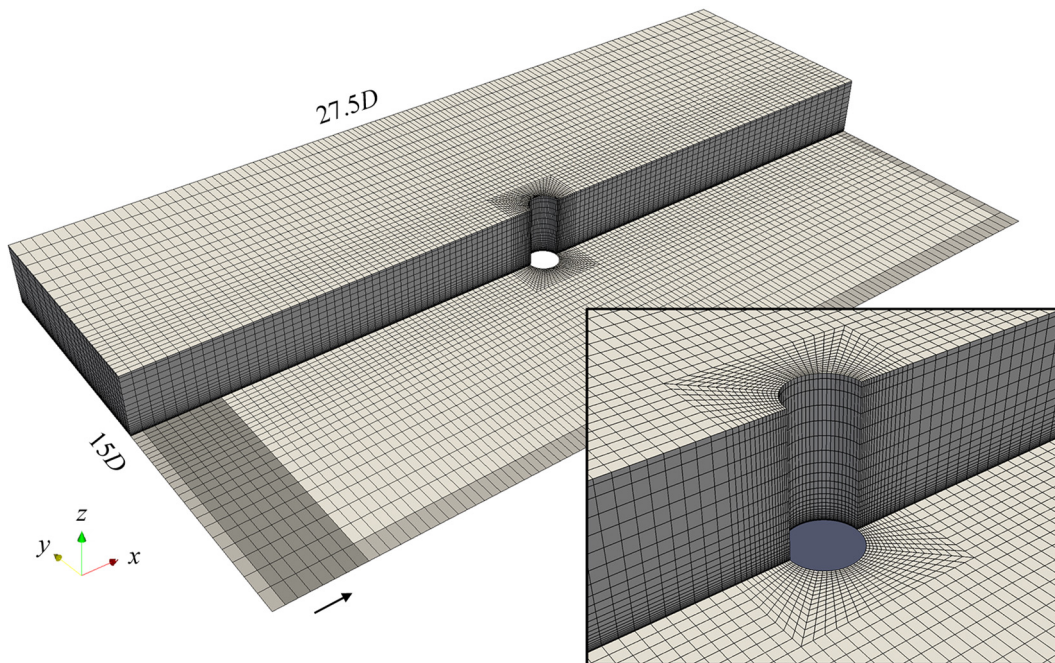


Figure 5.18: OpenFOAM model domain for cylinder scour investigations. Background: overall domain showing slice trough vertical and boundary meshes; front: mesh details around structure, given as cylinder boundary mesh. Arrow gives current direction.

Simulation Results Results of the simulated scour around the vertical, circular cylinder as well as the near-field of the structure are given in figure 5.21 for different moments of the simulation, which was overall run for a period of 90min. Regarding the flow field around cylindrical structures under current flow conditions, the formation of a horseshoe vortex system due to pressure gradients has been discovered as the main mechanism leading to local scour development. Furthermore, flow contraction at the side walls of the cylinder occurs, finally resulting in vortex shedding behind the structure. In the present numerical simulation, all these relevant features could be found well resolved by the flow model, see figures 5.19 and 5.20.

As a consequence, a scour hole with a semi-circular shape is formed around the

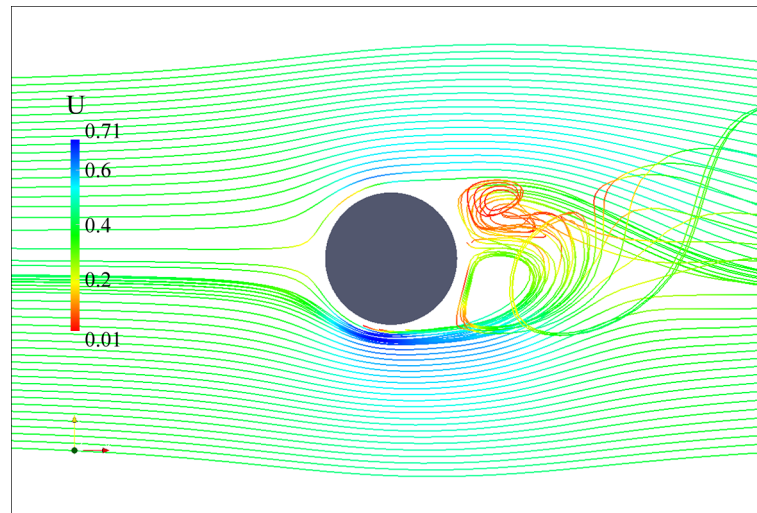


Figure 5.19: Flow field around the cylinder during scour simulation: Stream lines in x, y plane giving vortex shedding behind the cylinder. Velocities given as magnitudes $|\vec{u}|$; flow direction from left to right.

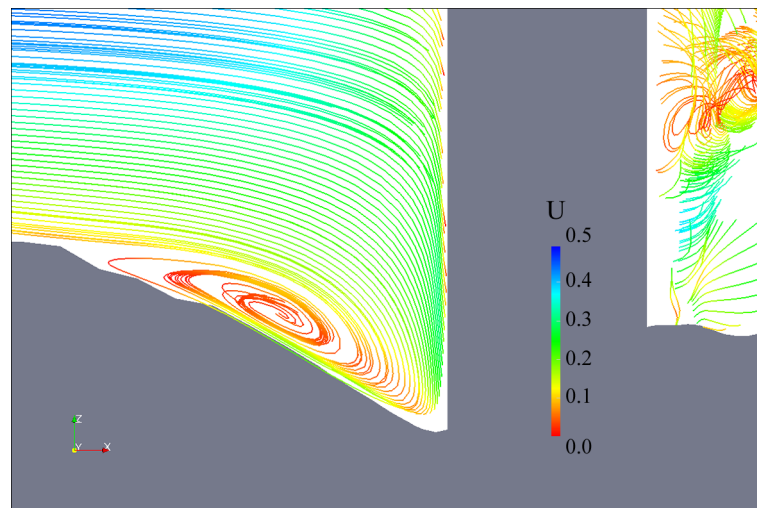


Figure 5.20: Flow field around the cylinder during scour simulation: Stream lines in x, z plane giving horseshoe vortex in developed scour hole upstream of the cylinder. Velocities given as magnitudes $|\vec{u}|$; flow direction from left to right.

cylinder. Deepening of the scour hole thereby takes place very rapidly, as given by the time plot in figure 5.22. The slope angle φ upstream of the cylinder equals the angle of repose $+\Delta\varphi$ in the developed scour hole, while it is less steep in the downstream part. In the first period of the scour development, an accumulation of sediment occurs downstream of the cylinder, resulting from sediment being transported out of the local scour pit, which is then further transported away by the flow during the remaining period of the simulation. The formation of ripples can be observed in the model, which start to develop around the structure first.

Results of the simulated scour depths upstream of the cylinder, which gives the maximum scour depth location, are plotted in figure 5.22 over simulation time. Furthermore, a comparison to experimental data and numerical simulation results from Roulund et al. (2005) and Göthel (2008) is given here.

It can clearly be stated that the present numerical model is capable of simulating the scour development around the cylinder very well. Data compare well to given experimental scour formation, also regarding the time-evolution of the scour depth upstream of the cylinder. At this point it has to be mentioned that the numerical models of Roulund et al. (2005) and Göthel (2008) do not incorporate the effects of suspended sediment transport, which is therefore a clear advancement of the present model approach. Although the model was run for a period of 90min only, it can be expected that final results will not significantly differ from the experimental data, as the general trends are given by the model. In the experiments, a maximum relative scour depth S/D around 1.24 at 180min was found, while the maximum depth in the present model is 1.18, but at 90 min.

5.4.3 Scour around Tripod under Waves

The implemented scour model approach was finally applied to the calculation of local wave-induced scour development around the tripod structure. A model scale of 1:40 was chosen, giving the model scale of the WKS wave flume experiments. Wave boundary conditions were investigated for a regular wave test case, given by test series r2130-01 and w2130-01, respectively (compare table 3.4 and table 5.1).

Model Setup Model parameters with regard to the sediment properties and model coupling are given in table 5.3. The general domain setup including boundary conditions and wave generation techniques was already described in §4.2 (and figure 4.1 therein). The model domain has an overall length of 15m and a width of 2.2m, as can be seen from figure 5.23 giving an overview over the model grid used for the scour simulations. The length of the wave generation zone is defined as 1.5m, based on theoretical considerations on the maximum horizontal displacement of orbital motions. The wave absorption zone has a length of 3.0m, while cells are

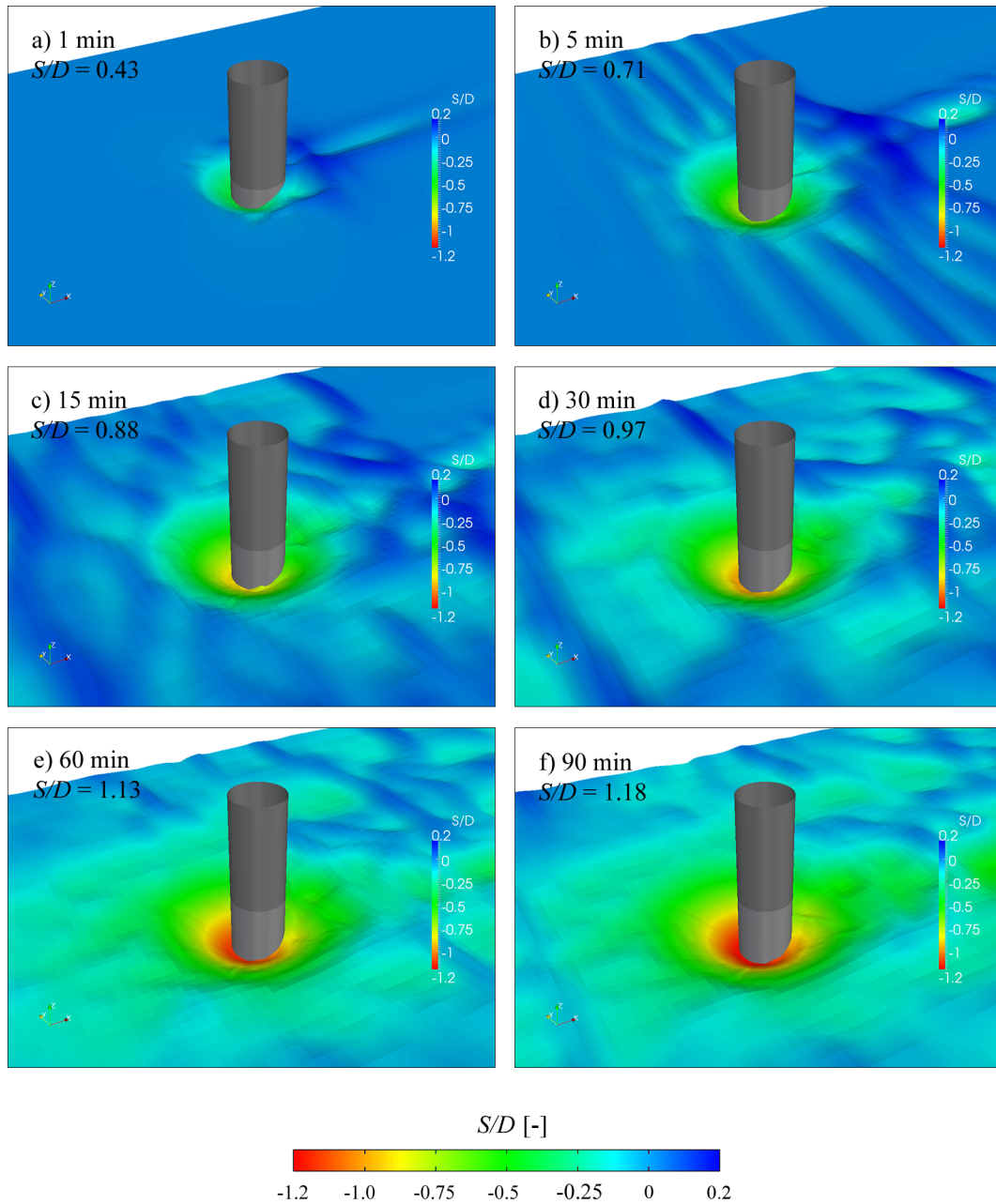


Figure 5.21: Plots of simulated scour around a circular cylinder under steady current flow at the moments of (a) 1min, (b) 5min, (c) 15min, (d) 30min, (e) 60min, (f) 90min. Values S/D in the figures give maximum relative scour depths upstream of the cylinder.

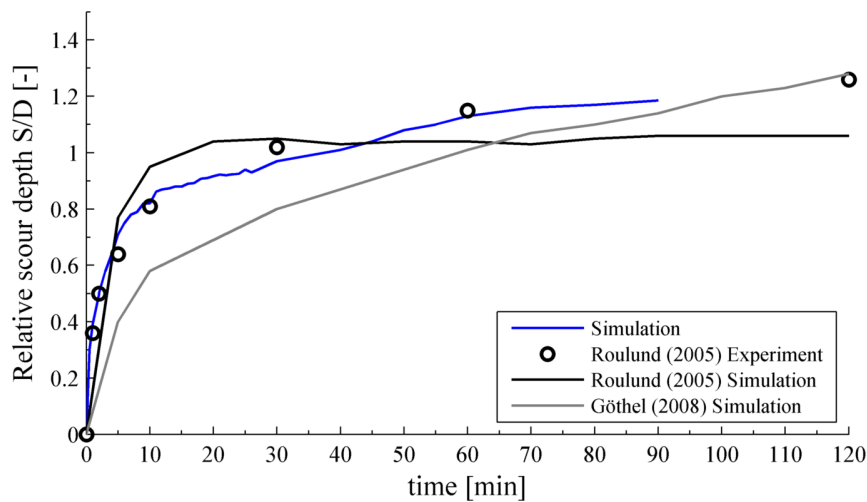


Figure 5.22: Local relative scour depth S/D over time for flow-induced scour at a vertical circular cylinder in comparison with existing data.

further expanded in positive x -direction. Roughness sections between concrete bed and movable bed section have lengths of 0.3m with a grain size of $d_{50} = 0.5\text{mm}$ in the model, while the movable bed itself is 4.0m long and 2.2m wide, i.e. giving the dimensions from the WKS flume setup.

The overall number of cells in the computational domain is approx. 500k. Cell dimensions are in a range of 1.25-5cm in the free field, with the smaller cell sizes in the area of the wave amplitude, 0.2-0.6cm in the near field of the structure (all directions) and approx. 1.5mm at the bottom (vertical) at simulation start, giving a value of $y^+ \approx 1 - 25$ here, see §4.2.3.

A smooth blending between the bed and roughness sections in x -direction was applied, resulting in an overall bed area of 3.0m times 2.2m, in which the mesh motion of the bed and inner nodes is performed. The calculation of entrainment and deposition of suspended particles was however performed in the entire section of the bed in order to smoothly increase the near-bed sediment concentration. Further motion smoothing into the direction of the bed center (x) had to be applied in order to minimize artificial ripple formation in the free areas around the structure.

It further has to be mentioned that for the tripod scour simulation, it was necessary to increase the number of vertical grid cells at the piles in order to sufficiently resolve the flow processes during scour deepening. As this number is fixed during the run and limited by the presence of the lower braces and pile sleeves, a small, circular area around the piles was artificially lowered by 1cm in the mesh generation process, i.e. forming an artificial scour hole here, see figure 5.23. As similar to this, certain scouring could be observed in the WKS experiments while slowly filling the flume, influences on the final scour development and results can be expected to be negligible here.

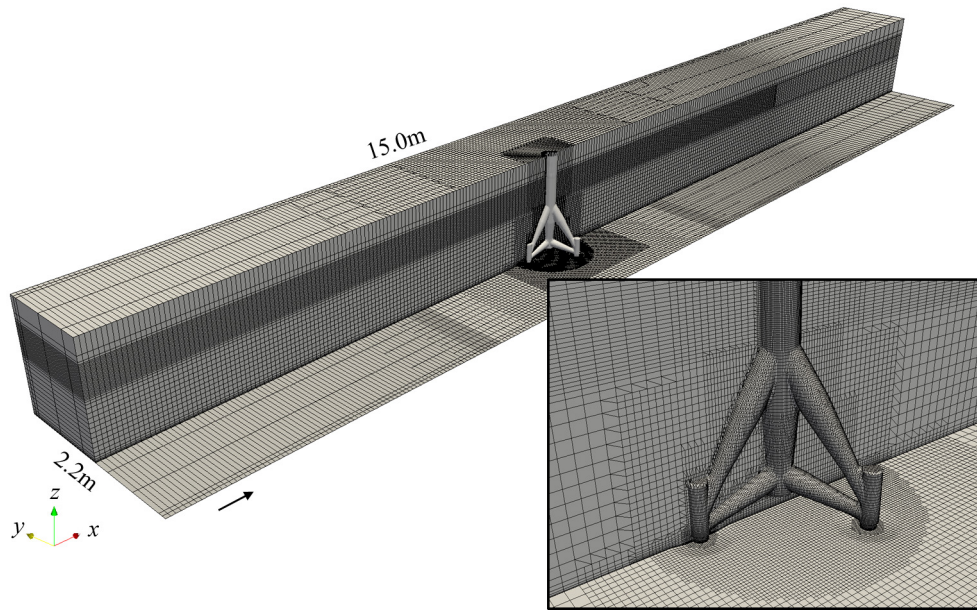


Figure 5.23: OpenFOAM model domain for tripod scour investigations. Background: overall domain showing slice trough vertical and boundary mesh; front: mesh details around structure, given as tripod boundary mesh. Arrow gives direction of wave propagation.

Table 5.3: Model parameters for test series w2130-01.

d_{50} [mm]	w_{so} [m/s]	θ_c [-]	μ_s [-]	μ_d [-]	φ [°]	$\Delta\varphi$ [°]	T [s]	n [-]
0.148	0.0153	0.059	0.58	0.49	30	2	3.0	2-20

Simulation Results Results of scour development simulations around the tripod structure for test series w2130-01 are given in figure 5.24 for the moments after 100, 250, 500, 1000, 2000 and 3000 wave cycles simulated in the model. The duration for the simulation was about 190 hours, computed on a 16-core AMD Opteron 6136 (2.4 GHz) Server node as a parallel computation process.

All in all equal to the findings from the laboratory experiments, it can be seen that the entire scouring process occurs as a local scour formation around the single piles and underneath the main column. Especially regarding the latter section, scour deepening takes place rapidly. A distinct global scour formation around the entire structure cannot be observed. Maximum observed scour depths in the simulation as given in the plots in figures 5.24 to 5.26 reach values of up to about 7cm in the area under the main column, while a depth around 6cm is already reached after 250 wave cycles passing the structure. Regarding a mean value and trend of scour evolution, scour depths under the main column are in a range of 5.5-6.5cm in a later stage, which can be expected as an (almost) equilibrium stage of the simulation. A similar, time-dependent behavior could be observed in the laboratory tests, where

90-100% of the maximum scour depths were reached after a period of 1500 wave cycles. Starting approx. from the time of 500 waves, distinct ripple formation is given in the area around the entire structure and especially in the rear part, while it propagates from the tripod middle section to the side areas.

Regarding the local scour depths around the front and rear piles as well as the maximum depth in the section under the main column, it was found that, in direct comparison to the WKS wave flume experiments, certain deviation is given in the numerical simulations, see figures 5.25 and 5.26 for a comparison. It should be noticed that, for the determination of the local scour depths at the rear piles, the pile shown in front of the given plots was considered. All in all, depths for both rear piles were however in a similar range over the entire simulation period. It is obvious to see that the maximum depths in the section underneath the main column are overpredicted by about 30-40% in the simulation. Furthermore, the location of the scour pit is shifted to the direction of the front pile, see figure 5.28 for a comparison with WKS wave flume experiments.

For the front pile itself, scour depths are in good agreement with experimental data. Scour depths at the rear pile are however underpredicted by about 20% compared to the experimental data. Certain scatter of scour depths over time, especially regarding the piles is given in the numerical model. This behavior is assumed to be mainly resulting from the choice of 20 repeating loops n for the present hydro- and morphodynamic model coupling approach for the bigger part of the simulation time. It can thus be assumed that local depth fluctuations could be minimized with a more frequent update of the flow field after conducting the bed elevation and mesh motion changes.

Regarding the locally underpredicted scour depths at the rear piles, two possible reasons can be given. On the one hand, similar behavior could be observed in other model implementations, see e.g. the work of Liu (2008), where wave-induced scour development around a large circular cylinder was investigated. Maximum scour depths were found in some distance from the structure, while a certain pile-up of sediment was given directly at the cylinder. For the present model, the reason for this behavior could not be fully figured out. It might however be related to a local underprediction of shear stresses under wave conditions directly at the bed-structure interface, as well as the calculation of suspended sediment concentrations in this area, which leads to an eased transport of sediments away from the structure. On the other hand, areal ripple formation was found in the rear part of the tripod as given before, finally influencing the local sediment transport processes here. This can furthermore be confirmed by the difference in scour formation observed directly behind the tripod (see figure 5.28), where slight sediment accumulation is given in the simulation, whereas erosion takes place in the experiments. It was however found in the experimental tests that the latter is assumed to partly be an artificial

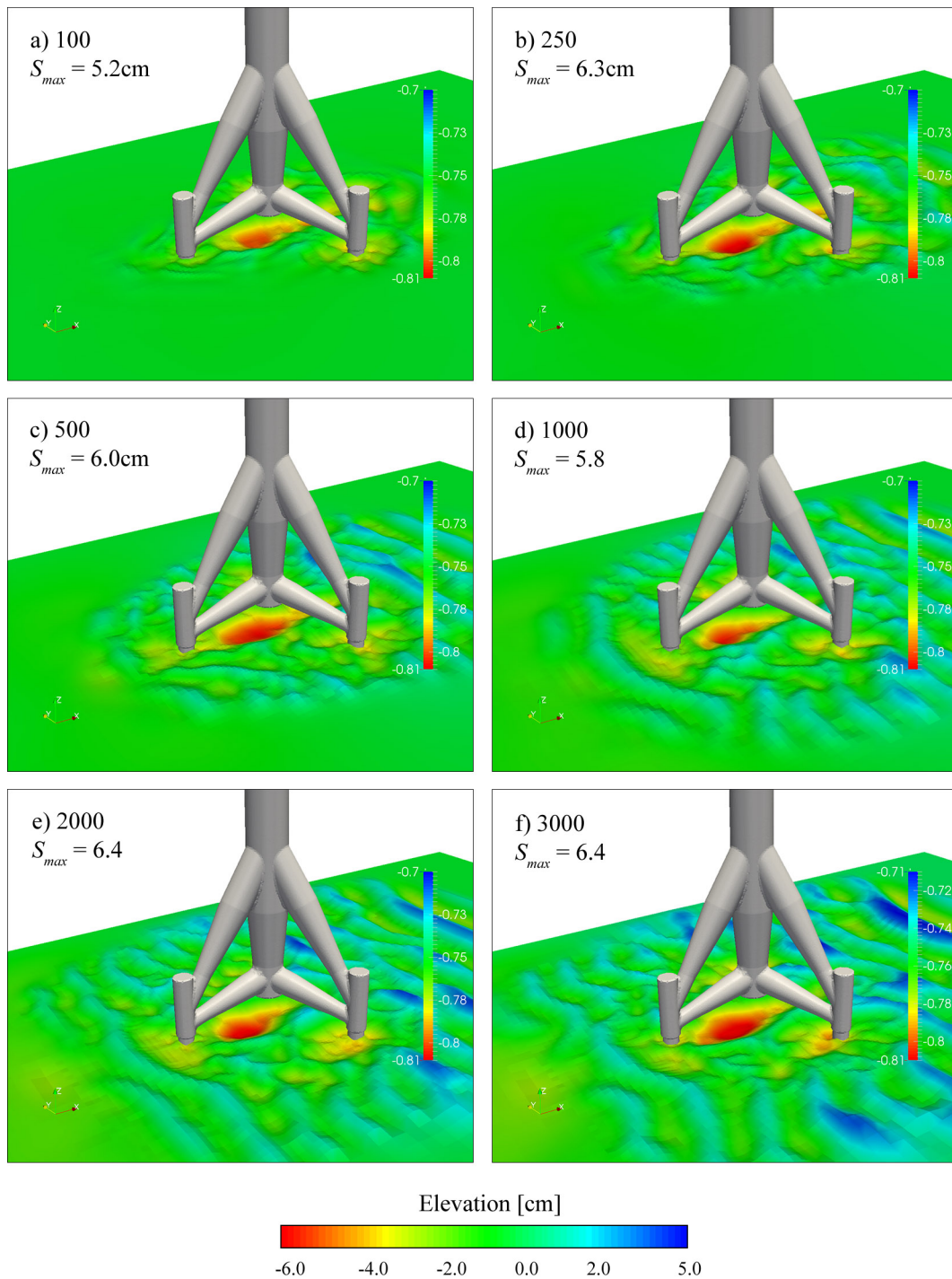


Figure 5.24: Results of numerical scour simulation for test w2130-01, 0°. Plots given at moments of (a) 100, (b) 250, (c) 500, (d) 1000, (e) 2000, (f) 3000 waves. Maximum scour depths depicted in the figures; wave propagation in positive x-direction from left to right.

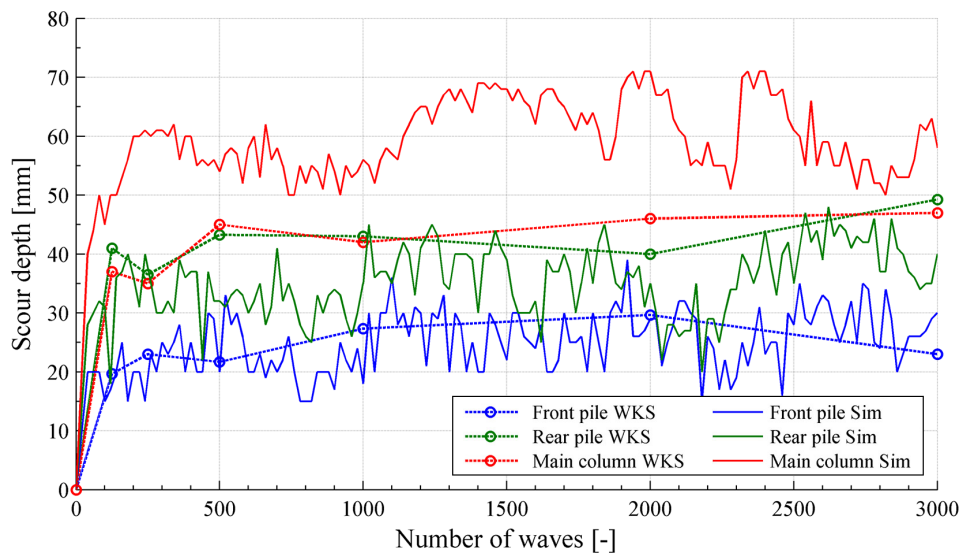


Figure 5.25: Comparison of local scour depths at piles and main column over number of waves for test series r2130-01 (WKS experiment, 'WKS') and w2130-01 (numerical simulation, 'Sim').

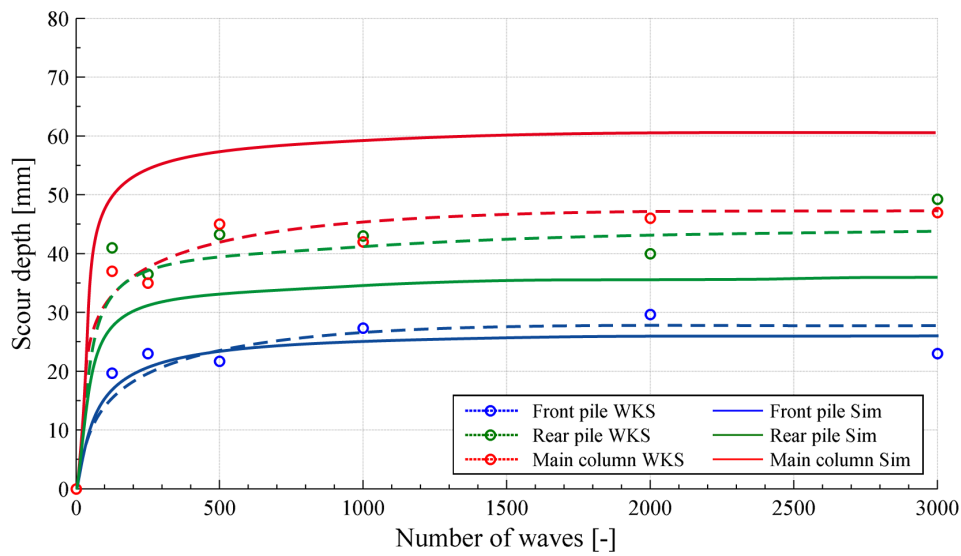


Figure 5.26: Trends of local scour depth evolution at piles and main column over number of waves for test series r2130-01 (WKS experiment, 'WKS') and w2130-01 (numerical simulation, 'Sim').

effect of the experimental setup, as such erosion pattern could not be found in the large-scale GWK wave flume experiments.

Bed shear stresses Regarding the local bed shear stress around the tripod, distributions are plotted in figure 5.27 for the moments of 0, 100, 500 and 2000 wave cycles, while the 0 wave case gives the initial, plane bed stage. The global ripple formation on the bed in case of scouring can clearly be detected from the local shear stresses, as values are comparatively higher at the crests of the bed ripples compared to the lower areas in between, resulting from shadowing effects in the latter case. In comparison to the bed shear stresses in plane bed calculations, local maximum values at the rear piles (giving the overall maximum values here) rapidly decrease over simulation time, resulting from the local scour formation and a thus enlarged flow section between the lower braces and the bed. For the moment after 2000 waves, maximum shear stresses are reduced to around 4.44N/m^2 (7.66N/m^2 in plane bed), while enhanced stress areas can be found almost exclusively on the bed ripple crests, which is however the natural phenomenon for wave-induced bed ripples.

5.4.4 Final Remarks

Some final remarks on the present numerical scour investigations should be given in the following. Regarding the scour development around the circular cylinder, it can be stated that the simulation results stay in very good agreement with experimental data. The model could therefore be verified for the calculation of flow-induced scour around structures. The implemented sand sliding procedure and numerical filter approach applied to topographical changes worked well in the model. Regarding the final filter setup, the choice of filter steps should however be considered carefully, as a too strong, areal filtering would directly have an influence on the final, local scour depths.

For the wave-induced scour development around the tripod structure, certain deviation from experimental data was observed. Despite this, it can however be concluded that hot spots and the overall trends of local scour formation at the tripod structure could be modeled with sufficient quality in the numerical simulation.

The present models were run on comparatively small model scales due to large computational costs even in parallel computations. It can be expected that results will be less influenced from updating and scaling effects as e.g. given in the wave-induced scour calculations when using more frequent flow field updating steps and all in all larger model scales. In order to achieve numerical results for complex flow and scour simulations within acceptable computational times then, either computer clusters based on CPU computing or accelerated calculations based on GPU technology (Graphics Processing Unit) seem to be a promising step forward.

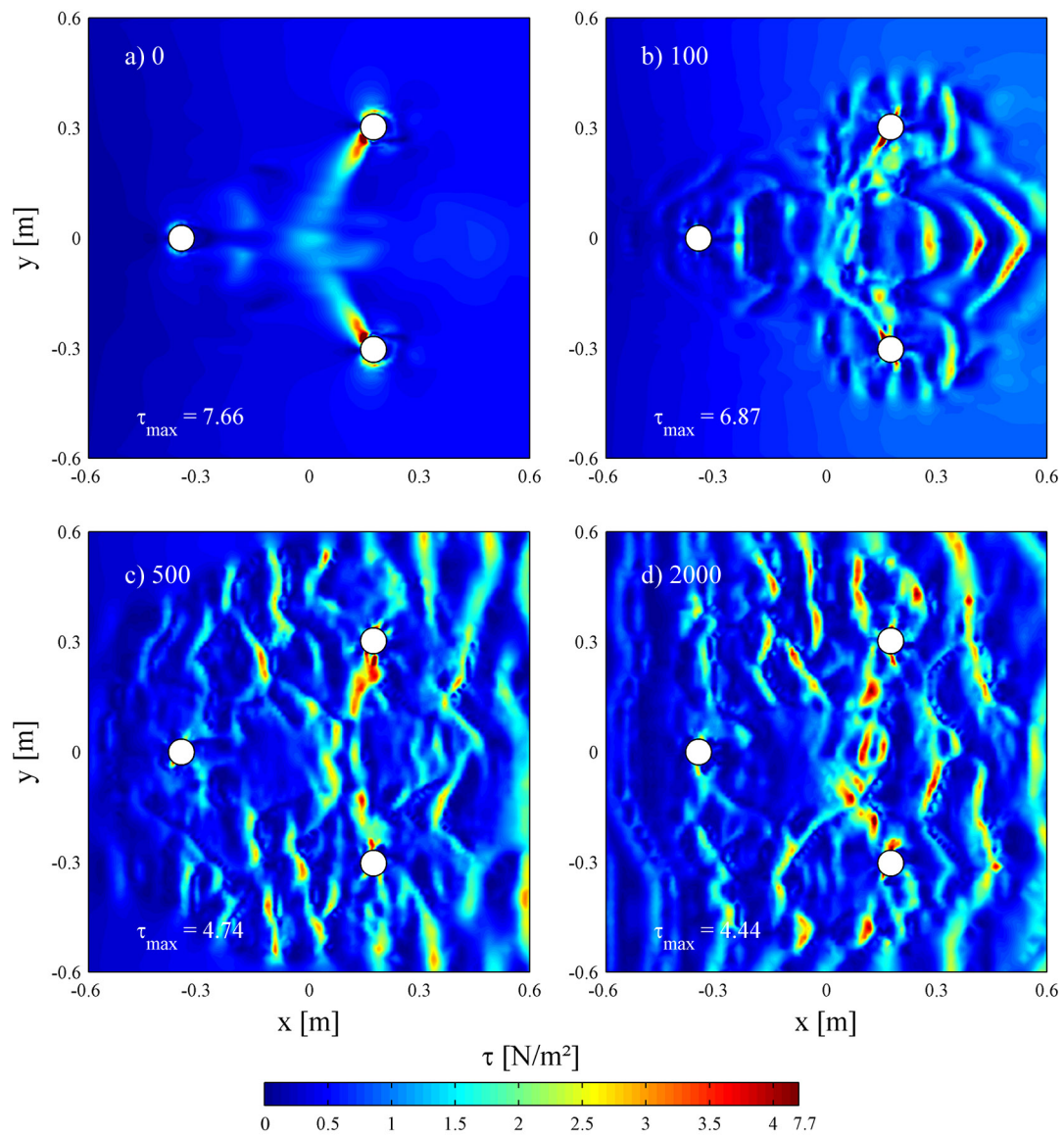


Figure 5.27: Bed shear stress distributions in the scour simulation at the time of (a) 0 waves giving the initial plan bed stage, (b) 100, (c) 500, (d) 2000 waves for the moment of wave crest passage at the centre of the structure. Max. values depicted in the figures.

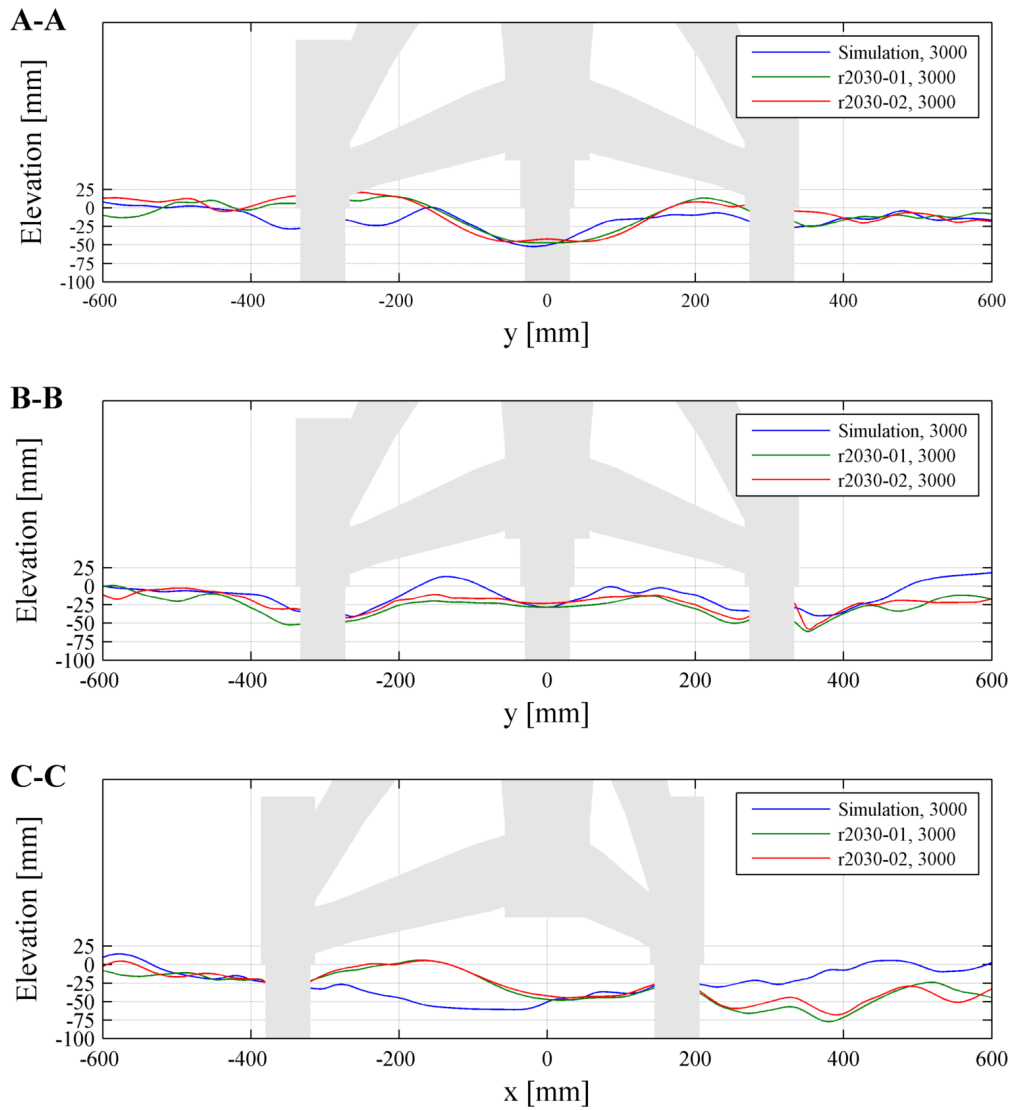


Figure 5.28: Comparison of cross sections for the numerical simulation and experimental results (r2130-01, r2130-02 and w2130-01) at the time step of 3000 wave cycles. Positions A-A, B-B, C-C are given in figure 3.6.

5.5 Conclusions

After the numerical model implementations on flow and scour processes, numerical results of the flow model were first validated against theoretical and experimental data on wave parameters as well as measured flow patterns around the tripod structure, all in all showing fairly good agreement.

Details of flow processes around the tripod, finally leading to enhanced bottom shear stresses and thus sediment mobility could be gained by means of numerical investigations, which have the general advantage of giving more detailed results of processes than could be gained in laboratory tests without tremendous effort. General blockage effects of the structure, especially in regions of the piles and beneath the lower braces and main column section in combination with local vortex formation during wave passage could be identified as the dominant processes for local scour formation.

The distribution of shear stresses under wave load conditions around the tripod structure was simulated for varying wave-encounter angles in the rigid-bed calculations, showing that the developing areas for local scour formation at the tripod in the laboratory tests can be directly detected from the hot spots of increased shear stresses. Locally, amplification factors of shear stresses around the foundation piles hold values around 8-13 at the beginning of the scour process. Furthermore, the influence of single load components on the total shear stress for an extreme event case, i.e. current flow alone, wave load and combined wave-current load was investigated. For the given event, local shear stresses at the foundation under combined load are up to a factor of 5 times higher than calculated by a simple addition of the single load component results, leading to the assumption that the maximum scour depths will be reached here.

The implemented sediment transport model approach was finally applied to the simulation of scour development for different structures under wave and current load. In a first step, the model was validated against experimental data and further numerical results for a vertical cylinder under steady current load, given in Roulund et al. (2005). The resulting scour depths and scour shape were found to agree fairly good with the observations in the experiments. In a second step, the model was validated against results on wave-induced scour development at the tripod structure derived from the small-scale laboratory tests. It was shown that scour patterns around the foundation, giving local scours at the single piles and under the main column as well as a global scour development could be reproduced with sufficient quality in the model. Deviance in local scour depths could however be observed at the single piles, while a certain shift of maximum scour depth was found in the section under the main column. It can however be assumed that those differences rather result from the load boundary conditions than from the transport model

implementation itself.

Despite this deviance in local scour results given above, it can generally be concluded that the present numerical model implementation is capable of simulating all relevant flow and sediment transport processes as well as load conditions for investigations on complex foundation structures. Although only scour development for a single tripod installation under wave conditions and a circular cylinder under current flow were actually tested, the general applicability to other structures and load conditions should be possible, as the model framework was developed in a flexible way. The numerical model can therefore serve as a valuable tool for complex structure investigations and structural optimization processes in engineering operations. Besides direct scour simulations, rigid-bed calculations can be used for a determination of regions exposed to high shear stresses, which can be applied for a first estimation of possible scour protection mechanisms. The present model generally has an advantage over other existing models, as to the author's knowledge, none of the existing approaches as referred to in this work are directly applicable for investigations on complex structures as it was carried out in the present work.

6 Summary & Outlook

The main objective of present investigations was to gain deeper knowledge of flow and scour evolution at complex foundation structures for offshore wind turbines, as it is given for tripod foundations, in order to improve scour prediction and reduce uncertainties in the dimensioning process, allowing more efficient foundation constructions in the future. In this context, investigations on local scour processes around a tripod foundation were carried out using a combined modeling approach, consisting of both laboratory experiments and numerical investigations on flow and scour processes. By this means, crucial insights and advancement of knowledge on scour development at and in the vicinity of tripod foundation structures could be achieved, which have not been available beforehand.

6.1 Experimental Investigations

In order to gain general knowledge of physical processes under wave load conditions, local and global scour development as well as local flow pattern leading to scour, physical model tests were carried out in wave flumes on two different model scales of $\lambda = 40$ and $\lambda = 12$. Small-scale laboratory tests, mainly in order to investigate the general scouring phenomena, were carried out in the wave flume of the Franzius-Institute, while large-scale model tests were carried out in the Large Wave Flume (GWK) in Hanover. As boundary conditions for the test series, several regular wave and JONSWAP wave spectra combinations were tested, while the tripod foundations were installed with varying wave-encounter angles in the flumes. Measurement of scour development was carried out by means of both point-wise and areal recording techniques. Furthermore, flow patterns around the structure were measured in the laboratory tests for a validation of numerical flow results.

As a main result of the investigation, it can be concluded that scour formation around the structure differs significantly from typical scour patterns that can be observed at single vertical pile structures. Three main regions of scour formation can thus be determined for a tripod structure under the given load conditions:

1. around the single piles, while larger depths can be found at the rear piles,
2. under the main column giving maximum depth values and the lower braces connected to the rear pile sleeves and
3. a global scour formation around the entire structure.

The overall scour pattern shows a combination of local and global scour formation, which was found to be more distinct in the large-scale tests. Furthermore, the characteristics of scour development at the structure depends significantly on the

incoming wave direction, as scour patterns differ depending on the wave-encounter angles. Maximum relative scour depths S/D of up to 1.13 at the piles and 0.63 beneath the main column could be observed in the large-scale experiments for the given wave conditions, with D as the diameter of the piles and the lower main column, respectively.

Suspended sediment transport could be determined as the dominant transport process for the given cases. Scour patterns resulting from wave spectra were found to be less pronounced than those from regular wave load tests with similar boundary condition parameters. Compared to in-situ measurements from a prototype foundation, at least a qualitatively good agreement between scour patterns could be achieved, showing that the global scour formation could be reproduced with sufficient quality in the large-scale model tests.

Further comparison of local scours at the structure showed larger depths in the large-scale tests compared to the small-scale findings when using equal, scaled boundary conditions, while the mean depth-increase factor was found to be around 1.7, mainly resulting from the fact that equal sediments with a median grain diameter of $d_{50} = 0.148\text{mm}$ were used as model sediment in both setups. The influence of mud mat installations, which are circular discs between the piles and the pile-sleeves for installation purposes, was further investigated in the laboratory tests, showing that local scour depths are reduced by 20-50% compared to those depths without mud mat installation.

6.2 Numerical Investigations

For numerical investigations on flow and scour processes, a fully three-dimensional numerical model using the Volume of Fluid method was applied within the OpenFOAM software framework in the present setup, solving the Reynolds Averaged Navier-Stokes equations in combination with a $k - \omega SST$ turbulence closure model. Wave, current and combined load conditions using free-surface modeling were generated on the basis of appropriate boundary conditions and wave damping at the domain outlet. Regular waves were simulated mainly based on 5th order Stokes wave theory, while a wave generation zone technique as given in Jacobsen et al. (2012) was finally applied. For wave spectra considerations, representative regular wave parameters were generated, while the translation coefficients resulted from scour considerations derived from the laboratory experiments.

In order to capture the relevant sediment transport processes leading to local scour, a sediment transport model including both bed load and suspended load was implemented in the code. The description of acting forces was carried out in vectorial form, including slope-dependent parameter modifications and a sediment sliding procedure. For bed load, the approach of Engelund and Fredsøe (1976) was applied,

while a new model approach for the suspended load was chosen, giving all in all better agreement with experimental data. Furthermore, new moving mesh approaches were implemented in order to ensure numerical stability when investigating complex foundation structure geometries. The hydro- and morphodynamic model coupling was carried out by means of a semi-strong coupling procedure. As sediment transport and local scour processes typically need long-term simulations and are therefore very time-consuming, parallel code implementations and computations were used throughout.

Numerical results of the flow model were validated against theoretical and experimental data on wave parameters and measured flow patterns around the tripod structure, all in all showing fairly good agreement. Details of flow processes around the tripod structure, finally leading to enhanced bed shear stresses and thus sediment mobility could be gained by means of numerical investigations, which have the general advantage of giving more detailed results of processes than could be gained in laboratory tests without tremendous effort. General blockage effects of the structure, especially in regions of the piles and beneath the lower braces and main column section in combination with local vortex formation during wave passage could be identified as the dominant processes for local scour formation.

The distribution of shear stresses under wave load conditions around the tripod structure was simulated for varying wave-encounter angles in rigid-bed calculations, showing that the developing areas for local scour formation at the tripod in the laboratory tests can be directly detected from the hot spots of increased shear stresses. Locally, amplification factors of shear stresses around the foundation piles hold values around 8-13 at the beginning of the scour process. Furthermore, the influence of single load components on the total shear stress for an extreme event case, i.e. current flow, wave load and combined wave-current load was investigated. For the given event, local shear stresses at the foundation under combined wave-current load are up to a factor of 5 times higher than calculated by a simple addition of the single load component results, leading to the assumption that the maximum scour depths will be reached here.

The implemented sediment transport model approach was finally applied to the simulation of scour development for different structures under wave and current load. In a first step, the model was validated against experimental data and further numerical results for a vertical cylinder under steady current load, given in Roulund et al. (2005). The resulting scour depths and scour shape were found to agree well with the observations in the experiments, although simulated scour depths were slightly lower in the end. In a second step, the model was validated against results on wave-induced scour development at the tripod structure derived from the small-scale laboratory tests. It was shown that scour patterns around the foundation, giving local scours at the single piles and under the main column as well as a global scour

development could be reproduced with sufficient quality in the model. Deviance in local scour depths could however be observed at the single piles, while a certain shift of maximum scour depth was found in the section under the main column. It can however be assumed that those differences rather result from the load boundary conditions than from the transport model implementation itself.

Despite this deviance in local scour results given above, it can generally be concluded that the present numerical model implementation is capable of simulating all relevant flow and sediment transport processes as well as load conditions for investigations on complex foundation structures. Although only scour development for a single tripod installation under wave conditions and a circular cylinder under current flow were actually tested, the general applicability to other structures and load conditions should be possible, as the model framework was developed in a flexible way. The model can therefore serve as a valuable tool for investigations on complex structures and structural optimization processes in engineering operations. Besides direct scour simulations, rigid-bed calculations can be used for a determination of regions exposed to high shear stresses, which can be applied for a first estimation of possible scour protection mechanisms. Although directly related, investigations on scour protection mechanisms were however not regarded in this thesis, as the focus of the investigations was on the scour development processes itself. The knowledge gained on physical processes leading to scour and the use of numerical modeling can however be directly applied for a further development of countermeasures.

The present model generally has an advantage over other existing models, as to the author's knowledge, none of the existing approaches as referred to in this work are directly applicable for investigations on complex structures as it was carried out in the present work.

6.3 Improvements and Future Work

Although the general applicability of the present modeling approach for scour investigation on foundation structures could be shown, an improvement of single methods could lead to further knowledge. Improvements can thereby be given as mainly to categories, while the first is related to the numerical and experimental modeling approach and the second one to general considerations on the present topic.

The coupling between hydro- and morphodynamic model components was carried out by repetition of pre-calculated flow periods, until the developing flow field after a morphological update was recalculated. A more frequent recalculation of the flow field would presumably lead to improved results regarding local scour development, as especially calculated shear stresses are only valid for small changes in bed geometry. The implemented VOF approach was found to cause velocity fluctuations at the water-air interface, reducing the time step of the calculations. Furthermore,

wave damping was found to occur in combination with the turbulence model application. Improvements in this field would therefore lead to a better representation of wave loads and further reduce computational times.

In the present model, only uniform sediments can be considered. A fractionated sediment transport approach would enable investigations on natural sediment distributions. Furthermore, a soil model could further incorporate influences on local scour processes. Approaches are e.g. given in Göthel (2008) and Liu (2008). Due to the presently applied wave generation approach, a coupling with other numerical codes, e.g. based on potential flow theory, should be fairly easy to set up in order to improve wave boundary conditions with regard to more realistic scenarios from the laboratory experiments.

As a direct application of the present model, further combinations of load conditions, i.e. wave and (tidal) current load with varying directions should be investigated in order to gain further knowledge on scour patterns and decisive load conditions. Furthermore, simulations based on larger model scales can be applied to a determination of scaling effects in the model, especially considering the model sediment.

Regarding the scaling effects observed by the comparison of small- and large-scale experimental results, future works using artificial, lightweight materials in small-scale tests would presumably lead to improved results and provide further knowledge on general scaling effects. New or modified scaling approaches might however be necessary for wave load considerations.

It was furthermore found by the study and by comparison of existing approaches for both bed load and suspended load as well as for the general initiation of motion, that related empirical works are mainly based on considerations for pure current flow situations. As local pressure and flow processes under waves and especially under combined load may however differ significantly in the near-bed region, improvements on transport and entrainment approaches may be necessary.

References

- Afshar, M. A. (2010). Numerical Wave Generation in OpenFOAM®. Master's thesis, Department of Shipping and Marine Technology, Chalmers University of Technology, Göteborg, Sweden. Report No. X-10/252.
- Amoudry, L. (2008). A review on coastal sediment transport modelling. POL Internal Document 189, Proudman Oceanographic Laboratory, Liverpool, U.K.
- Amoudry, L., Hsu, T.-J., and Liu, P. L.-F. (2005). Schmidt number and near-bed boundary condition effects on a two-phase dilute sediment transport model. *Journal of Geophysical Research C: Oceans*, 110(9):1–12.
- Bagnold, R. A. (1954). Experiments on the gravity-free dispersion of large spheres in a newtonian fluid under shear. In *Royal Soc., London*, number Proc. A 225, 49.
- Bagnold, R. A. (1966). Sediment transport problem from general physics. Geological Survey Professional Paper 422-I, United States Department of the Interior.
- Beek, F. V. and Wind, H. (1990). Numerical modeling of erosion and sedimentation around offshore pipelines. *Coastal Engineering*, 14:107–128.
- Bettess, R. (1990). *Survey of lightweight sediments for use in mobile-bed physical models*. Movable Bed Physical Models. Kluwer Academic Publishers, Dordrecht.
- Brørs, B. (1999). Numerical modeling of flow and scour at pipelines. *Journal of Hydraulic Engineering*, 125(5):511–522.
- BSH (2007). Standard - Konstruktive Ausführung von Offshore-Windenergieanlagen. No. 7005, Bundesamt für Seeschifffahrt und Hydrographie, Hamburg.
- Callaghan, D. P., Saint-Cast, F., Nielsen, P., and Baldock, T. E. (2006). Numerical solutions of the sediment conservation law; a review and improved formulation for coastal morphological modelling. *Coastal Engineering*, 53:557–571.
- Camenen, B. (2007). Simple and general formula for the settling velocity of particles. *Journal of Hydraulic Engineering*, 133(2):229–233.
- Cao, Y., Beck, R., and Schultz, W. (1993). An absorbing beach for numerical simulations of nonlinear waves in a wave tank. In *8th International Workshop on Water Waves and Floating Bodies*. St. John's, Canada.
- Cebeci, T. and Chang, K. C. (1978). Calculation of incompressible rough-wall boundary-layer flows. *AIAA Journal*, 16(7):730–735.

- CEM (2002). *Coastal Engineering Manual - Part VI*. U.S. Army Corps of Engineers, U.S. Army Corps of Engineers, Washington, D.C., EM 1110-2-1100 edition.
- Cheng, N.-S. (2002). Exponential formula for bedload transport. *Journal of Hydraulic Engineering*, 128(10):942–946.
- Clément, A. (1996). Coupling of two absorbing boundary conditions for 2d time-domain simulations of free surface gravity waves. *Journal of Computational Physics*, 126:139–151.
- Damgard, J. S., Whitehouse, R. J. S., and Soulsby, R. L. (1997). Bed-load sediment transport on steep longitudinal slopes. *Journal of Hydraulic Engineering*, 123(12):1130–1138.
- Davies, A. G. and Li, Z. (1997). Modelling sediment transport beneath regular symmetrical and asymmetrical waves above a plane bed. *Continental Shelf Research*, 17(5):555–582.
- de Sonnevile, B., Rudolph, D., and Raaijmakers, T. C. (2010). Scour reduction by collars around offshore monopiles. In *Proceedings ICSE-5*, San Francisco.
- den Boon, J. H., Sutherland, J., Whitehouse, R., Soulsby, R., Stam, C. J. M., Verhoeven, K., Hogedal, M., and Hald, T. (2004). Scour behaviour and scour protection for monopile foundations of offshore wind turbines. In *Proceedings EWEC 2004*.
- Dey, S. (1999). Time-variation of scour in the vicinity of circular piers. In *Proceedings of the ICE - Water Maritime and Energy*, volume 136, pages 67–75.
- DHI (2007). Borkum West - Hydrographische Standortbedingungen. Modellierung und Statistische Analyse. Technical report, Danish Hydraulic Institute DHI, Syke, Germany.
- Dietrich, W. E. (1982). Settling velocity of natural particles. *Water Resources Research*, 18(6):1615–1626.
- DIN (2009). DIN EN 61400-3. Windenergieanlagen - Teil 3: Auslegungsanforderungen für Windenergieanlagen auf offener See. IEC 61400-3:2009, Deutsches Institut für Normung e.V.
- DNV (2013). Design of Offshore Wind Turbine Structures. Offshore Standard DNV-OS-J101, Det Norske Veritas AS.
- Duc, B., Wenka, T., and Rodi, W. (2004). Numerical modeling of bed deformation in laboratory channel. *Journal of Hydraulic Engineering*, 130(9):894–904.

- Durran, D. R. (2001). Open boundary conditions: Fact and fiction. In Hodnett, P. F., editor, *IUTAM Symposium on Advances in Mathematical Modelling of Atmosphere and Ocean Dynamics*, pages 1–18. Kluwer Acad., Norwell Mass.
- Eadie, R. and Herbich, J. (1986). Scour about a single cylindrical pile due to combined random waves and a current. In *Coastal Engineering Proceedings*, pages 1858–1870.
- Einstein, H. A. (1950). The bed-load function for sediment transport in open channel flow. Technical Bulletin 1026, U.S. Dept. of Agriculture, Washington, D.C.
- Engelund, F. and Fredsøe, J. (1976). A sediment transport model for straight alluvial channels. *Nordic Hydrology*, 7:293–306.
- Ettmer, B. (2007). Physikalische Modellierung von Kolkprozessen. *Mitteilungsblatt der Bundesanstalt für Wasserbau*, 90:107–118.
- Exner, F. M. (1925). Über die Wechselwirkung zwischen Wasser und Geschiebe in Flüssen. Sitzungsbericht 134, Akad. der Wissenschaft Wien, Math.-Naturwiss., Abt. 2a.
- Fernandez Luque, R. (1974). *Erosion and transport of bed-load sediment*. PhD thesis, Department of Hydraulic Engineering, Delft University of Technology.
- Ferziger, J. H. and Peric, M. (2008). *Numerische Strömungsmechanik*. Springer-Verlag, Berlin, Heidelberg.
- Fredsøe, J. and Deigaard, R. (1995). *Mechanics of Coastal Sediment Transport*. Advanced Series on Ocean Engineering - Volume 3. World Scientific.
- Fuhrmann, D., Madsen, P., and Bingham, H. (2006). Numerical simulation of lowest-order short-crested wave instabilities. *Journal of Fluid Mechanics*, 563:415–441.
- Fuhrmann, D. R., Dixen, M., and Jacobsen, N. G. (2010). Physically-consistent wall boundary conditions for the k-omega turbulence model. *Journal of Hydraulic Research*, 48(6):793–800.
- Galassi, M., Davies, J., Theiler, J., Gough, B., Jungman, G., Alken, P., Booth, M., and Rossi, F. (2011). *GNU Scientific Library, Reference Manual*, 1.15 edition.
- Garcia, M. H. and Parker, G. (1991). Entrainment of bed sediment into suspension. *Journal of Hydraulic Engineering*, 117(4):414–435.
- GL (2005). Guideline for the Certification of Offshore Wind Turbines.
- Graf, W. H. (1984). *Hydraulics of sediment transport*. McGraw-Hill, New-York.

- Göthel, O. (2008). *Numerical modelling of flow and wave induced scour around vertical circular piles*. Bericht Nr. 76, Universität Hannover, Institut für Strömungsmechanik und Elektronisches Rechnen im Bauwesen.
- Guy, H. P., Simons, D. B., and Richardson, E. V. (1966). Summary of alluvial channel data from flume experiments, 1956-61. Professional Papers 462-1, U.S. Geological Survey, Washington, D.C.
- Hansen, M. (2011). Probabilistic safety assessment of offshore wind turbines. Annual report 2010, Leibniz Universität Hannover, Hannover, Germany.
- Hasbo, P. B. (1995). *Flow and Sediment Transport over Oblique Bed Forms*. Series paper no. 60, Institute of Hydrodynamics and Hydraulic Engineering, Technical University of Denmark.
- Hildebrandt, A. and Schlurmann, T. (2012). Wellenbrechen an Offshore Tripod-Gründungen. Versuche und Simulationen im Vergleich zu Richtlinien. *Bautechnik*, 89(5):301–308.
- Hirt, C. W. and Nichols, B. D. (1981). Volume of fluid (vof) method for the dynamics of free boundaries. *Journal of Computational Physics*, 39(1):201–225.
- Hoffmanns, G. J. C. M. and Verheij, H. J. (1997). *Scour Manual*. Balkema, Rotterdam.
- Hogedal, M. and Tue, H. (2005). Scour assessment and design for scour for monopile foundations for offshore wind turbines. In *Copenhagen Offshore Wind 2005*.
- Huang, C.-J., Zhang, E.-C., and Lee, J.-F. (1998). Numerical simulation of nonlinear viscous wavefields generated by a piston-type wavemaker. *Journal of Engineering Mechanics*, 124(10):1110–1120.
- Hughes, S. A. (1993). *Physical Models and Laboratory Techniques in Coastal Engineering*. World Scientific.
- Issa, R. I. (1986). Solution of the implicitly discretized fluid-flow equations by operator-splitting. *Journal of Computational Physics*, 62(1):40–65.
- Jacobsen, N. G. (2011). *A Full Hydro- and Morphodynamic Description of Breaker Bar Development*. DCAMM Special Report No. S136, Department of Mechanical Engineering, Technical University of Denmark.
- Jacobsen, N. G., Fuhrmann, D. R., and Fredsøe, J. (2012). A Wave Generation Toolbox for the Open-Source CFD Library: OpenFOAM®. *Int. J. Numer. Meth. Fluids*, 70:1073–1088.

- Jasak, H. (1996). *Error Analysis and Estimation for the Finite Volume Method with Applications to Fluid Flows*. PhD thesis, Imperial College of Science, Technology and Medicine.
- Jasak, H. and Tukovic, Z. (2007). Automatic mesh motion for the unstructured finite volume method. *Transactions of FAMENA*, 30(6):1–18.
- Jensen, J. H., Madsen, E. O., and Fredsøe, J. (1999). Oblique flow over dredged channels. ii: Sediment transport and morphology. *Journal of Hydraulic Engineering*, 125:1190–1198.
- Jiménez, J. A. and Madsen, O. S. (2003). A simple formula to estimate settling velocity of natural sediments. *Journal of Waterway, Port, Coastal and Ocean Engineering*, 129(2):70–78.
- Kalitzin, G., Medic, G., Iaccarino, G., and Durbin, P. (2005). Near-wall behavior of rans turbulence models and implications for wall functions. *Journal of Computational Physics*, 204:265–291.
- Kassiotis, C. (2008). Which strategy to move the mesh in the computational fluid dynamics code openfoam. Report for openfoam phd course at chalmers university of technology, École Normale Supérieure de Cachan, France.
- Kawata, Y. and Tsuchiya, Y. (1988). Local scour around cylindrical piles due to waves and currents combined. In *Proceedings 21st International Conference on Coastal Engineering*, number 21.
- Kovacs, A. and Parker, G. (1994). A new vectorial bedload formulation and its application to the time evolution of straight river channels. *Journal of Fluid Mechanics*, 267:153–183.
- Kubatko, E. J. and Westerink, J. J. (2007). Exact discontinuous solutions of exner’s bed evolution model: Simple theory for sediment bores. *Journal of Hydraulic Engineering*, 133:305–311.
- Lal, A. and Elangovan, M. (2008). CFD simulation and validation of flap type wave-maker. In *Proceedings of World Academy of Science, Engineering and Technology*, volume 36, pages 76–82.
- Lambers-Huesmann, M. and Zeiler, M. (2010). Personal communication on scour depths in the alpha ventus test site.
- Lau, L. Y. and Engel, P. (1999). Inception of sediment transport on steep slopes. *Journal of Hydraulic Engineering*, 125(5):544–547.

- Lesser, G., Roelvink, J., van Kester, J., and Stelling, G. (2004). Development and validation of a three-dimensional morphological model. *Coastal Engineering*, 51(8-9):883–915.
- Li, F. and Cheng, L. (2001). Prediction of lee-wake scouring of pipelines in currents. *Journal of Waterway, Port, Coastal and Ocean Engineering*, 127(2):106–112.
- Li, S. S., Millar, R. G., and Islam, S. (2008). Modelling gravel transport and morphology for the fraser river gravel reach, british columbia. *Geomorphology*, 95(3-4):206–222.
- Liang, D., Cheng, L., and Li, F. (2005). Numerical modeling of flow and scour below a pipeline in currents part ii. scour simulation. *Coastal Engineering*, 52(1):43–62.
- Link, O. (2006). *Untersuchung der Kolkung an einem schlanken zylindrischen Pfeiler in sandigem Boden*. PhD thesis, Technische Universität Darmstadt, Institut für Wasserbau und Wasserwirtschaft.
- Liu, P. L.-F., Al-Banaa, K. A., and Cowen, E. A. (2004). *Water Wave Induced Boundary Layer Flows above a Rippled Bed*, volume 9 of *PIV and Water Waves. Advances in Coastal and Ocean Engineering*. World Scientific.
- Liu, X. (2008). *Numerical Models for Scour and Liquefaction around Object under Currents and Waves*. Ph.d. thesis, University of Illinois at Urbana and Champaign.
- Long, W., Kirby, J. T., and Shao, Z. (2008). A numerical scheme for morphological bed level calculation. *Coastal Engineering*, 55:167–180.
- Luque, R. F. and van Beek, R. (1976). Erosion and transport of bed-load sediment. *Journal of Hydraulic Research*, 14(2):127–144.
- Madsen, O. S. and Grant, W. D. (1976). Quantitative description of sediment transport by waves. In *Proceedings of the 15th International Conference on Coastal Engineering*.
- Melville, B. W. and Coleman, S. E. (2000). *Bridge Scour*. Water Resources Publications, LLC, Colorado.
- Menter, F. R. (2009). Review of the shear-stress transport turbulence model experience form an industrial perspective. *International Journal of Computational Fluid Dynamics*, 23(4):305–316.
- Menter, F. R. and Esch, T. (2001). Elements of industrial heat transfer prediction. In *Proceedings of the 16th Brazilian Congress of Mechanical Engineering (COBEM)*.

- Meyer-Peter, E. and Müller, R. (1948). Formulas for bed-load transport. In *Proceedings of the 2nd Meeting of the International Association for Hydraulic Structures Research*, pages 39–64.
- Morgan, G., Zang, J., Greaves, D., Heath, A., Whitlow, C., and Young, J. (2010). Using the rasInterFoam CFD model for wave transformation and coastal modelling. In *Proceedings of 32nd Conference on Coastal Engineering, Shanghai, China*.
- Myrhaug, D. and Rue, H. (2005). Scour around group of slender vertical piles in random waves. *Applied Ocean Research*, 27(1):56–63.
- Nezu, I. (1977). *Turbulent Structure in Open Channel Flows*. PhD thesis, Kyoto University, Japan.
- Nielsen, P. (1992). *Coastal bottom boundary layers and sediment transport*. World Scientific, Singapore.
- Niemann, S. L., Fredsøe, J., and Jacobsen, N. G. (2011). Sand dunes in steady flow at low froude numbers: Dune height evolution and flow resistance. *Journal of Hydraulic Engineering*, 137(1):5–14.
- Nikuradse, J. (1933). Strömungsgesetze in rauhen Röhren. Technical Report 4, VDI-Forschungsheft.
- Noh, W. F. and Woodward, P. (1976). Slic (simple line interface calculation). In van de Vooren & P.J. Zandbergen, A., editor, *Proceedings of 5th International Conference of Fluid Dynamics*, volume 59 of *Lecture Notes in Physics*, pages 330–340.
- Olsen, N. and Melaaen, M. (1993). Three-dimensional calculation of scour around cylinders. *Journal of Hydraulic Engineering*, 119(9):1048–1054.
- Olsen, N. R. B., Hilde, M., and Kjellesvig, M. (1998). Three-dimensional numerical flow modeling for estimation of maximum local scour depth. *Journal of Hydraulic Research*, 36(4):579–590.
- Orlanski, I. (1976). A simple boundary condition for unbounded hyperbolic flows. *Journal of Computational Physics*, 21(3):251–269.
- Park, J., Kim, M., and Miyata, H. (1999). Fully non-linear free-surface simulations by a 3D viscous numerical wave tank. *Int. J. Numer. Meth. Fluids*, 29:685–703.
- Raudkivi, A. J. (1990). *Loose boundary hydraulics. 3rd edition*. Pergamon Press, Oxford, U.K.

- RAVE (2010). RAVE - Research at alpha ventus. Eine Forschungsinitiative des Bundesministeriums. Fraunhofer-Institut für Windenergie und Energiesystemtechnik IWES, Kassel, Germany.
- Richardson, J. F. and Zaki, W. N. (1954). Sedimentation and fluidisation. Part 1. *Trans. Inst. Chem. Eng.*, 32:35–53.
- Rodi, W. (1997). Comparison of les and rans calculations of the flow around bluff bodies. *Journal of Wind Engineering and Industrial Aerodynamics*, 69-71:55–75.
- Rodi, W., Ferziger, J., Breuer, M., and Pourquié, M. (1997). Status of large eddy simulation: Results of a workshop. *Journal of Fluids Engineering*, 119:248–262.
- Romate, J. (1992). Absorbing boundary conditions for free surface waves. *Journal of Computational Physics*, 99:135–145.
- Roulund, A. (2000). *Three-dimensional numerical modelling of flow around a bottom-mounted pile and its application to scour*. Series paper no. 70, Technical University of Denmark, Department of Hydrodynamics and Water Resources.
- Roulund, A., Sumer, B. M., Fredsøe, J., and Michelsen, J. (2005). Numerical and experimental investigation of flow and scour around a circular pile. *Journal of Fluid Mechanics*, 534:351–401.
- Rouse, H. (1938). *Nomogram for the settling velocity of spheres*. National Research Council, Division of Geology and Geography.
- Rubey, W. W. (1933). Settling velocities of gravel, sand and silt particles. *Am. Jour. Sci.*, 25:325–338.
- Rudolph, D. and Bos, K. J. (2006). Scour around a monopile under combined wave-current conditions and low kc -numbers. In *Proceedings of the International Conference on Scour and Erosion*.
- Rudolph, D., Bos, K. J., Luijendijk, A. P., Rietema, K., and Out, J. M. M. (2004). Scour around offshore structures - analysis of field measurements. In *Proceedings 2nd International Conference on Scour and Erosion*, volume 1, pages 400–407.
- Ryu, S., Kim, M. H., and Lynett, P. J. (2003). Fully nonlinear wave-current interactions and kinematics by a BEM-base numerical wave tank. *Computational Mechanics*, 32:336–346.
- Saito, E. and Shibayama, T. (1992). Local scour around a large circular cylinder on the uniform bottom slope due to waves and currents. In *Proceedings of the 23rd Coastal Engineering Conference*, pages 2799–2810.

- Schlichting, H. and Gersten, K. (2006). *Grenzschichttheorie*. Springer-Verlag, Berlin, Heidelberg, New York.
- Shepard, D. (1968). A two-dimensional interpolation function for irregularly-spaced data. In *Proceedings 1968 ACM National Conference*, pages 517–524.
- Shields, A. (1936). *Anwendung der Aehnlichkeitsmechanik und der Turbulenzforschung auf die Geschiebebewegung*. Number 26 in Mitteilungen der Preußischen Versuchsanstalt für Wasserbau und Schiffbau. Technische Hochschule Berlin, Germany.
- Shih, T.-S., Povinelly, L., Liu, N.-S., Potapczuk, M., and Lumley, J. (1999). A generalized wall function. Technical Report NASA/TM-1999-209398, National Aeronautics and Space Administration NASA, Glenn Research Center.
- Smith, J. D. and McLean, S. (1977). Spatially averaged flow over a wavy surface. *Journal of Geophysical Research*, 83:1735–1746.
- Smith, K. R. (2009). Computation of viscous multiphase hydrodynamics and ship motions during wave-slap events and wave excited roll. Master’s thesis, Pennsylvania State University, The Graduate School, College of Engineering.
- Soulsby, R. L. (1997). *Dynamics of marine sands: a manual for practical applications*. Thomas Telford, London.
- Soulsby, R. L. and Clarke, S. (2005). Bed shear-stresses under combined waves and currents on smooth and rough beds. Report TR 137, HR Wallingford.
- Soulsby, R. L., Hamm, L., Klopmann, G., Myrhaug, D., Simons, R. R., and Thomas, G. P. (1993). Wave-current interaction within and outside the bottom boundary layer. *Coastal Engineering*, 21(1-3):41–69.
- Stahlmann, A. and Schlurmann, T. (2010). Physical Modeling of Scour around Tripod Foundation Structures for Offshore Wind Energy Converters. In *Coastal Engineering Proceedings*, 1(32).
- Stahlmann, A. and Schlurmann, T. (2012a). Investigations on scour at tripod foundations [Kolkbildung an komplexen Gründungsstrukturen für Offshore-Windenergieanlagen: Untersuchungen zu Tripod-Gründungen in der Nordsee]. *Bautechnik*, 89(5):293–300.
- Stahlmann, A. and Schlurmann, T. (2012b). Investigations on Scour Development at Tripod Foundations for Offshore Wind Turbines: Modeling and Application. In *Coastal Engineering Proceedings*, 1(33).

- Sumer, B. M., Chua, L. H. C., Cheng, N.-S., and Fredsøe, J. (2003). Influence of turbulence on bed load sediment transport. *Journal of Hydraulic Engineering*, 129(8):585–596.
- Sumer, B. M. and Fredsøe, J. (2002). *The Mechanics of Scour in the Marine Environment*. World Scientific Pub. Co. Inc., 1st edition.
- Sumer, B. M., Fredsøe, J., Christensen, S., and Lind, M. T. (1999). Sinking/floatation of pipelines and other objects in liquefied soil under waves. *Coastal Engineering*, 38(2):53–90.
- Sumer, B. M., Hatipoglu, F., and Fredsøe, J. (2007). Wave scour around a pile in sand, medium dense, and dense silt. *Journal of Waterway, Port, Coastal, and Ocean Engineering*, 133(1):14–27.
- Sumer, B. M., Whitehouse, R. J. S., and Torum, A. (2001). Scour around coastal structures: a summary of recent research. *Coastal Engineering*, 44(2):153–190.
- Tukovic, Z. (2005). *Metoda Kontrolnih Volumena Na Domenama Promjenjivog Oblika*. PhD thesis, University of Zagreb. In Croatian Language.
- Ubbink, O. (1997). *Numerical prediction of two fluid systems with sharp interface*. PhD thesis, University of London, Imperial College of Science, Technology & Medicine.
- Ubbink, O. and Issa, R. I. (1999). A method for capturing sharp fluid interfaces on arbitrary meshes. *Journal of Computational Physics*, 153:26–50.
- Ungruh, G. and Zielke, W. (2003). Kolkberechnung an Offshore-Bauwerken: a state of the art review. Technical report, Institut für Strömungsmechanik und Elektronisches Rechnen im Bauwesen, Universität Hannover.
- van den Eynden, D., Brabant, R., Fettweis, M., Francken, F., Melotte, J., Sas, M., and van Lancker, V. (2010). Monitoring of hydrodynamic and morphological changes at the c-power and the belwind offshore wind farm sites. chapter 3: A synthesis. Technical report, Royal Belgium Institute of Natural Sciences, and International Marine and Dredging Consultants.
- van Driest, E. R. (1956). On turbulent flow near a wall. *Journal of Aeronautic Sciences*, 23(11):1007–1036.
- van Rijn, L. C. (1984a). Sediment pickup functions. *Journal of Hydraulic Engineering*, 110:1494–1502.
- van Rijn, L. C. (1984b). Sediment transport, part I: Bed load transport. *Journal of Hydraulic Engineering - ASCE*, 110(10):1431–1456.

- van Rijn, L. C. (1984c). Sediment transport, part II: Suspended load transport. *Journal of Hydraulic Engineering - ASCE*, 110(11):1613–1641.
- van Rijn, L. C. (1993). *Principles of sediment transport in rivers, estuaries and coastal seas*. Aqua Publications, Amsterdam.
- Wang, H.-W., Huang, C.-J., and Wu, J. (2007). Simulation of a 3D numerical viscous wave tank. *Journal of Engineering Mechanics*, 133(7):761–772.
- Wang, R.-K. and Herbich, J. B. (1983). Combined current and wave-produced scour around a single pile. CEO Report 269, Texas Eng. Expt. Station, Dept. Civ. Eng., Texas Univ. System.
- Warner, J. C., Sherwood, C. R., Signell, R. P., Harris, C. K., and Arango, H. G. (2008). Development of a three-dimensional, regional, coupled, wave, current and sediment transport model. *Computers and Geosciences*, 34:1284–1306.
- Weilbeer, H. (2001). *Numerische Simulation von Strömung und Kolkung an Wasserbauwerken*. Bericht Nr. 66, Universität Hannover, Institut für Strömungsmechanik und Elektronisches Rechnen im Bauwesen.
- Weller, H. G., Tabor, G., Jasak, H., and Fureby, C. (1998). A tensorial approach to computational continuum mechanics using object-oriented techniques. *Computers in Physics*, 12(6):620–631.
- Whitehouse, R. (1998). *Scour at Marine Structures: A Manual for Practical Applications*. Thomas Telford Ltd., London.
- Whitehouse, R., Harris, J., Sutherland, J., and Rees, J. (2008). An assessment of field data for scour at offshore wind turbine foundations. In *Proceedings 4th International Conference on Scour and Erosion*.
- Whitehouse, R. J. S., Harris, J. M., Sutherland, J., and Rees, J. (2011). The nature of scour development and scour protection at offshore windfarm foundations. *Marine Pollution Bulletin*, 62:73–88.
- Wilcox, D. C. (1998). *Turbulence Modeling for CFD*. DCW Industries, Inc., La Canada, 2nd edition.
- Wilcox, D. C. (2006). *Turbulence Modeling for CFD*. DCW Industries, Inc., La Canada, 3rd edition.
- Wilson, K. C. (1966). Bed-load transport at high shear stress. *Journal of the Hydraulics Division*, 92(6):49–59.

- Wilson, K. C. (1977). Analysis of bed-load motion at high shear stress. *Journal of Hydraulic Engineering*, 113(1):97–103.
- Wu, W. (2004). Depth-averaged two-dimensional numerical modeling of unsteady flow and nonuniform sediment transport in open channels. *Journal of Hydraulic Engineering*, 130(10):1013–1024.
- Wu, W., Rodi, W., and Wenka, T. (2000). 3d numerical modeling of flow and sediment transport in open channels. *Journal of Hydraulic Engineering*, 126(1):4–15.
- Yalin, M. S. and Karahan, E. (1979). Inception of sediment transport. *Journal of the Hydraulics Division*, 105(11):1433–1443.
- Zanke, U. (1977). *Berechnung der Sinkgeschwindigkeit von Sedimenten*, volume 46 of *Mitteilungen des Franzius-Instituts für Wasserbau*. Technische Universität Hannover, Germany.
- Zanke, U. (1982a). *Grundlagen der Sedimentbewegung*. Springer-Verlag, Berlin, Heidelberg, New York.
- Zanke, U. (1982b). *Kolke am Pfeiler in richtungskonstanter Strömung und unter Welleneinfluß*, volume 54 of *Mitteilungen des Franzius-Instituts für Wasserbau und Küsteningenieurwesen*. Universität Hannover, Germany.
- Zanke, U. C. E., Hsu, T.-W., Roland, A., Link, O., and Diab., R. (2011). Equilibrium scour depths around piles in noncohesive sediments under currents and waves. *Coastal Engineering*, 58:986–991.
- Zyserman, J. A. and Fredsøe, J. (1994). Data analysis of bed concentration of suspended sediment. *Journal of Hydraulic Engineering*, 120:1021–1042.

List of Figures

2.1	Boundary layer development and universal y^+ distribution. Symbols in (b): dots: measured, solid line: best fit, dashed line: approximation functions.	6
2.2	Current velocity profiles in smooth and rough bed conditions. Modified after van Rijn (1993).	7
2.3	Compilation of eight different prediction models for bed shear stress calculation under combined wave-current load, giving the effect of the load components on the resulting stresses τ_m and τ_{max} . Taken from Soulsby and Clarke (2005).	11
2.4	Modified Shields diagram for initiation of motion of particles, from Sumer and Fredsøe (2002).	13
2.5	Driving and stabilizing forces acting on a bed particle during flow. .	15
3.1	Sketch of the experimental setup in the WKS wave flume. Tripod structure is given symbolically.	33
3.2	Tripod installation in the WKS wave flume for scour experiments. .	34
3.3	Sieve analysis of bed material for scour experiments, $d_{50} = 0.148\text{mm}$. .	35
3.4	Pictures giving LDS Laser distance sensor for surface profile collection and ADV flow measuring probe with positioning platform.	37
3.5	ADV measuring positions in horizontal (x,y) plane. Crosses give data positions applied for numerical model verification, see §5.2.2.	39
3.6	Results of scour development for test series r2130-01 after 3000 wave cycles, (a) front view, (b) rear view. Cross section positions for figure 3.10 are given in upper plot (a). Wave-encounter angle 0°	42
3.7	Erosion and transport of suspended particles at the rear pile at different time steps during wave passage for test series r2130-03. $H_m=20.6\text{cm}$, $T_m=3.0\text{s}$, $d=0.75\text{m}$, 0° wave encounter angle. Arrows in lower left corners give current near-bottom flow direction.	44
3.8	Surface elevation and vortex formation during wave passage at the tripod main column at time steps of (a) wave crest, (b) wave trough passage. Wave-encounter angle 0° . Wave direction from upper left to lower right corner.	45
3.9	Results of scour development for test series r2130-01 in the WKS wave flume experiments at time steps of 250, 500, 1000, 2000, 4000 and 6000 wave cycles.	46
3.10	Cross sections for test series r2130-01 at time steps of 250, 500, 1000, 2000 and 6000 wave cycles. Positions A-A, B-B and C-C are given in figure 3.6.	47

3.11	Development of local scour depths over time for test series r2130-01, given as local mean values over number of wave cycles. Symbols: dots: moments of record; dashed lines: connection for clarity; solid lines: trends of scour evolution.	48
3.12	Comparison of cross sections for test series r2130-01 and r2130-02 at the time step of 3000 wave cycles. Positions A-A, B-B and C-C are given in figure 3.6.	49
3.13	Results of scour development for test series r2130-04 after 3000 wave cycles, (a) front view, (b) rear view. Wave-encounter angle 180° . . .	51
3.14	Results of scour development for test series r2130-05 after 3000 wave cycles, (a) front view, (b) rear view. Wave-encounter angle 90° . . .	52
3.15	Results of scour development for test series s2130-02 after 3000 wave cycles, (a) front view, (b) rear view. Wave-encounter angle 0°	55
3.16	Comparison of cross sections for test series r2130-01, r1523-01 and s2130-02 at the time step of 4000 wave cycles. Positions A-A, B-B, C-C are given in figure 3.6.	56
3.17	Sketch of the experimental setup in the GWK wave flume. Tripod structure is given symbolically.	57
3.18	Tripod installation in the GWK wave flume for scour experiments. .	58
3.19	Multi-beam echo sounder and positioning platform installation for collection of bed surface profiles during GWK scour experiments. .	59
3.20	Echo sounder and underwater camera installation for point-wise, continuous scour recording in the GWK experiments.	60
3.21	Scour development for test series r7655-01 and r7655-02 after 3000 wave cycles in the GWK wave flume. Direction of wave propagation is from front to back.	62
3.22	Results of scour development for test series r7655-01 after 3000 wave cycles, (a) front view, (b) rear view. Cross section positions for figure 3.10 are given in upper plot (a). Wave-encounter angle 0°	63
3.23	Development of local scour depths over time for test series r7655-01, given as local mean values over number of wave cycles. Symbols: dots: moments of record; dashed lines: connection for clarity; solid lines: trends of scour evolution.	64
3.24	Results of scour development for test series r7655-02 after 3000 wave cycles, (a) front view, (b) rear view. Cross section positions for figure 3.10 are given in upper plot (a). Wave-encounter angle 180° . . .	65
3.25	Results of scour development for test series s7255-02 after 3000 wave cycles, (a) front view, (b) rear view. Cross section positions for figure 3.10 are given in upper plot (a). Wave-encounter angle 0°	66

3.26	Comparison of cross sections for test series r7655-01, s7255-02 at the time step of 3000 wave cycles. Positions A-A, B-B, C-C are given in figure 3.22.	67
3.27	Plot of scour depths from a multi-beam survey at the M7 tripod in the alpha ventus test site. Record from April 2010, given as 1x1m grid values. Modified after Lambers-Huesmann and Zeiler (2010). . .	68
3.28	Comparison of local relative scour depths S/D over time for test series r2130-01 and r7655-01 (reduced by 13%), given as local values over number of wave cycles. Symbols: dots: 1:40 test records; light dashed lines: 1:12 test records; thick lines: trends of scour evolution.	71
4.1	Sketch of the numerical model domain including wave generation and absorption zones. The location of foundation structure is represented by a vertical pile for simplicity.	82
4.2	Schematic diagram of the numerical model domain as vertical slice in an area without foundation structure, giving the horizontal layering method of the model grid.	84
4.3	Detail of the OpenFOAM computational grid for flow and scour simulations for the tripod structure. Grid given as slice trough vertical as well as bottom and tripod structure boundary mesh.	85
4.4	Sketch of the η_b blending function variation in the wave generation and absorption zones. Modified after Jacobsen (2011).	93
4.5	Sketch of the mapping procedure between 3D FVM flow model domain and 2D FAM bottom boundary mesh.	95
4.6	Sketch of forces acting on the particle on a sloping bed.	96
4.7	Sketch of the distance-based mesh motion functionality.	111
4.8	Flow chart of the flow field and sediment transport model coupling procedure during scour simulation process.	116
5.1	Comparison of surface elevation between model results, laboratory experiments and wave theory at location $x = 0.0\text{m}$ (main column axis).	118
5.2	Comparison of theoretical and modeled horizontal velocity profiles at location $x = 0.0\text{m}$ (main column axis) for one wave passage. Times from left to right: 1.5s (wave trough), 2.25s (zero-crossing), 0.5s, 2.7s and 3.0s (wave crest).	119
5.3	Comparison of local flow components in numerical model and experiment at position 3 around tripod structure.	121
5.4	Comparison of local flow components in numerical model and experiment at position 7 around tripod structure.	122
5.5	Comparison of local flow components in numerical model and experiment at position 14 around tripod structure.	123

- 5.6 Calculated flow pattern around tripod at $t = 0\text{s}$ (wave crest passage) for test series w2130-01 as cross sections for (a) x, y plane at $z = -0.74\text{m}$, (b) x, y plane at $z = -0.70\text{m}$, (c) x, z plane at $y = 0.0\text{m}$ and (d) y, z plane at $x = 0.15\text{m}$. Velocities are given as magnitudes $|\vec{u}|$ 125
- 5.7 Calculated flow pattern around tripod at $t = 0.75\text{s}$ (zero crossing) for test series w2130-01 as cross sections for (a) x, y plane at $z = -0.74\text{m}$, (b) x, y plane at $z = -0.70\text{m}$, (c) x, z plane at $y = 0.0\text{m}$ and (d) y, z plane at $x = 0.15\text{m}$. Velocities are given as magnitudes $|\vec{u}|$ 126
- 5.8 Calculated flow pattern around tripod at $t = 1.5\text{s}$ (wave trough passage) for test series w2130-01 as cross sections for (a) x, y plane at $z = -0.74\text{m}$, (b) x, y plane at $z = -0.70\text{m}$, (c) x, z plane at $y = 0.0\text{m}$ and (d) y, z plane at $x = 0.15\text{m}$. Velocities are given as magnitudes $|\vec{u}|$ 127
- 5.9 Calculated flow pattern around tripod at $t = 2.25\text{s}$ (zero crossing) for test series w2130-01 as cross sections for (a) x, y plane at $z = -0.74\text{m}$, (b) x, y plane at $z = -0.70\text{m}$, (c) x, z plane at $y = 0.0\text{m}$ and (d) y, z plane at $x = 0.15\text{m}$. Velocities are given as magnitudes $|\vec{u}|$ 128
- 5.10 Bed shear stress distributions for wave-encounter angles (a) 0° , (b) 180° and (c) 90° . Moments of wave crest (left) and wave trough (right) passage at centre of structure. 132
- 5.11 Amplification factors for figure 5.10a, test series w2130-01. Moments of wave crest (left) and wave trough (right) passage at centre of structure. Shear stress τ_0 corresponds to wave crest passage in undisturbed case. 133
- 5.12 Bed shear stress distributions for (a) current, (b) wave and (c) wave-current load. Moments of wave crest (left) and wave trough (right) passage at centre of structure. In plot (a), right is same as left, but using different color coding. 134
- 5.13 Calculated bed shear stress distributions (left) and flow pattern (right) for wave load cases w2130-01 (a) and w2130-02 (b), 1:40 model scale, given at moments of wave crest passage at centre of structure. Shear stress given at bed boundary; flow field given as cross section in x, y plane at $z = -0.70\text{m}$ as magnitude $|\vec{u}|$. Max. values depicted in the figures. 137
- 5.14 Calculated bed shear stress distributions (left) and flow pattern (right) for wave load cases w2130-03 (a) and w2330-01 (b), 1:40 model scale, given at moments of wave crest passage at centre of structure. Shear stress given at bed boundary; flow field given as cross section in x, y plane at $z = -0.70\text{m}$ as magnitude $|\vec{u}|$. Max. values depicted in the figures. 138

5.15	Calculated bed shear stress distribution (left) and flow pattern (right) for wave load case w7655-01, 1:12 model scale, given at moment of wave crest passage at centre of structure. Shear stress given at bed boundary; flow field given as cross section in x, y plane at $z = -2.33\text{m}$ as magnitude $ \vec{u} $. Max. values depicted in the figures.	139
5.16	Present suspended sediment reference concentration (c_b) approach (red line) in comparison with existing approaches and data from literature.	141
5.17	Test setup for cylinder scour experiments, from Roulund et al. (2005).	142
5.18	OpenFOAM model domain for cylinder scour investigations. Background: overall domain showing slice through vertical and boundary meshes; front: mesh details around structure, given as cylinder boundary mesh. Arrow gives current direction.	143
5.19	Flow field around the cylinder during scour simulation: Stream lines in x, y plane giving vortex shedding behind the cylinder. Velocities given as magnitudes $ \vec{u} $; flow direction from left to right.	144
5.20	Flow field around the cylinder during scour simulation: Stream lines in x, z plane giving horseshoe vortex in developed scour hole upstream of the cylinder. Velocities given as magnitudes $ \vec{u} $; flow direction from left to right.	144
5.21	Plots of simulated scour around a circular cylinder under steady current flow at the moments of (a) 1min, (b) 5min, (c) 15min, (d) 30min, (e) 60min, (f) 90min. Values S/D in the figures give maximum relative scour depths upstream of the cylinder.	146
5.22	Local relative scour depth S/D over time for flow-induced scour at a vertical circular cylinder in comparison with existing data.	147
5.23	OpenFOAM model domain for tripod scour investigations. Background: overall domain showing slice through vertical and boundary mesh; front: mesh details around structure, given as tripod boundary mesh. Arrow gives direction of wave propagation.	148
5.24	Results of numerical scour simulation for test w2130-01, 0° . Plots given at moments of (a) 100, (b) 250, (c) 500, (d) 1000, (e) 2000, (f) 3000 waves. Maximum scour depths depicted in the figures; wave propagation in positive x-direction from left to right.	150
5.25	Comparison of local scour depths at piles and main column over number of waves for test series r2130-01 (WKS experiment, 'WKS') and w2130-01 (numerical simulation, 'Sim').	151
5.26	Trends of local scour depth evolution at piles and main column over number of waves for test series r2130-01 (WKS experiment, 'WKS') and w2130-01 (numerical simulation, 'Sim').	151

5.27	Bed shear stress distributions in the scour simulation at the time of (a) 0 waves giving the initial plan bed stage, (b) 100, (c) 500, (d) 2000 waves for the moment of wave crest passage at the centre of the structure. Max. values depicted in the figures.	153
5.28	Comparison of cross sections for the numerical simulation and experimental results (r2130-01, r2130-02 and w2130-01) at the time step of 3000 wave cycles. Positions A-A, B-B, C-C are given in figure 3.6. .	154
A.1	Results of scour development for test series r2130-02 in the WKS wave flume experiments at time steps of 500, 1000, 2000 and 3000 wave cycles. Wave-encounter angle 0°	183
A.2	Results of scour development for test series r2130-02 after 3000 wave cycles, (a) front view, (b) rear view. Cross section positions for figure A.3 are given in upper plot (a).	184
A.3	Cross sections for test series r2130-02 at time steps of 500, 1000, 2000 and 3000 wave cycles. Positions A-A, B-B and C-C are given in figure A.2.	185
A.4	Comparison of cross sections for test series r2130-01 and r2130-02 at the time step of 500 wave cycles. Positions A-A, B-B and C-C are given in figure 3.9.	186
A.5	Comparison of cross sections for test series r2130-01 and r2130-02 at the time step of 1000 wave cycles. Positions A-A, B-B and C-C are given in figure 3.9.	187
A.6	Comparison of cross sections for test series r2130-01 and r2130-02 at the time step of 2000 wave cycles. Positions A-A, B-B and C-C are given in figure 3.9.	188
A.7	Results of scour development for test series r2130-03 in the WKS wave flume experiments at time steps of 250, 500, 1000, 2000 and 3000 wave cycles. Wave-encounter angle 0°	189
A.8	Results of scour development for test series r2130-03 after 3000 wave cycles, (a) front view, (b) rear view. Cross section positions for figure 3.10 are given in upper plot (a). Wave-encounter angle 0°	190
A.9	Cross sections for test series r2130-03 at time steps of 250, 500, 1000, 2000 and 3000 wave cycles. Positions A-A, B-B and C-C are given in figure A.8.	191
A.10	Results of scour development for test series r2130-04 in the WKS wave flume experiments at time steps of 250, 500, 1000, 2000 and 3000 wave cycles. Wave-encounter angle 180°	192
A.11	Results of scour development for test series r2130-05 in the WKS wave flume experiments at time steps of 250, 500, 1000, 2000 and 3000 wave cycles. Wave-encounter angle 90°	193

A.12	Results of scour development for test series r1523-01 in the WKS wave flume experiments at time steps of 1000, 2000, 3000 and 4000 wave cycles. Wave-encounter angle 0°	194
A.13	Results of scour development for test series r1523-01 after 3000 wave cycles, (a) front view, (b) rear view. Wave-encounter angle 0°	195
A.14	Cross sections for test series r1523-01 at time steps of 1000, 2000, 3000 and 4000 wave cycles. Positions A-A, B-B and C-C are given in figure A.13.	196
A.15	Comparison of cross sections for test series r2130-01, r1523-01 and s2130-02 at the time step of 3000 wave cycles. Positions A-A, B-B and C-C are given in figure 3.9.	197
A.16	Results of scour development for test series s2130-02 in the WKS wave flume experiments at time steps of 1000, 2000, 3000 and 4000 wave cycles. Wave-encounter angle 0°	198
A.17	Cross sections for test series s2130-02 at time steps of 1000, 2000, 3000 and 4000 wave cycles. Positions A-A, B-B and C-C are given in figure 3.15.	199
B.1	Results of scour development for test series r7655-01 in the GWK wave flume experiments at time steps of 500, 1000, 2000 and 3000 wave cycles. Wave-encounter angle 0°	200
B.2	Cross sections for test series r7655-01 at time steps of 500, 1000, 2000 and 3000 wave cycles. Positions A-A, B-B and C-C are given in figure 3.22.	201
B.3	Results of scour development for test series r7655-02 in the GWK wave flume experiments at time steps of 500, 1000, 2000 and 3000 wave cycles. Wave-encounter angle 180°	202
B.4	Cross sections for test series r7655-02 at time steps of 500, 1000, 2000 and 3000 wave cycles. Positions A-A, B-B and C-C are given in figure 3.24.	203
B.5	Cross sections for test series s7255-02 at the time step of 3000 wave cycles. Positions A-A, B-B and C-C are given in figure 3.25.	204
C.1	Comparison of local flow components between numerical model and experiment at position 1 around tripod structure.	205
C.2	Comparison of local flow components between numerical model and experiment at position 9 around tripod structure.	206
C.3	Comparison of local flow components between numerical model and experiment at position 11 around tripod structure.	207

C.4	Amplification factors for figure 5.10b, test series r2130-04. Moments of wave crest (left) and wave trough (right) passage at centre of structure. Shear stress τ_0 corresponds to wave crest passage in undisturbed case.	208
C.5	Amplification factors for figure 5.10c, test series r2130-05. Moments of wave crest (left) and wave trough (right) passage at centre of structure. Shear stress τ_0 corresponds to wave crest passage in undisturbed case.	208
C.6	Amplification factors for figure 5.12a, test series c0206-01. Shear stress τ_0 corresponds to undisturbed case.	209
C.7	Amplification factors for figure 5.12b, test series w2319-01. Moments of wave crest (left) and wave trough (right) passage at centre of structure. Shear stress τ_0 corresponds to wave crest passage in undisturbed case.	209
C.8	Amplification factors for figure 5.12c, test series w2319-01. Moments of wave crest (left) and wave trough (right) passage at centre of structure. Shear stress τ_0 corresponds to wave crest passage in undisturbed case.	210

List of Tables

2.1	Typical boundary layer classifications depending on y^+	7
3.1	Parameter scaling by Froude model law.	31
3.2	Soil parameters of bed material.	35
3.3	Probes and sensors applied in WKS wave flume experiments.	36
3.4	Compilation of conducted experimental scour tests in the WKS wave flume.	39
3.5	Probes and sensors applied in GWK wave flume experiments.	58
3.6	Compilation of conducted experimental scour tests in the GWK wave flume.	61
5.1	Wave and current condition test parameters for numerical investigations.	124
5.2	Model parameters for flow-induced scour simulation.	143
5.3	Model parameters for test series w2130-01.	148

A Appendix - WKS Experiments

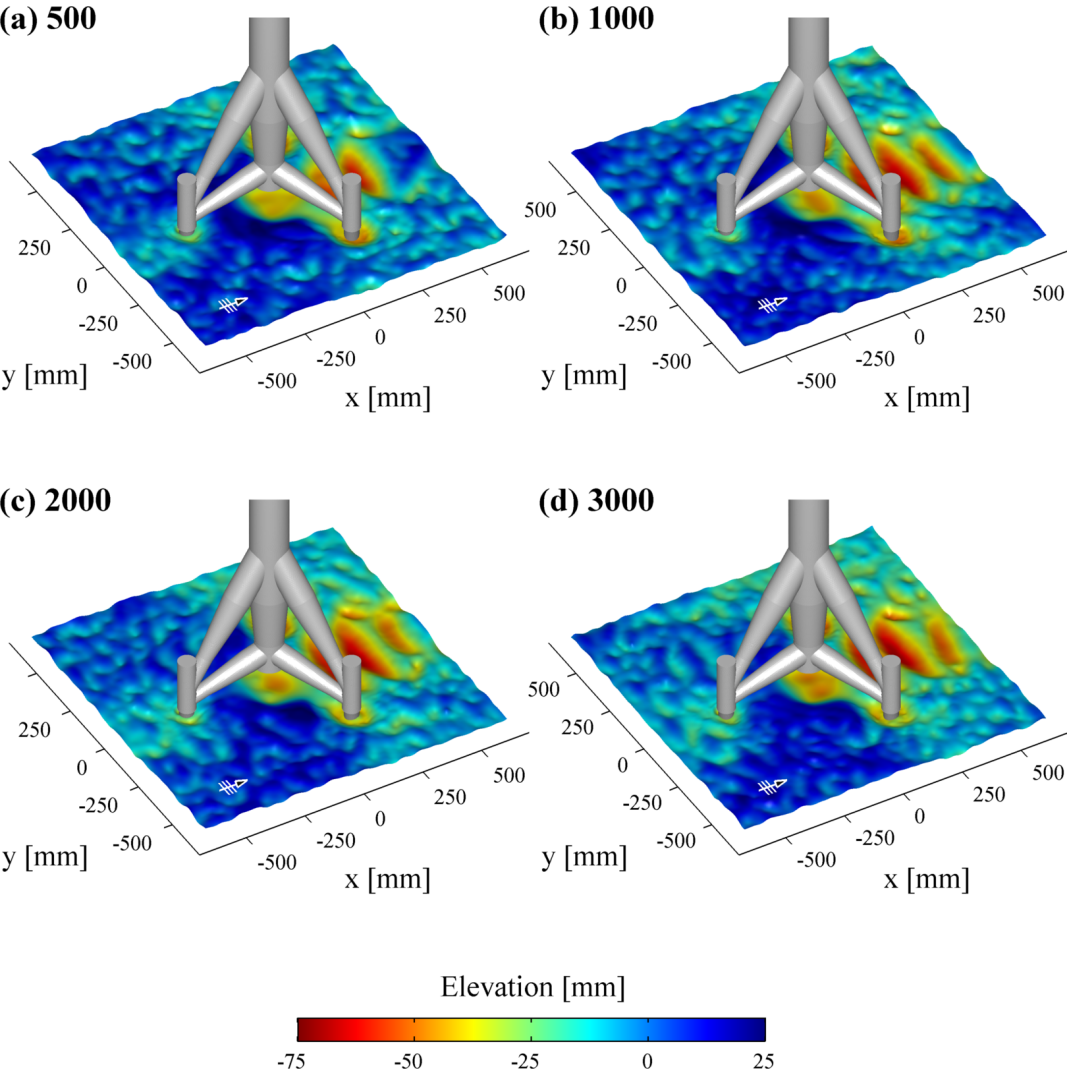


Figure A.1: Results of scour development for test series r2130-02 in the WKS wave flume experiments at time steps of 500, 1000, 2000 and 3000 wave cycles. Wave-encounter angle 0°.

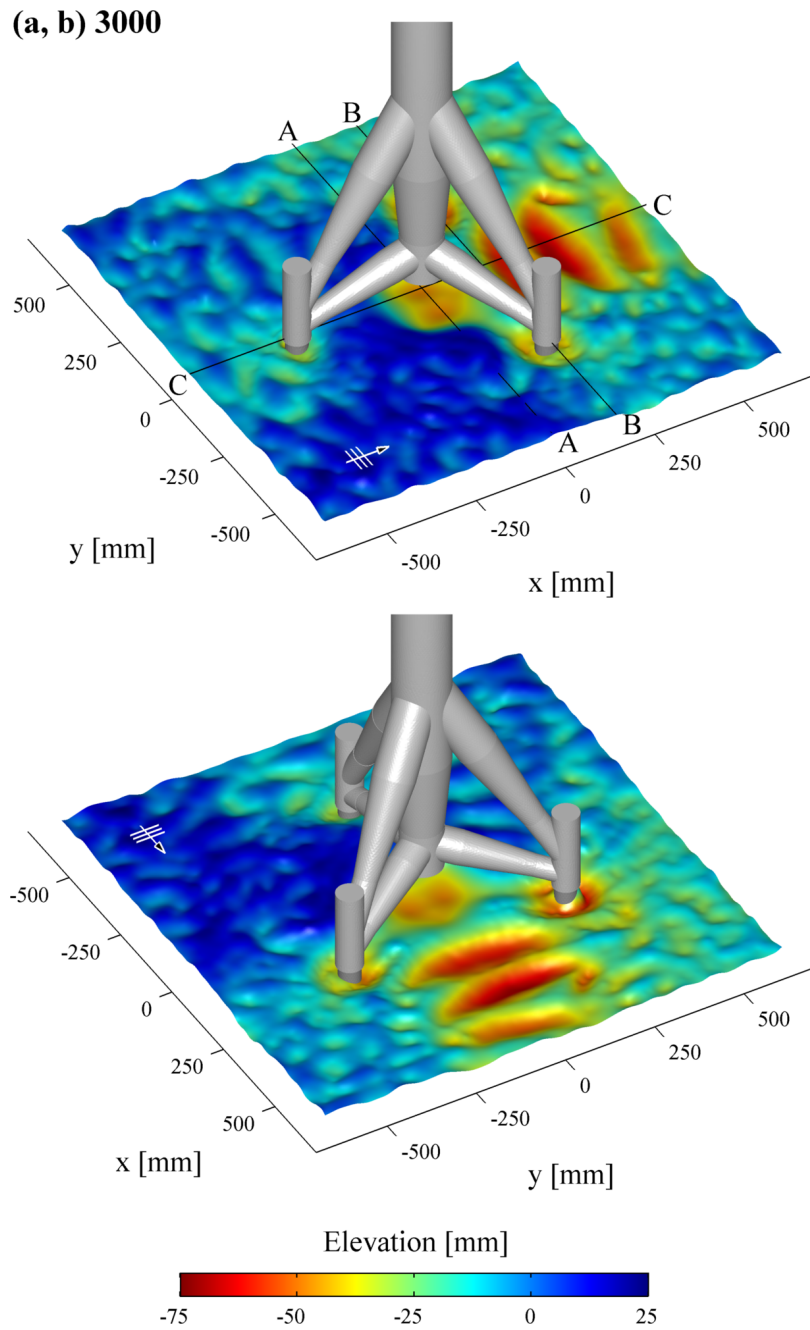


Figure A.2: Results of scour development for test series r2130-02 after 3000 wave cycles, (a) front view, (b) rear view. Cross section positions for figure A.3 are given in upper plot (a).

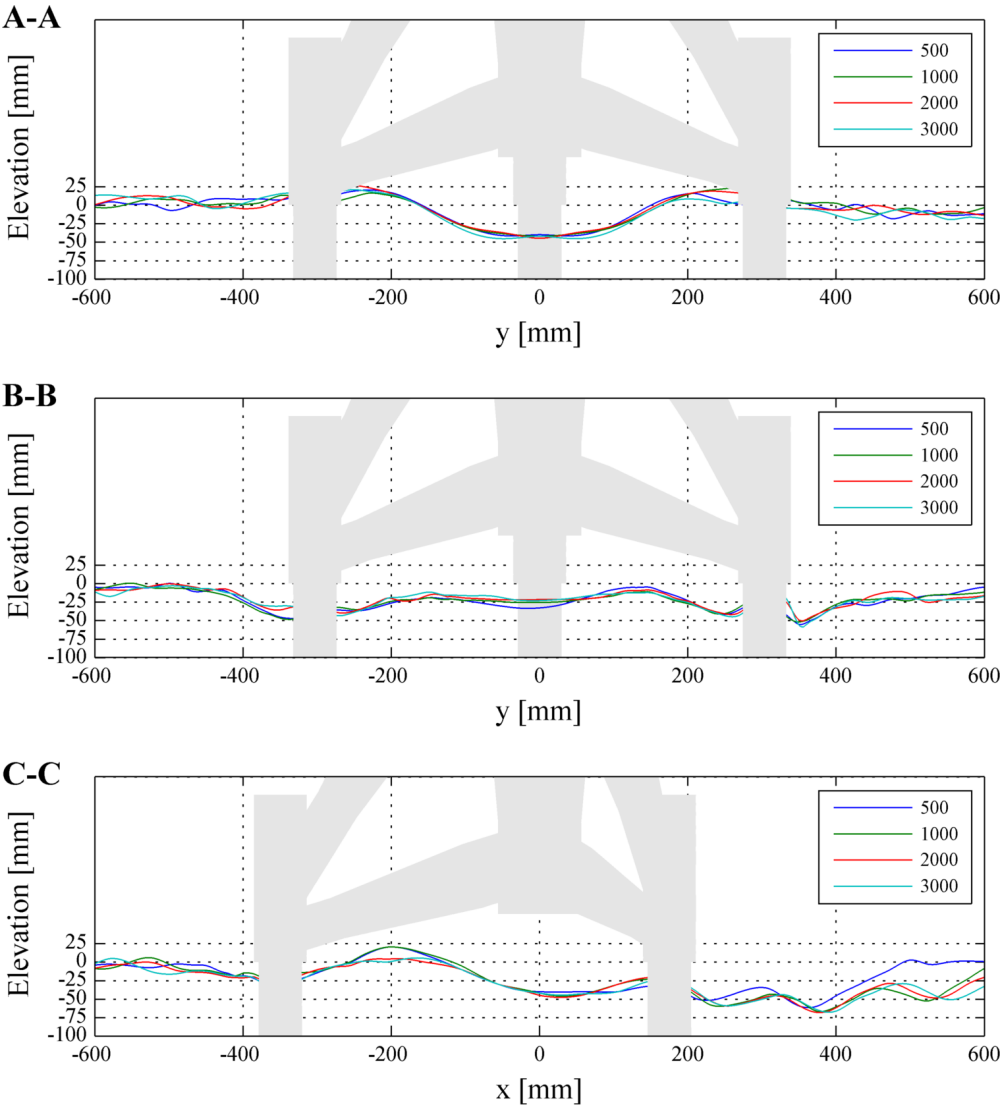


Figure A.3: Cross sections for test series r2130-02 at time steps of 500, 1000, 2000 and 3000 wave cycles. Positions A-A, B-B and C-C are given in figure A.2.

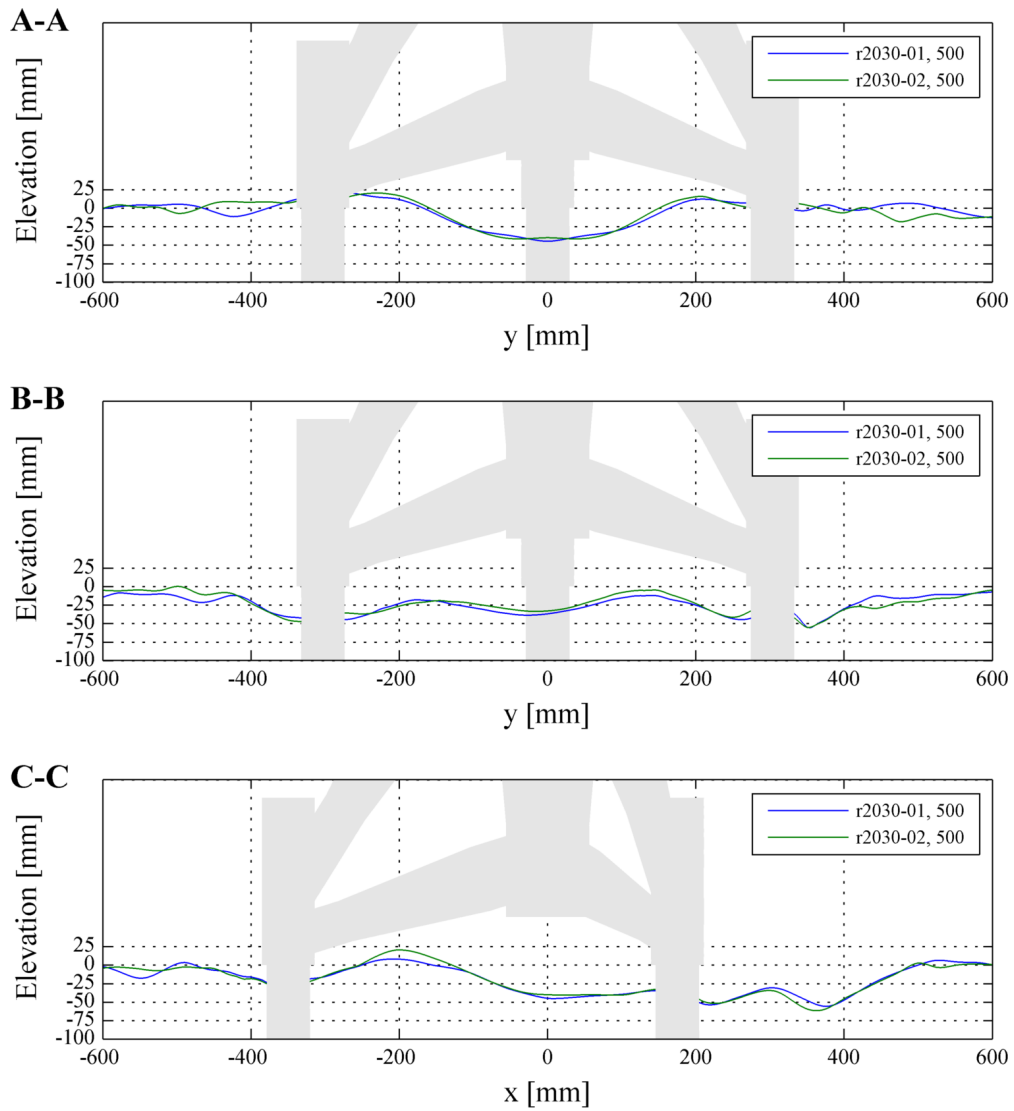


Figure A.4: Comparison of cross sections for test series r2130-01 and r2130-02 at the time step of 500 wave cycles. Positions A-A, B-B and C-C are given in figure 3.9.

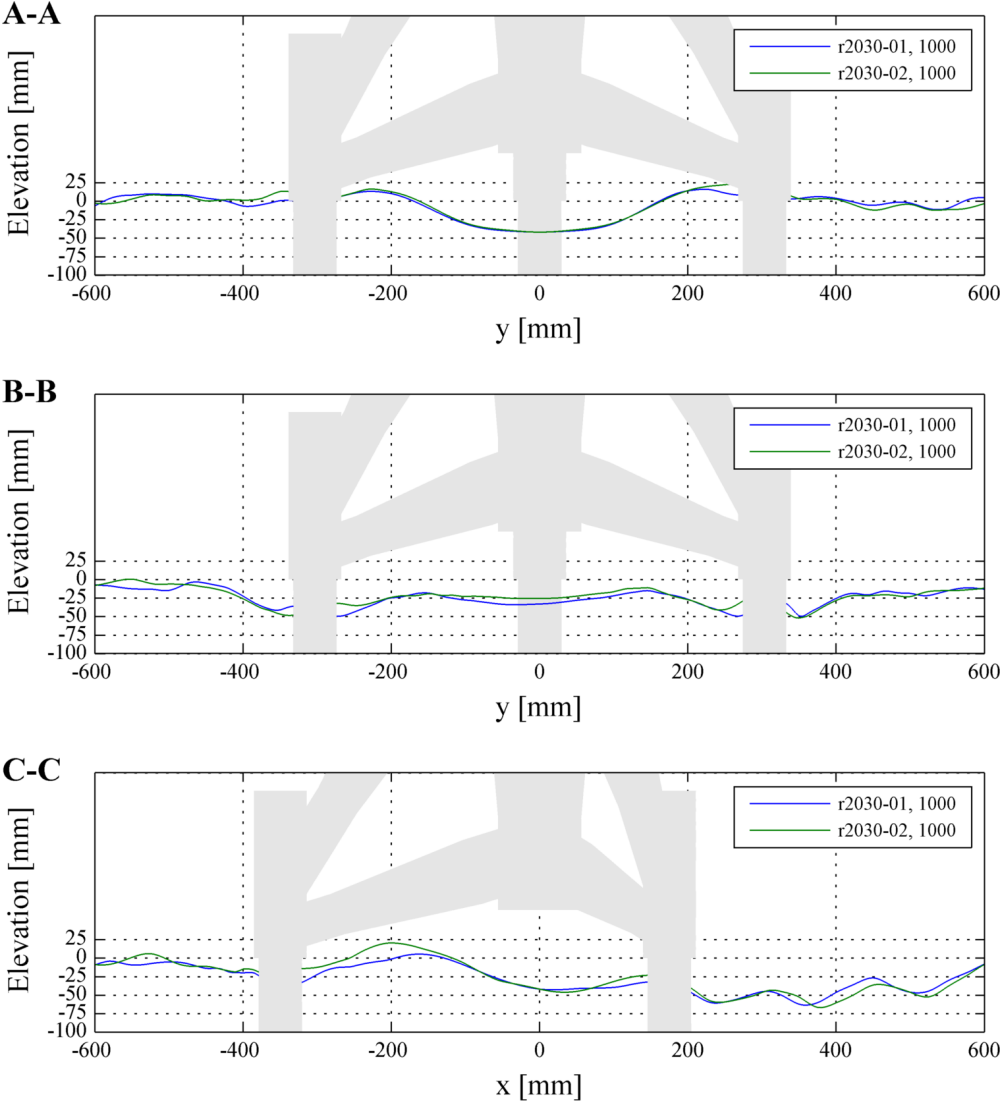


Figure A.5: Comparison of cross sections for test series r2130-01 and r2130-02 at the time step of 1000 wave cycles. Positions A-A, B-B and C-C are given in figure 3.9.

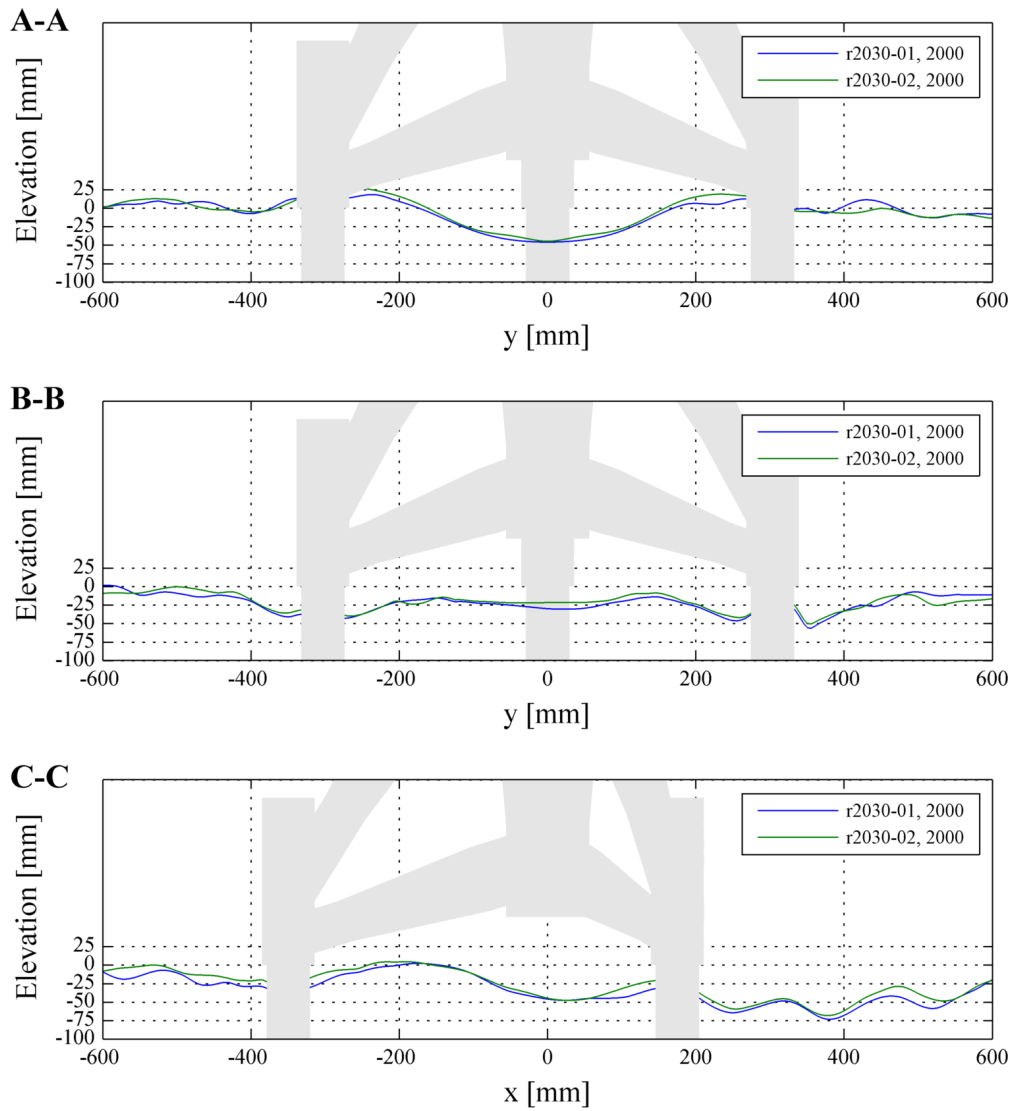


Figure A.6: Comparison of cross sections for test series r2130-01 and r2130-02 at the time step of 2000 wave cycles. Positions A-A, B-B and C-C are given in figure 3.9.

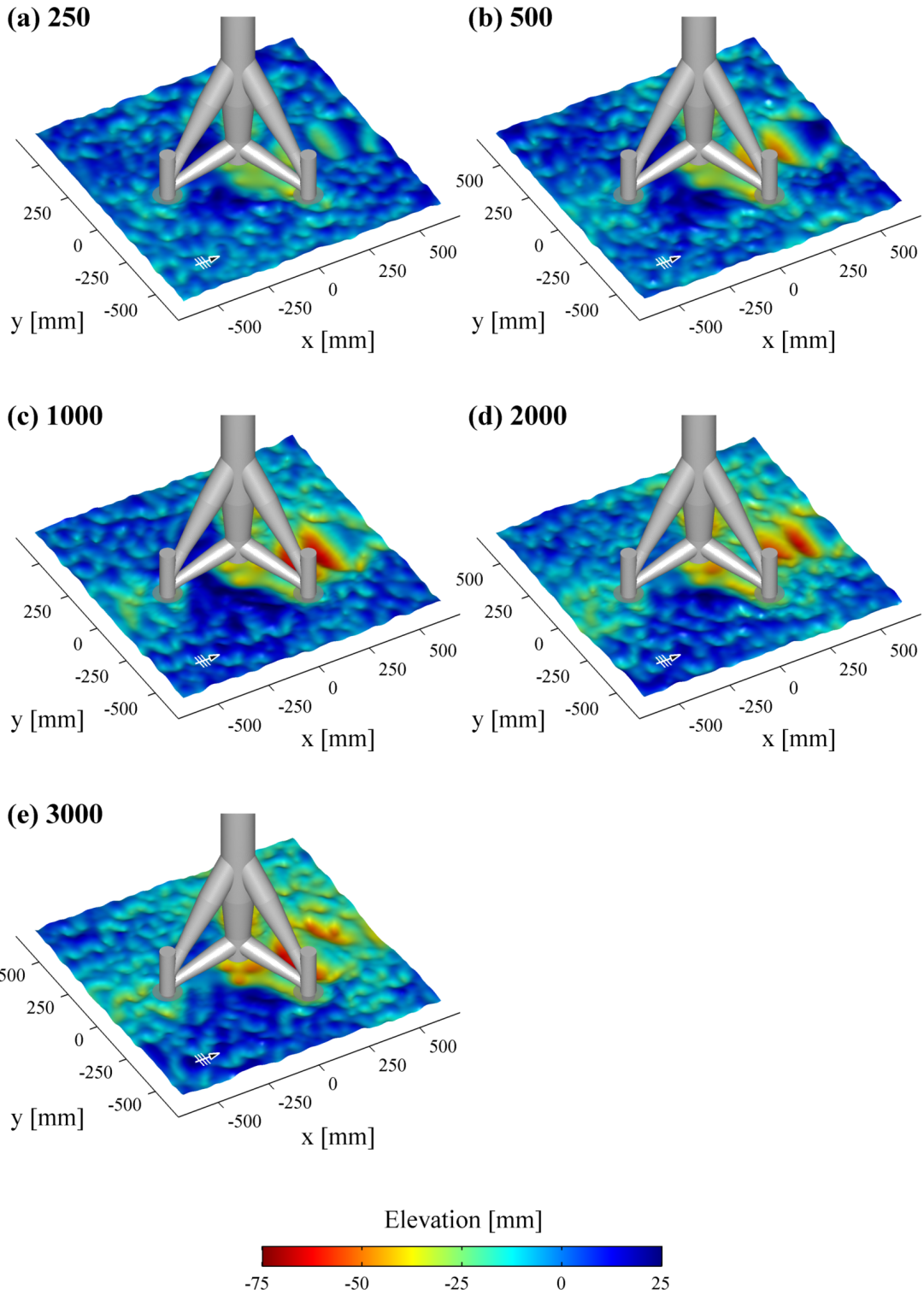


Figure A.7: Results of scour development for test series r2130-03 in the WKS wave flume experiments at time steps of 250, 500, 1000, 2000 and 3000 wave cycles. Wave-encounter angle 0° .

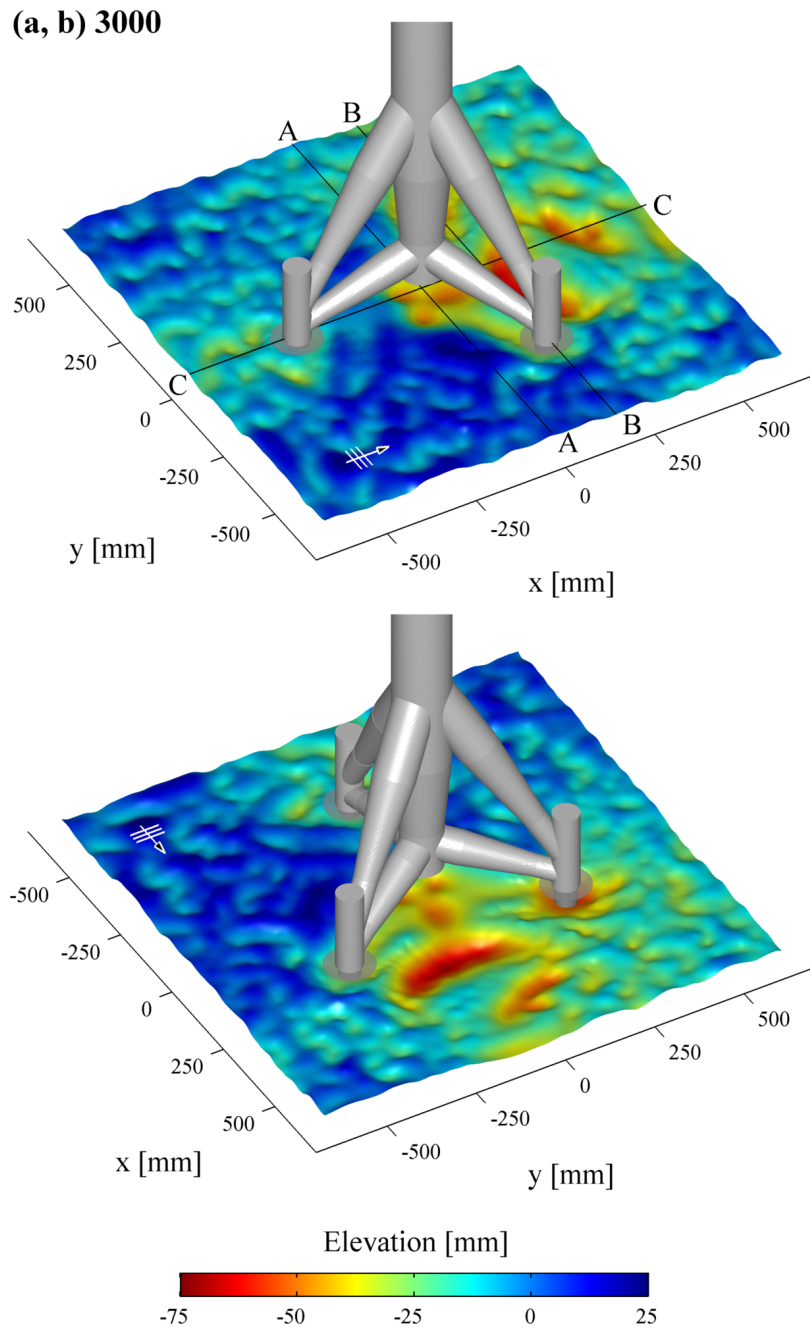


Figure A.8: Results of scour development for test series r2130-03 after 3000 wave cycles, (a) front view, (b) rear view. Cross section positions for figure 3.10 are given in upper plot (a). Wave-encounter angle 0° .

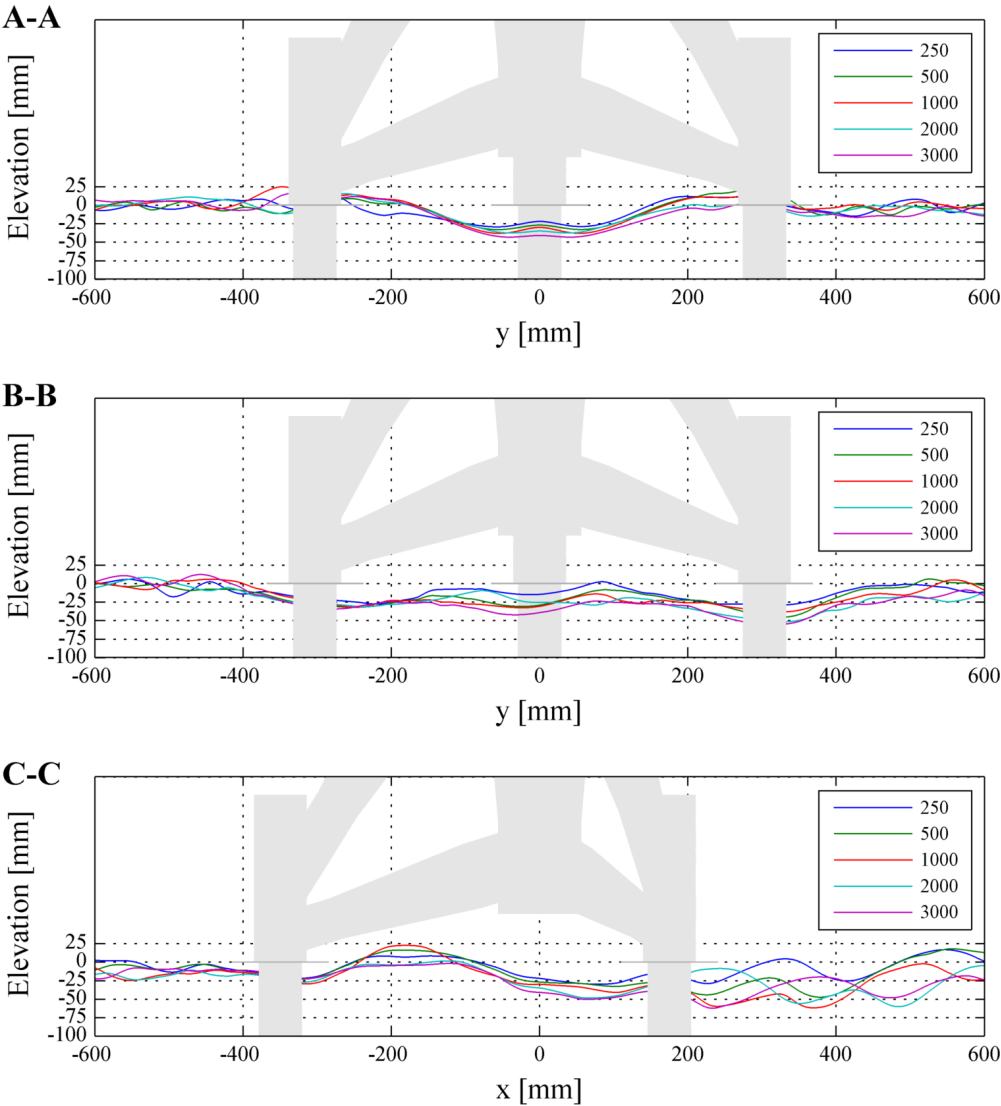


Figure A.9: Cross sections for test series r2130-03 at time steps of 250, 500, 1000, 2000 and 3000 wave cycles. Positions A-A, B-B and C-C are given in figure A.8.

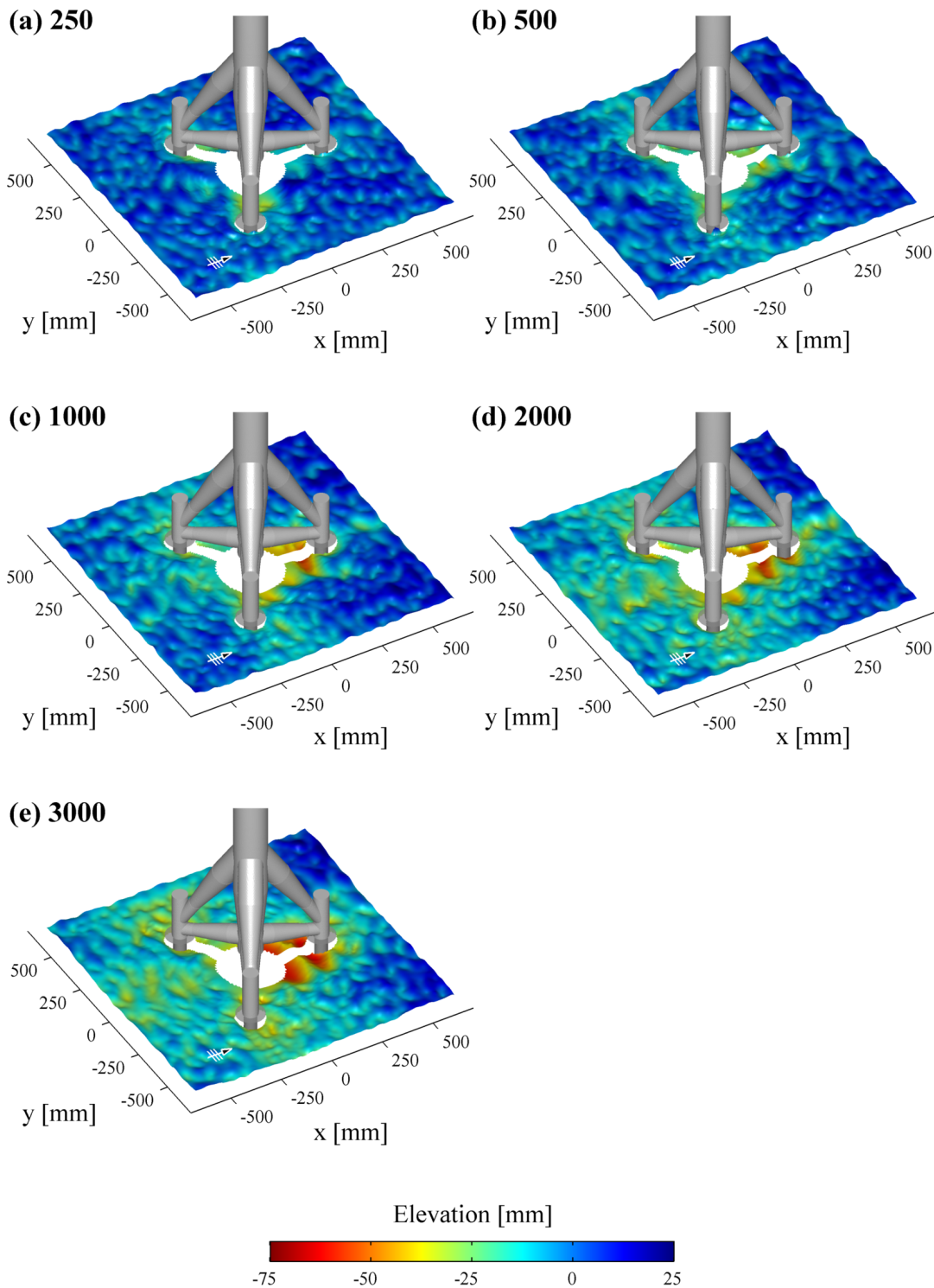


Figure A.10: Results of scour development for test series r2130-04 in the WKS wave flume experiments at time steps of 250, 500, 1000, 2000 and 3000 wave cycles. Wave-encounter angle 180° .

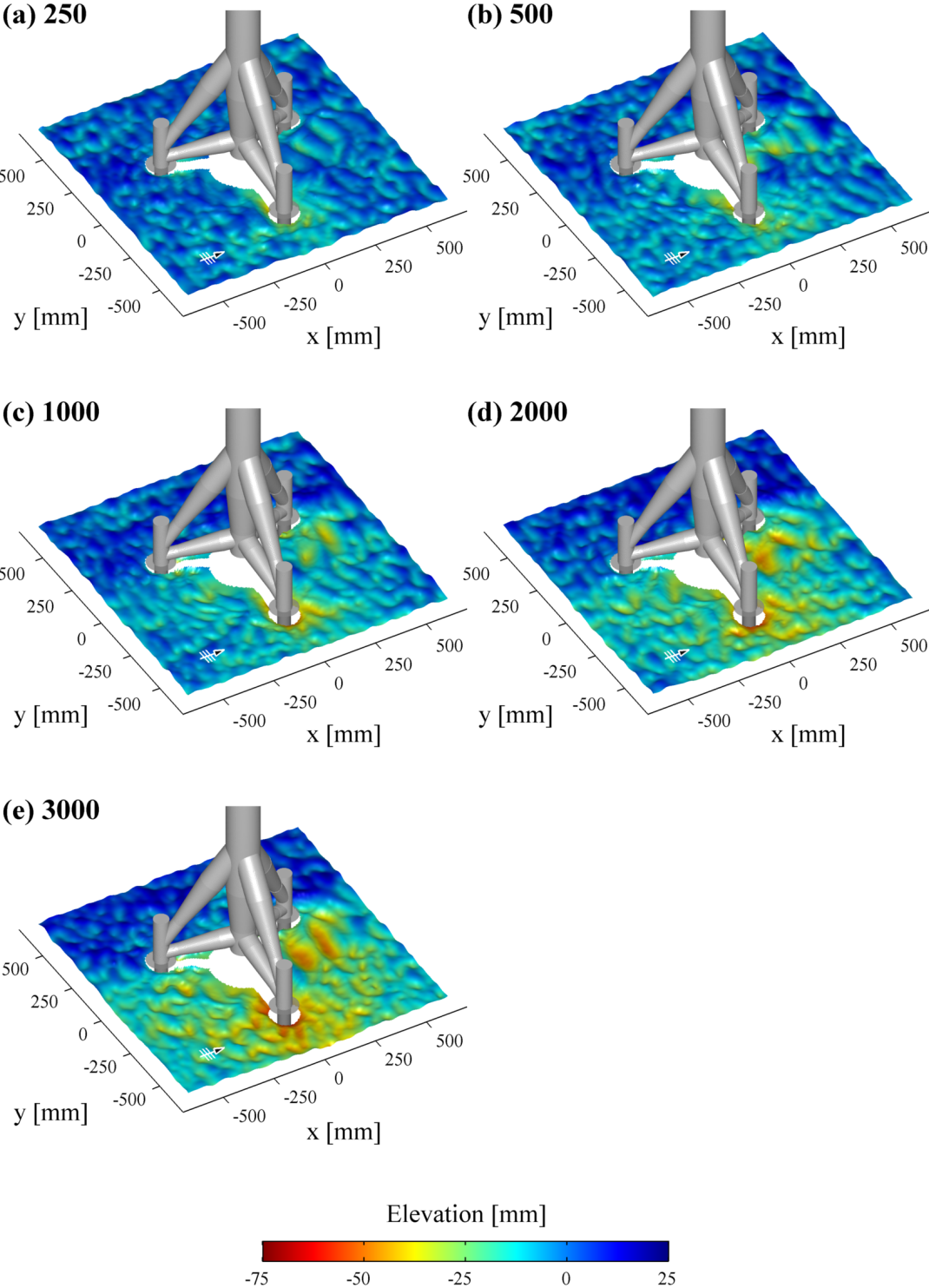


Figure A.11: Results of scour development for test series r2130-05 in the WKS wave flume experiments at time steps of 250, 500, 1000, 2000 and 3000 wave cycles. Wave-encounter angle 90°.

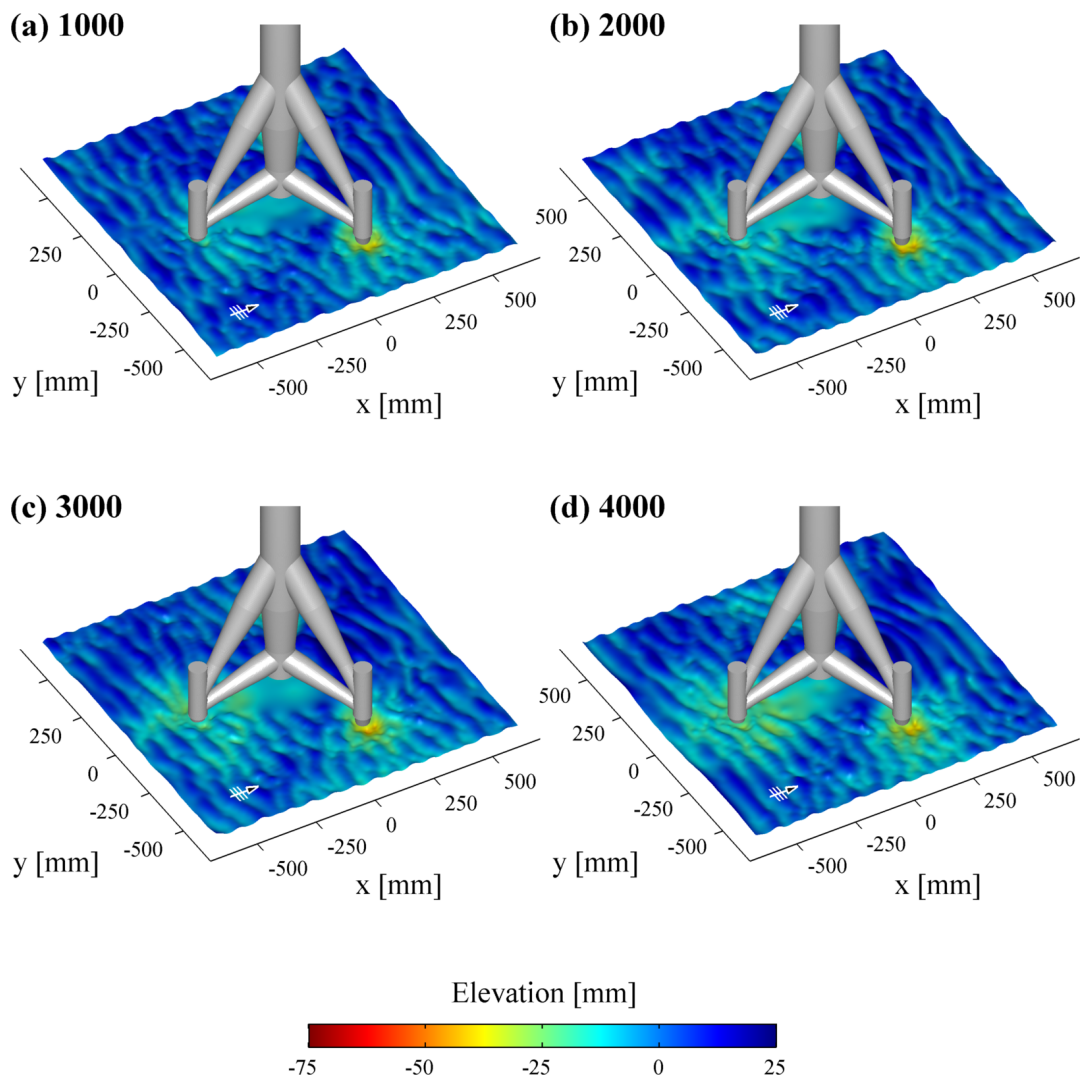


Figure A.12: Results of scour development for test series r1523-01 in the WKS wave flume experiments at time steps of 1000, 2000, 3000 and 4000 wave cycles. Wave-encounter angle 0° .

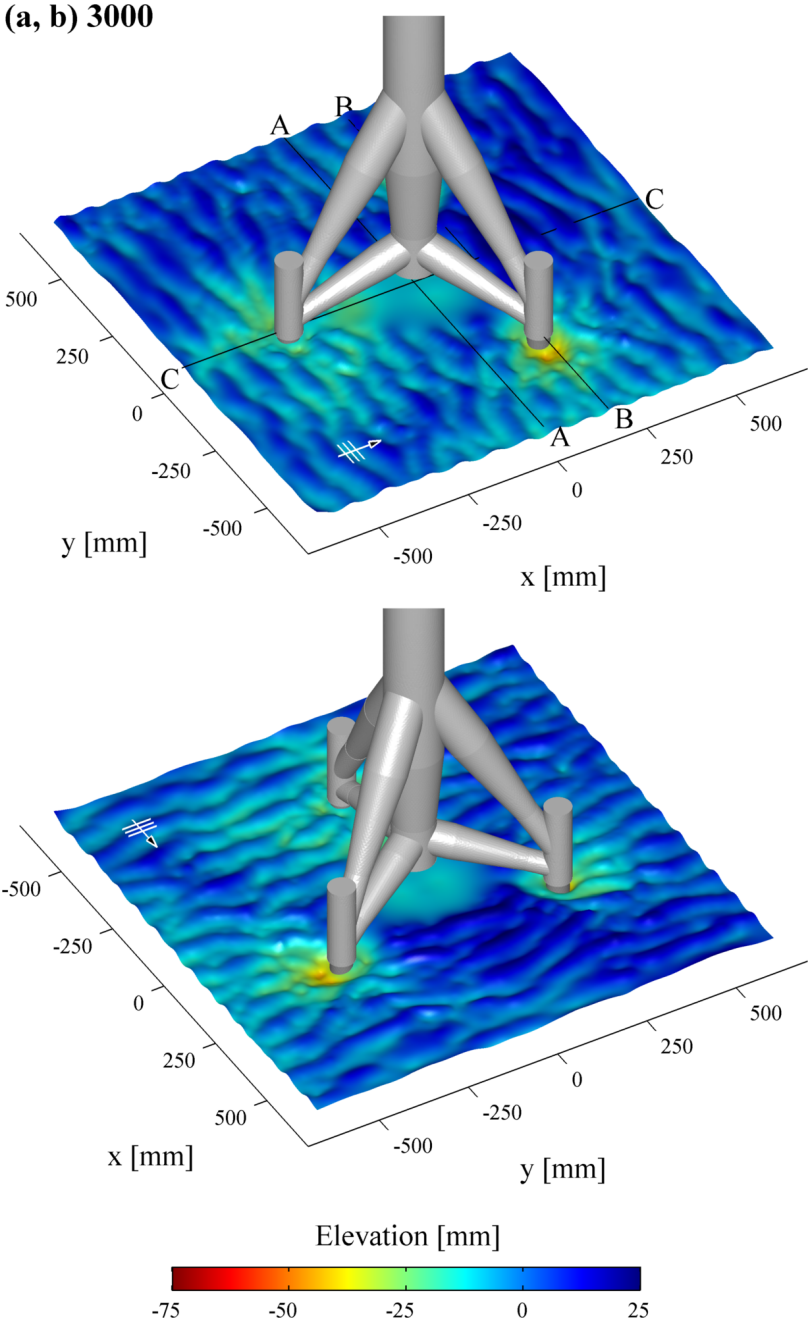


Figure A.13: Results of scour development for test series r1523-01 after 3000 wave cycles, (a) front view, (b) rear view. Wave-encounter angle 0° .

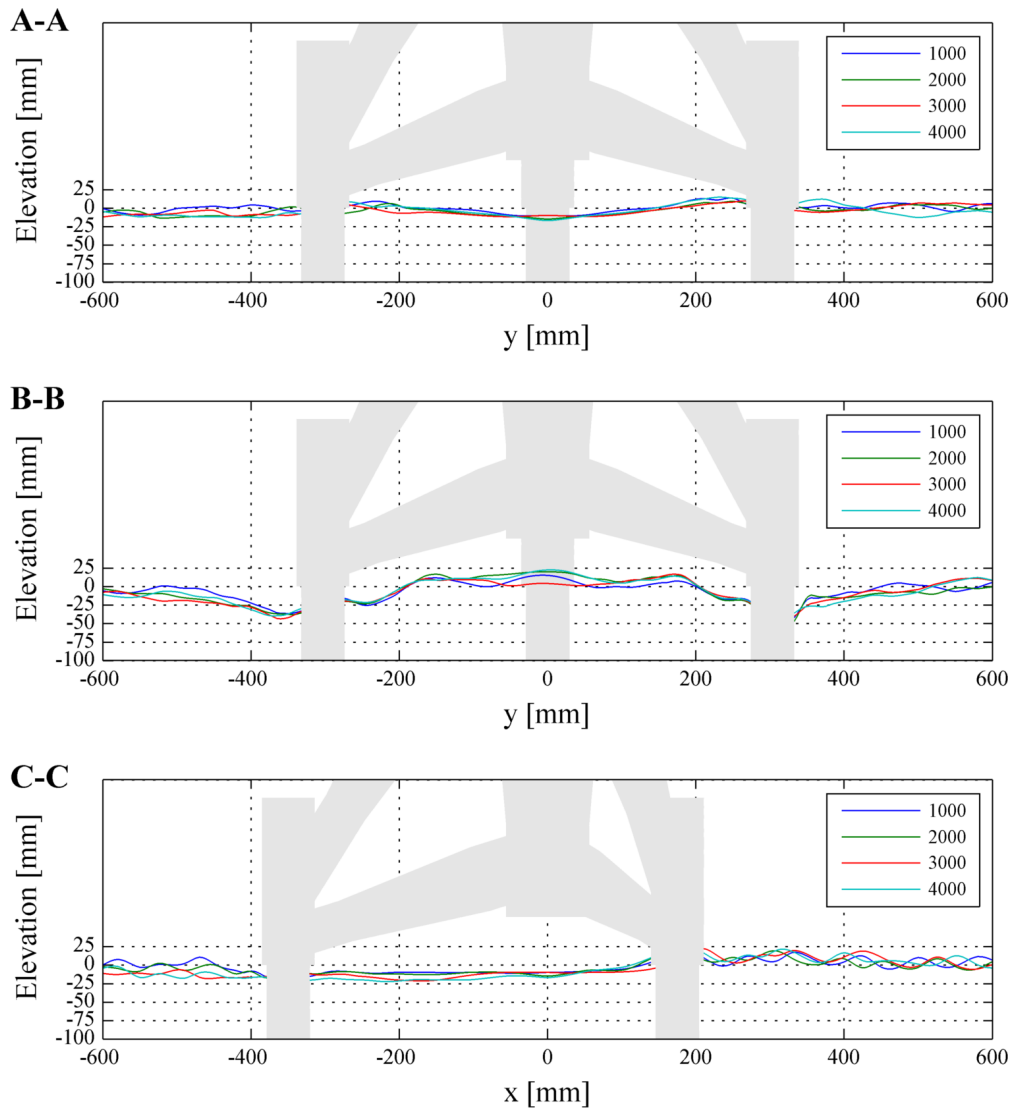


Figure A.14: Cross sections for test series r1523-01 at time steps of 1000, 2000, 3000 and 4000 wave cycles. Positions A-A, B-B and C-C are given in figure A.13.

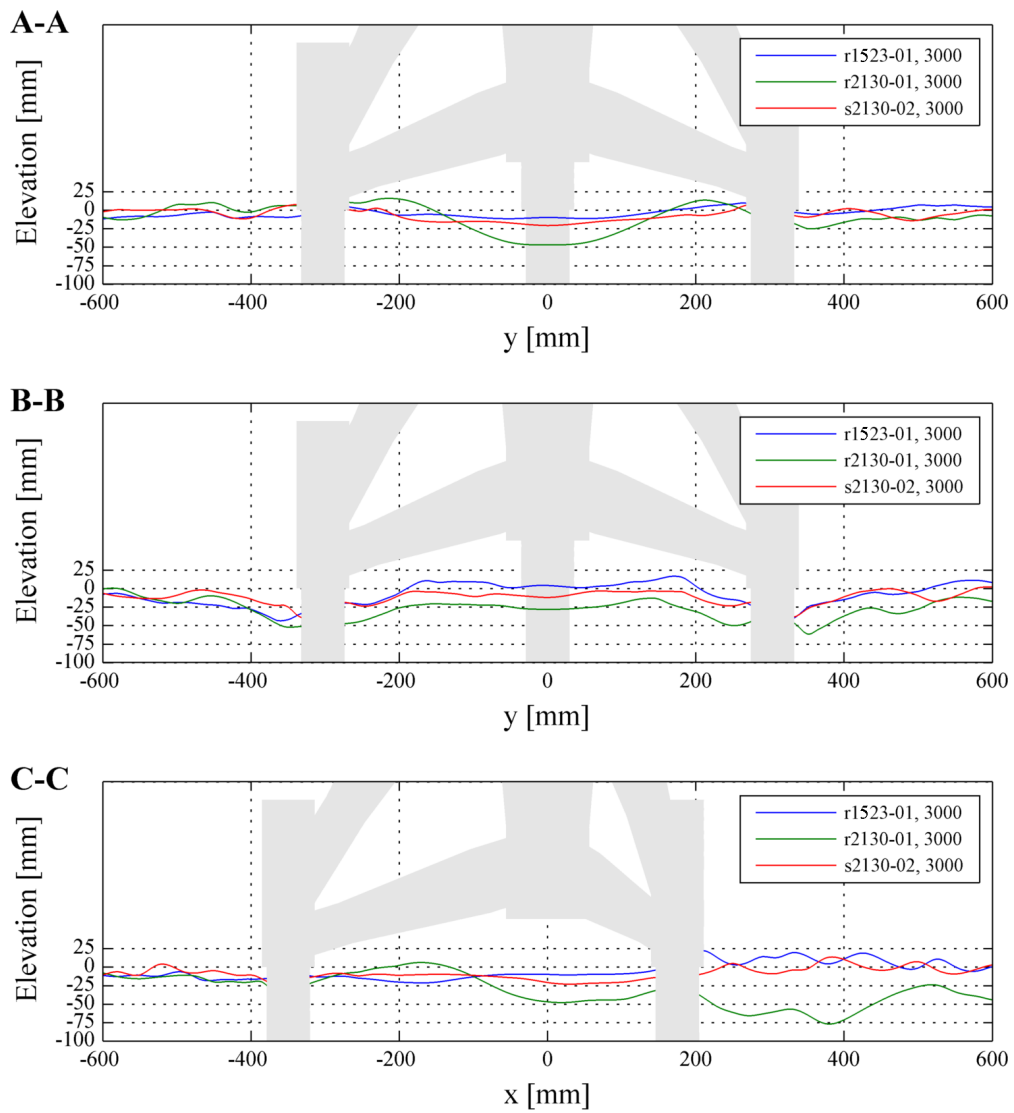


Figure A.15: Comparison of cross sections for test series r2130-01, r1523-01 and s2130-02 at the time step of 3000 wave cycles. Positions A-A, B-B and C-C are given in figure 3.9.

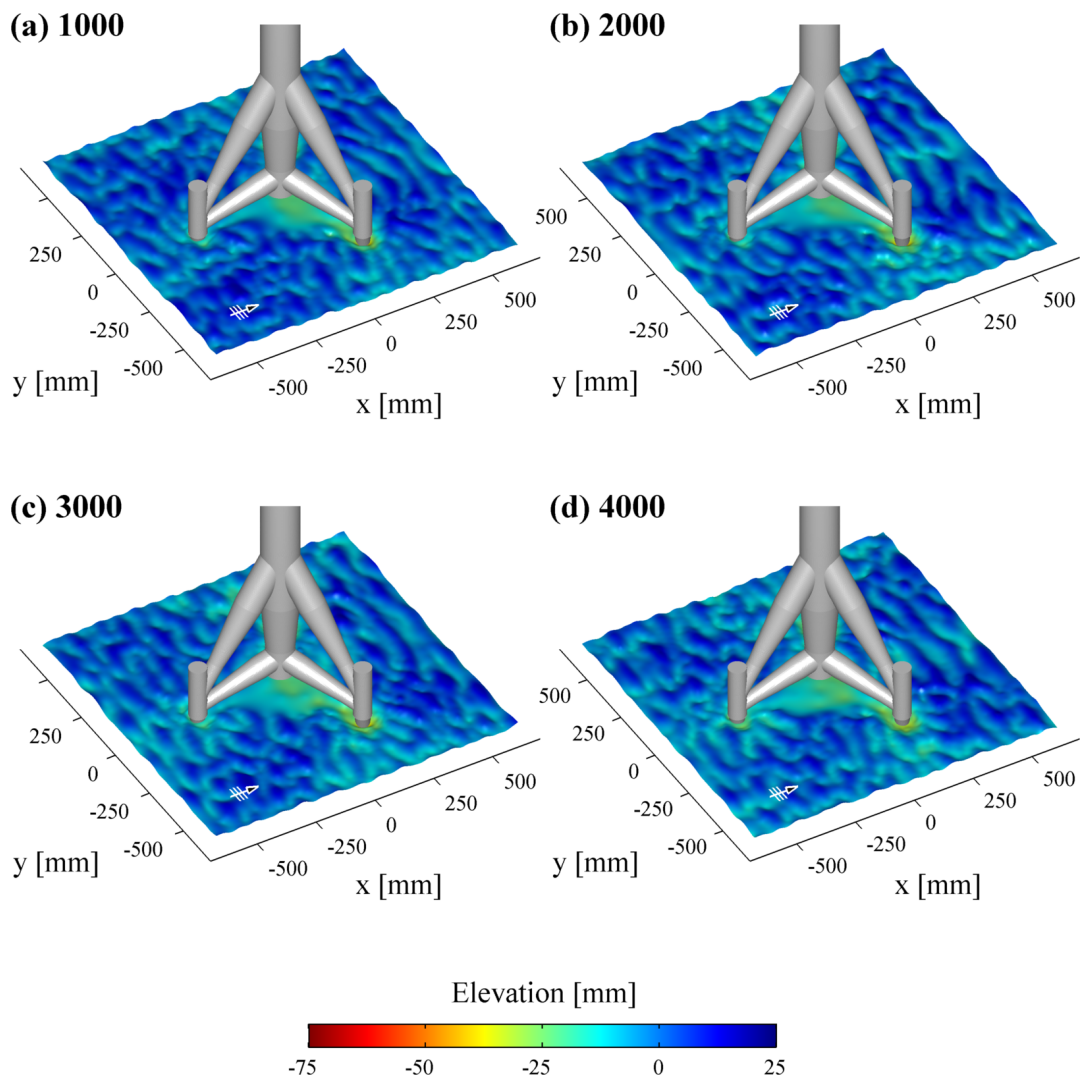


Figure A.16: Results of scour development for test series s2130-02 in the WKS wave flume experiments at time steps of 1000, 2000, 3000 and 4000 wave cycles. Wave-encounter angle 0° .

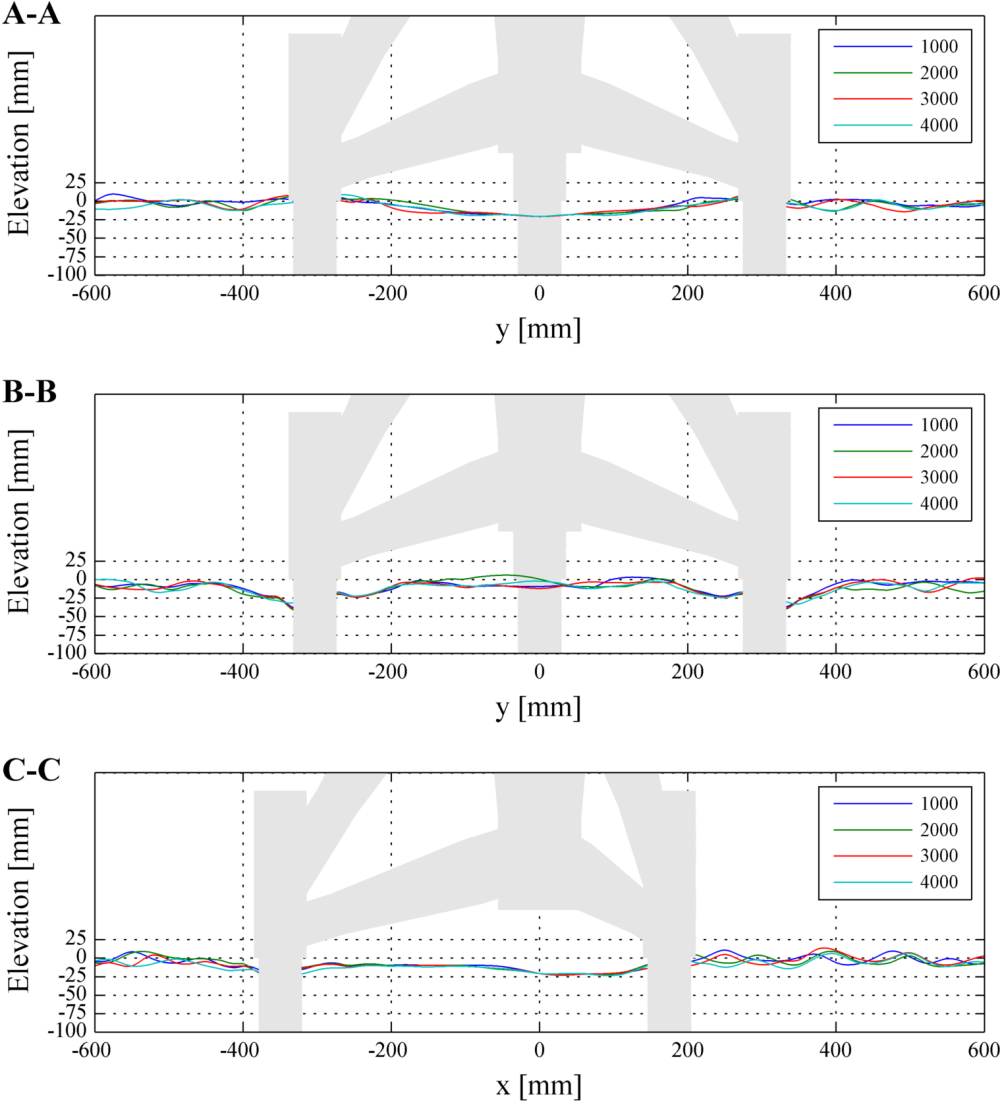


Figure A.17: Cross sections for test series s2130-02 at time steps of 1000, 2000, 3000 and 4000 wave cycles. Positions A-A, B-B and C-C are given in figure 3.15.

B Appendix - GWK Experiments

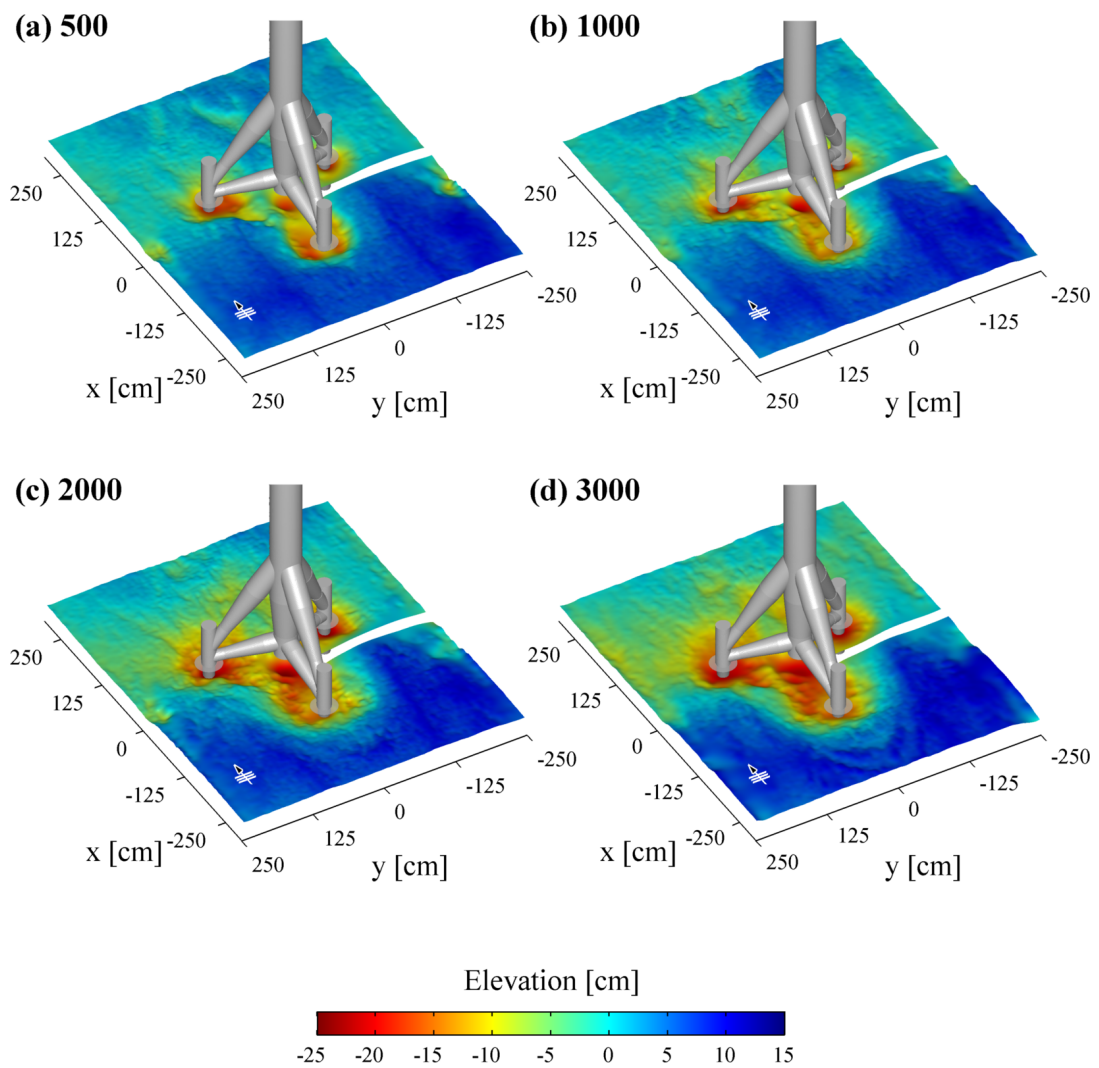


Figure B.1: Results of scour development for test series r7655-01 in the GWK wave flume experiments at time steps of 500, 1000, 2000 and 3000 wave cycles. Wave-encounter angle 0° .

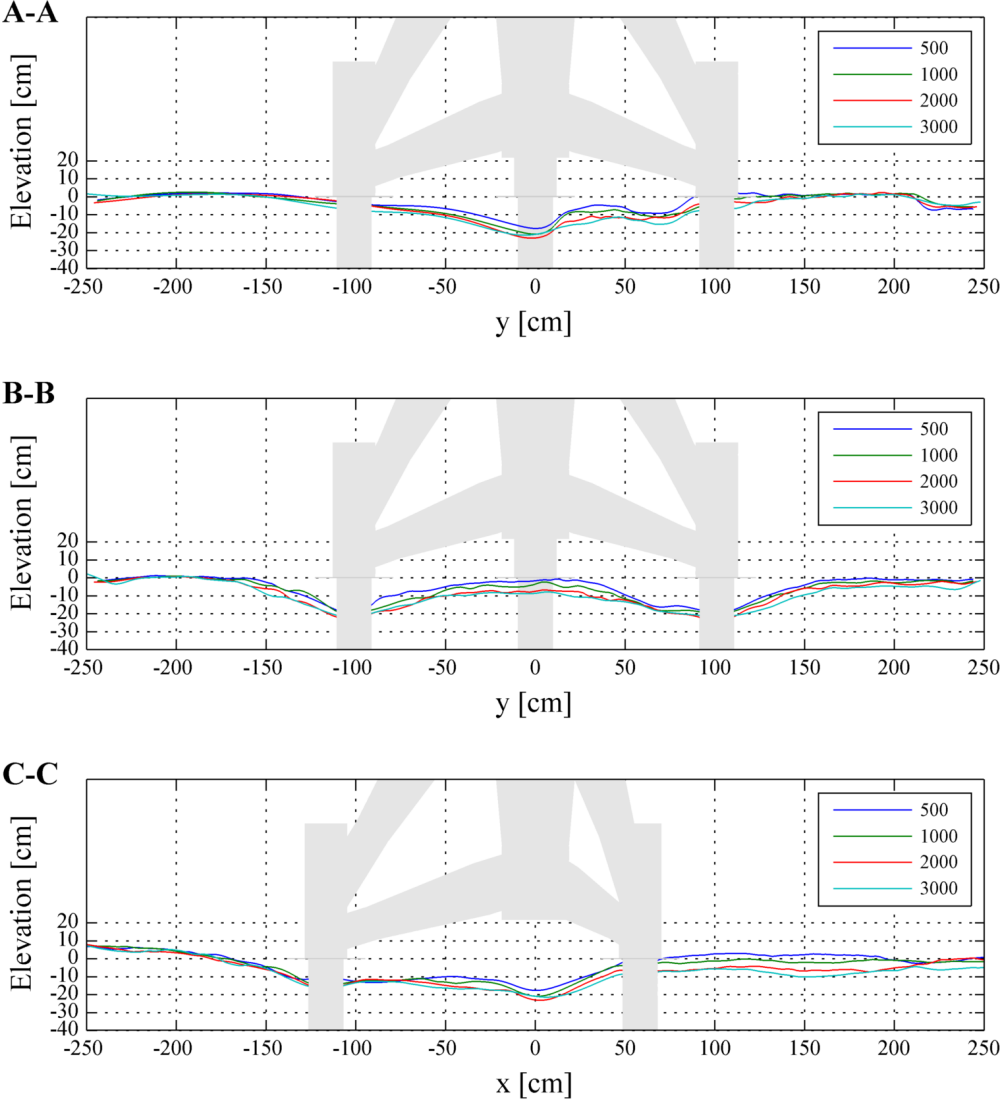


Figure B.2: Cross sections for test series r7655-01 at time steps of 500, 1000, 2000 and 3000 wave cycles. Positions A-A, B-B and C-C are given in figure 3.22.

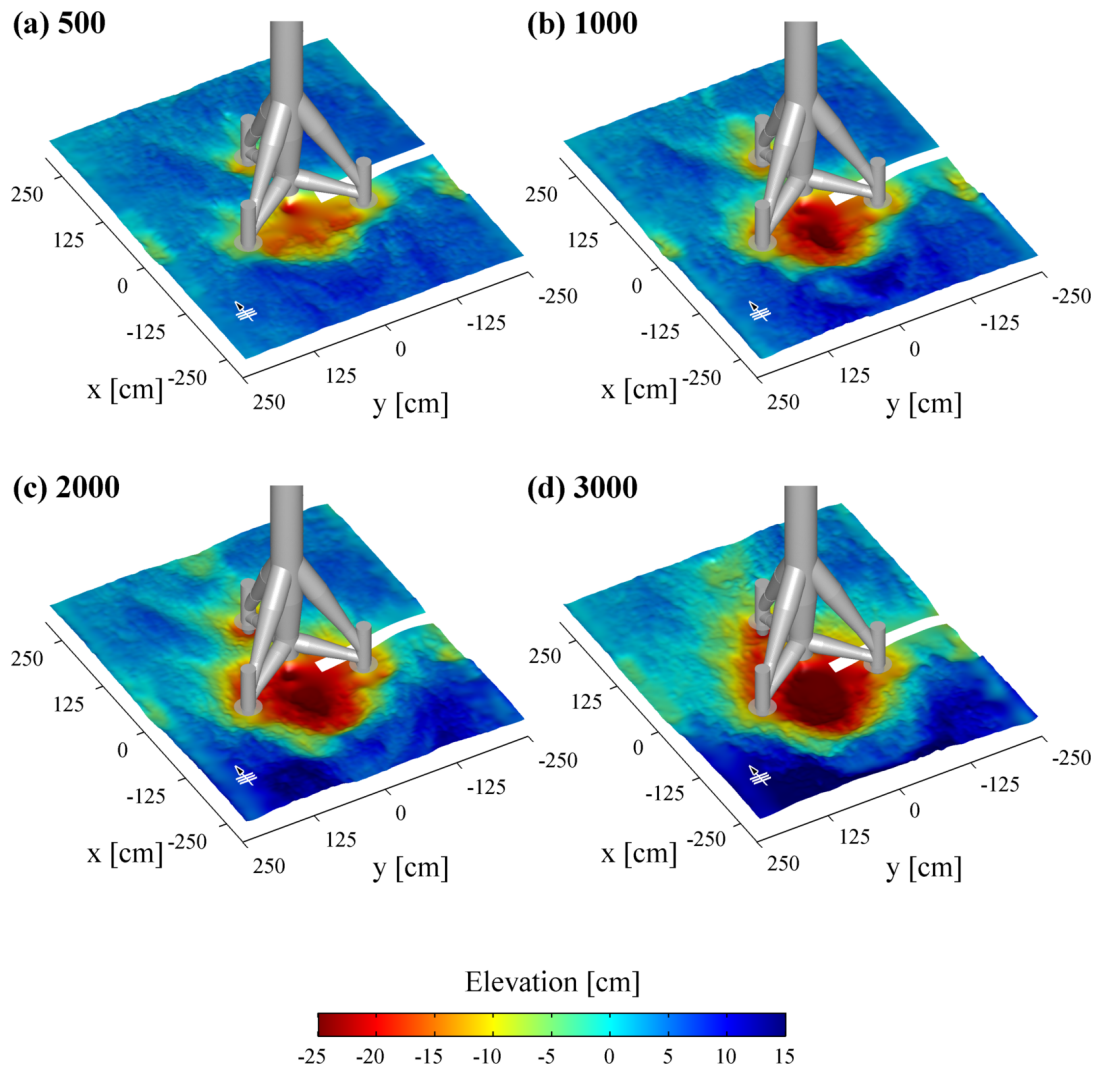


Figure B.3: Results of scour development for test series r7655-02 in the GWK wave flume experiments at time steps of 500, 1000, 2000 and 3000 wave cycles. Wave-encounter angle 180°.

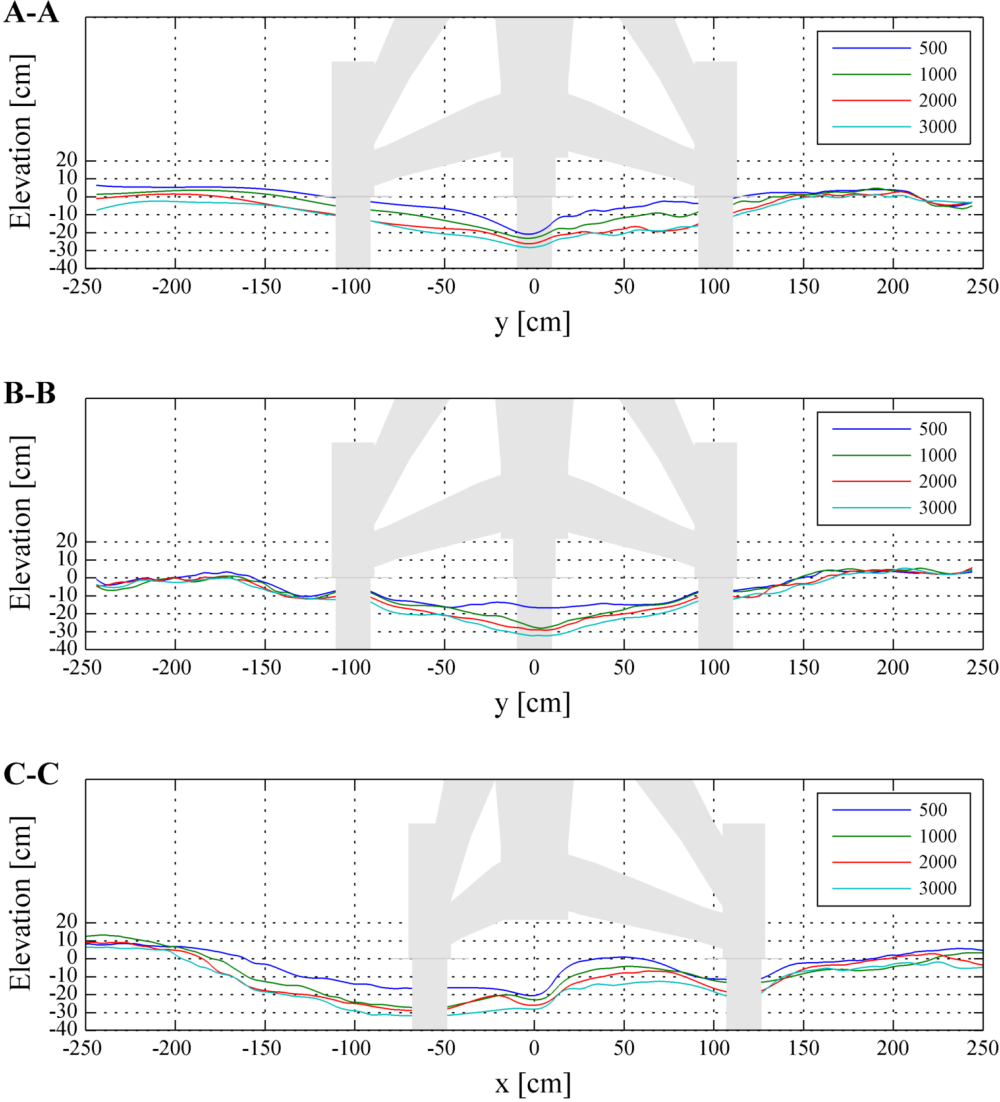


Figure B.4: Cross sections for test series r7655-02 at time steps of 500, 1000, 2000 and 3000 wave cycles. Positions A-A, B-B and C-C are given in figure 3.24.

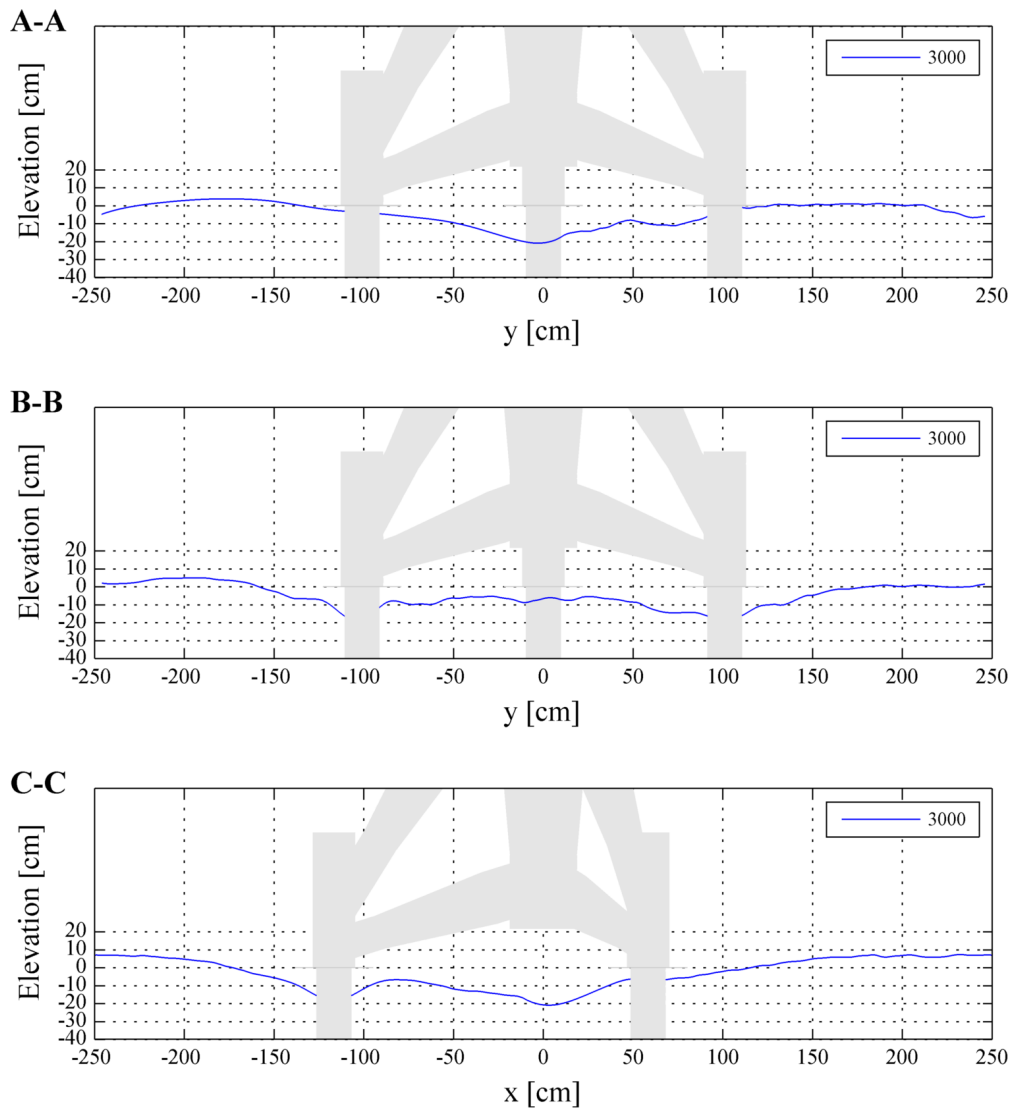


Figure B.5: Cross sections for test series s7255-02 at the time step of 3000 wave cycles. Positions A-A, B-B and C-C are given in figure 3.25.

C Appendix - Numerical Model Application

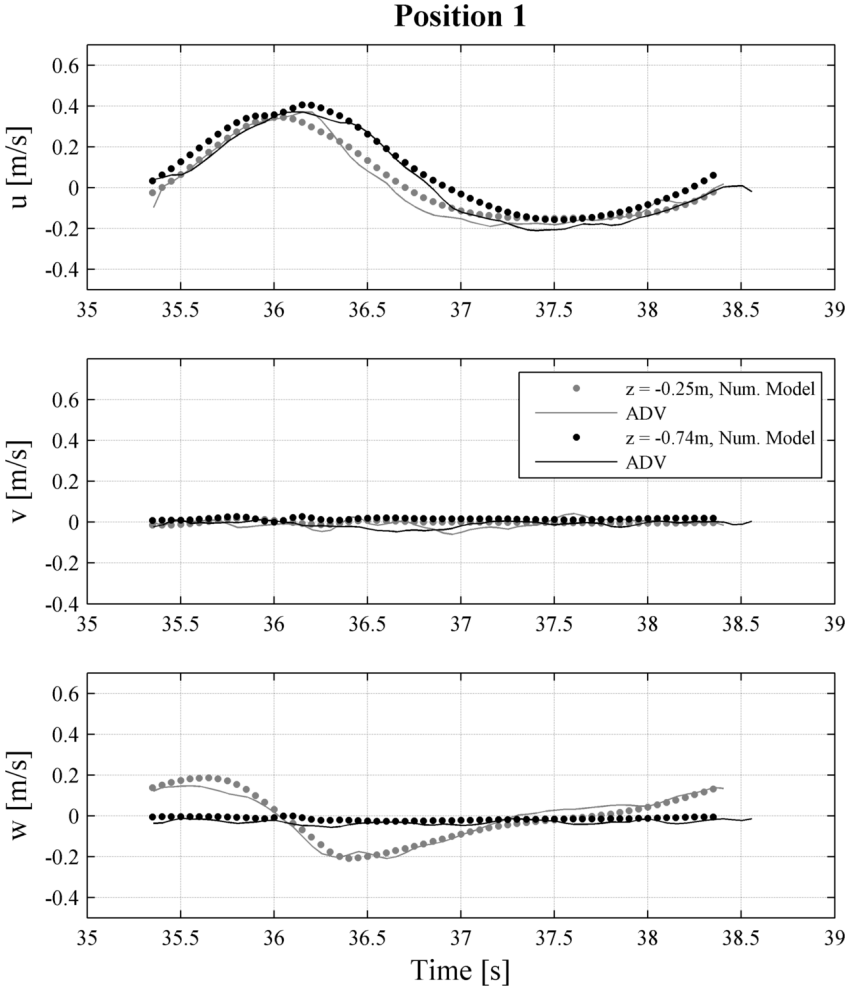


Figure C.1: Comparison of local flow components between numerical model and experiment at position 1 around tripod structure.

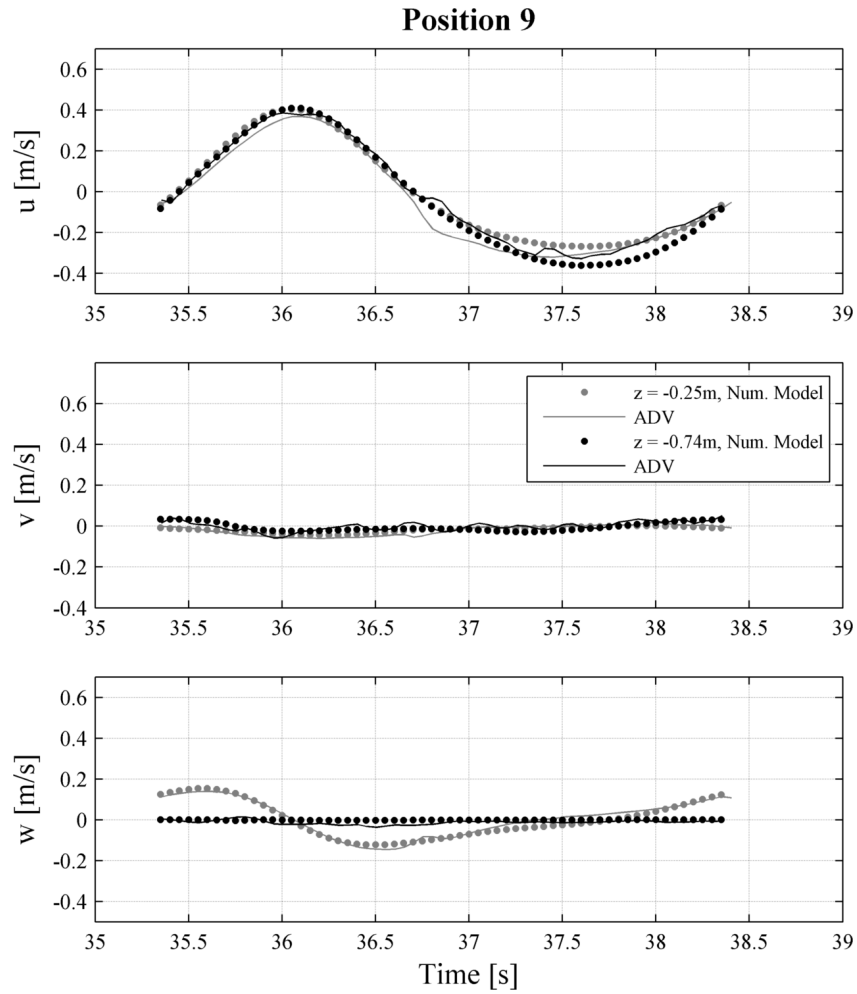


Figure C.2: Comparison of local flow components between numerical model and experiment at position 9 around tripod structure.

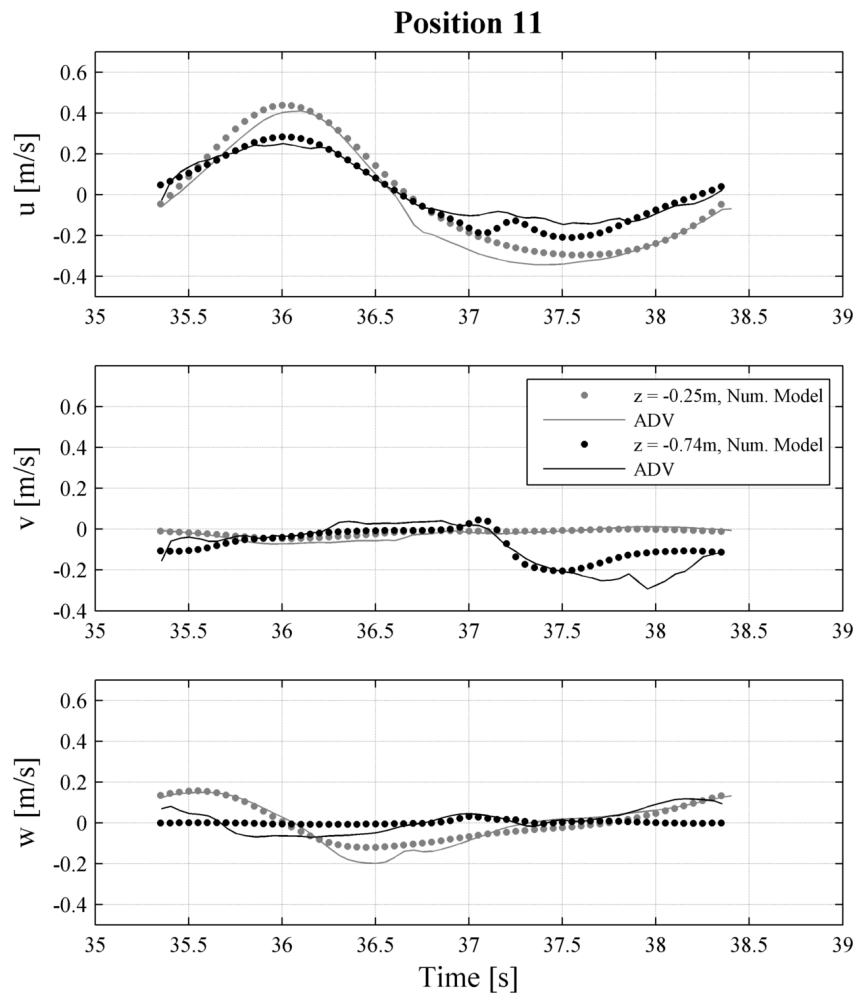


Figure C.3: Comparison of local flow components between numerical model and experiment at position 11 around tripod structure.

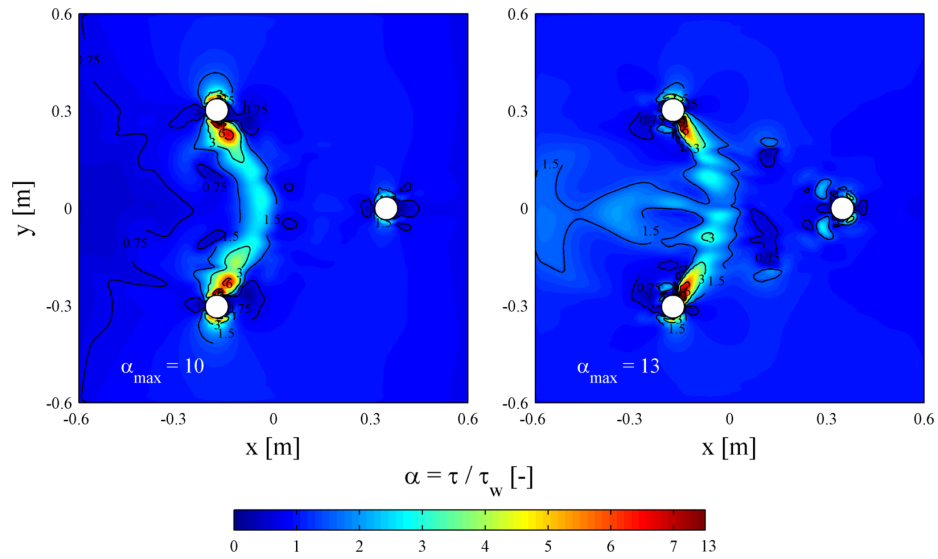


Figure C.4: Amplification factors for figure 5.10b, test series r2130-04. Moments of wave crest (left) and wave trough (right) passage at centre of structure. Shear stress τ_0 corresponds to wave crest passage in undisturbed case.

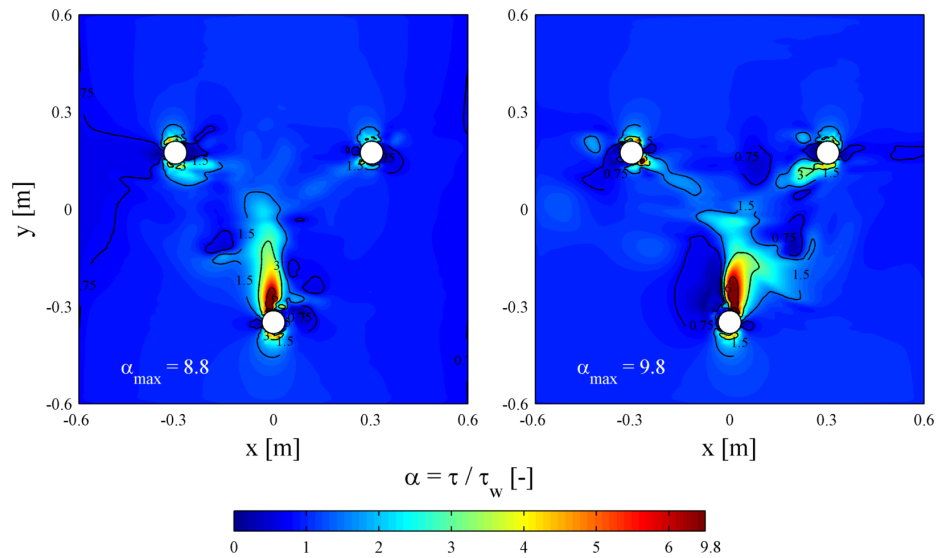


Figure C.5: Amplification factors for figure 5.10c, test series r2130-05. Moments of wave crest (left) and wave trough (right) passage at centre of structure. Shear stress τ_0 corresponds to wave crest passage in undisturbed case.

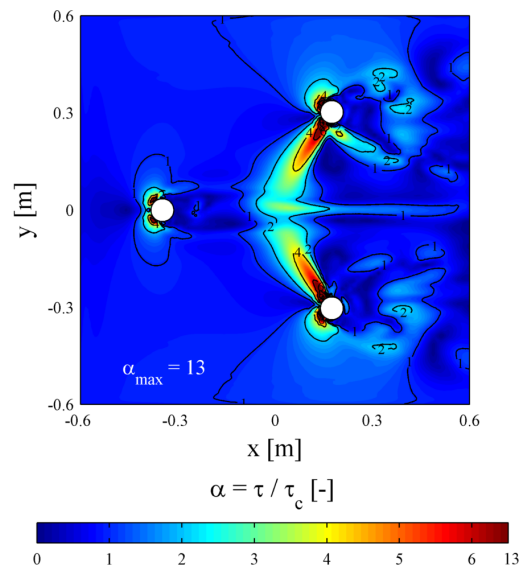


Figure C.6: Amplification factors for figure 5.12a, test series c0206-01. Shear stress τ_0 corresponds to undisturbed case.

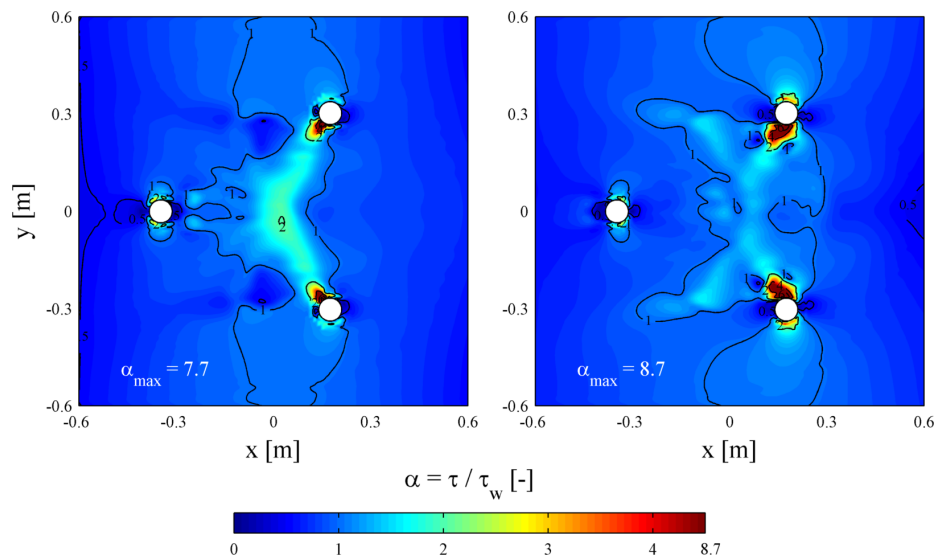


Figure C.7: Amplification factors for figure 5.12b, test series w2319-01. Moments of wave crest (left) and wave trough (right) passage at centre of structure. Shear stress τ_0 corresponds to wave crest passage in undisturbed case.

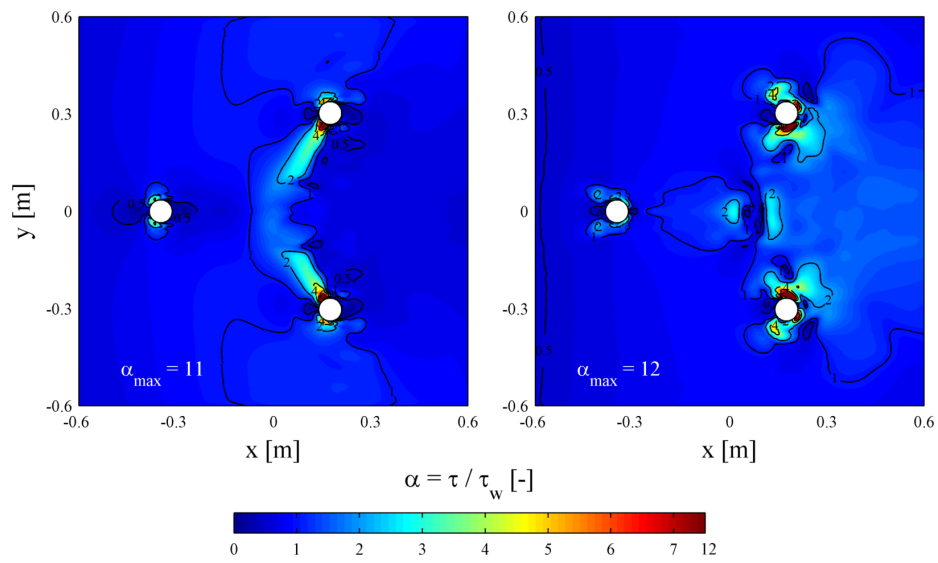


Figure C.8: Amplification factors for figure 5.12c, test series w2319-01. Moments of wave crest (left) and wave trough (right) passage at centre of structure. Shear stress τ_0 corresponds to wave crest passage in undisturbed case.

D Curriculum Vitae

Personal Data

Name	Arne Stahlmann
Date of Birth	February 4, 1982
Place of Birth	Düsseldorf, Germany
Nationality	German
Personal Status	Married
Email	stahlmann@fi.uni-hannover.de
Phone	+49 (0)511-762.2584

Work Experience

02/2008 - current	<p>Research Engineer at Franzius-Institute for Hydraulic, Waterways and Coastal Engineering, Leibniz Universität Hannover</p> <p><i>Projects involved:</i></p> <p>INSERT: Prozesse der Hydro-, Sediment- und Morphodynamik bei Interaktion von Richtungsseegang mit Strömung</p> <p>DELIGHT: Delta Information System for Geoenvironmental and Human Habitat Transition</p> <p>WMAA: Scientific assessment of the flood risk profile and future design storm surge levels of Gansevoort project of Whitney Museum of American Art, NYC, USA</p> <p>ALBATROS I: Stabilität und Verhalten von temporären Unterwasserbaugruben</p> <p>GIGAWIND alpha ventus: Untersuchungen zur Kolkbildung an komplexen Gründungsstrukturen</p> <p>Kolkbildung und Dimensionierung des Kolkschutzes für das STRABAG Schwerkraftfundament</p> <p>TSLP: Design and Review of the “Third Set of Locks Panama Canal”</p> <p>Stellungnahme zur Seegangsbelastung der Umschlaganlage Voslapper Groden</p>
-------------------	---

Work Experience

- 05/2004 - 12/2007 Student assistant at Franzius-Institute for Hydraulic, Waterways and Coastal Engineering, Leibniz Universität Hannover
- Projects involved:*
- LAST-MILE: Numerical Last-mile Tsunami Early Warning and Evacuation Information System
- Development of floodwater action plans: numerical simulations and CAD/GIS application
- Investigations on ship motion and ship-induced forces: in-situ measurements and data analyses

Education

- 02/2008 - current Research Engineer and PhD Student, Leibniz Universität Hannover
- 10/2002 - 02/2008 University education in Civil Engineering at Leibniz Universität Hannover
- Degree: Diplomingenieur, Dipl.-Ing.
- Specialization: Water and Environmental Engineering
- Diploma thesis: "Ausbreitung und Wellenaufbau langperiodischer Wellen (Tsunami) im küstennahen Bereich vor West-Sumatra"
- 06/2001 School education degree at Gymnasium Uslar, Germany
- Degree: Allgemeine Hochschulreife (Abitur, equivalent to A-levels)

Languages

- | | |
|----------|---------------|
| German | Mother tongue |
| Englisch | Fluent |
| French | Basic skills |

Hannover, December 2013